Lehrstuhl E15
Physik - Department

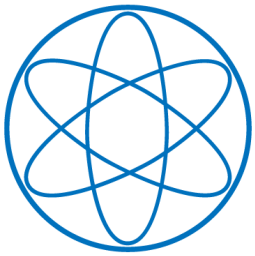

Reconstruction and Measurement of Cosmogenic Signals in the Neutrino Experiment Borexino

Dissertation
von

Johannes Quirin Meindl

Technische Universität
München

Technische Universität München
Physik-Department
Lehrstuhl für Experimentalphysik und Astroteilchenphysik
Univ.-Prof. Dr. Stefan Schönert

Reconstruction and Measurement of Cosmogenic Signals in the Neutrino Experiment Borexino

Johannes Quirin Meindl

Vollständiger Abdruck der von der Fakultät für Physik der Technischen Universität München zur Erlangung des akademischen Grades eines

Doktors der Naturwissenschaften (Dr. rer. nat.)

genehmigten Dissertation.

Vorsitzender:	Univ.-Prof. Dr. B. Garbrecht
Prüfer der Dissertation:	
	1. Univ.-Prof. Dr. L. Oberauer
	2. Priv.-Doz. Dr. H. Kroha

Die Dissertation wurde am 22.04.2013 bei der Technischen Universität München eingereicht und durch die Fakultät für Physik am 14.06.2013 angenommen.

Abstract

Underground laboratories around the globe provide low-count rate experiments with the necessary shielding against the large flux of cosmic muons present at the Earth's surface. Depending on the depth of the underground site, the muon flux is reduced by up to eight orders of magnitude. Hower, the residual muons, and the neutrons and radioisotopes they produce in nuclear spallation processes, still pose a significant background for many of these experiments.
This thesis focusses on cosmogenic background signals in the neutrino experiment Borexino, which is located at the *Laboratori Nazionali del Gran Sasso* underground site at a depth of 3800 meters of water equivalent. The work encompasses the identification, spatial reconstruction, and measurement of rates and production yields of these cosmogenic events.
For the efficient tagging of long-lived cosmogenic radioisotopes of lifetimes in the order of seconds and longer, the spatial reconstruction of the parent muon is essential. Based on the characteristic light emission profile of muons crossing the inner detector of Borexino, a new muon track reconstruction algorithm was developed. Furthermore, to increase the performance of the existing muon track reconstruction of Borexino's outer detector, a routine was programmed to automatically calibrate the photomultiplier tubes in timing and charge response.
Muons entering the experiment can cause fast secondary signals from decays and captures of stopped muons, and the captures of muon-induced neutrons. To identify these events in the high noise environment after the muon, dedicated search algorithms were developed. Based on the detected signals, these fast muon-correlated events are studied. The fraction and lifetime of stopped muons are found to be in agreement with expectations. The production yield of cosmogenic neutrons is measured to $(3.10 \pm 0.07_{\mathrm{stat}} \pm 0.08_{\mathrm{syst}}) \cdot 10^{-4}\, n/(\mu \cdot (g/cm^2))$. The corresponding capture time in the Borexino scintillator pseudocumene is determined to $\tau_n = (259.7 \pm 1.3_{\mathrm{stat}} \pm 2.0_{\mathrm{syst}})\, \mu s$.
The production yields of all major cosmogenic radioisotopes (^{12}N, ^{12}B, ^{8}He, ^{9}C, ^{9}Li, ^{8}B, ^{6}He, ^{8}Li, ^{11}Be, ^{10}C, and ^{11}C) are measured, exploiting the correlations in time and space with the parent muon and possible accompanying neutrons.

Zusammenfassung

Experimente mit niedrigen Zählraten werden in Untergrundlaboren betrieben, um sie gegen den hohen kosmischen Myonenfluss auf der Erdoberfläche abzuschirmen. Abhängig von der Tiefe des Untergrundlabors wird der Myonenfluss um bis zu acht Größenordnungen reduziert. Dennoch verursachen die verbleibenden Myonen, sowie die durch Kernspallation erzeugten Neutronen und Radioisotope, einen signifikanten Untergrund in vielen dieser Experimente.
Diese Arbeit beschäftigt sich mit den kosmogenen Untergrundsignalen im Neutrinoexperiment Borexino, welches sich im *Laboratori Nazionali del Gran Sasso* Untergrundlabor in einer Tiefe von 3800 Meter Wasseräquivalent befindet. Sie umfasst die Identifikation, räumliche Rekonstruktion und Messung der Produktionsraten dieser kosmogenen Ereignisse.
Die räumliche Rekonstruktion der Myonenspur ist unerlässlich, um langlebige kosmogene Radioisotope ($\tau \geq 1\,s$) effizient zu selektieren. Auf Grundlage der charakteristischen Lichtemission, die Myonen beim Durchqueren des inneren Borexino-Detektors erzeugen, wurde ein neuer Algorithmus zur Myonspurrekonstruktion entwickelt. Um die Präzision der bereits existenten Myonspurrekonstruktion des äußeren Borexino-Detektors zu erhöhen, wurde darüber hinaus eine Routine zur automatischen Kalibrierung des Zeit- und Ladungssignals der Photomultiplier entwickelt.
Wenn Myonen den Detektor durchqueren, können sie verschiedene sekundäre Signale erzeugen. Einerseits kann das Myon selbst zerfallen oder eingefangen werden, andererseits kann auch der Einfang myon-induzierter Neutronen ein Signal verursachen. Im Rahmen dieser Arbeit wurden Suchalgorithmen entwickelt, um diese schnellen, sekundären Ereignisse in dem starken Untergrundrauschen nach dem Myon zu identifizieren. Der beobachtete Anteil an gestoppten Myonen, sowie deren Lebensdauer, stimmt mit den Erwartungen überein. Die Produktionsrate kosmogener Neutronen beträgt $(3.10 \pm 0.07_{\text{stat}} \pm 0.08_{\text{syst}}) \cdot 10^{-4}\, n/(\mu \cdot (\text{g/cm}^2))$. Außerdem wurde die Neutroneinfangszeit im Borexino-Szintillator Pseudocumol gemessen: $\tau_n = (259.7 \pm 1.3_{\text{stat}} \pm 2.0_{\text{syst}})\,\mu s$. Basierend auf der räumlichen und zeitlichen Korrelationen mit dem primären Myon und potenziellen Begleitneutronen, wurden die Produktionsraten aller wichtigen kosmogenen Radioisotope (^{12}N, ^{12}B, ^{8}He, ^{9}C, ^{9}Li, ^{8}B, ^{6}He, ^{8}Li, ^{11}Be, ^{10}C und ^{11}C) bestimmt.

Contents

1 Introduction **1**

1.1 Neutrino Physics . . . 2

1.1.1 Neutrinos in the Standard Model . . . 3

1.1.2 Oscillations in Vacuum . . . 3

1.1.3 Oscillations in Matter . . . 5

1.1.4 Open Questions . . . 7

1.2 Natural Neutrino Sources . . . 7

1.2.1 The Sun . . . 7

1.2.2 The Earth . . . 11

1.2.3 Supernovae . . . 12

2 The Borexino Experiment **15**

2.1 Detection Technique . . . 15

2.2 Detector Design . . . 16

2.2.1 Inner Detector . . . 16

2.2.2 Outer Detector . . . 18

2.2.3 Detector Operations . . . 19

2.3 Physics Program and Results . . . 20

2.3.1 Solar Neutrinos . . . 21

2.3.2 Geo-Neutrinos . . . 26

2.3.3 Supernova Neutrinos . . . 27

2.3.4 The CNGS Neutrino Beam . . . 27

3 Borexino Data Acquisition and Simulation **31**

3.1 Photomultiplier Tubes . . . 31

3.1.1 Response Function . . . 32

3.1.2 Late Pulses and Afterpulses . . . 33

3.2 Data Acquisition Systems 35
3.2.1 Trigger System 35
3.2.2 Inner Detector 36
3.2.3 Outer Detector 36
3.3 Echidna Data Processing Software 37
3.3.1 Data Calibration 37
3.3.2 Physics Reconstruction 38
3.3.3 Energy Observables 39
3.4 Princeton Analog System 42
3.5 Borexino Simulation Framework 42
3.5.1 Physics Generator 42
3.5.2 Geometry 43
3.5.3 Electronics Simulation 43
3.5.4 Echidna Processing 43

4 Cosmic Muons **45**
4.1 Muon Detection and Flux 46
4.1.1 Outer Detector Muon Flags 46
4.1.2 Inner Detector Muon Flag 48
4.1.3 Muon Detection Efficiencies 48
4.1.4 Muon Flux 49
4.2 Outer Detector Muon Tracking 49
4.3 Outer Detector Calibration 50
4.3.1 LED Calibration System 51
4.3.2 Calibration Algorithms 52
4.3.3 Resolution Improvement 55
4.3.4 Outer Detector Maintenance 57
4.4 Inner Detector Muon Tracking 61
4.4.1 Muon Light Emission 62
4.4.2 Entry Point Reconstruction 62
4.4.3 Symmetry Plane Reconstruction 65
4.4.4 Exit Point Reconstruction 68
4.5 Global Muon Tracking 73
4.6 Tracking Performance 75
4.6.1 Reconstruction Resolution 79

4.6.2 Cosmic Muon Angular Distribution 81

5 Cosmogenic Neutrons 83
5.1 Neutron Detection 84
5.2 Energy Observable: Number of cluster hits 91
5.3 Muon Event Clusters 91
5.3.1 Muons and Muon Decays 91
5.3.2 Neutron Captures and accidental Coincidences 101
5.4 Neutron Event Clusters 103
5.4.1 Statistical Neutron Fluctuations 104
5.4.2 Energy Response 104
5.4.3 Neutron Detection Efficiency 106
5.4.4 Energy Treshold Definition 112
5.4.5 Position Reconstruction 113
5.5 Neutron Capture Time 117
5.6 Uncorrelated Background and Noise Events 122
5.7 Effective Detection Volume 124
5.8 Neutron Production Rate and Yield 129
5.9 Rate of neutron-producing Muons and Neutron Multiplicity 131

6 Cosmogenic Radioisotopes 137
6.1 Theory of Simultaneous Fits 138
6.2 Energy Observable: Cluster charge 139
6.3 Generation of Spectral Shapes 141
6.4 Cosmogenic Production Rates and Yields 155
6.4.1 ^{12}N and ^{12}B 156
6.4.2 ^{8}He and ^{9}Li 157
6.4.3 ^{8}B, ^{6}He and ^{8}Li 159
6.4.4 ^{9}C 161
6.4.5 ^{11}Be 163
6.4.6 ^{10}C 164
6.4.7 ^{11}C 166
6.5 Compilation of Results and Comparison to Kamland 169

7 Conclusion 171

8 Appendix **177**

Chapter 1

Introduction

With the first direct discovery of the neutrino particle in 1956 by Cowan and Reines [1], a new field of science was born: experimental neutrino physics. While these first experiments employed reactors as neutrino sources, Davis eventually lead this field to the stars, by detecting the first neutrinos from the Sun in 1968 [2]. This exciting field has been growing ever since, contributing to fundamental particle physics, cosmology, astrophysics, and geophysics.
As only weakly-interacting particles, neutrinos are unaffected by electromagnetic fields, thus mainting their directionality and pointing back to their origin. In addition, they barely interact with matter, allowing to probe the interior of their source. These properties make neutrinos ideal messengers to investigate the inner processes of celestial bodies/phenomena, like nuclear fusion in the Sun, radiogenic heat production in the Earth, and Supernova explosions. With focus on solar fusion reactions, the neutrino-detector Borexino was commissioned in 2007. Employing the liquid-scintillator technology at record high radiopurity levels, Borexino was the first experiment to directly measure solar neutrino fluxes below 3.5 MeV [3, 4, 5]. To this moment, Borexino is still unique in this capability. The Ph.D. work presented in this thesis was performed in the framework of the Borexino experiment.

The physics goals and design of the solar neutrino experiment Borexino are described in Chapter 2, while Chapter 3 is dedicated to the data acquisition, reconstruction, and simulation infrastructure. Chapters 4 to 6 present the work performed in this thesis on the reconstruction and measurement of cosmogenic signals in Borexino. These are composed of cosmic muons, as well as the neutrons and cosmogenic radioisotopes they produce in nuclear spallation processes inside the detector. Chapter 4 presents the work performed in this thesis on Borexino's muon tracking capabilities, which plays a key role in the efficient tagging of long-lived cosmogenic isotopes. To improve the tracking resolution of the

water-filled Outer Detector, an algorithm was written to automatically calibrate the instrumented photomultiplier tubes. Furthermore, a muon track reconstruction algorithm was developed for the scintillator-filled Inner Detector, based on the characteristic light emission profile of a crossing muon. The neutrons induced by these muons are subject of Chapter 5. It covers the neutron detection algorithms devised as part of this thesis, as well as a detailed description of the detected physics events. Based on calibrations with reference systems and Monte Carlo simulations, the mean neutron capture time and the production yield of cosmogenic neutrons at the Borexino depth of $3800\,m$ of water equivalent are derived. In addition, the fraction and lifetime of stopped muons is investigated. Chapter 6 focuses on the radioisotopes produced by muons. Using a simultaneous fit of the energy and time distribution of candidate events, the production rates and yields of all major cosmogenic istopes (^{12}N, ^{12}B, ^{8}He, ^{9}C, ^{9}Li, ^{8}B, ^{6}He, ^{8}Li, ^{11}Be, ^{10}C, and ^{11}C) have been measured in this thesis.

The first part of the current Chapter presents the basic properties of the neutrino particle, describing the mechanisms of flavor oscillations in vacuum and matter. The second part focuses on natural neutrino sources, producing neutrinos of significant flux at low energies (i.e. below $10\,MeV$).

1.1 Neutrino Physics

When Davis performed in the 1970's the first measurement of solar neutrinos to probe the fusion processes in the Sun, he got surprising results: his radiochemical experiment located at the Homestake mine detected only one third of the (electron-)neutrino flux predicted by solar models [2]. Due to the temperature and pressure dependance of solar fusion processes, it was first speculated that these models contained wrong assumptions on the conditions in the solar core. However, these speculations were invalidated by helioseismological measurements, confirming the solar models [6]. Astrophysical reasons could not explain the deficit, and the *Solar Neutrino Problem* (SNP) persisted for more than 30 years [7]. Eventually in 2002, the SNO experiment proved, that the deficit in solar neutrino detection is in fact caused by neutrino physics beyond the *Standard Model of Particle Physics* [8]: the ability of neutrinos to dynamically oscillate in flavor. While the neutrino within the Standar Model will be presented in the first part of this Section, the second part is dedicated to the description of the mechanism of the neutrino oscillations in vaccum and matter.

1.1.1 Neutrinos in the Standard Model

In the *Standard Model of Particle Physics* (SM) [9], leptons and antileptons are divided in three generations, each consisting of a charged lepton and a (neutral) neutrino of corresponding flavor.

$$\begin{pmatrix} e \\ \nu_e \end{pmatrix} \begin{pmatrix} \mu \\ \nu_\mu \end{pmatrix} \begin{pmatrix} \tau \\ \nu_\tau \end{pmatrix} \tag{1.1}$$

The leptons are subject to the weak interaction, which is procurred in *Neutral Current* (NC) and *Charged Current* (CC) reactions by the vector bosons Z^0 ($m_Z = 92\,GeV$) and $W^\pm$ ($m_W = 80\,GeV$), respectively. As a result of Heisenberg's uncertainty principle, the large masses of these exchange bosons decrease the range and strength of the weak-interaction at low energies. Typical interaction cross-sections are in the order of 10^{-44} to $10^{-43}\,cm^{-2}$.
While the exchange of Z^0 does not affect the lepton type, the exchange of $W^\pm$ results in a lepton conversion within the same generation (preserving the lepton flavor). As the weak interaction maximally violates parity, Z^0 and $W^\pm$ couple only to left-handed particles (and right-handed anti-particles). While the charged leptons can also interact electromagnetically, the neutral neutrinos underly only the weak interaction. As they are assumed to be massless in the SM, they are always in a pure chirality eigenstate. As a result of the maximal parity violation, neutrinos are exclusively left-handed in the SM, while anti-neutrinos exist only as right-handed particles. However, the assumption of massless neutrinos has been invalidated by the experimental observation of neutrino oscillations [8, 10, 11, 12]. In fact, the property of neutrinos to carry mass is fundamental for the field of neutrino physics beyond the SM, including neutrino oscillations (mixing angles, and CP-violating phases), the values and hierarchy of neutrino mass eigenstates (normal or inverted), and the nature of the neutrino (Dirac or Majora particle).

1.1.2 Oscillations in Vacuum

The neutrino flavor eigenstates $|\nu_\alpha\rangle$ ($\alpha = e, \mu, \tau$) can be expressed as the rotation of the neutrino mass eigenstates $|\nu_i\rangle$ ($i = 1, 2, 3$). These mass eigenstates and their eigenvalues m_i describe stationary solutions of the Dirac equation of free particles. The transformation can be written as:

$$\begin{pmatrix} \nu_e \\ \nu_\mu \\ \nu_\tau \end{pmatrix} = \mathbb{U} \begin{pmatrix} \nu_1 \\ \nu_2 \\ \nu_3 \end{pmatrix} \tag{1.2}$$

Parameter	**Value** $[eV]$	**Parameter**	**Value**
m^2_{12}	$7.50^{+0.19}_{-0.20} \cdot 10^{-5}$	$\sin^2(2\theta_{12})$	$0.857^{+0.023}_{-0.025}$
$m^2_{13} \simeq m^2_{23}$	$\pm(2.32^{+0.12}_{-0.08}) \cdot 10^{-3}$	$\sin^2(2\theta_{13})$	0.098 ± 0.013
		$\sin^2(2\theta_{23})$	> 0.95

Table 1.1: Neutrino quadratic mass splittings and mixing angles [14]. The sign of m^2_{13} and m^2_{23} is yet unknown.

Here, the rotation matrix $\mathbb{U}$ denotes the unitary 3x3 *Pontecorvo Maki Nakagawa Sakata* (PMNS) matrix:

$$\begin{aligned}\mathbb{U} &= \begin{pmatrix} 1 & 0 & 0 \\ 0 & c_{23} & s_{23} \\ 0 & -s_{23} & c_{23} \end{pmatrix} \begin{pmatrix} c_{13} & 0 & s_{13}e^{-i\delta} \\ 0 & 1 & 0 \\ -s_{13}e^{-i\delta} & 0 & c_{13} \end{pmatrix} \begin{pmatrix} c_{12} & s_{12} & 0 \\ -s_{12} & c_{12} & 0 \\ 0 & 0 & 1 \end{pmatrix} \\ &= \begin{pmatrix} U_{e1} & U_{e2} & U_{e3} \\ U_{\mu 1} & U_{\mu 2} & U_{\mu 3} \\ U_{\tau 1} & U_{\tau 2} & U_{\tau 3} \end{pmatrix} \end{aligned} \tag{1.3}$$

The parameters s_{ij} and c_{ij} refer to $\sin\theta_{ij}$ and $\cos\theta_{ij}$, with θ_{ij} being the respective rotation angle. The phase δ denotes a potential CP-violating phase. If the neutrino is of Majorana nature, two additional CP-violating phases are introduced [13]. The PMNS matrix $\mathbb{U}$ is unequal to the identity matrix ($\mathbb{I}$) and thus allows for a conversion of flavor eigenstates via mass eigenstate mixing. Assuming a neutrino of energy E created with the flavor eigenstate $|\nu_\alpha\rangle$, the probability to oscillate after time t to an arbitrary flavor $|\nu_\beta\rangle$ is given by:

$$P_{\alpha\beta}(t) = |\langle\nu_\alpha(t)|\nu_\beta\rangle|^2 \tag{1.4}$$

$$= \delta - 4\sum_{i>j} \mathcal{R}\left(U^*_{\alpha i}U_{\beta i}U_{\alpha j}U^*_{\beta j}\right)\sin^2\left(\frac{\Delta m^2_{ij}\,c^4}{4E\hbar}t\right) + 2\sum_{i>j}\mathcal{I}\left(U^*_{\alpha i}U_{\beta i}U_{\alpha j}U^*_{\beta j}\right)\sin\left(\frac{\Delta m^2_{ij}\,c^4}{4E\hbar}t\right) \tag{1.5}$$

$$\text{with } \Delta m^2_{ij} = m^2_i - m^2_j \tag{1.6}$$

Table 1.1 presents the current results on neutrino properties in terms of quadratic mass splittings (Δm^2_{ij}) and mixing angles (θ_{ij}). It is worth noting, that the mixing angle θ_{13} is much smaller than the angles θ_{12} and θ_{23}. In addition, the value of Δm^2_{12} is by two orders of magnitude smaller than the quadratic mass splittings of $\Delta m^2_{13} \simeq \Delta m^2_{23}$. The combination of these effects usually allows to ignore one of the mass eigenstates in the neutrino oscillation, reducing the oscillation solution to a two-flavor scenario. The probablity of flavor conversion in this approximation

is given by:

$$P_{\alpha\beta}(t) = \sin^2(2\theta) \cdot \sin^2\left(\frac{\Delta m^2\, c^4}{4E\hbar} t\right) \quad \text{for } \alpha \neq \beta \tag{1.7}$$

As the neutrinos propagate at approximately the speed of light, this equation also translates to an oscillation of the neutrino flavor in space. The corresponding oscillation length l^{osc} is given by

$$l^{\text{osc}} = \pi \frac{4E\hbar}{\Delta m^2\, c^3} \simeq 2.48\, m\, \frac{E\,[MeV]}{\Delta m^2\,[eV^2]} \tag{1.8}$$

The probability of a neutrino to remain in its flavor eigenstate (i.e. $P_{\alpha\alpha}(t)$) is refered as 'survival probability'. As can be seen from Equ. (1.7), neutrino oscillations require massive neutrinos of different masses ($\Delta m^2_{ij} \neq 0$), as well as a rotation of neutrino flavor eigenstates with respect to the mass eigenstates ($\mathbb{U} \neq \mathbb{I}$).

1.1.3 Oscillations in Matter

When neutrinos traverse matter, their oscillation behaviour is changed with respect to the vacuum-oscillation due to the additional interaction with electrons. While all neutrino flavors can interact via NC reactions with the electrons, the ν_e feature an additional interaction channel via CC reactions. This introduces a phase shift of the ν_e relative to the flavors $\nu_{\mu,\tau}$. As a result, the neutrino mass eigenstates in matter are rotated with respect to the vacuum mass eigenstates. The resulting neutrino mixing angle in matter is given by:

$$\tan 2\theta_{\text{M}} = \frac{\sin 2\theta}{\cos 2\theta - A} \tag{1.9}$$

$$\text{with } A = \frac{2\sqrt{2} G_{\text{f}} N_e E}{\Delta m^2\, c^4} \tag{1.10}$$

Here, θ and Δm^2 denote the mixing angle and quadratic mass splitting of the vacuum oscillation. The parameter A describes the difference in scattering amplitude between ν_e and $\nu_{\mu,\tau}$, and depends on the Fermi constant G_{f}, the local electron-density N_e, and the neutrino energy E. The corresponding neutrino oscillation length in matter is given by

$$l^{\text{osc}}_{\text{M}} = l^{\text{osc}} \frac{\sin^2(2\theta)}{\sin^2(2\theta_{\text{M}})} \tag{1.11}$$

Depending on the energy of the neutrinos and the electron density, the modification of the mixing angle can lead to a matter-enhanced flavor conversion, the so-called *Mikheyev Smirnov Wolfenstein* (MSW) effect [15, 16].

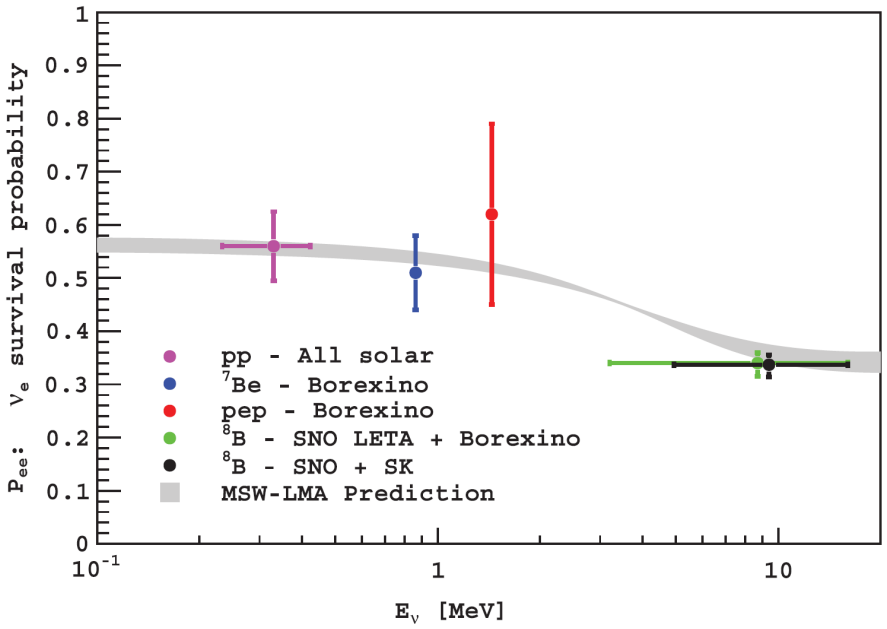

Figure 1.1: The solar ν_e survival probability as predicted by the MSW-LMA oscillation solution. The band is given by the 1σ range of the oscillation parameters. In addition, experimental results are shown. [5]

As will be described in Section 1.2.1, our Sun generates ν_e in several fusion processes. In case of energetic neutrinos in a region of high electron density, the relation $A \gg \cos 2\theta$ holds and thus the matter mixing angle θ_{M} is close to 90°. As a result, the $|\nu_e\rangle$ flavor eigenstate is close to the vacuum mass eigenstate $|\nu_2\rangle$. In case the oscillation length $l_{\mathrm{M}}^{\mathrm{osc}}$ is large compared to the spatial variation of the electron density, the neutrino remains in state $|\nu_2\rangle$ while propagating outwards of the Sun. When the neutrino eventually enters the vacuum, the probability to be detected in the flavor eigenstate $|\nu_e\rangle$ is only:

$$P \quad = \quad |\langle\nu_2|\nu_e\rangle|^2 = \sin^2(\theta_{12}) \simeq 30\% \tag{1.12}$$

The remaining neutrinos have dominantly oscillated to the ν_μ flavor, which features a large component of the mass eigenstate $|\nu_2\rangle$. The electron interaction cross-section of solar ν_e is about a factor 6 higher than for $\nu_{\mu,\tau}$. In consequence, neutrino detectors are more senstive to the ν_e-flux, and thus observe a deficit in the neutrino interaction rate compared to the expectation without flavor oscillation (i.e. a pure solar ν_e-flux). The strength of the matter-induced flavor conversion is energy-dependant via the scattering amplitude A (Equ. (1.10)), and contributes significantly above $\simeq 5\,MeV$. In consqeuence, solar neutrinos of sub-MeV energies (i.e. $A \ll \cos 2\theta$) are subject to vacuum oscillations only. Figure

1.1 presents the energy-dependant survival probability of solar ν_e according to the MSW-LMA oscillation solution. The Figure also contains measurements of different solar neutrino branches for comparison (see Section 1.2.1). It has to be noted, that the MSW-effect can only occur for solar neutrinos if the quadratic mass splitting Δm^2_{12} is of positive value (see Equ. (1.9) and (1.10)). Due to the confirmation of the MSW-effect by experiments, the positive sign in Δm^2_{12} is well established.

1.1.4 Open Questions

While the sign of Δm^2_{12} is known, this is not the case for Δm^2_{23} ($\simeq \Delta m^2_{13}$). In case of a positive sign, the eigenstates are ordered by the so-called *normal hierachy* (i.e. $m_1 < m_2 < m_3$), while a negative sign corresponds to the *inverted hierarchy* ($m_3 < m_1 < m_2$). Furthermore, the absolute values of the neutrino masses are still under investigation [17, 18, 19]. So far, only upper limits on the neutrino masses exist, with the most stringent one originating from cosmological obervations. At a 95% confidence limit, the sum of the neutrino masses $\sum m_{\nu_i}$ is less than $0.58\,eV$ [20]. In addition to the quantification of the absolute mass scale, the sheer fact that at least two neutrinos posses masses leads to the question on the nature of the neutrino. Is it a Majorana particle, and thus its own anti-particle, or is it of Dirac nature? Depending on this, the number of possible CP-violating phases in neutrino oscillations is three or one.

1.2 Natural Neutrino Sources

While many intrinsic properties of the neutrino are still subject of research, our understanding about this particle has grown to the point, that we can employ it as a probe of the internal processes of natural neutrino sources. In the following, this Section will focus on the brightest (known) sources of neutrinos, i.e. the Sun, the Earth, and Supernova explosions.

1.2.1 The Sun

The Sun emits neutrinos in the fusion of four protons to a ^{4}He nucleus via the net reaction

$$4p \rightarrow {}^4\mathrm{He} + 2e^+ + 2\nu_e \tag{1.13}$$

Only about 2% of the total energy release of $26.73\,MeV$ is applied to the electron-neutrinos. It is expected by *Solar Standard Models* (SSM) that the Sun is in a quasi-steady thermal equilibrium, i.e. the power emitted on its surface is equal to the power generated in its interior. According to this, the Sun generates for every

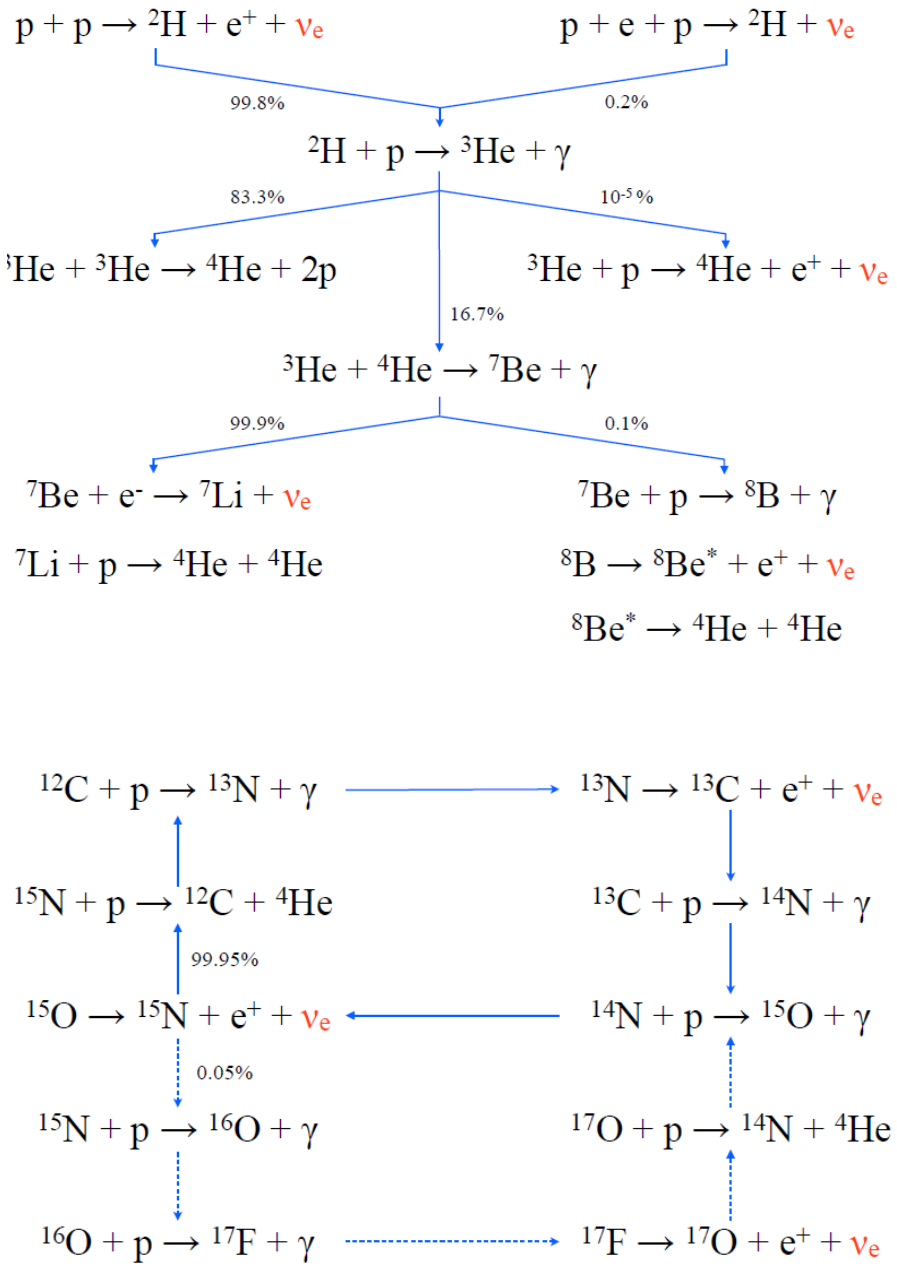

Figure 1.2: Schematics of the solar fusion processes in the pp-chain (top) and the CNO-cycle (bottom) [21]. The emission of neutrinos is highlighted in red. The branching ratios are based on [22].

13 MeV of emitted photon energy about one neutrino. With the solar constant of

Neutrino branch	E_ν	Solar neutrino fluxes	
	$[MeV]$	GS98	AGSS09
pp	[0,0.42]	5.98	6.03
pep	1.44	1.44	1.47
hep	[0,18.8]	8.04	8.31
^{7}Be	0.86, 0.38	5.00	4.56
^{8}B	[0,14.6]	5.58	4.59
^{13}N	[0,1.2]	2.96	2.17
^{15}O	[0,1.7]	2.23	1.56
^{17}F	[0,1.7]	5.52	3.40

Table 1.2: Solar neutrino fluxes, as predicted by the GS98 (high metallicity) and AGSS09 (low metallicity) *Standard Solar Models* [23]. The fluxes are given in units of 10^{10} (pp), 10^{9} (^{7}Be), 10^{8} (pep, ^{13}N, ^{15}O), 10^{6} (^{8}B, ^{17}F), and 10^{3} (hep) $cm^{-2}s^{-1}$. The different metallicities result in noticeable differences in the predicted neutrino fluxes from the CNO-cycle (i.e. neutrinos from ^{13}N, ^{15}O, and ^{17}F).

$S = 1367\,Wm^{-2}$ [1], the Sun generates a neutrino flux of $6.6 \cdot 10^{14}\,m^{-2}s^{-1}$ at the distance of the Earth. As a result, our host star is the most prominent (continuous) source of neutrinos to be measured on Earth.

The fusion of protons to Helium is procured by two reaction sequences, i.e. the pp-chain and the CNO-cycle. The pp-chain accounts for about 99% of the total energy production in our Sun, and is depicted in Figure 1.2. As can be seen, neutrinos are generated in the processes:

$$\text{pp-}\nu \quad : \quad p + p \rightarrow {}^{2}\text{He} + e^{+} + \nu_e \tag{1.14}$$

$$\text{pep-}\nu \quad : \quad p + e^{-} + p \rightarrow {}^{2}\text{He} + \nu_e \tag{1.15}$$

$$\text{hep-}\nu \quad : \quad {}^{3}\text{He} + p \rightarrow {}^{4}\text{He} + e^{+} + \nu_e \tag{1.16}$$

$$^{7}\text{Be-}\nu \quad : \quad {}^{7}\text{Be} + e^{-} \rightarrow {}^{7}\text{Li} + \nu_e \tag{1.17}$$

$$^{8}\text{B-}\nu \quad : \quad {}^{8}\text{B} \rightarrow {}^{8}\text{Be}^{*} + e^{+} + \nu_e \tag{1.18}$$

The corresponding energies and fluxes are given in Table 1.2, while the spectra are shown in Figure 1.3.
The subdominant CNO-cycle is named after the participating elements in this reaction sequence, i.e. Carbon, Nitrogen, and Oxygen. As it is shown in Figure 1.2, ^{12}C serves as a catalyst for the fusion of the four protons to Helium, with

[1] The solar constant states the average intensity of the solar electromagnetic radiation on the Earth's surface.

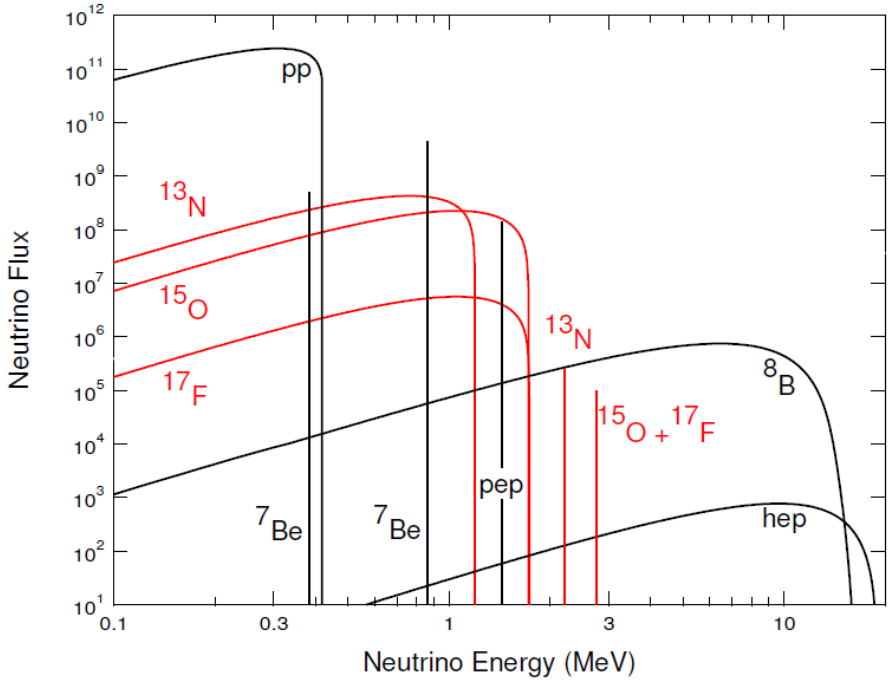

Figure 1.3: Expected solar neutrino spectra of the pp-chain (black lines) and the CNO-cycle (red lines) [22]. Line fluxes are given in $cm^{-2}s^{-1}$ and spectral fluxes in $cm^{-2}s^{-1}MeV^{-1}$. The presented fluxes are based on the SSM of Bahcall et al. of 2005. The most recent values on the solar fluxes (SSM AGSS09) are given in Table 1.2.

neutrinos being produced in the reactions:

$$^{13}\text{N-}\nu \quad : \qquad ^{13}\text{N} \rightarrow ^{13}\text{C} + e^+ + \nu_e \tag{1.19}$$

$$^{15}\text{O-}\nu \quad : \qquad ^{15}\text{O} \rightarrow ^{15}\text{N} + e^+ + \nu_e \tag{1.20}$$

$$^{17}\text{F-}\nu \quad : \qquad ^{17}\text{F} \rightarrow ^{17}\text{O} + e^+ + \nu_e \tag{1.21}$$

Expected fluxes, energies, and spectra are given in Table 1.2 and Figure 1.3. As Carbon has a higher Coloumb barrier than the nuclei in the pp-chain, it requires higher energies for a considerable reaction rate. For the temperatures in our Sun of $1.5 \cdot 10^7\,K$, this fusion mechanism contributes only $\simeq$1% to the total energy production. However, due to its strong temperature-dependance, the CNO-cycle is the dominant energy production mechanism at temperatures above $\simeq 1.8 \cdot 10^7\,K$. This is the case for heavy stars larger than about 1.5 solar masses. In terms of astrophysics, elements heavier than Helium are considered as metals. As the CNO-cycle is dependant on the metal abundance in the solar plasma, the metallicity of the Sun is directly connected to the CNO-induced solar neutrino fluxes. In this thesis, two prominent SSM's are considered, which are based on two different

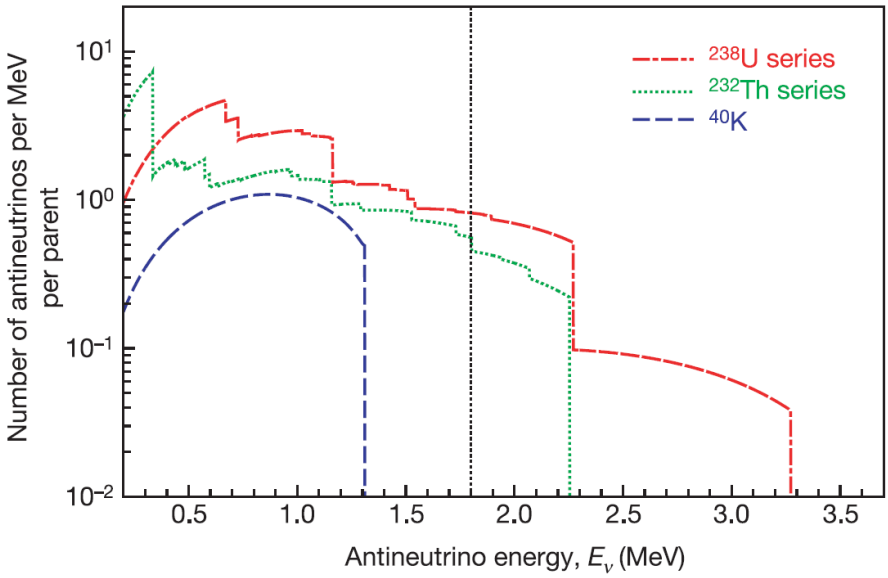

Figure 1.4: Expected energy spectra of geo-neutrinos ($\overline{\nu}_e$) emitted in the decay chains of ^{238}U, ^{232}Th, and ^{40}K. The black dotted vertical line presents the energy threshold of the inverse beta-decay channel (i.e. $1.8\,MeV$). With an endpoint of $1.4\,MeV$, this reaction channel is insensitive to $\overline{\nu}_e$ from the ^{40}K contribution. [26]

measurements on the solar metallicity [24, 25]: The GS98 (high metallicity) and the AGSS09 (low metallicity) models [23]. A measurement of the CNO-neutrinos would allow to test these models. The measurements of the solar neutrino fluxes by the Borexino experiment are presented in Sec. 2.3.1.

1.2.2 The Earth

According to the *Bulk Silicate Earth* geophysical model, about 50% of the total terrestrial heat flow of $47\,TW$ are expected to be of radiogenic origin, i.e. caused by the decays of ^{40}K and the progenies of ^{238}U and ^{232}Th [27]. The $\overline{\nu}_e$ emitted in the corresponding β-decays are called geo-neutrinos, which serve as direct probes of the abundances and distribution of these radioactive elements in our planet's crust and mantle. Thus, a direct measurement of geo-neutrinos provides a test of different Earth composite models. The liquid-scintillator technology is perfectly suited for the detection of these $\overline{\nu}_e$ via the inverse beta-decay:

$$p + \overline{\nu}_e \rightarrow n + e^+ \tag{1.22}$$

The coincidence of the prompt positron and the delayed signal from the neutron capture (mean capture time of several hundred μs in liquid scintillator) provides

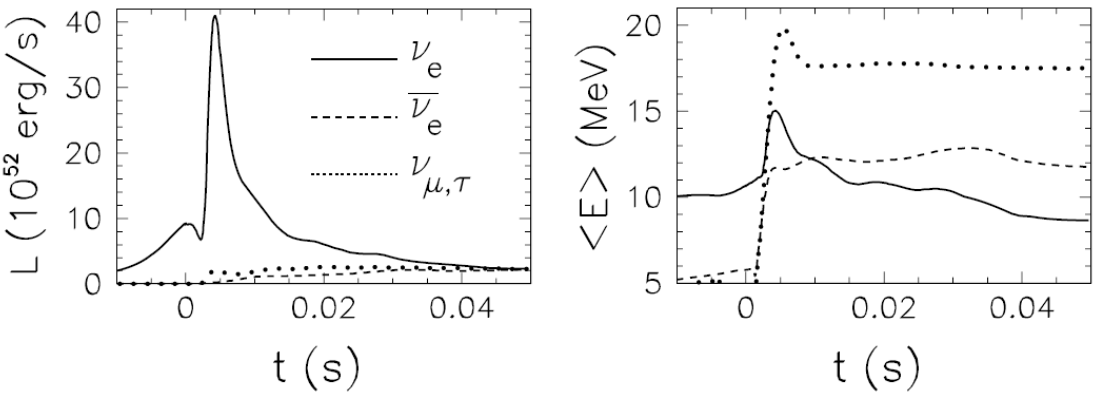

Figure 1.5: Expected luminosity (left) and mean-energy (right) distributions of neutrinos emitted in the first $50\,ms$ of a core-collapse Supernova of a 10.8 $M_\odot$ progenitor star [28]. The neutronization process of the stellar core generates a prompt ν_e-burst, followed by the build-up of $\overline{\nu}_e$ and $\nu_{\mu,\tau}$ ($\overline{\nu}_{\mu,\tau}$). The figure is based on numerical simulations by [29]. Quantities are given in the laboratory frame of a distant observer.

a distinctive signal and thus a powerful background suppression. With an energy threshold of $1.8\,MeV$, this reaction channel is sensitive to the geo-neutrino contributions of the ^{238}U and ^{232}Th chains. However, with an endpoint of $1.4\,MeV$, the contribution of ^{40}K is below the energy threshold (see Figure 1.4). The results of the Borexino experiment on geo-neutrinos are presented in Section 2.3.2.

1.2.3 Supernovae

The energy released in the fusion processes of a star generates the necessary radiative pressure to counterbalance the gravitational pull of the stellar mass. When the thermonuclear fuel is exhausted, gravitation dominates and the star contracts. With increasing density, the temperature rises until the conditions are met for heavier nuclides to fuse. With the re-ignition of nuclear fusion, the star enters a new equilibrium state. For a massive star of more than $\simeq 8\,M_\odot$, this process continues till the fusion of Silicon to Iron. As Iron has the highest binding energy, the nuclear fusion is at its end, and the star becomes unstable against its own gravitation. Infalling stellar material increases the pressure beyond the electron degeneracy pressure, compacting the core to nuclear densities ($\simeq 10^{14}\,g/cm^3$). The core transforms to a proto-neutron star, emitting a prompt ν_e-burst in the neutronization process (see Figure 1.5). As the mean path length of γ's in this high-density matter is extremely short, almost all energy is released by the core via Kelvin-Helmholtz cooling, emitting neutrinos of all flavors in a time interval

of $\simeq$10 s. About 99% of the gravitational collapse energy is released in a total of 10^{58} neutrinos, putting the Supernova type IIa explosion to one of the brightest neutrino sources in the universe. The average neutrino energies are expected to be in the range of $12 - 18\,MeV$ [30].

Chapter 2

The Borexino Experiment

First design studies on the Borexino project started in the 80's with the goal to build a detector capable of measuring in real-time solar neutrinos in the sub-MeV energy range. The requirements of the low energy threshold, high energy resolution, and expected low solar neutrino interaction rate were met by conceiving a $300\,t$ organic liquid-scintillator detector. However, the expected solar neutrino signal of only tens of events per day in $100\,t$ of target material puts stringent requirements on the radiopurity of the scintillator and the surrounding construction materials. With a necessary radioactivity equivalent of less than $10^{-9}\,Bq/kg$, the core of Borexino had to be 9-10 orders of magnitude less radioactive than any naturally occurring material on Earth.
To develop and test techniques for the purification of the scintillator, a prototype detector of the Borexino experiment, *the Counting Test Facility*, was built in the early 90's. Although reduced in scale to a target mass of about $4\,t$, this prototype exhibits all key features of the main detector. Demonstrating the feasibility of the required low radioactive background levels for solar neutrino detection in a large scale liquid-scintillator detector, construction of the Borexino experiment started in 1996 at the underground site of *Laboratori Nazionali del Gran Sasso* (LNGS). The experiment has been comissioned in May 2007 and is taking data ever since.

2.1 Detection Technique

The electrons of the liquid-scintillator molecules offer a target for elastic scattering via neutral current interaction for neutrinos of all flavors:

$$\nu_x + e^- \rightarrow \nu_x + e^- \tag{2.1}$$

Due to the low energy of solar neutrinos in the order of MeV and below, charged current interactions are limited to ν_e[1]. In consequence, the interaction cross section of ν_e is about a factor of 6 higher than for $\nu_{\mu,\tau}$. The scattered electron deposits its energy in the scintillator, producing light which is detected by an array of photomultiplier tubes (PMT). With a mean free path of at most a few centimeters in the scintillator, the recoil electron is an almost point like light source. Therefore, it provides no directional information on the original neutrino. Moreover, β- and γ-emission from radioactive background in the detector produce signals, which are indistinguishable from ν-signals on an event-by-event basis. Therefore, an ultra-high level of radio-purity is the main requirement for a determination of low-energetic solar neutrino fluxes.

2.2 Detector Design

To achieve the extremely low levels of radioactive background signals in the central target volume of liquid scintillator, the principle of graded shielding is applied to suppress the contribution of external background. In addition, the radiopurity of the construction and screening materials increases towards the center.
The Borexino experiment consists of two independent subdetectors, separated by the *Stainless Steel Sphere*: the *Inner Detector* and *Outer Detector*, filled with liquid scintillator and water, respectively (see Figure 2.1). In the following the main detector components of Borexino will be presented. Further descriptions on the Borexino design can be found in [31, 32].

2.2.1 Inner Detector

Liquid Scintillator and Inner Vessel

The *Inner Detector* (ID) contains at its center the active volume of $280\,t$ of ultra-clean liquid scintillator (density $\rho = 0.88\,t/m^3$). The scintillator mixture consists of the organic solvent *pseudocumene* (PC, 1,2,4-trimethylbenzene, $C_6H_3(CH_3)_3$) and the wavelength shifter PPO (2,5-diphenyloxazole, $C_{15}H_{11}NO$) at a concentration of $1.5\,g/l$. PC molecules are excited by charged particles traversing the scintillator and transfer non-radiatively their excitation energy to the PPO. Subsequently, PPO radiates the energy in photons with a fast decay time of $\simeq 3\,ns$ at a peak wavelength of $\simeq 360\,nm$. At these wavelenghts the light attenuation length of the scintillator mixture is $\simeq 8\,m$, providing a high transparency. The PC/PPO solution

[1] Charged current interaction of $\nu_{\mu,\tau}$ would require the generation of a μ, respectively τ lepton in the final state. However, this is impossible due to the large mass auf μ and τ ($m_\mu = 106\,MeV$, $m_\tau = 1.78\,GeV$) with respect to the low-energetic solar neutrinos.

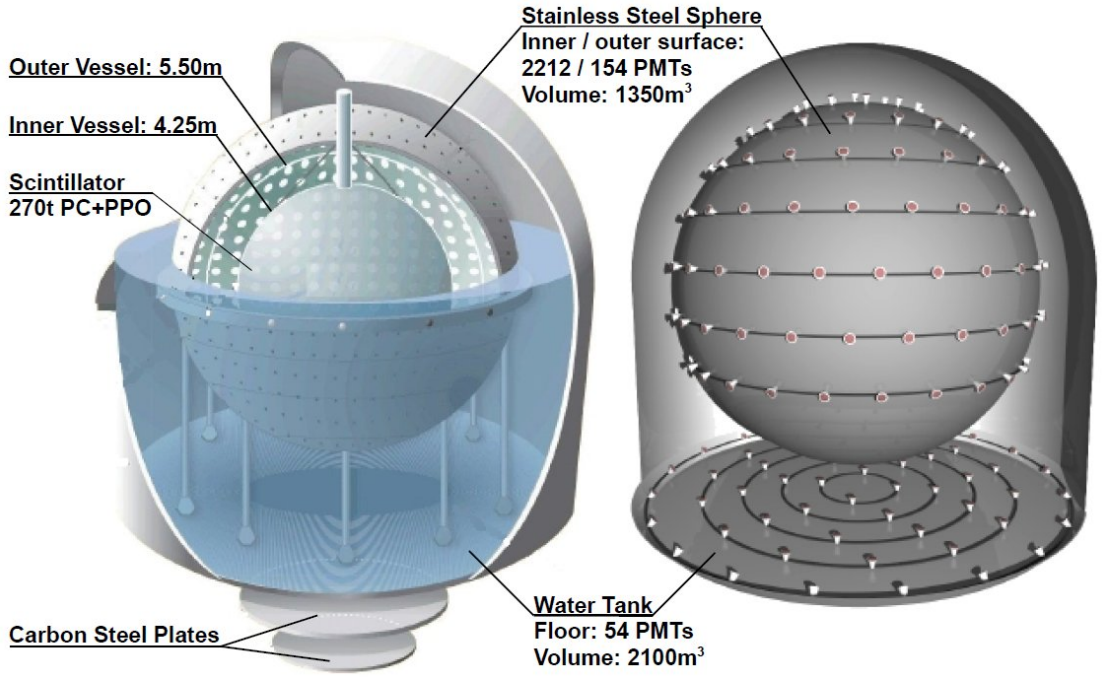

Figure 2.1: Schematics of the Borexino experiment. *Left:* Sectional drawing of the water tank and Stainless Steel Sphere. The 2212 photomultiplier tubes on the inner surface of the sphere are represented as white disks. *Right:* Layout of the water tank instrumentation consisting of 208 photomultiplier tubes. Of these, 154 are mounted on the outer surface of the sphere, while the remaining 54 are distributed in 5 concentric rings on the floor of the water tank.

has a high scintillation yield of $\simeq 10^4$ photons per MeV of deposited energy.
To achieve the necessary ultra-high radiopurity, the scintillator was purified on-site at the time of filling, removing contaminants from dust (^{283}U, ^{232}Th, ^{40}K), from air (^{39}Ar, ^{85}Kr) and from cosmogenically produced ^{7}Be. The design goal of a Uranium/Thorium contamination at the level of $< 10^{-16}\ g/g$ was surpassed with concentrations of $(1.6\pm0.1)\cdot10^{-17}\ g/g$ and $(6.8\pm1.5)\cdot10^{-18}\ g/g$, respectively. These contaminations constitute record low-levels of background in the energy range of 0.2-5.0 MeV [4].
The scintillator is contained in a transparent nylon membrane of a radius of 4.25 m and a thickness of 125 μm, the so-called *Inner Vessel* (IV). The IV is hold by nylon strings to counteract the byoance forces caused by a small density difference between scintillator and buffer liquid. Apart from positioning the active volume, the IV acts as a radon (^{222}Rn) barriere. In addition to optical clarity, the nylon has approximately the same refractive index as PC, thus preventing optical aberrations of the emitted scintillation light. As the IV is in direct contact with the active

volume, it was subject of intensive radiopurity controls and production standards. Though low in intrinsic background, an additional software based radial cut of $3\,m$ is usually necessary to reject remaining contents of radioacitve impurities on the IV surface as well as external background, thus defining the *Fiducial Volume* (FV) of a corresponding mass of $100\,t$.

Buffer Liquid and Outer Vessel

The IV is surrounded by $1024\,t$ of buffer liquid composed of PC and DMP (dimethylphytalate) at a concentration of $5.0\,g/l$. It serves as a shield from external γ radiation from the construction material, and matches the density and refractive index of the active liquid scintillator mixture contained in the IV, thus reducing buyoncy and avoiding optical aberrations. The DMP quenches the residual scintillation produced by the PC by a factor of $\simeq$20, thus strongly suppressing signals from the buffer region. The *Outer Vessel*, an additional nylon membrane of $5.50\,m$ and same thickness as the IV, is mounted inside the buffer region close the SSS. It provides an additional barriere against radon diffusion to the sensitive central volume, thus enhancing the effectivenes of the system.

Stainless Steel Sphere

The *Stainless Steel Sphere* (SSS) of a radius of $6.82\,m$ forms the central mechanical support structure of the Borexino experiment. On its inner surface 2212 inward facing 8“ PMTs are uniformly distributed. Of these, 1838 are equipped with aluminium light concentrators, enhancing the light detection efficiency by a factor of about 2 and at the same time limiting the field of view of the PMTs regarding buffer events. To retain some detection efficiency concerning events outside the IV for background studies, the remaining 385 ID PMTs don't poses concentrators and thus have a larger field of view. The total optical coverage of the SSS's inner surface is 30%. Together with its inner components, the inner surface of the SSS forms the *Inner Detector*. In addition, the outer surface of the SSS forms part of the *Outer Detector*, which is described in the next section. It is important to note, that the SSS optically separates the *Inner* and the *Outer Detector* thus creating two independent detectors in terms of light propagation.

2.2.2 Outer Detector

The *Outer Detector* (OD) is a Water Čerenkov detector contained in a steel dome of $18\,m$ diameter and a height of $16.9\,m$. It is filled with $2400\,t$ of ultra-pure de-ionized water and serves as a passive shielding against external γ and neutron radiation, as well as an active muon veto and muon tracker. The characteristic

Čerenkov light cone, emitted by the muons is monitored by 208 8“ PMTs; 154 of these are mounted in 8 horizontal planes on the upper $3/4^{\text{th}}$ of the SSS outer surface while the remaining 54 PMTs are distributed in 5 concentric circles on the floor of the water tank (see Figure 2.1). To increase the muon detection efficiency, 95% of the OD inner surface is covered with highly reflective Tyvek sheets.

2.2.3 Detector Operations

Since the comissioning in May 2007, the collaboration has performed several operations on the Borexino experiment. The spectrum covers liquid-handling operations, scintillator purification, electronics modifications and extensive calibration campaigns. In the following, special focus is put on the operations with impact on the work performed in this thesis. Additional information on upgrades is given in the Chapters covering the respective Borexino components.

Inner Vessel Stability

In autumn 2008, a small leak in the IV of 1-2 mm in diameter was discovered. The loss of scintillator into the buffer region and the corresponding deflation caused a significant deformation of the IV. This was counteracted by repeatedly refilling the vessel with scintillator (about $15\,t$ in total) and reducing the byoance forces by lowering the DMP concentration in the surrounding buffer liquid to $2\,g/l$. The evaluation of the IV shape via an ID camera system and the position reconstruction of the vessel surface events show, that the leak rate has become negligible and the vessel shape stable since February 2010. Further details on the impact of the leak on the IV volume are given in Section 5.7.

Calibration Campaigns

Triggered by the IV leak, the collaboration performed an on-axis calibration of the experiment in October 2008, employing α, β, and γ sources. The sources were lowered with a wire through an access port at the north pole of the IV into the scintillator. A sophisticated off-axis calibration campaign followed in January and July 2009, using a hinge rod system to scan the detector response in the whole IV volume. Besides a set of α, β, and γ sources, this campaign encompassed a diffused laser and an AmBe neutron emitter source. The extended calibration campaign provided crucial input on the detector reponse in terms of position and energy reconstruction, as well as particle identification via pulse shape analysis. The corresponding decrease in the systematic uncertainties of the fiducial volume mass and energy response was key to the precision measurement of the solar ^{7}Be flux to a total uncertainty of 5% [33].

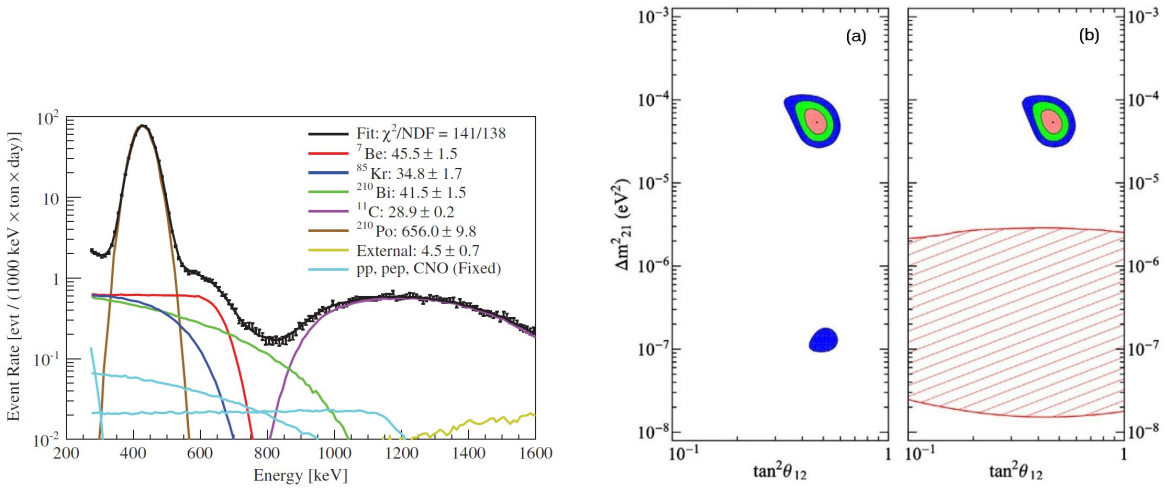

Figure 2.2: Solar ^{7}Be-neutrino measurement. *Left:* Analytical spectral fit of the ^{7}Be-ν electron-recoil shoulder based on 153.6 ton years of fiducial exposure [33]. The fit results in the legend have units $[counts/(d\,100\,t)]$. *Right:* Allowed neutrino oscillations parameter space based on solar neutrino data before (a) and after (b) including Borexino [35]. The Borexino ^{7}Be day-night data excludes the hatched red region at 99.73% C.L., excluding the LOW neutrino oscillation parameter region at $8.5\,\sigma$. The LMA parameter region does not change significantly with the inclusion of the Borexino results.

2.3 Physics Program and Results

Originally designed for the measurement of the solar ^{7}Be-neutrino flux, Borexino surpassed the expectations regarding radiopurity, thus expanding the scientific spectrum of the experiment. Especially in the field of sub-MeV solar neutrino physics, Borexino pioneered with the first real-time detection and precision measurement of ^{7}Be-ν, the measurement of ^{8}B-ν at an unpredecented low (electron-recoil) energy threshold of $3\,MeV$, and the first evidence of pep-ν combined with an upper limit on the CNO-ν flux. Also in the field of terrestrial neutrinos Borexino contributed with the first measurement of geo-neutrinos at a $3\,\sigma$ confidence level. The respective scientific achievements are described in detail in [3, 4, 5, 33, 34], therefore only a brief summary of the results and future goals are covered in this Section.

2.3.1 Solar Neutrinos

^{7}Be-Neutrinos

The mono-energetic $862\,keV$ solar ^{7}Be-ν provide a distinctive Compton-like recoil spectrum with a shoulder at $665\,keV$ electron energy (see Figure 2.2). Besides testing the *Solar Standard Model* (SSM), ^{7}Be-ν provide an excellent probe of the vacuum-dominated regime of neutrino oscillations according to the MSW-LMA oscillation scenario (see Sec. 1.1.3). Furthermore, the possible presence of a day-night effect caused by Earth-matter-induced regeneration of solar ν_e allows to investigate the parameter space of neutrino oscillations using solar-neutrino data only.
Borexino published in September 2011 a precision measurement of the solar ^{7}Be-ν, yielding a neutrino-induced electron scattering rate of $(46.0 \pm 1.5_{\text{stat}}{}^{+1.5}_{-1.6\text{syst}})\,(d\,100\,t)^{-1}$ [33], derived as the average from an analytical and a Monte-Carlo-based spectral fit to the data. Using the neutrino oscillation parameters of [9], this measurement translates to a flux of $\Phi(^7\text{Be}) = (4.84 \pm 0.24) \cdot 10^9 cm^{-2} s^{-1}$, corresponding to a ratio of measurement to the GS98 (high metallicity) SSM expectation of 0.97 ± 0.09 (see Sec. 1.2.1). On the other hand, fixing the ^{7}Be-ν rate according to the SSM expectation, a ν_e surivival probability of $P_{ee} = 0.51 \pm 0.07$ at $862\,keV$ was found. In addition, the absence of a day-night asymmetry in the ^7Be-ν interaction rate was published in November 2011 [35], reporting an asymmetry of

$$A_{\text{dn}} = 2\frac{R_{\text{N}} - R_{\text{D}}}{R_{\text{N}} + R_{\text{D}}} = 0.001 \pm 0.012_{\text{stat}} \pm 0.007_{\text{syst}} \tag{2.2}$$

whereat R_{N} and R_{D} denote the ^{7}Be-ν rate at night and at day, respectively. The result is compatible with zero and in agreement with the prediction of the MSW-LMA solution, excluding the LOW region at more than $8.5\,\sigma$ without using reactor anti-neutrino data, i.e. without invoking CPT symmetry (see Figure 2.2).

^{8}B-Neutrinos

The ^{8}B-ν flux had been measured in the past by the Water Čerenkov detectors SNO and Super-Kamiokande at energies above $3.5\,MeV$ and $5\,MeV$, respectively [36, 37]. Due to its high light yield and extreme radiopurity, Borexino was able to push the detection threshold of ^{8}B-ν to an unmatched level of $3\,MeV$ electron recoil energy, imposed mainly by the external $2.6\,MeV$ γ-ray background from the radioactive decay of ^{208}Tl contained in the PMTs and the SSS. At these relatively low energies, a significant spectral deformation is expected according to the MSW-LMA solution. In addition, hypothetical non-standard interactions are predicted to influence the ν_e survival probability P_{ee} in this transition region between

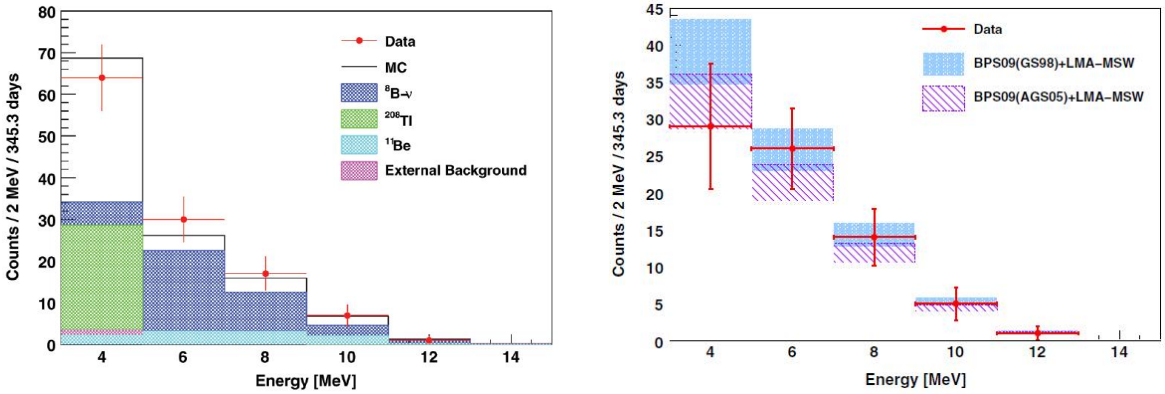

Figure 2.3: Solar ^{8}B-neutrino measurement [4]. *Left:* Comparison of the final spectrum after data selection (red dots) with Monte Carlo simulations (black line). The simulation contains the contributions from oscillated solar ^{8}B-ν (blue) and internal ^{208}Tl (green), cosmogenic ^{11}Be (cyan), and external (violet) background. *Right:* Background-subtracted ^{8}B-ν spectrum in comparison with expectations based on the MSW-LMA neutrino oscillation solution and ^{8}B-ν flux predictions from the SSMs GS98 (high metallicity) and AGS05 (low metallicity; model has been updated in 2009 to AGSS09), respectively.

matter- and vacuum-dominated oscillations. As the ^{8}B-ν flux is also dependant on the metallicity[2] of the Sun, a high precision measurement would benefit the validation of the two prominent SSMs, namely the GS98 (high metallicity) and the AGSS09 (low metallicity) models [23].
A significant background in the ^{8}B-ν analysis is posed by cosmogenic radionuclides produced by cosmic muons crossing the IV. The short-lived isotopes ($\tau < 2\,s$) can be rejected by imposing a $2\,s$ veto after each muon, reducing the lifetime by 29.2%. A list of cosmogenic isotopes can be found in Table 6.1 on page 138. However, for the suppression of the long-lived ^{10}C (β^{+}-emitter, $\tau = 27.8\,s$, $Q = 3.65\,MeV$), this technique would induce an unacceptably large lifetime loss. Fortunately, the production of ^{10}C is accompanied in $\simeq$90% of all cases with at least one free neutron in the final state. Utilizing the correlations in space and time of ^{10}C with its knock-off neutron(s) and the parent muon, this background can be suppressed with minimal lifetime loss (0.16%). This method to tagg the cosmogenic Carbon isotopes ^{10}C and ^{11}C is called the *Three-fold Coincidence* (TFC) technique. However, the TFC technique is not applicable for the long-lived cosmogenic radioisotope ^{11}Be (β^{-}-emitter, $\tau = 19.9\,s$, $Q = 11.5\,MeV$), which does not intrinsically yield a free neutron along its production. In consequence, it is statistically taken into account

[2]In astrophysics, elements heavier than Helium are considered as metals.

as contamination in the ^{8}B-ν analysis [3].
Based on 488 live days of data acquisition, Borexino measured a neutrino-electron elastic scattering interaction rate of $(0.22 \pm 0.04_{\text{stat}} \pm 0.01_{\text{syst}})\,(d\,100\,t)^{-1}$ above $3\,MeV$ [4]. This corresponds to a ^{8}B-ν flux of $\Phi(^8\text{B}) = (2.4 \pm 0.4_{\text{stat}} \pm 0.1_{\text{syst}}) \cdot 10^6 cm^{-2} s^{-1}$, in good agreement with the results from SNO and Super-Kamiokande. Assuming the high-metallicity SSM, an average ν_e survival probability of $P_{ee} = 0.29 \pm 0.10$ above $3\,MeV$ was found. Figure 2.3 presents the spectral shape of the final candidate events in comparison with predictions from Monte Carlo simulations. In addition, the background-subtracted ^{8}B-ν spectrum is shown in comparison with predicictions from the SSMs GS98 and AGS05.
Unfortunately, so far the statistics are not sufficient for detailed studies on the ^{8}B-ν spectral shape to reveal non-standard interactions or deviations from the expected MSW-LMA neutrino oscillation solution.

pep/CNO-Neutrinos

The monoenergetic pep-ν are emitted with an energy of $1.44\,MeV$, causing a Compton-like electron recoil shoulder at $1.22\,MeV$. The pep-branch is directly related to the fundamental pp-branch, with the ratio between the two neutrino fluxes being only weakly model dependant and known to about 1% accuray. Thus, a measurement of pep-ν allows an indirect determination of the pp-ν flux, which is connected to the initial fusion reaction of the pp-cycle, denoting 98% of the total energy production in our Sun. In consquence, it provides a strong constraint on the total solar neutrino luminosity.
The remaining 2% of the total energy output in our Sun are contributed by the sub-dominant CNO cycle. However, as the fusion rates are highly temperature dependant, it is expected to be the main energy production mechanism in heavy stars (> 1.5 solar masses). The CNO-ν flux is composed of the three neutrino emissions connected to the decays of ^{13}N (Q=$1.19\,MeV$), ^{15}O (Q=$1.73\,MeV$), and ^{17}F (Q=$1.75\,MeV$). As the CNO cycle is strongly dependant on the metallicity of the Sun, a measurement of this neutrino flux would provide a direct test of the current SSMs, with the high-metallicity GS98 model predicting a 40% higher flux than the low-metallicity AGSS09 model [23].
In Borexino, the muon-induced radioactive isotope ^{11}C (β^+-emitter, $Q = 1.98\,MeV$) constitutes the dominant background in the energy range of interest ($0.7-1.5\,MeV$), surpassing the signal of pep- and CNO-ν by an order of magnitude (see Figure 2.4). As ^{11}C is produced in 95% of the cases with at least one free neutron in the final state, the TFC technique can be applied analogously to the ^{10}C suppression of the ^{8}B-ν analysis. At a lifetime loss of 51.5%, the ^{11}C background is reduced by a factor

[3] The residual rate of ^{11}Be was scaled to Borexino from rates measured by the Kamland collaboration.

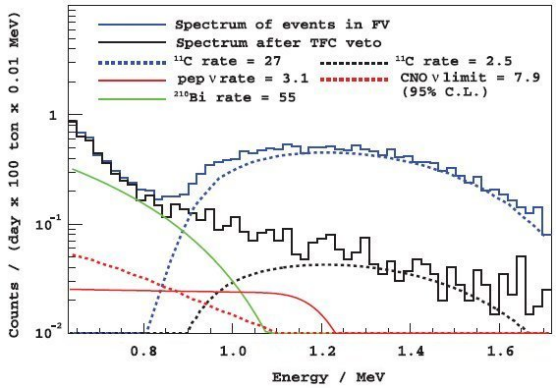

Figure 2.4: Energy spectrum before (blue) and after (black) suppressing the cosmogenic radionuclide ^{11}C with the Three-fold Coincidence veto. Rate values in the legend are integrated over all energies and are quoted in units of $[counts/(d\,100\,t)]$. The best estimates for the pep-ν rate, as well as the upper limit of the CNO-ν signal are shown along the intrinsic ^{210}Bi contamination. [5]

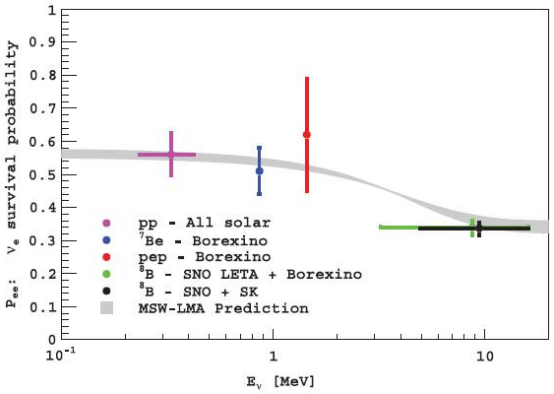

Figure 2.5: Measurements of the solar electron neutrino survival probability as a function of energy. The predicted MSW-LMA band is given by the 1σ range of the oscillation parameters. [5]

of $\simeq$10. In addition, a novel pulse shape discrimination method has been developed and applied by the Borexino collaboration to partly disentangle β^+ and neutrino-like energy depositions in the detector, further reducing the ^{11}C background. Based on a multivariate fit, the Borexino collaboration reported the first evidence for solar pep-ν in 2012 by measuring an interaction rate of $(3.1 \pm 0.6_{\text{stat}} \pm 0.3_{\text{syst}})\,(d\,100\,t)^{-1}$ corresponding to a flux of $\Phi(\text{pep}) = (1.6 \pm 0.3) \cdot 10^8 cm^{-2} s^{-1}$ [5]. Alternatively, setting the pep-ν flux to the expected value according to the MSW-LMA scenario, a ν_e surivival probability of $P_{ee} = 0.62 \pm 0.17$ at $1.44\,MeV$ was found. Combined with the measurements of solar ^{7}Be-ν and ^{8}B-ν, Borexino is the first experiment to probe all three regimes of neutrino oscillations according to the MSW-LMA solution, i.e. matter- and vacuum-dominated regimes as well as the intermediate transition regime (see Figure 2.5). Unfortunately, the measurement of the CNO-ν flux was hindered by an intrinsic contamination of ^{210}Bi in the liquid scintillator. This beta-emitter ($Q = 1.16\,MeV$) features a decay spectrum very similar to the CNO-ν recoil-energy spectrum, at a $\simeq$10 times higher rate. Due to this, only an upper limit on the CNO-ν interaction rate of $< 7.9\,counts/(d\,100\,t)$ at 95% C.L. was reported by the Borexino collaboration, corresponding to a neutrino flux of $\Phi(\text{CNO}) < 7.7 \cdot 10^8 cm^{-2} s^{-1}$ (95% C.L.) [5].

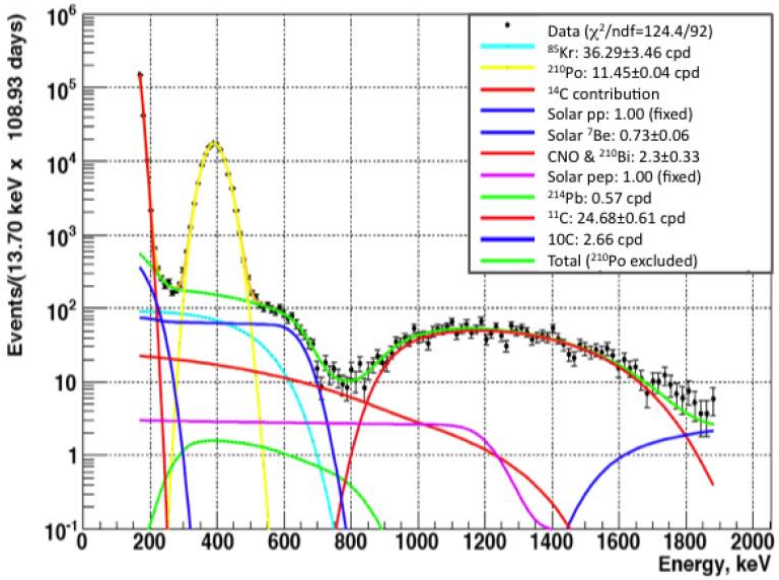

Figure 2.6: Fit of the Borexino energy spectrum after 300 days of measurement. The fit contains the solar neutrino fluxes of the pp (fixed), ^{7}Be, pep (fixed), and CNO (together with ^{210}Bi) branches, alongside the major contaminants ^{14}C, ^{210}Po,^{214}Pb, ^{85}Kr, and cosmogenic ^{10}C and ^{11}C. The rates of background components are given in $[counts/(d\,100\,t)]$ (cpd). The pp-ν signal manifests as a small kink in the valley between the dominant (red) ^{14}C and (yellow) ^{210}Po decay spectra. [38]

pp-Neutrinos

The neutrinos emitted in the pp fusion process constitute 91% of the total solar neutrino flux. Therefore, a measurement of the pp-ν would considerably constrain the expected neutrino luminosity of our Sun. As neutrinos leave the Sun quasi-instanteously, a comparison with the solar photon luminosity allows to check the stability of its thermonuclear energy production on a time scale of $10^5 - 10^6$ years. With an expected neutrino-electron interaction rate of $140\,counts/(d\,100\,t)$, the pp-ν produce a significant signal in Borexino. However, this signal is covered to a large extent by the intrinsic low-energetic background from ^{14}C decays (Q = $157\,keV$), naturally present within the organic liquid scintillator (see Figure 2.6). At these low energies the energy response of Borexino is only $\simeq$10%, smearing the ^{14}C distribution up to $\simeq 200\,keV$. In addition to a precise understanding of the detector response at these energies (e.g. electron quenching [4]), also pile-up

[4] At low particle energies, the increase in ionization densities results in a decrease of the scintillation light yield, i.e. the amount of generated light per amount of deposited energy. This

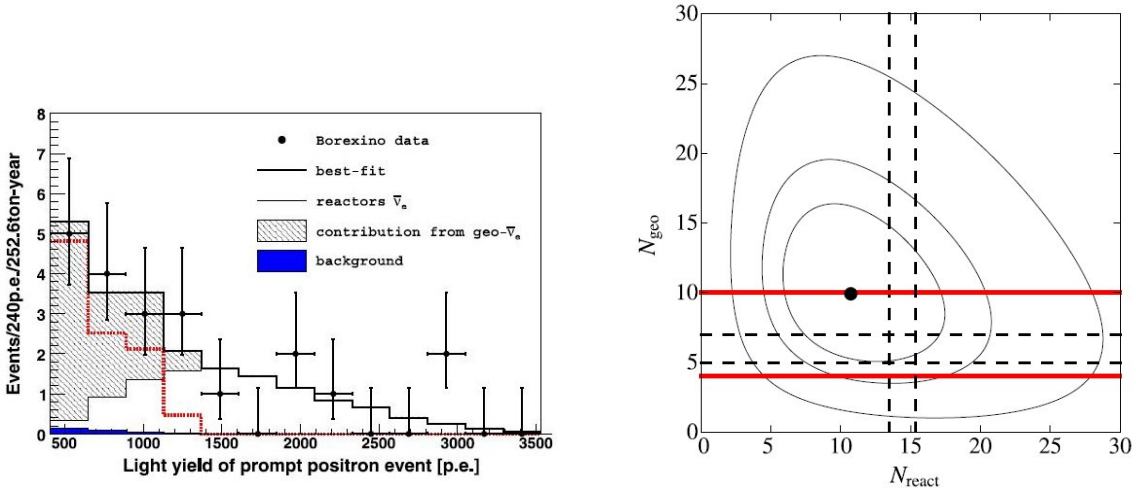

Figure 2.7: Geo-neutrino measurement [34]. *Left:* Energy spectrum of the prompt events fullfilling the delayed coincidence condition, mapped in number of photo-electrons (p.e.) detected by the PMTs (500p.e. $\cong 1\,MeV$). The spectrum is fitted with Monte Carlo generated probability density functions, disentangling the numbers of geo-$\overline{\nu}_e$ (N_{geo}), reactor-$\overline{\nu}_e$ (N_{react}), and background events. *Right:* Allowed regions for N_{geo} and N_{react} at 68%, 90%, and 99.73% C.L. Vertical dashed lines: 1σ interval of the expected N_{react} (including neutrino oscillations). Horizontal dashed lines: range for N_{geo} predictions based on the *Bulk Silicate Earth* geochemical model. Horizontal solid red lines: predictions of the Maximal and Minimal Radiogenic Earth models.

events of ^{14}C have to be taken into account. No results on the pp-ν have been yet published by the Borexino collaboration.

2.3.2 Geo-Neutrinos

As has been described in Section 1.2.2, with the inverse beta-decay (IBD) the liquid-scintillator technology provides a sensitive detection channel for the $\overline{\nu}_e$ produced in the interior of our planet by the radioactive decays of ^{40}K and the progenies of ^{238}U and ^{232}Th. The total energy released in these decays is expected to generate about 50% of the terrestrial heat flow of $47\,TW$ [27]. A background for this measurement arises from the radionuclides ^{8}He and ^{9}Li, which are produced in-situ in nuclear spallation processes by cosmic muons crossing the experiment. These cosmogenic isotopes are subject to β^--decay, which can populate excited states in

quenching effect is described by the Birks formula. [39]

the daughter nuclei, which are unstable to neutron emission. The combined βn signal perfectly mimicks the expected IBD signal. These cosmogenic isotopes are efficiently removed though by a $2\,s$ veto after every crossing muon. Leaving only $\overline{\nu}_e$ in the sample, the main background originates from $\overline{\nu}_e$ emitted in the energy production of nuclear power plants. However, Italy conducted in the late 80's a nuclear power phase-out, leaving the LNGS at a mean distance of $\simeq 1000\,km$ to European power plants. Borexino profits from this low reactor anti-neutrino environment, and accomplished the first observation of geo-neutrinos at a $4.2\,\sigma$ C.L. (see Figure 2.7). The detected interaction rate of $(3.9^{+1.6}_{-1.3})\,counts/(y\,100\,t)$ limits the energy output of an active geo-reactor at the Earth's core to $3\,TW$ at 95% C.L. [34]. The present statistics are not sufficient to rule out an Earth composite model (see Figure 2.7). As Borexino is located on the European continental plate, while Kamland, which has also detected geo-ν [40], is located at the thinner oceanic crust, both experiments yield complementary information on the distribution of the radiogenic heat production.

2.3.3 Supernova Neutrinos

The neutrino signal of a core-collapse Supernova (SN) at the galactic center ($10\,kpc$ distance to earth) would produce a total of 180-190 events in Borexino, distributed over several reaction channels, namely elastic scattering on electrons and protons, inverse β-decay on protons, as well as neutrino capture and inelastic scattering on ^{12}C. This would allow to test Supernova models, neutrino mass limits, and possibly the neutrino mass hierarchy.
Since July 2009, Borexino is a member of the *SuperNova Early Warning System* (SNEWS), a collaboration of neutrino detectors sensitive to a galactic core collapse SN. The neutrino burst of a SN would arrive at Earth hours before the optical signal, triggering several of these experiments in coincidence and hereby warning astronomers of the imminent event. Based on the track reconstruction capabilities of the respective detectors and the relative timing of the neutrino signals, SNEWS could also provide a direction of the expected SN light flash. Currently, the SNEWS collaboration consists of Super-Kamiokande [41], LVD [42], IceCube [43], and Borexino.

2.3.4 The CNGS Neutrino Beam

Since 2007 the *CERN Neutrinos to Gran Sasso* (CNGS) project provides a ν_μ-beam of $17\,GeV$ mean energy from CERN to the $730\,km$ distant LNGS laboratory. While the baseline is short compared to the expected oscillation length of $17 \cdot 10^3\,km$, nonetheless a small fraction of 2% of the ν_μ is expected to oscillate to

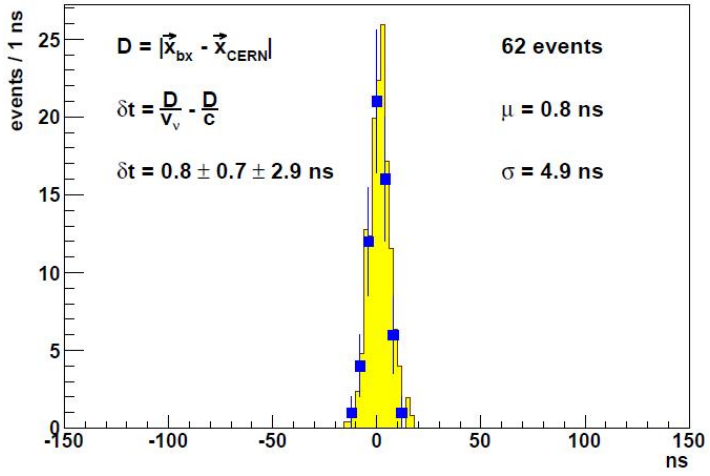

Figure 2.8: Distribution of the neutrino time-of-flight relative to a particle moving at the speed of light (data points). The mean value is consistent with zero and the width agrees with Monte Carlo simulation of known time jitters (yellow filled histogram). [46]

ν_τ. At the LNGS underground site, two experiments aim for the first appearance measurement of these ν_τ: the OPERA and ICARUS projects located in Hall C and B, respectively [44, 45]. Due to its large mass and cross-section, Borexino is a target for these ν_μ-induced events as well. The incident ν_μ-beam not only interacts with the detector material, but also with the rock at the LNGS site, producing muons in charged-current reactions. As the induced muons are aligned in time and direction with the CNGS ν_μ-beam spills, these events can easily be tagged and removed from solar neutrino analyses. On the other hand, these events provide an excellent tool to test Borexino's muon veto and tracking performance. For details on the respective muon tracking tests, see Section 4.6.

Triggered by the OPERA publication in September 2011 [47], claiming the detection of neutrinos traveling faster than the speed of light, Borexino performed its own neutrino velocity measurement in 2012 [46]. To accomplish this, the collaboration upgraded the Borexino trigger system with a new facility to a ns-timing precision in terms of the absolute GPS-time. In addition, an independent geodetic survey at the LNGS site was performed. The distance between the Borexino reference point and the CERN target was measured to $D = (730472.082 \pm 0.038)\, m$. To investigate the OPERA claim, the CERN provided a ν_μ-beam of $\simeq 2\, ns$ bunch width in May 2012. The Borexino time-of-flight analysis was based on beam-induced muons crossing the ID, offering a cross-section of $147\, m^2$. Using the ID muon track reconstruction code, the entry point of the muon in the SSS is re-

constructed to a precision of $\simeq 50\,cm$. This allows for a track-by-track correction of the time-of-flight determination based on the curved geometry of the SSS, thus increasing the overall timing resolution of the neutrino speed measurement. Figure 2.8 presents the final distribution of the 62 candidate events after for all known effects. The yellow filled area presents the results from a Geant4-based Monte Carlo simulation, well reproducing the measured distribution. In agreement with results obtained by the MINOS and ICARUS collaborations [48, 49], Borexino published in July 2012 the time-of-flight difference of the CNGS ν_μ's relative to the speed of light c as

$$\begin{aligned} \delta t &= t_{\mathrm{Bx}} - t_{\mathrm{CERN}} - \frac{D}{c} \\ &= (0.8 \pm 0.7_{\mathrm{stat}} \pm 2.9_{\mathrm{sys}})\, ns \end{aligned}$$

The result is consistent with zero, yielding a relative deviation of the neutrino velocity to the speed of light of $|v - c|/c < 2.1 \cdot 10^{-6}$ at 90% C.L. [46].

Chapter 3

Borexino Data Acquisition and Simulation

Depending on the particle type, its kinetic energy, and the Borexino subvolume it is contained in, light emission is caused by the scintillation mechanism, the Čerenkov effect or a combination of both. The Borexino subdetectors, the so-called *Inner Detector* (ID) and *Outer Detector* (OD), are designed to detect the emitted photons with high efficiency via an array of photomultiplier tubes (PMT). Based only on the timing and charge information of each PMT signal, all accessable information of the physics event has to be reconstructed.
This Chapter provides an overview on the reconstruction of a physics event. The first part of the chapter outlines the hardware signal read-out, consisting of photon detection via PMTs and the signal processing by the different data acquisition (DAQ) systems and their respective electronics chains. In the second part, the Borexino offline data reconstruction code *Echidna* is presented, along with all physics observables necessary for the analyses performed in Chapters 4, 5, and 6. The last part of the Chapter is commited to the Borexino simulation framework, which is an important tool for studies of selection cut efficiencies and detector response functions.

3.1 Photomultiplier Tubes

Equipped with an array of 2212 and 208 PMTs, respectively, Borexino's ID and OD are sensitive to light emission caused by the energy deposition of charged particles in the respective Borexino subvolume. A schematic of a PMT is given in Figure 3.1. A photon hitting the photocathode can create an electron (a so-called *photo-electron*) via the photo-electric effect, which in turn is accelerated and focussed by the internal high-voltage potential on the first dynode. On impact with the

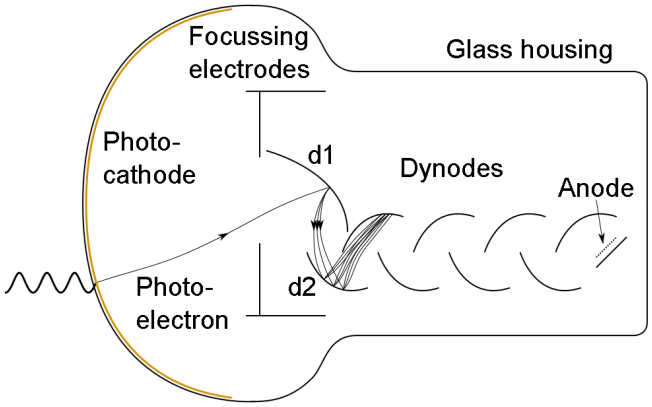

Figure 3.1: Schematics of a photomultiplier tube. A photo-electron generated by an incident photon on the photocathode is accelarated by an electrical field, producing an electron avalanche along the dynode chain. The amplified signal is eventually read out at the anode. [50]

dynode, the electron energy is sufficient to knock out secondary electrons from the material. This process repeats, as the avalanche of electrons is accelerated and amplified along the chain of dynodes. Depending on the total voltage applied to the PMT, the average multiplication factor is 3-5 per step [51]. Eventually, the electron avalanche arrives at the anode and the corresponding charge signal is read out. While the majority of pulses follow this mechanism, there exist a multitude of subdominant species of PMT pulses. Depending on the vertex and type of first interaction inside the PMT, the potential production of bremsstrahlung and/or ionized molecules, additional pulses of varrying signal heights and timing can be generated. Further descriptions on PMTs can be found in [52, 53, 54].

3.1.1 Response Function

In Borexino, the PMT high-voltage is adjusted to amplifiy a single initial photo-electron by a factor of $2 \cdot 10^7$ [31]. Figure 3.2 presents the response function in collected charge of a typical Borexino PMT [51, 55]. Due to the statistical nature of the avalanche formation, the PMT response to a *Single Photo-Electron* (SPE) can be described by a gaussian distribution. In addition, an exponential contribution of under-amplified pulses and dark noise is present. The latter is caused by thermionic emission of electrons from the photocathode or dynode chain. A well pronounced valley, characterizing the separation between gaussian peak and exponential distribution, was one of the criterias in PMT selection for the Borexino experiment. This separation is utilized in the suppression of dark noise

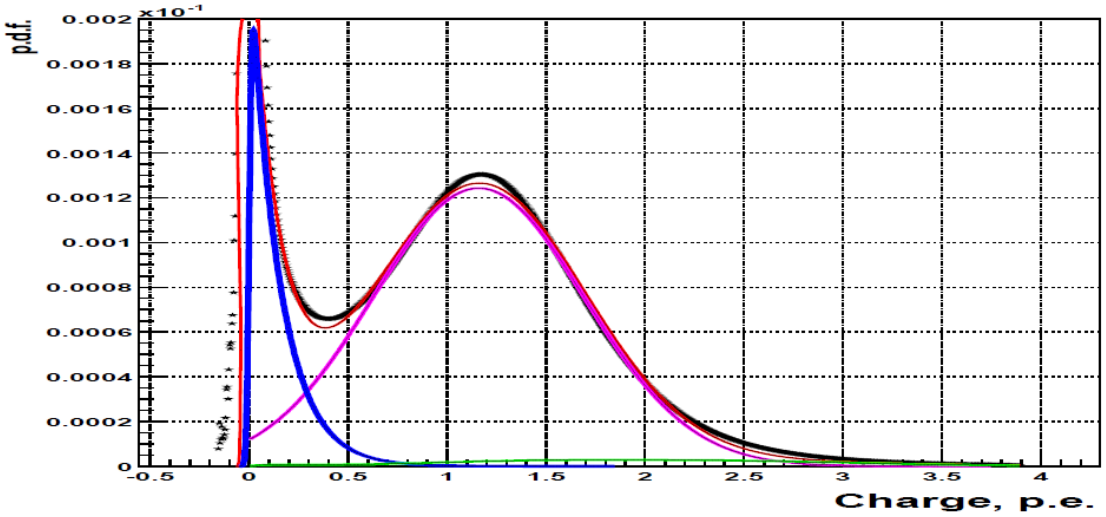

Figure 3.2: Normalized average charge spectrum of the ETL9351 Borexino PMT (black data points) [51]. The PMT response function can be approximated by the sum (red) of a gaussian SPE response (pink) and a exponential contribution of under-amplified pulses and dark noise (blue). The PMT features a good separation between the two components, with a ratio of the gaussian peak to the intermediate valley of about 2:1. The shown charge response was subject to a first-order calibration in terms of intitial photo-electrons (*p.e.*). A precise calibration would yield the gaussian mean value at a charge of 1 *p.e.*.

hits via a hardware threshold, which is set for each PMT close to the individual minimum of the valley. As part of detector operation and maintenance, each individual Borexino PMT is calibrated regularly via (external) light sources to translate the charge collected at the anode to the corresponding number of initial photo-electrons. The latter is directly connected to the photon illumination of the PMT and therefore a critical observable of a physics event. In this process, the relative timing between the PMTs is evaluated as well, a requirement for reconstructing the position of an event. In case of the ID, this calibration is accomplished by using a laser source, while the OD is calibrated via a LED-system. For more details on the PMT calibration, see Sections 3.3.1 and 4.3.

3.1.2 Late Pulses and Afterpulses

With respect to the studies performed in this thesis, the delayed PMT signals from *late pulses* and *afterpulses* are of interest. Late pulses are caused by the initial photo-electron scattering from the first dynode without producing secondary electrons. This can be the result of an elastic scattering, or inelastic scattering with

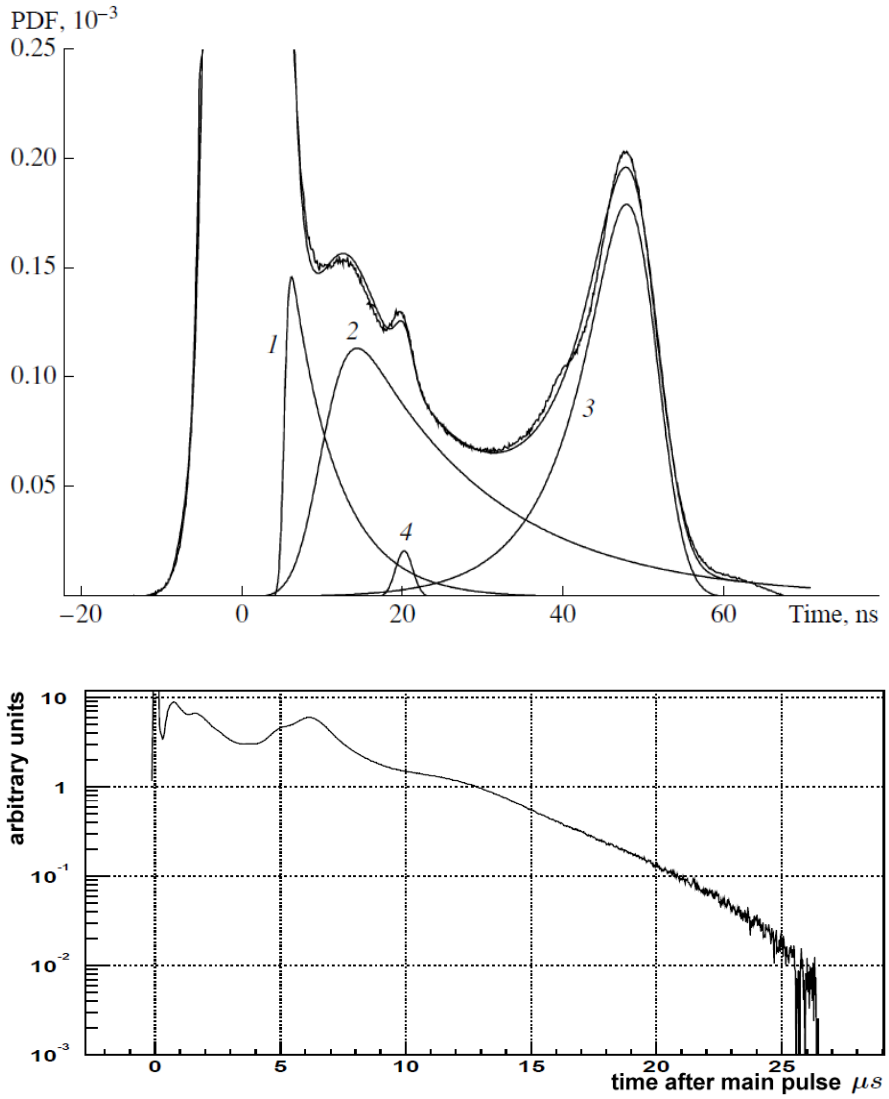

Figure 3.3: Time profiles of late pulses (top plot) and ionic afterpulses (bottom plot) of the ETL9351 Borexino PMT [51, 56]. The timing information is given relative to the normal pulses. *Top:* Curves 1, 2 correspond to inelastically scattered photo-electrons, while curve 3 describes the signals from elastically scattered photo-electrons. The gaussian function (4) models light reflection in the laser system. *Bottom:* Due to the large drift times of ionized molecules, signal delays are in the order of microseconds. The axis-labeling was edited with respect to the original Figure 22 from [51].

the deposited energy dissipating as heat in the dynode material. The scattered electron describes a loop in the electric field of the PMT and is focussed again on

the dynode. The additional transit time to create the electron avalanche results in a delay of the signal up to 100 ns. For the ETL9351 Borexino PMT, the fraction of late pulses to normal pulses is about 6% [56]. The top plot in Figure 3.3 presents the time profile of late pulses.
Signals with a delay in the order of microseconds are caused by (ionic) afterpulses. Despite the high vacuum of $\simeq 10^{-5}\,Pa$ inside the PMT, residual gas molecules can be ionized by an electron avalanche initiated by an incident photon or thermionic emission. The positively ionized molecules drift in the electric field to the cathode where they knock out several electrons, initiating multiple secondary delayed avalanches. As a result of the long drift times of the ionic molecules inside the PMT, the corresponding pulses are delayed up to 30 μs relative to the normal pulses. The bottom plot of Figure 3.3 presents the averaged afterpulse spectrum of the ETL9351 Borexino PMT. The probability of a regular pulse to generate an ionic afterpulse in this type of PMT is about 5% [51].

3.2 Data Acquisition Systems

The raw information on timing and charge of the PMT pulses is processed by the electronics chains of the Borexino data acquisition systems. As a detailed description of the electronic signal processing can be found in [31, 32, 57, 58], only a short summary is given in the following.

3.2.1 Trigger System

The global trigger is issued by the *Borexino Trigger Board* (BTB) if at least one of the Borexino subdetectors flags a physics event. The ID causes such a trigger signal, if at least 25 PMT hits are registered within a time gate of 60 ns, corresponding to a visible energy of 50 keV. For the OD system, at least 6 PMT hits within 150 ns are required to trigger the experiment. By receiving the global trigger, data acquisition is stopped and the PMT information in charge and timing of both ID and OD are read and sent to the central PC (*BxBuild*). The standard trigger time gate of both subdetectors comprises 16 μs, well suited for the detection of fast coincidences of radioactive decays within a single time gate (e.g. $^{212}\mathrm{Bi} \xrightarrow[\tau=60.6\,min]{\beta^-} {}^{212}\mathrm{Po} \xrightarrow[\tau=299\,ns]{\alpha} {}^{208}\mathrm{Pb}$). To detect muon-induced neutrons, featuring a mean capture lifetime of $\simeq 260\,\mu s$ in *pseudocumene* (PC), an additional subsequent trigger gate of 1.6 ms is generated. This *neutron trigger* is issued in case of muons crossing Borexino, thus triggering both ID and OD.

3.2.2 Inner Detector

The information of the 2212 ID PMTs is administered by 14 racks, each handling 158 channels. For each PMT, the front-end (FE) electronic generates two signals, i.e. the timing and charge information of the PMT pulse. The charge information is obtained via integration of the first $80\,ns$ of the pulse, followed by a $60\,ns$ dead time for writing the data to the internal memory buffer. With a multiple hit probability of $\simeq$10% in the solar ^{7}Be-ν window ($E \lesssim 1\,MeV$), the PMTs operate mainly in the single photo-electron regime. However, especially for physics events at off-center positions or higher energies, multiple photon hits become more likely. In case a PMT hit is followed by additional hits during the charge integration time gate of $80\,ns$, the total collected charge of all hits is recorded. However, the recorded timing information always refers to the start of the PMT pulse and thereby only to the first hit; the timing information of additional hits within the $80\,ns$ time gate is lost. The FE signals of a rack are fed to its read-out electronics, 20 digital boards of 8 channels each, designated as *Laben* boards[1]. In this final step, the data is digitized and sent to the *BxBuild* PC.

Analog Systems

In addition to the charge and timing information of each individual PMT, the ID front-end electronics provide analog sum signals of 98 PMT assemblies, each consisting of up to 24 channels grouped by solid angle sectors, plus an additional channel built from the total analog sum of all channels. This compactified analog ID data stream allows for the application of fast waveform digitizers, enhancing Borexinos performance for high event rates. The accessable physics cover Supernova-, reactor-, Geo-, and solar ^{8}B-neutrinos, but also the detection of muon-induced spallation neutrons. The grouping of channels however comes at the price of significantly reduced information on the timing topology of the events, making position reconstruction with this configuration unfeasible.
Based on the analog sum output, three systems applying waveform digitizers were installed in Borexino: the so-called *Flash ADC* (FADC) system with a $400\,MHz$ digitization rate, and the *Princeton Analog* and *v1731* systems with $500\,MHz$ each.

3.2.3 Outer Detector

The electronics for operating the 208 OD PMTs is installed in two additional racks. The signal is decoupled from the high-voltage powering the PMTs and fed to 16

[1]These boards were designed and built in collaboration with the Laben S.p.A. company

Charge-to-Time converters (QTC) of 16 channels each. Similar to the ID the signal is integrated over the first 80 ns of the pulse, providing a charge information of the event in the water tank. The QTC boards send a logic pulse containing charge and timing information of the PMT pulses to two Time-to-Digital converters (TDC), which in turn digitize the signal and transmit it to the *BxBuild* machine.

3.3 Echidna Data Processing Software

Echidna is a *ROOT* based *C++* software code developed by the Borexino collaboration for offline processing of the collected raw data [59]. This highly modular framework features low-level data calibration as well as high-level event reconstruction. Based on the charge and timing topology of the detected PMT hits, *Echidna* reconstructs a multitude of physics observables of an event, like energy, position of the interaction vertex, particle type (α, β/γ, μ), track (in case of μ's), and many more. The *Echidna* output is saved in a *ROOT* file, containing the raw and reconstructed information in a customized *ROOT* tree (*BxTree*). The information is structured in a data master class (*BxEvent*), consisting of a set of instances. At the current state, *Echidna* encompasses by default the data of the ID and the OD. Information of the *v1731* and FADC analog systems is reprocessed optionally.
Mach4, an additional reconstruction code developed within the collaboration, uses the low-level calibrated *Echidna* data as input, providing an independent high-level event reconstruction. The output of *Mach4* is eventually merged with the *Echidna* *ROOT* files, producing the so-called *Mach4-on-Echidna* (MOE) data files.
The software development and data analyses performed in the course of this thesis are based purely on the *Echidna* framework. A list with a brief description of physics observables associated with these works is given in the Appendix in Tables 8.1 - 8.3. For better understanding, the following subsections present the basic offline reconstruction chain of *Echidna*.

3.3.1 Data Calibration

As the physics reconstruction relies on the charge and timing of PMT hits, a thorough and regular calibration of the data acquisition channels is necessary. To this end, several calibration methods are applied in the Borexino experiment. The electronics chains of ID and OD are tested with a pulser system, while the full data channel (i.e. PMT and electronics combined) is checked by illuminating the PMTs. This is accomplished by feeding an external light sources through a system of optical fibers to each PMT. In case of the ID PMTs, light pulses of a laser are distributed via a set of multiplexers and fibers to all 2212 PMTs, while for the OD each of the 208 PMTs is addressed by an individial LED. In addition, artifically

created random triggers are used to monitor the dark noise rates of the PMTs. Once per week, a calibration run of 250k of these service triggers is taken. In addition, ID calibration triggers are also injected during standard data taking runs, making up the first 1000 events and being issued continuously with a rate of $0.1\,Hz$ into the DAQ. Based on this data, the raw information of PMT hits (*raw_hits*) is corrected to the so-called *decoded_hits*.
The LED calibration of the OD data channels is one of the topics of this thesis, and can be found in Section 4.3.

3.3.2 Physics Reconstruction

Besides PMT hits generated by the scintillation light of a physics event, the trigger time gate is also populated by dark noise and afterpulse hits. To identify the hits associated with the scintillation event, the *Echidna* clustering module searches in the trigger time gate for groups of time-correlated decoded hits. Clusters of hits identified in this way are the input of any high-level physics reconstruction in Borexino, like energy, position, and pulse shape. Usually, only one cluster is expected within the standard trigger gate of $16\,\mu s$, however fast radioactive decays (e.g. $^{85}\mathrm{Kr} \xrightarrow[\tau=10.8\,y]{\beta^-} {}^{85m}\mathrm{Rb} \xrightarrow[\tau=1.0\,\mu s]{\gamma} {}^{85}\mathrm{Rb}$) and accidental coincidences produce additional clusters. While the clustering in these cases is comparatively simple, the situation becomes more complex concerning the detection of muon-induced spallation neutrons. After their production, these neutrons quickly thermalize and eventually get captured mainly on the scintillator-intrinsic Hydrogen ($\tau \simeq 260\,\mu s$ in PC), generating a $2.2\,MeV$ gamma. To detect these neutron capture γ's, a subsequent dedicated neutron trigger gate of $1.6\,ms$ length is generated for muons crossing both the ID and OD. In case the muon traverses the active volume in the *Inner Vessel* (IV), several GeV of energy are deposited inside the scintillator, causing a significant light ouput. The result is a high contamination of the neutron gate by PMT afterpulse hits and muon-induced noise. The situation further aggravates if muon-induced hadronic and electromagnetic showers are present, depositing their energy in the IV. With the Borexino electronics being designed for low energy physics events, these tremendous light emissions can saturate a fraction of the *Laben* digital boards. The saturated boards are not available for the neutron detection, resulting in a degenerated signal of the $2.2\,MeV$ gamma. The combination of a high background-hits environment, signal degeneration, and large neutron mutliplicities up to 600 make the identification of the neutron capture γ's very challenging. However, as main tools in tagging and removing the cosmogenic radionuclides $^{10}\mathrm{C}$ and $^{11}\mathrm{C}$ from solar neutrino data, a highly efficient detection of the muon-induced neutrons is essential. The development of a clustering algorithm for the efficient identification of these neutron captures was part of this thesis, and

is described in detail in Section 5.1.

3.3.3 Energy Observables

Echidna provides a multitude of energy observables for a physics event, based on the corresponding cluster of PMT hits. For analyses performed in the course of this thesis, the number of hits, respectively the total collected charge of a cluster are used as energy observables. Both variables are described in the following.

Number of PMT hits

One of the basic energy observables of a cluster is the number of associated PMT hits. As has been laid out in Sec. 3.2.2, a Borexino data acquisition channel is unable to resolve multiple photon hits which occur within 80 ns to each other. The occurence of such multiple hits on a PMT is recorded as a single hit with a charge equal to the total collected charge, and with the time information of the first hit. This leads to non-linearities for physics events at high energies and/or off-center positions. Assuming that for a PMT the timing information of all additional hits (after the first) is lost, the correlation between the detected number of hits N_{hits} and the deposited energy E can be retrieved by stochastic considerations. For physics events at the center, each PMT has the same probability p of recording at least a single hit, given by:

$$\begin{aligned} p &= 1 - \left(1 - \frac{1}{N_{\text{PMT}}}\right)^{N_{\text{tot}}} \\ &= 1 - \left(1 - \frac{1}{N_{\text{PMT}}}\right)^{E \cdot \mathcal{Q}(E) \cdot LY_{\text{hits}} \cdot N_{\text{PMT}}} \end{aligned} \tag{3.1}$$

Here, N_{PMT} denotes the number of live PMTs during the data acquisition of the physics event (in average $\simeq$1800 during data taking). The variable N_{tot} describes the number of expected hits without the multiple-photon limitation; it is connected to the energy E deposited by the physics event, the visible light yield in Borexino ($LY_{\text{hits}} \simeq 500\,\text{hits}/(MeV \cdot 2000\,\text{PMTs})$), and the energy-dependant quenching factor of the respective particle $\mathcal{Q}(E)$. The quenching factor describes the reduction of the scintillation light yield due to non-radiative deexcitation processes in the liquid scintillator. These processes scale with the density of molecules ionized by the incident particle, and thus are most prominent at low particle energies. Quenching effects are described in the later part of this section. The expectation

value of the detected hits is given by:

$$\begin{aligned} N_{\text{hits}}(E) &= N_{\text{PMT}} \cdot p \\ &= N_{\text{PMT}} \cdot \left(1 - \left(1 - \frac{1}{N_{\text{PMT}}}\right)^{E \cdot \mathcal{Q}(E) \cdot LY_{\text{hits}} \cdot N_{\text{PMT}}}\right) \end{aligned} \tag{3.2}$$

As a standard procedure in Borexino, energy observables are normalized to 2000 live PMTs, converting Equ. (3.2) to:

$$\begin{aligned} N_{\text{hits}}^{\text{norm}}(E) &= \frac{2000}{N_{\text{PMT}}} \cdot N_{\text{hits}}(E) \\ &= 2000 \cdot \left(1 - \left(1 - \frac{1}{N_{\text{PMT}}}\right)^{E \cdot \mathcal{Q}(E) \cdot LY \cdot N_{\text{PMT}}}\right) \end{aligned} \tag{3.3}$$

The equation provides a first order approximation of the expected number of PMT hits for a physics event at the detector center. As the probability to detect multiple photon hits increases with the radius of the event, the $N_{\text{hits}}^{\text{norm}}(E)$ observable decreases at off-center positions. Assuming a source, which provides particles homogeneously distributed over the spherical IV, the geometrical increase of events with the radius ($\sim r^2$) results in a $N_{\text{hits}}^{\text{norm}}(E)$ distribution peaking at a lower value than calculated with Equ. (3.3). This effect is observed in the $N_{\text{hits}}^{\text{norm}}(E)$ distribution of the $2.2\,MeV$ γ's emitted in the capture of cosmogenic neutrons on Hydrogen (Chapter 5). While the γ's yield about 820 hits at the detector center, the peak of the spatially integrated distribution is shifted to $\simeq$730 hits.

Charge

As has been mentioned, the Borexino electronics are unable to disentangle multiple photons hitting the same PMT within $80\,ns$ to each other. However, the total charge of these hits is recorded, and thus the total number of incident photons on a PMT can be reconstructed. Summing up the charge information of all PMT signals which are associated with a detected cluster, the total charge information of the cluster is built. This cluster charge N_{ch} scales almost linearly with the deposited energy E, and can be parameterized as:

$$\begin{aligned} N_{\text{ch}}(E) &= E \cdot \mathcal{Q}(E) \cdot LY_{\text{ch}} \cdot N_{\text{PMT}} \\ N_{\text{ch}}^{\text{norm}}(E) &= \frac{2000}{N_{\text{PMT}}} \cdot N_{\text{ch}}(E) \\ &= E \cdot \mathcal{Q}(E) \cdot LY_{\text{ch}} \cdot 2000 \end{aligned} \tag{3.4}$$

The light yield in N_{ch} is given by $LY_{\text{ch}} \simeq 500\,p.e./(MeV \cdot 2000\,\text{PMTs})$. The total charge normalized to 2000 live PMTs is given by $N_{\text{ch}}^{\text{norm}}(E)$. Due to the

attenuation length of $\simeq 8\,m$ in Borexino, the total photon flux on the ID surface is almost independent of the position of the physics event as a consequence of Gauss's theorem. Therefore, the cluster charge is almost position-independent.

Quenching

While the quenching effect is described by the Birks formula [39], the effective energy-dependant quenching factor $\mathcal{Q}_\chi(E)$ of particle type χ can be parameterized in Borexino based on calibration data. A detailed description on quenching factors in Borexino can be found in [21]. The reference does not provide a convenient parameterization for the quenching factor of γ's. Based on the data presented in the reference, a first order approximation of this quenching factor has been calculated in this thesis. The following quenching factors are used:

$$\begin{aligned} \mathcal{Q}_\beta(E) &= \frac{a + b \cdot \ln(E) + c \cdot \ln^2(E)}{1 + d \cdot \ln(E) + e \cdot \ln^2(E)} && (3.5) \\ \text{with } a &= 1.01935,\ b = 0.127233,\ c = 6.06714 \cdot 10^{-5} \\ d &= 0.116877,\ e = 0.0074905 \\ \mathcal{Q}_\gamma(E) &= 1 - \frac{1}{1 + \frac{E}{a}^b} && (3.6) \\ \text{with } a &= 0.208,\ b = 1.880 \\ \mathcal{Q}_\alpha(E) &= a + \frac{b}{E} && (3.7) \\ \text{with } a &= 0.179,\ b = 0.529 \end{aligned}$$

The given formulas assume the particle energy in units of $[MeV]$.

Muon and Neutron Events

For standard applications, the cluster charge is the preferable energy observable due to its high energy-linearity and position-independence. However, in case a muon crosses the scintillator, the large light output can distort the charge information of the recorded PMT hits. The muon induces a huge pulse in the front-end boards, which results in an oscillation of the channel's integrator output used for the charge determination. The baseline requires up to several $100\,\mu s$ to recover. Thus, clusters recorded during the muon-triggered $16\,\mu s$ gate and the subsequent $1.6, ms$ neutron gate feature a distorted charge information. The number of recorded hits is used as standard energy observable for these triggers instead. For each analysis presented in this thesis, the used energy observable will be stated.

3.4 Princeton Analog System

Due to the limitations of Borexino's main DAQ, an auxiliary data acquisition system was installed in June 2007 by the working group of the Princeton University: the *Princeton Analog System* (PAS). A muon triggering the OD initiates the PAS, which in turn records the culmulative analog output of all 2212 ID PMTs in a time gate of $1.6\,ms$ with an Acqiris $500\,MHz$, 8 bit digitizer card (Acqiris DP235). Provided that the Borexino electronics are powered, the system acquires data independently from the main DAQ. The data is processed offline, identifying scintillation pulses caused by neutron captures with a peak search algorithm. As this system is only based on the acquisition of the ID total analog sum, a position reconstruction of scintillation events is impossible.

3.5 Borexino Simulation Framework

With the complexity of the Borexino experiment and its data processing chain, the necessity of a detailed Monte Carlo simulation is evident. The Borexino collaboration met this task by developing a *Geant4* based Monte Carlo [60], reproducing the whole information path from the particle interaction, scintillation light propagation and detection, to the electronics simulation and full *Echidna* data reconstruction. Due to the input from laboratory measurements and calibration campaigns in Borexino, the simulation code has reached a high accuray in reproducing the data. It plays a significant role in the complete understanding of the detector behaviour and provides important cross-checks for the software development of the *Echidna* reprocessing code. Beyond that, it is a essential part of the data analysis as a tool for studying cut efficiencies, and as source of a probability density functions, containing the full detector response.

3.5.1 Physics Generator

The physics processes are addressed by the *G4Bx* Monte Carlo, using the Geant4 framework [60]. The simulation contains in detail the geometry and material properties of the experiment, as well as the respective light emission mechanisms. A generated particle deposits energy in the subvolumes of the experiment, producing scintillation and/or Čerenkov light. *G4Bx* is tracking these photons individually, taking into account all optical interactions (refraction, reflection, absorption, reemission, scattering) with the surrounding media. The photons are tracked until they are absorbed in the passive medium, or detected on the photocathodes of the PMTs.

3.5.2 Geometry

The user can choose between different spatial distributions for the generation of particles, as well as the ID configuration in material composition and geometry. The latter one is a tribute to the different stages of Borexino during the initial filling phase. However, also after the comissioning of Borexino the geometry of the ID was not static, as the shape and volume contained inside the *Inner Vessel* (IV) was changing over the time. This was caused by a small leak appearing in the IV in autumn 2008, resulting in a slow deflation and consequent deformation of the vessel. By reducing the DMP concentration in the buffer and regular refilling of the IV with scintillator, an almost spherical shape of the vessel has been restored and maintained since beginning 2010 (see Section 5.7). For proper detector modeling, *G4Bx* offers the possibily to import a shape profile of the IV, besides the default spherical IV shape of 4.25 m radius.

3.5.3 Electronics Simulation

To take the influence of the electronics into account, the output file of *G4Bx* is processed with the Borexino electronics simulation *BxElec*. The full signal processing is modeled, containing PMT characteristics (e.g. jitter, resolution, dark noise, after-pulses), trigger time gate, analog charge integration, and many more. As the list of working channels is stored in the Borexino database, *BxElec* can simulate the electronics configuration of each taken run individually. In combination with the run-by-run modeling of the IV shape discussed before, the Borexino Monte Carlo simulation allows for a full and precise modeling of the detector response in time. The output of *BxElec* is a binary file identical in format to the real raw data taken by Borexino.

3.5.4 Echidna Processing

The *Echidna* reconstruction code can be run on the output of *BxElec*, producing the final response of the data processing chain to the simulated physics. The produced file contains physics parameters of the original input particles in the *mctruth* class, providing information like particle type, energy, direction, position, daughter particles, and many more. A list of the Monte Carlo variables used for the analyses of this thesis can be found in the Appendix, Table 8.3.

Chapter 4

Cosmic Muons

Due to the low interaction rate of solar neutrinos, the Borexino experiment was built at the *Laboratori Nazionali del Gran Sasso* (LNGS) underground site to provide a low cosmic muon flux environment. With a rock coverage of $\simeq 1\,km$ corresponding to about 3800 m.w.e.[1], the muon flux is reduced by six orders of magnitude relative to the surface to $1.2\,m^{-2}h^{-1}$, corresponding to about 4300 muons per day crossing the *Stainless Steel Sphere* (SSS). As primarily low-energetic muons are stopped in the rock overburden, the mean energy of the cosmic muons is shifted from $1\,GeV$ at surface level to $(283 \pm 19)\,GeV$ at the depth of the underground laboratory [61]. The muons loose about $2\,MeV/cm$ in the water and scintillator liquids of Borexino by atomic excitation and ionization. Muon tracks crossing the active scintillator contained in the *Inner Vessel* (IV) produce a visible energy signal of $50\,MeV$ up to $2\,GeV$ by minimum ionization. If the muon initiates a hadronic shower, even larger amounts of its kinetic energy are deposited inside the detector. However, due to the high muon energy, only $\simeq$1% of the residual muons stop inside the experiment (see Section 5.3).
With the solar neutrino signal being well below $20\,MeV$, muons crossing the IV pose no risk of misidentification. However, muons traversing only the buffer region feature a visible energy spectrum extending into the solar neutrino window. This is the result of the DMP light quencher solved in the buffer liquid, the limited field of view of the ID PMTs equipped with light concentrators ($\simeq$83% of all ID PMTs), and the shorter path lengths at the periphery of the SSS. These so-called *buffer muons* constitute one of the main backgrounds in the neutrino analyses.
Furthermore, hadronic and electromagnetic showers generated by the residual muons can produce secondary background events in the scintillator, namely neutrons and a multitude of radioactive isotopes. The muon-induced neutrons and short-lived radionuclides ($\tau < 2s$) can be easily tagged and vetoed via the time

[1] meter of water equivalent

coincidence with the preceding parent muon. However, in case of the long-lived Carbon isotopes ^{10}C ($\tau = 27.8\,s$) and ^{11}C ($\tau = 29.4\,min$), this approach would yield a intolerable deadtime close to 100%. Utilizing the spatial vicinity of the cosmogenic radionuclides to the parent muon track, the deadtime can be significantly reduced by vetoing only a cylindrical volume along the track, instead of the whole detector. In addition, as the production of muon-induced neutrons and cosmogenic isotopes is of interest on its own, the muon tracking plays a key role in candidate selection, determination of lateral production profiles, and detection efficiencies of muon-induced cosmogenic background events.
This Chapter begins with an overview on muon detection, its corresponding efficiencies and the resulting measured muon flux at the LNGS underground site. Afterwards, this Chapter focuses on the muon track reconstruction applied in Borexino. The *Outer Detector* (OD) muon tracking is presented, followed by a description of the OD photomultiplier (PMT) calibration software, which was developed in the course of this work. As one of the central parts of this thesis, the *Inner Detector* (ID) muon track reconstruction algorithm is laid out in detail. After a short overview on the global tracking, this Chapter finishes with the presentation of Borexino's tracking performance. For the application of the muon tracking in the study of muon-induced neutrons and cosmogenic isotopes, the reader is directed to the Chapters 5 and 6, respectively.

4.1 Muon Detection and Flux

As no light propagation between the two Borexino subdetectors is possible, the *Inner Detector* and the *Outer Detector* provide independent means of muon identification. Therefore, in case of muons crossing both detectors (i.e. crossing the SSS), the combination of both muon flags significantly increases the overall muon detection efficiency of the experiment. In the following, the muon identification flags and their respective efficiencies are represented, combined with the most recent Borexino muon flux measurement.

4.1.1 Outer Detector Muon Flags

With a mean energy of $280\,GeV$, muons crossing Borexino's water tank are well above the Čerenkov threshold of $160\,MeV$, thus emitting a characteristic Čerenkov light cone. This light is eventually detected by an array of 208 PMTs mounted on the outside of the SSS and the water tank floor. The *Muon Trigger Board* (MTB) issues a muon trigger if 6 PMTs are hit within a gate of $150\,ns$, providing a first stage hardware muon flag. While the trigger condition is tuned to be insensitive to the dark noise of the OD PMTs, it is subject to light entering the OD via leaks.

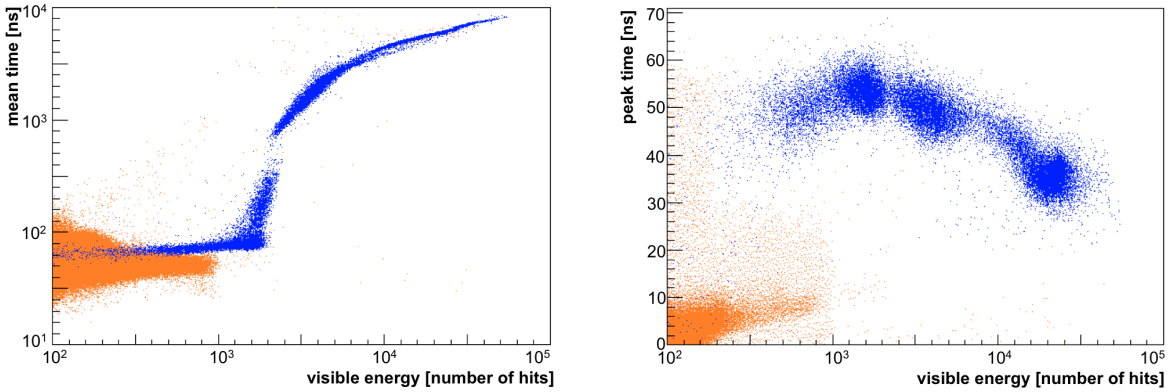

range in number of hits	peak time	mean time
100 - 900	$> 40\,ns$	-
900 - 2100	$> 30\,ns$	-
> 2100	-	$> 100\,ns$

Figure 4.1: Mean-time (*left*) and peak-time (*right*) variables of ID physics events as a function of the visible energy. A physics event is identified by the detection of a group of time-correlated PMT hits. Based on the time distribution of these hits inside the cluster, the mean-time and peak-time of the event are calculated. The variable $N_{\text{hits}}^{\text{norm}}$ is used as energy observable, which is given by the number of clustered hits normalized to 2000 live PMTs (see Sec. 3.3.3). Blue dots represent events flagged by the *Outer Detector* MTB tag as muon, orange dots correspond to neutrino-like events. The ID pulse shape criteria for muon identification are given in the table. [32]

The risk of vetoing a physics event in the ID due to this overefficiency is low, though ($\lesssim 10^{-5}$).
A second muon flag is provided by the *Echidna* software OD clustering module (*bx_muon_findcluster*). Using the PMT hits recorded in the muon trigger gate, the algorithm searches for groups of time-correlated hits of neighbouring PMTs on the SSS and the water tank floor, therefore rejecting accidental triggers caused by light leaks. While more refined, this software *Muon Cluster Reconstruction* (MCR) flag suffered in the past of electronic instabilities in the OD TDC boards. In dozen of runs, the OD data acquisition got stuck while the data taking contiued for hours. Though the MTB reliably issued muon triggers, the individual information on OD PMT hits was lost. To guarantee a stable detector response, any analysis in this thesis is based on the MTB muon flag concerning the OD.

Tag	vs. high-energy events	vs. CNGS-induced events
$\varepsilon_{\mathrm{IDF}}$	-	$0.9586^{(24)}_{(25)}$
$\varepsilon_{\mathrm{MTB}}$	0.9925(2)	-
$\varepsilon_{\mathrm{MCR}}$	0.9928(2)	-

Table 4.1: Efficiencies of the Borexino muon identification tags: *Inner Detector Flag* (IDF), *Muon Trigger Board* (MTB), and *Muon Cluster Reconstruction* (MCR). The efficiencies were derived via test samples from high-energy ID events and muon events induced by the *CERN to Gran Sasso* (CNGS) ν_μ-beam. All numbers are lower limits as the presence of non-muon events in the samples cannot be excluded. [32]

4.1.2 Inner Detector Muon Flag

The standard physics events observed by the ID are point-like (also called neutrino-like) energy depositions of α, β, and γ particles within the scintillator filled IV at the center of the detector. The hits of these events arrive almost simultaneously at the PMT covered inner surface of the ID. Muons on the other hand emit light along the track via (residual) scintillation and the Čerenkov effect, producing a significantly different pulse shape. Due to the spatial extent of energy deposition, the hit clusters identified by the ID clustering algorithm feature longer rise- and mean-times, identifying these track-like events. Figure 4.1 presents these variables as functions of the visible energy, and lists the pulse shape criteria for the *Inner Detector muon Flag* (IDF) applied in Borexino.

4.1.3 Muon Detection Efficiencies

Detailed studies on the detection efficiencies have been carried out by the Borexino collaboration, and can be found in [32, 62]. Table 4.1 presents the efficiencies for the three muon flags (IDF, MTB, MCR) in the energy range above 80 clustered hits (corresponding to $160\,keV$), as derived via test samples from high-energy ID events and muon events induced by the *CERN to Gran Sasso* (CNGS) ν_μ-beam. Testing the muon flags against each other, consistent results are obtained. The combination of the three muon flags results in a muon tagging efficiency of at least 99.992% [32].

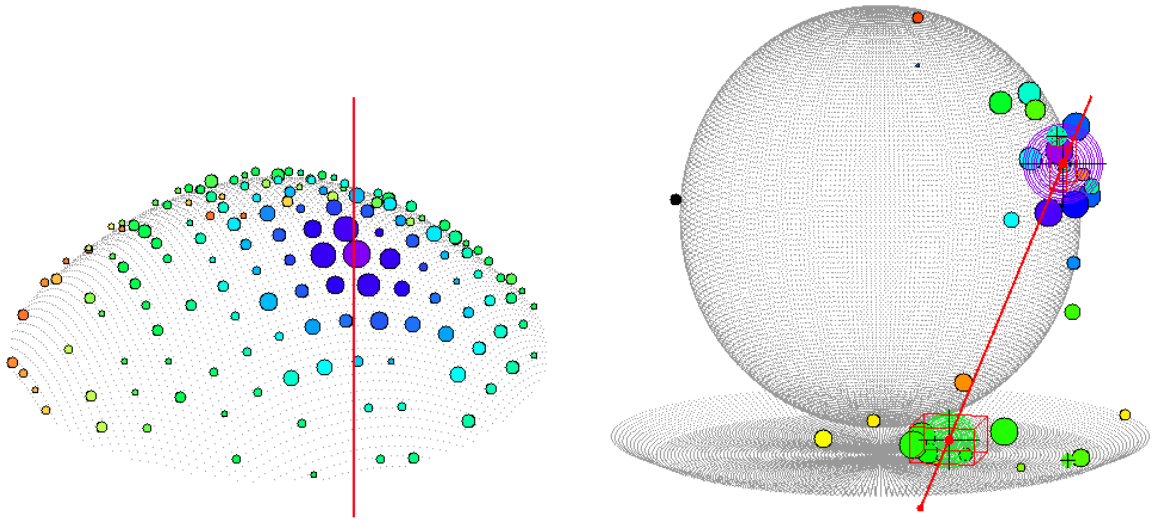

Figure 4.2: OD PMT activation profile created by the Čerenkov light cone of a muon crossing the SSS. The size of a dot indicates the number of photons registered by the respective PMT, while colors code the photon arrival time (early: violet; late: red). *Left:* View on the PMT hit pattern at the muon entry point on the SSS, consisting of isochronous discs around the entry point [32]. *Right:* Full OD event display of a typical muon event [62]. The muon tracking algorithm identifies two clusters of time-correlated PMT hits, thus defining the muon track.

4.1.4 Muon Flux

A cosmic muon rate of $(4310 \pm 2_{\text{stat}} \pm 10_{\text{syst}})\, d^{-1}$ has been measured in Borexino [63]. The systematic error stems from the muon detection efficiency uncertainty and possible threshold effects. With respect to the SSS cross-section, this rate translates to a muon flux of $(3.41 \pm 0.01) \cdot 10^{-4}\, m^{-2} s^{-1}$ in Hall C of the LNGS underground laboratory.

4.2 Outer Detector Muon Tracking

The Čerenkov light emitted by a muon traversing the Borexino water tank provides an instrument for tagging and tracking the passing muon. A corresponding tracking algorithm was developed by the Borexino collaboration with the focus on muons crossing the SSS, thus depositing energy in the neutrino sensitive ID [32, 62]. The characteristic Čerenkov light is emitted by the ultra-relativistic muons at an angle of

$$\alpha_{\text{C}} = \arccos\left(\frac{1}{n}\right) = 41\,^{\circ} \tag{4.1}$$

in water ($n = 1.33$). The result is a disc-like isochronous PMT hit pattern around the muon entry point on the SSS surface, with the early hits being located at the center of the disc and later hits at the periphery (see Figure 4.2). Similar discs are created at the muon exit point on the SSS surface, respectively the penetration point on the water tank floor. The tracking code searches for these discs by identifying clusters of time-correlated PMT hits in the OD, and calculates the baricenter of those clusters according to the equation:

$$\vec{R}_{\mathrm{bc}} = \frac{\sum_i w_i \vec{r}_i}{\sum_i w_i} \quad \text{with} \quad w_i(q_i, t_i) = q_i \cdot \mathrm{e}^{-(t_i - t_0)/\tau} \tag{4.2}$$

Here, q_i and t_i denote the charge and time of the i^{th} PMT hit associated with the respective cluster. The time information is referenced to the first hit of the cluster at t_0. The decay constant τ is set to $20\,ns$, an empirical value obtained by tuning the reconstruction algorithm on the data. The baricenter is calculated in Eucledian space and eventually projected radialy on the SSS surface. While the reflectivity of the Tyvek sheets covering the inner surface of the OD significantly enhances the muon detection efficiency, this reflection light can also cause fake clusters in the tracking. Final arbiter in the selection of valid clusters are the collected total charge of each cluster, as well as a time-of-flight check assuming ultra-relativistic muons. Figure 4.2 presents a sample muon event reconstructed by the OD muon tracking algorithm.
As will be presented in Section 4.6, the OD muon tracking returns reliable results for the majority of cosmic muons. However, the reconstruction suffers in case of horizontal tracks crossing the SSS at the lower quarter of the hemisphere, which is unpopulated by PMTs. A schematics of the OD PMT instrumentation can be found in Figure 2.1 on page 17.

4.3 Outer Detector Calibration

Analogous to the ID, physics events in the OD are reconstructed on the basis of the charge and timing information of photon-induced PMT signals. Specifically Equ. (4.2) illustrates the strong dependance of the OD muon track reconstruction on the proper calibration of each of the 208 OD PMTs. The necessary calibration is accomplished with an external UV-LED system, providing a PMT illumination well defined in timing and intensity. The calibration observables are evaluated in an offline data processing and written to the database. The development of the corresponding *Echidna* reconstruction modules was part of this work, and is presented in the following.

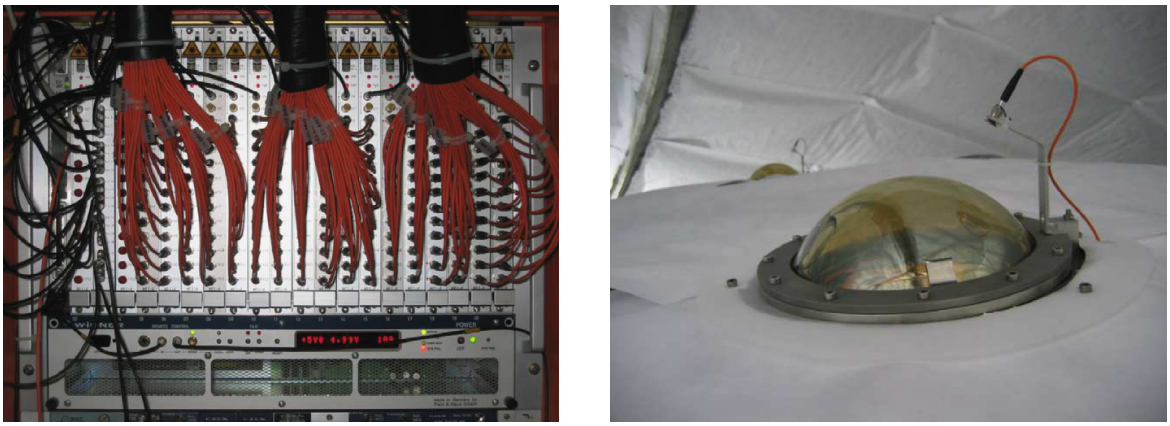

Figure 4.3: The OD calibration system. *Left:* The external UV-LED system addresses each OD PMT through an individual optical fiber. *Right:* Encapsulated OD PMT with the optical fiber mounted at an off-axis position. [31]

4.3.1 LED Calibration System

The LEDs are mounted in 18 custom VME boards of 12 LEDs, each emitting light at a peak emisison of 370 nm with a time jitter of 0.8 ns [32]. This light is fed via optical fibers of 55 m length to the OD PMTs (see Figure 4.3). Providing a synchronous time signal, this system allows for a measurement of the relative time offsets and jitters of each data channel, consisting of the PMT itself and the subsequent electronics chain. A description on the basic functionality of a PMT can be found in Section 3.1. The intensity of each LED is tuned to create with a probability of 5% per light pulse a photo-electron on the corresponding PMT photocathode. Thus, the chance to create multiple photo-electrons with a single pulse is reduced to a permille level. The resulting *Single Photo-Electron* (SPE) spectrum is used for the charge calibration of the PMT. The application of this LED system requires an initial cross-calibration of all LEDs to guarantee synchronous time signals and proper intensities for a SPE PMT response. This was achieved by using an outside reference PMT of the same type as the OD PMTs (ETL9351), adjusting the programmable delay lines and voltages of each LED on the VME boards.
As the LEDs are easily excited, they cause to a certain degree random light emission when the VME-boards are powered. To avoid this additional noise during normal data acquisition (DAQ), the LED system is only powered during the weekly calibration run. This timescale is sufficient for monitoring the slow drifts in the channel responses.

4.3.2 Calibration Algorithms

Once per week, a dedicated calibration run is taken to monitor and calibrate the detector response of Borexino. In these runs, the LED OD calibration triggers account for about half of all 250k injected service triggers. With the LEDs addressing the PMTs in SPE mode (i.e. $\simeq$5% photo-electron detection probability), each live PMT is expected to record about 6k photon hits. The DAQ raw-file is processed with the *Echidna* data reconstruction software in a special calibration mode. Based on the decoded hits of each OD channel, two calibration software modules (*bx_calib_muon_time_alignment* and *bx_calib_muon_charge_peak*) evaluate the time alignment and charge response. Fitting gaussian functions to the timing and charge response distributions, the associated central values and standard deviations are retrieved. The modules ignore service channels, as well as channels of little photon statistics, flagging their calibration as failed. The latter one occurs when the channel is broken or its respective LED calibration chain defective. Though, even with a sufficient number of detected photons, a channel calibration can fail if it does not fulfill certain quality checks as specified in the description of the calibration modules. Channels with failed calibration are set to an average value derived from all OD channels.
Both modules retrieve tuning parameters from a configuration file (*echidna.cfg*), allowing for adjustments of the module behaviour. The control parameters accessible via the configuration file are listed in the Appendix in Table 8.4.

Time Calibration

Figure 4.4 shows a typical timing response of an OD channel taken during a calibration run. The PMT is illuminated by the LED-induced light pulses, which populate the dominant peak structure at $\simeq$740 ns. Furthermore, a small population of *late pulses* is present about 50 ns after the main peak. A description of late pulses can be found in Section 3.1. As the first step, the module generates a sum histogram of the decoded hit times of all OD channels, and identifies the maximum of this distribution as the *average timing offset*. After this, the hit time distribution of each channel is produced and evaluated individually as described in the following.
After the maximum of the respective LED peak has been identified, the peak is fitted with a gaussian within a certain *time_allowance* (default: $\pm$10 ns) to the maximum position in a binned log-likelihood fit (see Figure 4.4). The fit returns the mean value and the sigma of the calibration peak, which have to satisfy quality criteria. The mean value is required to be within a certain range (*max_time_offset*, default: $\pm$20 ns) to the *average timing offset* of all channels. The peak sigma, characterizing the shape of the channel time response, is obliged to fall within

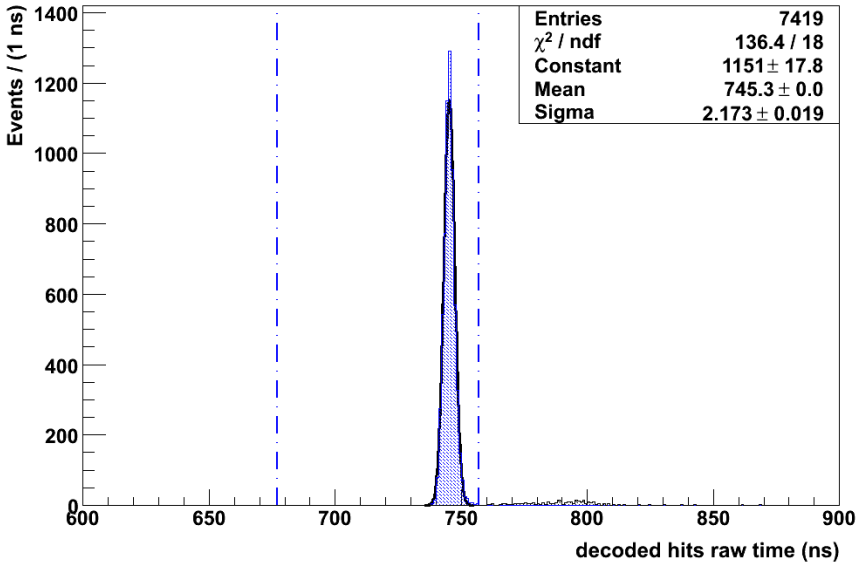

Figure 4.4: Time profile of PMT hits recorded by a single OD channel during a calibration run. Of the full gate length of $16\,\mu s$, only a $300\,ns$ wide subrange centered at the LED-induced peak is shown. The small population around $790\,ns$ originates from LED-induced *late pulses* in the PMT. The timing information of the PMT channel is extracted with a gaussian fit to the primary peak. PMT hits located in the blue shaded area between the dashed vertical lines are used for the charge calibration of the PMT (see Figure 4.5).

meaningful values ([*min_time_rms*, *max_time_rms*], default: [0,10] ns). A certain drift of the LED peak to the last channel calibration is allowed within limits (*time_drift*, default: $\pm 10\,ns$). If the channel calibration results don't fulfill the required constrains, the mean and root-mean-square of the channel hit distribution are taken as calibration values, which in turn are subjected to the same quality requirements. If these values suffice neither, the calibration of the channel has failed. For a successfully calibrated channel, the position of the LED peak is referenced to the *average timing offset* of all PMTs, and written along with the peak sigma to the database. Otherwise, the mean and sigma are recorded as '0' in the database, and the channel is flagged as uncalibrated.

Charge Calibration

The upper plot in Figure 4.5 shows the charge response of the OD channel to all hits collected during LED calibration triggers, containing dark noise, late pulses, afterpulses, and LED hits. For a description of late pulses and afterpulses, see

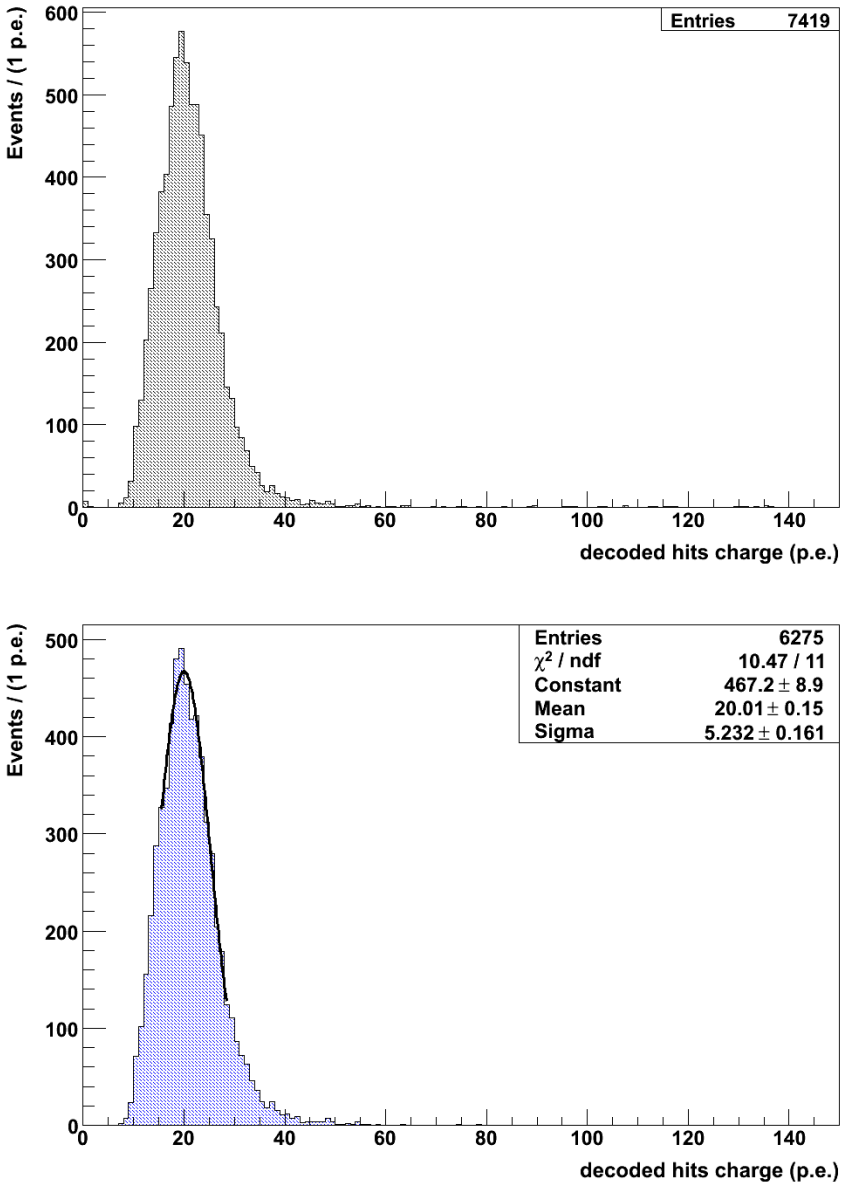

Figure 4.5: Charge distribution of PMT hits recorded by a single OD channel during a calibration run, before (top plot) and after (bottom plot) selecting PMT hits on-time with the LED light pulses (see Figure 4.4). *Bottom:* The SPE shape information of the PMT channel is extracted with a gaussian fit within a dynamic fit range.

Sec. 3.1. To enhance the LED signal, the *bx_calib_muon_charge_peak* calibration module reads only hits in a small time interval around the LED timing peak,

as indicated in Figure 4.4 by the blue shaded area between the dashed vertical lines. The parameters for the time interval can be controlled via the configuration file and are usually set to a central value of *time_offset* = 717 ns with a range of *time_allowance*= $\pm 40\,ns$. The corresponding charge spectrum is presented in the lower plot of Figure 4.5. Compared to Figure 3.2 in Chapter 3, the shown calibration spectrum is truncated. This is the result of a hardware threshold applied to the PMT signals to suppress darknoise hits in the Borexino experiment. The threshold is individually set for each PMT close to the minimum between the exponential darknoise and the photon-induced gaussian distribution (see Sec. 3.1). Analogous to the time calibration module, a summed hit-charge histogram of all OD channels is created to derive the *average charge peak* from the maximum position. For each individual channel a gaussian fit is used for extracting the mean value and sigma of the LED-induced SPE spectrum. Due to the mentioned truncation of the charge spectrum and the existence of patholigical OD channels, an algorithm was implemented to dynamically identify the fit range of the gaussian function. The algorithm identifies the maximum of the distribution, associated with the mean value of the gaussian, and averages the corresponding height over the neighbouring charge bins to increase the statistical significance. Based on this maximum height $h_{\max}$, the fit range is evaluated by approaching the maximum from both sides, defining the start of the fit as the point the distribution surpasses lefthand-sided the first time $2/3^{\text{rd}}$ of $h_{\max}$. The end of the fit is set by a right-hand sided sweep at a threshold of $1/4^{\text{th}}$ of $h_{\max}$. An example fit is shown in the lower plot of Figure 4.5. The quality control of the resulting values in mean and sigma is analogous to the one described in the time calibration. In addition, the χ^2 of the fit divided by the number of degrees of freedom is required to be within reasonable values ([*chi2_min*,*chi2_max*], default: [0.1,4]). If the calibration was successful, the extracted mean value and sigma are written to the Borexino database. Otherwise, the database entry for that channel is filled with a mean value set to the *average charge peak* of all OD channels, and is flagged as uncalibrated.

4.3.3 Resolution Improvement

The impact of the individual channel timing alignment is presented for a typical calibration run in Figure 4.6. Fitting a gaussian to the overall time distribution, a significant improvement in the width from $3.5\,ns$ before the calibration to $2.1\,ns$ afterwards is visible. This refers directly to an improvement in the individual channel timing resolution. Figure 4.6 also shows the corresponding overall SPE charge response before and after the calibration. The former distribution is referenced to the mean charge of all channels for comparison, while the later one is corrected for the individual calibration values. The application of the charge calibration increases the resolution, bringing out the SPE spectral structure in more detail. The

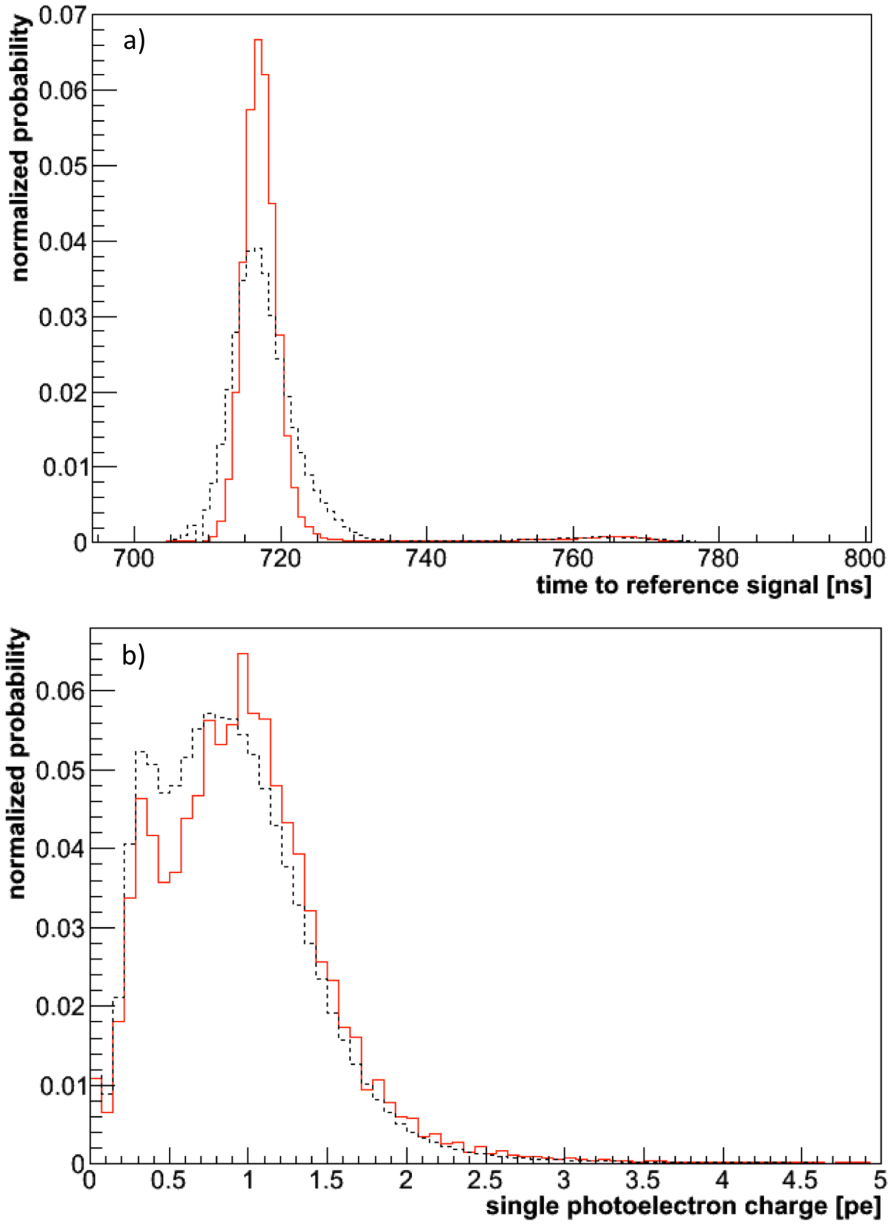

Figure 4.6: Impact of the LED calibration on the OD photomultiplier response. Timing (a) and SPE charge (b) distributions before (black dashed line) and after (solid red line) applying calibration data. [32]

reconstruction of physics events in the OD, especially the muon tracking, benefits of this improvement of resolution in timing and charge response.

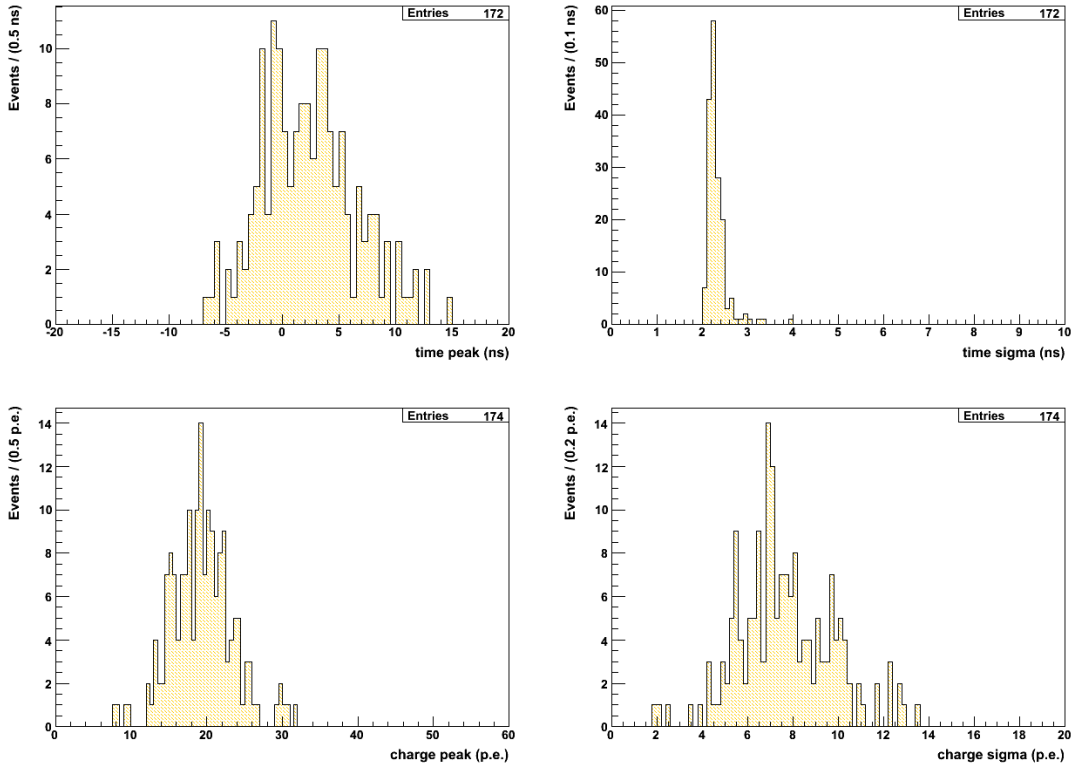

Figure 4.7: Results of a typical calibration run. Shown are the profiles of the peak positions and standard deviations derived from the LED-induced OD PMT response distributions in time (upper plots) and charge (lower plots). The time peak is given relative to the average peak position of all OD PMTs. Of the 208 OD PMTs, 172 were successfully calibrated in timing and 174 in charge response. A total of 33 channels is without signal, being either dead (26) or suffering from a defective LED calibration chain (7).

4.3.4 Outer Detector Maintenance

The calibration data obtained with the LED system does not only serve as input for physics reconstruction in the OD, but provides a tool for detector monitoring and maintenance. While the majority of channels has been stable in in the last 5 years of data taking, several channels have broken since. By retrieving the calibration data from the database, these broken channels and channels of strange behaviour can be identified for electronics maintenance checks. In the course if this thesis, identification criteria and visualization routines for these problematic channels have been developed and incorporated in the Borexino maintenance framework.

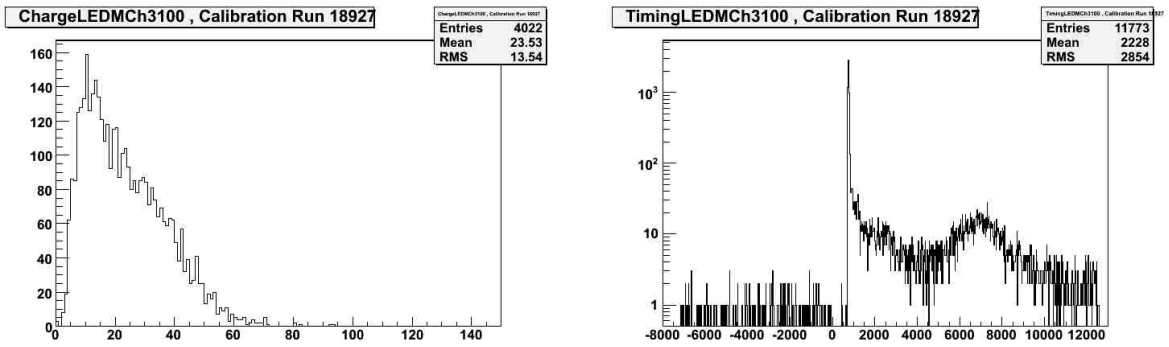

Figure 4.8: Maintenance plots for an OD channel identified as problematic. Shown are the charge (left plot) and timing (right plot) distributions of LED calibration triggers, with the x-axis in units of photo-electrons and nanoseconds, respectively. The y-axis is given in arbitrary units. The charge distribution shows a deformation with respect to a healthy channel (see Figure 4.5), while the timing distribution features a relatively large contribution from (ionic) afterpulses, causing a pronounced structure at about $6\,\mu s$ after the main peak.

Problematic Channel Identification and Visualization

Figure 4.7 presents the results of a typical calibration run. The 4 plots show the peak positions and standard deviations of successfully calibrated channels, as derived by the calibration modules from the corresponding timing and charge response distributions. A detailed study of a large set of calibration data has been performed and the following quality criteria developed:

- charke peak position $\in [5, 30]\, p.e.$
- charke sigma $< 13\, p.e.$
- time peak position[2] $\in [-10, 10]\, ns$
- time sigma $< 3\, ns$

Based on these criteria, problematic OD channels are identified in each calibration run. For each of these channels, several maintenance plots are created, which are accessible via a secured Borexino webpage to the electronics crew for the weekly detector maintenance. OD channel information is collected from 2 sources. The DAQ run processed by the macro provides the charge response distributions based on electronics pulser and random service triggers. The LED calibration response is read from the latest preceding calibration run saved in the Borexino

[2]relative to the average peak position of all OD PMTs

storage area, if not stated otherwise in the input parameters of the macro. As can been seen in Figure 4.8, the LED-induced charge response distribution of the shown OD channel features a pathological structure compared to Figure 4.5. In addition, the time distribution contains a large fraction of afterpulses, which are visible as a delayed time structure with a peak at about $6\,\mu s$ after the main peak. While the probability of a regular pulse to produce an afterpulse is about 5% in a standard ETL9351 Borexino PMT [51], this probability is by a factor of 5 higher for the shown OD PMT. For a description on the phenomenom of afterpulses, see Sec. 3.1.

Long-term Stability

The PMT time offset is found to be stable from run to run within $0.5\,ns$, while the position of the LED-induced SPE charge peak features a 10% spread. The maximum deviations found are $4\,ns$ in timing and 40% in the SPE charge position [32]. Figure 4.9 presents the long-term stability in channel calibration of the OD, beginning with the comissioning of the LED system in July 2008 up to November 2012. The plot depicts the number of channels with a successful calibration in both time and charge. Uncalibrated channels are the result of a malfunction of the data acquision channel (PMT and electronics chain), or of insufficient direct light by the calibration system due to a defect LED or broken connection fiber. Of a total of 33 OD PMTs without signal, 26 have been identified as broken data acquisition channels, while 7 don't receive light from the LED system.
The initial 2 years show fluctuations in the number of calibrated channels due to hardware and software tuning operations on the calibration system, which finished at the end of 2009 (about run 11000). Though not noticable on time scales of several months, the long-term stability shows a slow but steady drop in the number of calibrated channels. The source of this has been identified as a slow degradation of the LED light intensities. With the calibration modules requiring a minimum amount of detected hits, a slow but steady drop in light output led to a decrease of about 15% in accomplished channel calibrations. As a transitional solution, the configuration parameter for the required minimum photon statistics (*minimum_efficiency*) was lowered from 0.005 to 0.002 at the 27^{th} of October 2011 (run 16971), and further to the current default value of 0.001 at the 8^{th} of May 2012 (run 18376). At the beginning of August 2012, the LED intensities were readjusted by performing a LED hardware cross-calibration using the external reference PMT, as described in Section 4.3.1.

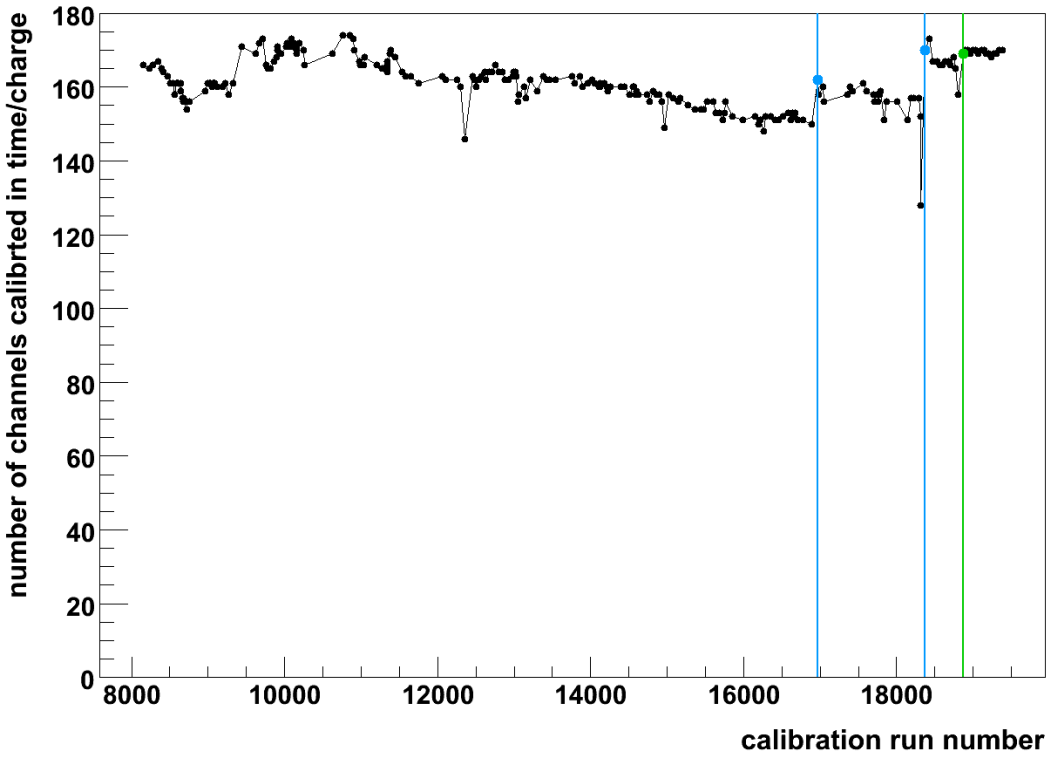

Figure 4.9: History of OD channel calibrations, from July 2008 (run 8149) till November 2012 (run 19380). The data points represent the number of OD channels calibrated both in time and charge via the given calibration runs. A slow but steady decrease in the number of calibrated channels is visible, caused by the slow degradation of the LED light intensities. To counteract this, the calibration module behaviour was changed in terms of the required minimum photon statistics per channel at the 27^{th} of October 2011 (run 16971) and the 8^{th} of May 2012 (run 18376), indicated by the blue markers in the Figure. In a hardware operation performed at the beginning of August, the LED intensities were readjusted. The first calibration run taken with the restored intensities is run 18867 (green marker).

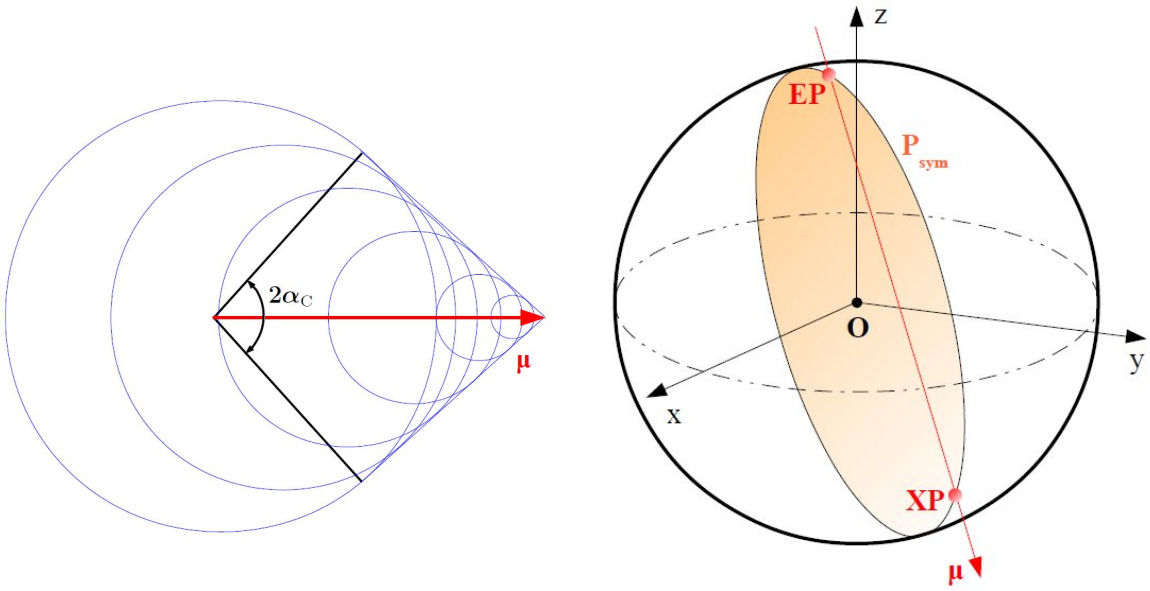

Figure 4.10: Symmetries in muon light emission and ID illumination. *Left:* A muon crossing the ID generates spherical waves of scintillation light, which superimpose to a forward running light cone. The cone features an opening angle identical to a regular Čerenkov cone. With a refractive index of the scintillator liquid of $n = 1.5$, the corresponding Čerenkov angle α_C is 48 °. In addition, the scintillation light causes a spherical light front propagating backwards. *Right:* The symmetries in the (spherical) Borexino geometry and the (axial) light emission along the muon track result in a illumination of the ID surface, which is symmetric to the plane P_{sym}. This symmetry plane is defined by the origin O of the ID sphere and the muon track. The muon entry (EP) and exit point (XP) are located on the great circle defined by P_{sym} and the ID surface.

4.4 Inner Detector Muon Tracking

With a granularity of 2212 PMTs at sub-nanosecond timing precision, the distinct PMT activation profile generated by the emission characteristic of a muon crossing the ID provides a powerful tool for tracking cosmic muons. In the course of this thesis, a track reconstruction algorithm was developed and implemented as a module (*bx_laben_tof_tracker*) in the *Echidna* software framework in collaboration with Michael Wurm. The module is designed for muons crossing the ID, reconstructing the track by retrieving the *Entry Point* (EP) and *Exit Point* (XP) of the muon on the SSS. This is accomplished by a time-of-flight analysis, based on the first photon hits detected by each PMT.
In the first step, the muon EP is identified by the isochronous disc-like hit pat-

tern caused by the first muon-induced photons inside the ID, and a subsequent fit to the photon arrival times. To identify the XP, the code capitalizes on the strong symmetry of the problem, with Borexino's ID being spherically and the muon-induced light emission being axially symmetric along the track. As a result, the plane defined by the muon track (containing EP & XP) and the center of the ID divides the PMT activation profile in two symmetric hemispheres (see Figure 4.10). By subdividing the sphere in equidistant PMT rings, this symmetry plane P_{sym} can be identified by fitting the photon arrival time patterns of each ring. The activation profile of PMTs located in the ring defined by P_{sym} exhibits a clear discontinuity at the muon XP. By reconstructing the EP and XP, the muon track is fully described.

4.4.1 Muon Light Emission

A muon crossing the ID emits light due to the scintillation mechanism and the Čerenkov effect. These processes generate incoherent and coherent light, respectively. The Čerenkov photons are emitted instantaneously, while the scintillation photon radiation follows an exponential light emission decay ($\tau \simeq 3\,ns$ in Borexino). A muon generates about $2 \cdot 10^5$ (10^4) scintillation photons per decimeter of track length in the scintillator (buffer) liquid, of which 10^4 (500) are detected by the ID PMTs. Due to the high photon statistics, the first scintillation photons detected by the PMTs have been emitted almost instantenously by the muon. For the ID muon track reconstruction, only the first photon hits on each PMT are used.
As illustrated in Figure 4.10, the spherical scintillation light emitted along the muon track superposes to a photon wave front consisting of a forward running cone and a backward running sphere. The emission angle of the cone is identical to the muon-induced Čerenkov cone ($\alpha_{\text{C}} = 48\,^\circ$), defined by the refractive index of the scintillator medium of $n = 1.5$ (see Equ. (4.1) on page 49). For muon track sections crossing the active volume contained inside the IV, scintillation clearly dominates the light output. For track sections in the buffer volume, the scintillation light emission is supressed by a factor of 20 due to the quencher DMP, resulting in a scintillation light output of the same order as the Čerenkov light. While the respective weights of scintillation and Čerenkov light to the total light output may vary, the shape of the conical wave front is unaffected.

4.4.2 Entry Point Reconstruction

As a result of the backward running light sphere caused by scintillation, PMTs close to the EP of the muon are the first to be illuminated in the ID. A first generation

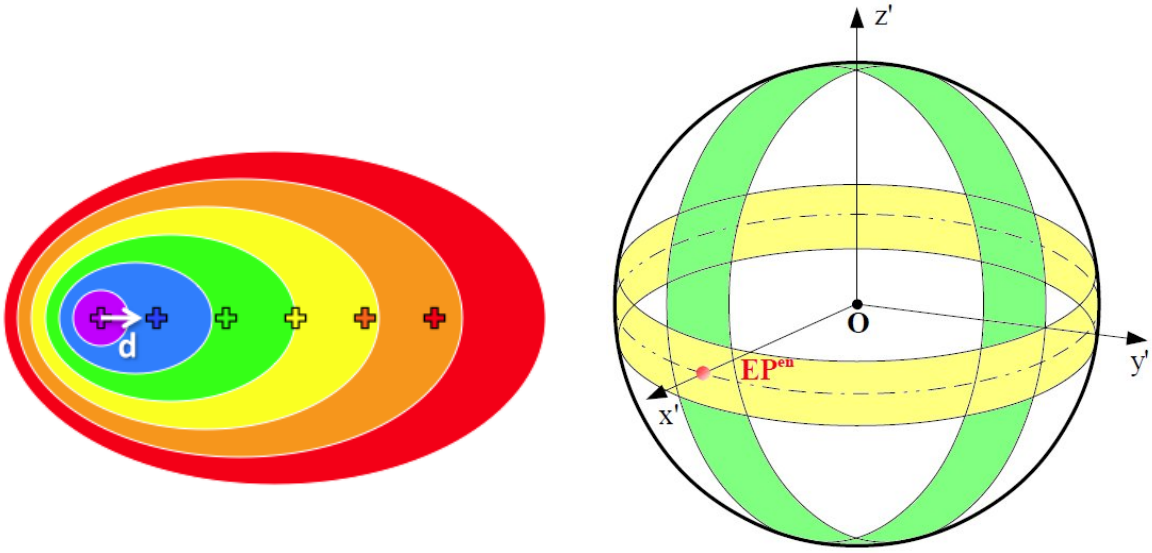

Figure 4.11: Entry point reconstruction. *Left:* Schematics of the ID illumination profile at the muon entry point [32]. The isochronous PMT hits form ellipses with the entry point in one focus. The excentriticy of the ellipses is related to the inclination of the muon track relative to the ID surface. The very first hits (symbolized by the violet area) are almost centered on the entry point position and are used for a first entry point estimate $\vec{EP}^{\text{en}}$. *Right:* Rotated coordinate system CS', featuring $\vec{EP}^{\text{en}}$ in the equatorial plane at $(R_{\text{S}}, 0, 0)$. Two perpendicular rings of PMTs are selected ($|\theta'| = 0.3\,rad$ and $|\phi'| = 0.3\,rad$) to identify the azimuth ϕ'_{EP} and zenith θ'_{EP} angles of the muon entry point via a time-of-flight analysis. The two rings intersect at the estimated entry point $\vec{EP}^{en}$.

ID muon tracking module *bx_laben_energy_tracker*, developed by Michael Wurm, reconstructs the EP via the disc-like hit pattern of the hits recorded in the first $5\,ns$ of the muon event. Depending on the inclination of the muon to the SSS surface, the shape of the hit pattern is spherical (perpedindicular inclination) or elliptical, with the EP lying approximately in the focus of the disc (see Figure 4.11). Analogous to the OD reconstruction (see Equ. (4.2)), the baricenter of the disc is calculated and projected on the SSS surface, defining $\vec{EP}^{\text{en}}$. The reconstructed entry point is described in spherical coordinates as

$$\vec{EP}^{\text{en}} = R_{\text{S}} \begin{pmatrix} \cos(\phi^{\text{en}}_{\text{EP}})\ \sin(\theta^{\text{en}}_{\text{EP}}) \\ \sin(\phi^{\text{en}}_{\text{EP}})\ \sin(\theta^{\text{en}}_{\text{EP}}) \\ \cos(\theta^{\text{en}}_{\text{EP}}) \end{pmatrix} \tag{4.3}$$

The parameter R_{S} denotes the SSS radius of $6.82\,m$. For more details on the reconstruction of the $\vec{EP}^{\text{en}}$, see [62].

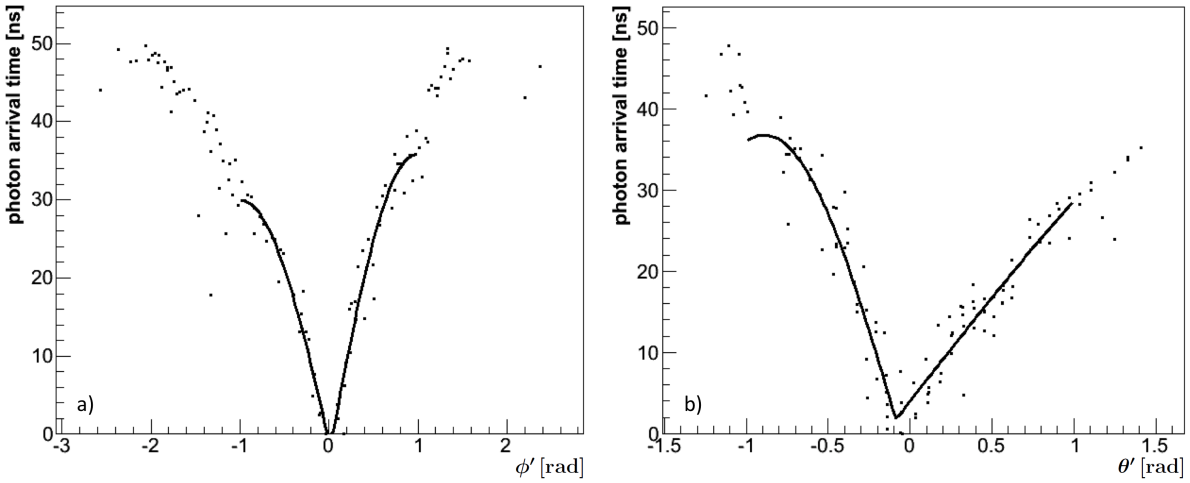

Figure 4.12: Photon arrival times as a function of the PMT azimuth ϕ' (left plot) and zenith θ' (right plot) angles in the rotated coordinate system CS'. PMTs have been selected in two perpendicular geodetic rings as depicted in Figure 4.11. An offset of π was applied in the presentation of the θ' distribution, for instance $\theta' = 0\,rad$ in the equatorial plane. Best fit values give results close to zero for both ϕ'_{EP} and θ'_{EP}, meaning that the first estimate entry point $\vec{EP}^{\mathrm{en}}$ is close to one reconstructed by the time-of-flight analysis ($\vec{EP}$). [32]

This point serves as a first estimate for the reconstruction of the entry point $\vec{EP}$ by the second generation *bx_laben_tof_tracker* module, with the respective angles ϕ_{EP} and θ_{EP}. To avoid topological effects of the spherical coordinates at the poles, the Borexino coordinate system CS is rotated according to the transformation matrix:

$$M(\upsilon, \zeta) = R_y(\upsilon) R_z(\zeta) \tag{4.4}$$

$$\text{with } \upsilon = \frac{\pi}{2} - \theta_{\mathrm{EP}}^{\mathrm{en}} \,,\, \zeta = -\phi_{\mathrm{EP}}^{\mathrm{en}} \tag{4.5}$$

This transformation consists of the basic rotations around the z- and y-axis and results in a coordinate system CS' with $\vec{EP}^{\mathrm{en}}$ being in equatorial plane at the coordinates (R_{S},0,0). Coordinates in this system are denoted with an apostroph. The *bx_laben_tof_tracker* module searches for the muon EP based on the hit time pattern by selecting two perpendicular PMT rings via $|\theta'| = 0.3\,rad$ and $|\phi'| = 0.3\,rad$ for the determination of ϕ'_{EP} and θ'_{EP} respectively. The corresponding geometry is illustrated in Figure 4.11. Plotting the photon arrival times at the PTMs versus the respective spherical angles, a clear V-like shape is visible, with the minimum identifying the muon EP (ϕ'_{EP}, θ'_{EP}). To extract the position of the minimum in ϕ' and θ', the empiricial fit function

$$t(\varphi') = t_0 + \begin{cases} a^- \cdot \sin(c^-(\varphi'_{\mathrm{EP}} - \varphi')) & \text{if } (\varphi' < \varphi'_{\mathrm{EP}}) \\ a^+ \cdot \sin(c^+(\varphi' - \varphi'_{\mathrm{EP}})) & \text{else} \end{cases} \tag{4.6}$$

is used. With regard to the curved surface geometry and a possible inclination of the muon track relative to the surface, the fit function provides separate weights $a^{\pm}$ and slopes $c^{\pm}$ as free parameters. In addition, a time offset t_0 is allowed. Figure 4.12 shows fits of the $\vec{EP}$ in ϕ' and θ'. In the example, the best fit values of ϕ'_{EP} and θ'_{EP} are close to zero, meaning that the first estimate entry point $\vec{EP}^{\mathrm{en}}$ is close to one reconstructed by the time-of-fligh analysis ($\vec{EP}$). Applying the inverse Rotationmatrix M^{-1}, one receives the coordiantes of the entry point ϕ_{EP} and θ_{EP} in the Borexino coordinate system CS.

4.4.3 Symmetry Plane Reconstruction

Due to the symmetries in the Borexino geometry and the light emission along the muon track, the photon arrival time pattern at the ID PMTs is symmetric to the plane P_{sym} defined by the ID center and the muon track (see Figure 4.10). While by default the identificiation of the XP on the ID surface is a mathematical problem in 2 dimensions, utilizing the fact that the XP is also located within this symmetry plane disentangles its reconstruction into two 1-dimensional problems. To find P_{sym}, the basic coordinate system is transformed according to Equ. (4.4), using

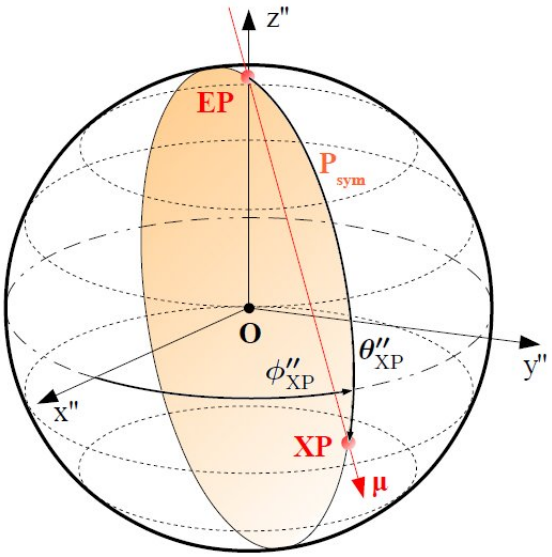

Figure 4.13: Rotated coordinate system CS'', with $\vec{EP}$ at the zenith at $(0, 0, R_{\mathrm{S}})$. The ID PMT surface is divided in 12 equidistant rings, of which 6 are illustrated. Based on the photon arrival time pattern in each ring, the symmetry plane P_{sym} and the associated angle ϕ''_{XP} are identified (see Figure 4.14).

the angles of the new entry point ($\upsilon = -\theta_{\mathrm{EP}}$, $\zeta = -\phi_{\mathrm{EP}}$). The new coordinate system CS'' features the entry point $\vec{EP}$ at the zenith at (0,0,R_S) (see Figure 4.13). Coordinates in this system are denoted by a double-apostroph. In this coordinate frame, the symmetry plane P_{sym} is defined by ϕ''_{XP} ($\pm\pi$), containing the XP at the spherical angles ϕ''_{XP} and θ''_{XP}. To identify P_{sym}, the ID PMT surface is divided in 12 equidistant PMT rings, as indicated in Figure 4.13. According to *Fermat's Principle*, the first PMT in each ring to be hit by the photon wave front is the one closest to the muon track (i.e. $\phi'' = \phi''_{\mathrm{XP}}$). In consqeuence, the hit time pattern for each ring in ϕ'' follows a V-like shape, with the minimum being at ϕ''_{XP}. For each ring i ($\in [1, 12]$), the following semi-empirical function is fitted to the photon arrival time distribution:

$$t_i(\phi'') = \frac{n}{c} \cdot \sqrt{R_{\mathrm{S}}^2 + \rho_{\mathrm{I},i}^2 - 2R_{\mathrm{S}}\,\rho_{\mathrm{I},i}\,(\cos\phi''\cos\phi''_{\mathrm{XP}} + \sin\phi''\sin\phi''_{\mathrm{XP}})} + t_{0,i} \qquad (4.7)$$

The parameters R_{S}, n, and c denote the SSS radius, the refractive index of the scintillator, and the vacuum speed of light respectively. Furthermore, the function allows for a constant offset in time, described by $t_{0,i}$. The fit-function is a simplified description of the expected PMT activation profile. It is motivated by the expected hit time pattern in plane i, accounting only for light emission of the intersection point $\vec{I}_i$ of the muon with the respective plane. The distance of the i^{th} intersection point to the z''-axis is given by $\rho_{\mathrm{I,i}}$. Applied to data, the function provides an

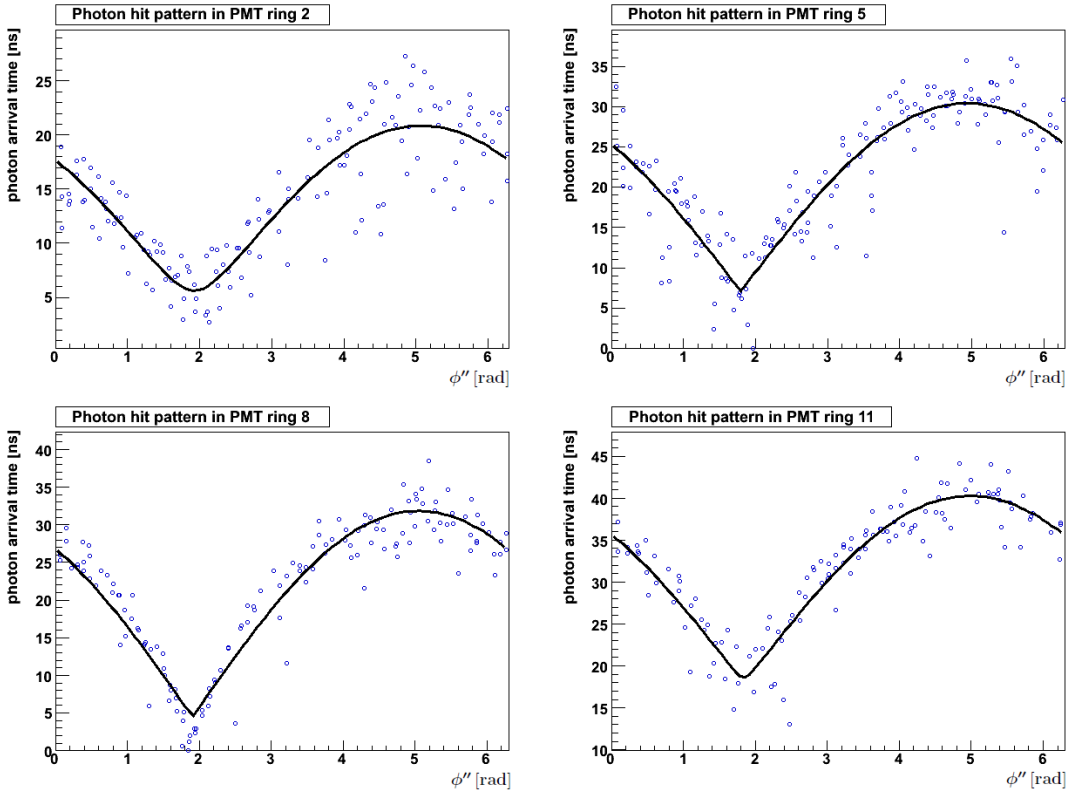

Figure 4.14: Exemplary photon arrival times of a sample muon event. Shown are 4 of the 12 equidistant PMT rings. Each profile i is fitted with Equ. (4.7), retrieving the azimuth angle $\phi''_{\mathrm{XP},i}$ in the coordinate system CS''. The fit results of all PMT rings is eventually combined to a global result of ϕ''_{XP}. For the shown muon, the azimuth angle is found to be $(1.90 \pm 0.05)\,rad$, corresponding to $(109 \pm 3)\,^\circ$.

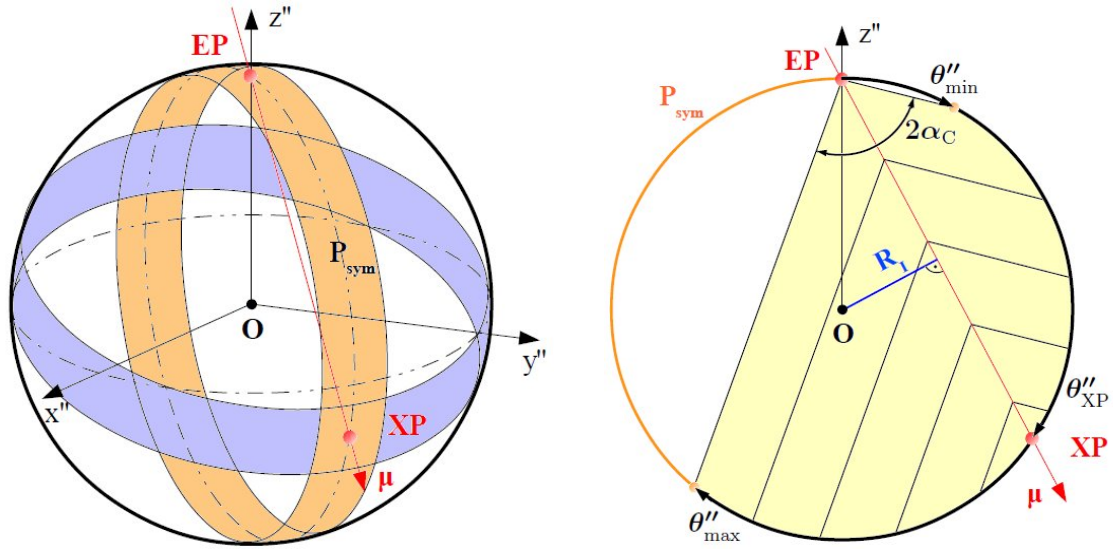

Figure 4.15: Rotated coordinate system CS'', with $\vec{EP}$ at the zenith at $(0, 0, R_S)$. *Left:* a PMT ring (orange) centered around P_{sym} is selected to identify the zenith angle θ''_{XP}. As the last step of the XP reconstruction, the azimuth angle ϕ''_{XP} is reevaluated within the respective perpendicular geodetic PMT ring (blue). *Right:* top view on the symmetry plane P_{sym} containing the muon track at impact parameter R_I. The muon emits light under an angle of α_C, illuminating the ID surface only within a certain azimuth interval $[\theta''_{min}, \theta''_{max}]$. The backward running scintillation light sphere (see Figure 4.10) is not used for the XP determination and therefore not shown.

excellent and reliable reconstruction of $\phi''_{XP,i}$ for each ring i (see Figure 4.14). The best fit values and their corresponding uncertainties σ_i serve in the calculation of a weighted mean value of ϕ''_{XP}.

4.4.4 Exit Point Reconstruction

With the determination of ϕ''_{XP} via the symmetry plane, only θ''_{XP} is missing in the identification of the XP. For this purpose, a PMT ring of $\pm 0.75\,m$ relative to P_{sym} is selected, as illustrated by the orange ring in Figure 4.15. Assuming light emission along the muon track under the Čerenkov angle ($\alpha_C = \arccos(\frac{1}{n}) = 48\,°$),

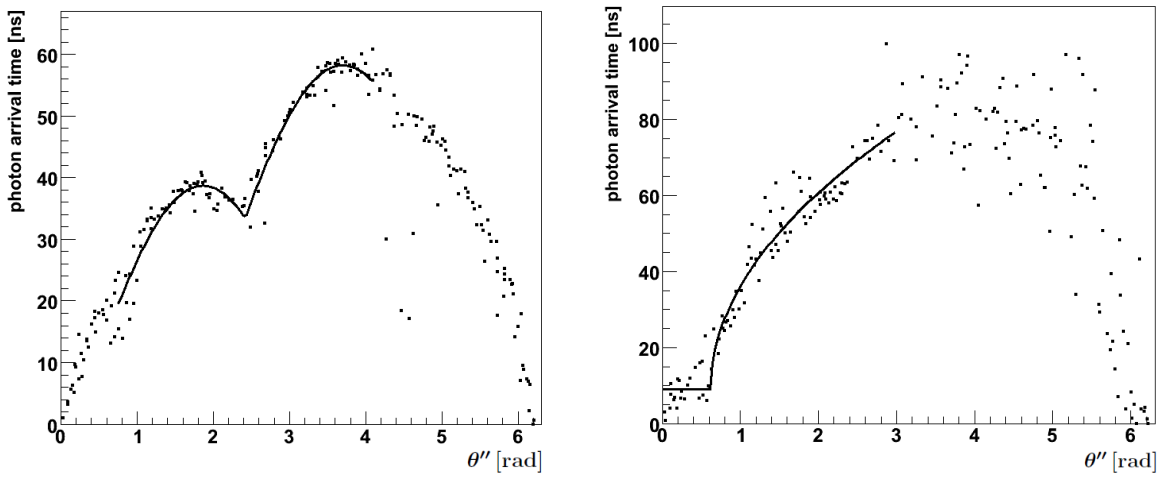

Figure 4.16: Photon arrival times as a function of the PMT zenith angle θ'' in the rotated coordinate system CS''. The PMTs have been selected in a geodetic ring defined by the symmetry plane P_{sym} (orange ring in Figure 4.15). *Left:* The sample muon track crosses the active IV volume, generating about 26k photon hits. A clear discontinuity is visible at a zenith angle of $2.4\,rad$, identifying the XP (θ''_{XP}). The distribution is fitted with function (4.8). *Right:* The shown muon track crosses the experiment in the buffer liquid, generating about 2500 hits inside the ID. The expected kink at the XP is less pronounced due to the lower photon statistics. The XP zenith angle is retrieved by fitting function (4.10) to the time profile.

the expected hit time profile in θ'' is derived by analytical calculus:

$$\begin{aligned} t(\theta'') &= \frac{2R_{\mathrm{S}} \cdot |\sin(\frac{1}{2}\theta'')|}{c \cdot \sqrt{1-\frac{1}{n^2}}} \cdot \Bigg(\sin\Big(\arccos\Big(\frac{1}{n}\Big) - \frac{1}{2}|\theta'' - \theta''_{\mathrm{XP}}|\Big) \\ &\quad + n \cdot \sin\Big(\frac{1}{2}|\theta'' - \theta''_{\mathrm{XP}}|\Big)\Bigg) + t_0 \qquad (4.8) \\ \theta'' &\in [\theta''_{\mathrm{min}}, \theta''_{\mathrm{max}}] := [\theta''_{\mathrm{XP}} - \alpha_{\mathrm{C}}, \theta''_{\mathrm{XP}} + \alpha_{\mathrm{C}}] \cap [0, 2\pi] \end{aligned}$$

Again the parameters R_{S}, n, and c denote the SSS radius, the refractive index of the scintillator, and the vacuum speed of light respectively. The variable t_0 takes a constant time offset into account. The forward running light cone emitted by the muon illuminates only azimuth angles θ'' within deviations of the Čerenkov angle α_{C} to the *true* value of the XP angle θ''_{XP}. This is taken into account by the interval selection of θ'' in the definition of Equ. (4.8). The corresponding geometry is illustrated in Figure 4.15. To get a first estimate of θ''_{XP}, its geometrical relation with the impact parameter R_{I} of the muon track

$$\theta''_{\mathrm{XP}} = 2 \arccos\left(\frac{R_{\mathrm{I}}}{R_{\mathrm{S}}}\right) \qquad (4.9)$$

is used. The impact parameter of a muon is defined as the distance between the muon track and the origin of the ID sphere, as shown in the right plot of Figure 4.15. A first estimate of R_{I} is provided by the *bx_laben_energy_tracker* module, which gives a rough reconstruction of the impact parameter based on the visible energy deposition in the ID [62]. The derived angle θ''_{XP} serves as starting value for the fit-routine of the *bx_laben_tof_tracker* module, described by Equ. (4.8). As θ''_{XP} is a parameter for both the fit-range and the fit-function itself, the fit-routine is self-referential. This self-reference is treated by iterating the fit multiple times, adjusting each time the fit-range to the latest value of θ''_{XP}, and converging on the *true* value of the XP azimuth angle. Figure 4.16 presents the final output of the iteration procedure, featuring a clear discontinuity at θ''_{XP}. This kink results from the projection of the muon light cone on the curved surface of the Borexino ID.

A basic correlation between the impact parameter of the muon track R_{I} and the number of detected hits in the ID is illustrated in Figure 4.17. The fit routine of θ''_{XP} according to Equ. (4.8) works best for muon tracks with impact parameters of less than $4.5\,m$, corresponding to a total amount of more than 4000 detected PMT hits. Due to the spherical geometry, track lengths inside the ID drop significantly for bigger impact parameters, consequently resulting in much lower photon statistics for the ID muon track reconstruction. For tracks featuring only a number of

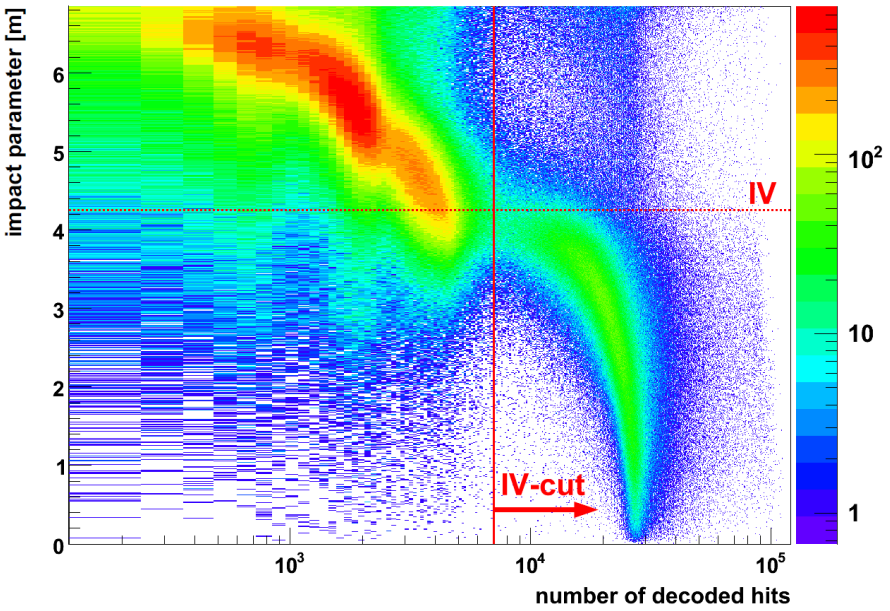

Figure 4.17: The impact parameter determined by the OD tracking versus the number of ID hits in the muon event. Muons crossing the active IV volume generate a large amount of light, populating the main band above 7000 hits. Muons crossing only the buffer liquid are located in the band below 7000 hits. The curvature of the observed bands is connected to the relation of the muon impact parameter and the corresponding path lengths in the ID liquids.

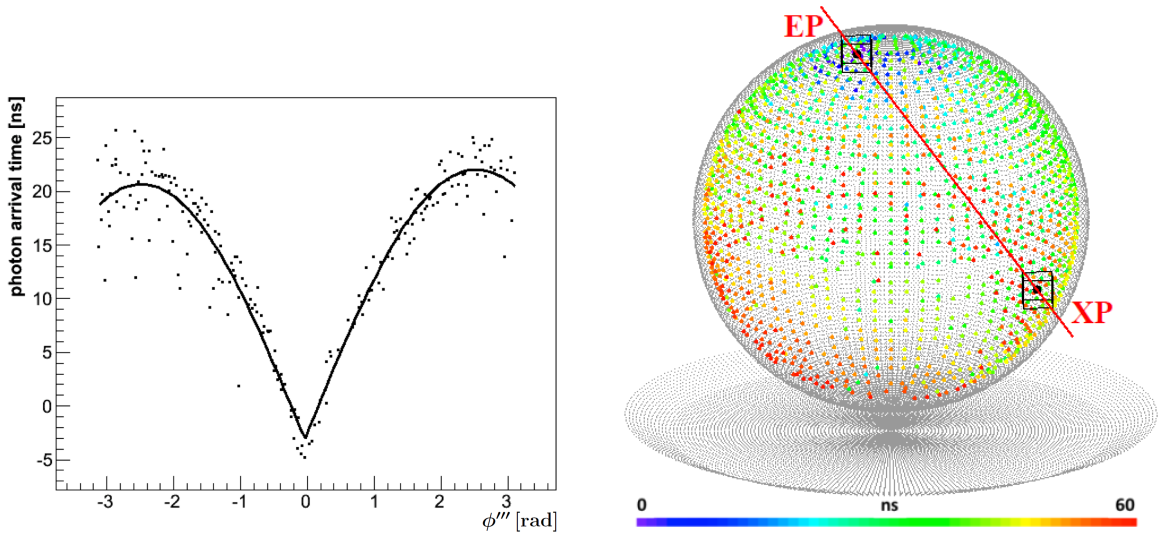

Figure 4.18: *Left:* Photon arrival times as a function of the PMT azimuth angle ϕ''' in the rotated coordinate system CS''' [32]. The PMTs have been selected in a geodetic ring perpendicular to the symmetry plane P_{sym} (blue ring in Figure 4.15). In this coordinate frame, the XP is located at $(R_{\text{S}}, 0, 0)$ and P_{sym} is described by $\phi''' = 0$. The best fit value of ϕ'''_{XP} is close to zero, meaning that P_{sym} was reconstructed properly. *Right:* Muon track reconstructed by the ID tracking algorithm. The boxes indicate the uncertainties on the reconstructed entry and exit point. The timing information of the photon hits is color-coded.

detected hits in the range of [2500,4000], an alternative empirical fit function is applied to stress the discontinuity at θ''_{XP}:

$$t(\theta'') = t_0 + \sqrt{a \cdot \sin(c(\theta'' - \theta''_{XP}))} \tag{4.10}$$

The function provides a weight a and a slope c as free parameters to accommodate for the curved surface geometry and the incliation of the muon track relative to the ID surface. Figure 4.16 presents a muon track fitted in this way. For muons with an impact parameter of more than $5\,m$, corresponding to less than 2500 detected hits, photon statistics are too poor to resolve θ''_{XP}, being too close to the EP. For these cases, the muon track is treated as tangential to the ID, touching the surface only in the EP.

As the last step, the polar angle ϕ''_{XP} is reevaluated more precisely at the location of the XP by selecting a geodetic PMT ring of $\pm 0.75\,m$ perpendicluar to the plane defined by $\theta'' = \theta''_{\mathrm{XP}}$ (see blue ring in Figure 4.15). The procedure is analogous to determination of the EP angles. Via the rotational matrix $M(\frac{\pi}{2} - \theta_{\mathrm{XP}}, -\phi_{\mathrm{XP}})$ of Equ. (4.4), a third coordinate system CS''' is defined with the current XP lying in the equatorial plane at $(R_{\mathrm{S}}, 0, 0)$. The V-like shape of the corresponding azimuth distribution ϕ''' is fitted with Equ. (4.6), retrieving ϕ'''_{XP} (see Figure 4.18). With the XP being fully described, the coordinates are transformed back to the Borexino coordinate system. Figure 4.18 illustrates a fully reconstructed muon track together with the timing information of each first PMT hit.

4.5 Global Muon Tracking

The two Borexino subdetectors provide truly indepedent reconstructions of muon tracks crossing the SSS. In terms of physics, the light-tight SSS prevents photon exchange between the ID and OD. Concerning the *Echidna* data analysis software, the muon track reconstruction modules rely on purpose solely on data provided by their respective subdetector. The independent reconstructions are finally merged by the global muon tracking module (*bx_global_tracker*) to a single best fit muon track. Fitting a straight line to the 4 track points provided by the ID and OD muon reconstruction modules, the global track is characterized via 4 fit parameters according to the parameterization:

$$\vec{T}(x) = \begin{pmatrix} 0 \\ \alpha \\ \gamma \end{pmatrix} + x \begin{pmatrix} 1 \\ \beta \\ \delta \end{pmatrix} \tag{4.11}$$

The 3-dimensional problem is split in two fits of 2-dimensional projections on the xy and xz planes. An additional fifth variable is recorded, containing the informa-

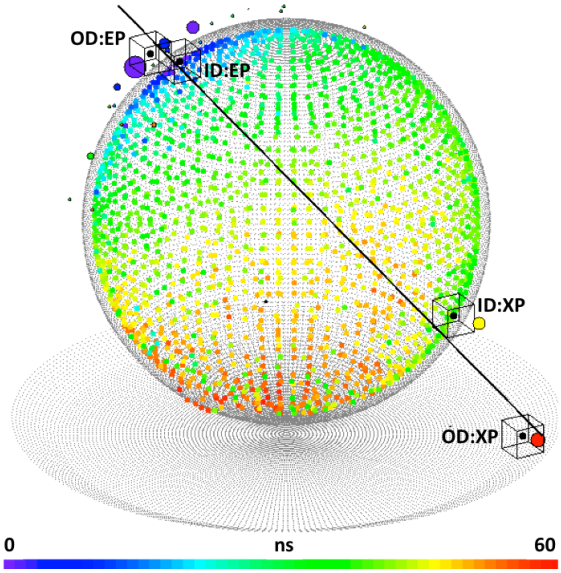

Figure 4.19: Global muon track, reconstructed with the track points provided by ID and OD tracking algorithms. The boxes indicate the uncertainties on the reconstructed entry and exit points. Also included is the information on the ID PMT hit time distribution (small colored dots) and the OD hits (colored circles). [32]

tion on the muon track direction. The proper alignment of the 4 track points is checked via the χ^2 value of the fit. In case of misalignment, the global tracker reconstructs the muon using the subsample of 3 points, which yields the best straight line alignment. Figure 4.19 presents the result of a global track reconstruction, based on the four track points including their respective uncertainties (indicated by boxes). In addition, the PMT activation profile of the ID, as well as the identified OD clusters are shown. More information on the global muon track reconstruction can be found in [62].

4.6 Tracking Performance

Extensive effort has been put by the Borexino collaboration in studying the resolution and systematic uncertainties of the respective muon track reconstructions, i.e. the ID, OD, and global muon tracking systems. The performance checks encompass:

- **External Muon tracker**
  Originally a prototope of the OPERA muon tracker, the *External Muon Tracker* (EMT) serves as an auxilliary system on top of the Borexino steel dome since spring 2010. It consists of two arrays of drift tubes perpendicular to each other, allowing for a 3-dimensional reconstruction of muon tracks. The EMT provides a angular resolution of better than $5\,mrad$ and a spatial resolution of $\simeq 300\,\mu m$. Though high in resolution, with a sensitive area of about $1\,m^2$, the muon count rate is rather low. On average, only $9.6\,\mu$/day are expected to cross both the EMT and the OD. Requiring an additional intersection with the ID or the IV reduces this rate to 6.1 and $2.1\,\mu$/day respectively. Due to its orientation, the EMT is mainly sensitive to vertical muons.

- **Muon-induced Neutrons**
  Interacting with the organic scintillator, muons can produce neutrons in spallation processes on ^{12}C nuclei. The neutrons thermalize and are eventually captured mainly by the scintillator-intrinsic Hydrogen. In the corresponding formation of a deuteron, a $2.2\,MeV$ γ is emitted. The γ from a neutron capture inside the IV produces about 700 PMT hits, allowing for a position reconstruction. The lateral distance profile of these neutrons to the parent muon-track yields information on the track reconstruction accuracy.

- **CNGS muons**
  As described in Section 2.3, μ_ν created by the *CERN Neutrinos to Gran*

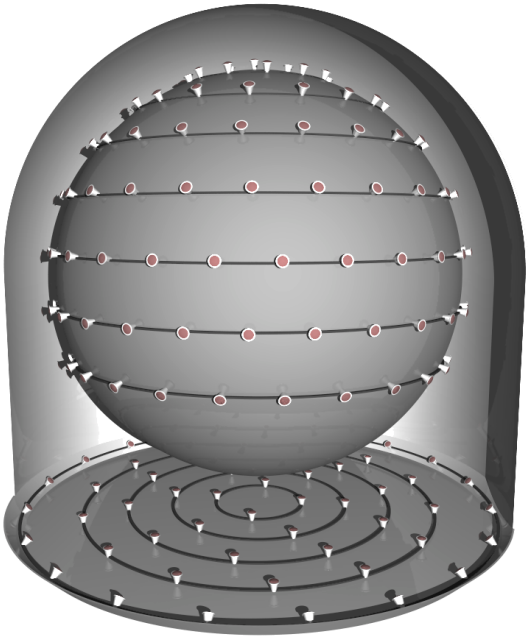

Figure 4.20: Schematics of the Borexino Outer Detector instrumentation, consisting of 208 8“ PMTs. The upper $3/4^{\text{th}}$ of the SSS outer surface is equipped with 154 PMTs, while the remaining 54 PMTs are distributed in 5 concentric circles on the floor of the water tank.

Sasso (CNGS) project can interact with the upstream rock at the LNGS underground lab, producing muons in a *Charged Current* (CC) reaction. With a mean energy of $17\,GeV$ the majority of these muons is well aligned with the μ_ν-beam, pointing back to the CERN. In the reference frame of the LNGS, the beam exhibits an inclination angle of $\theta = 93.2\,^\circ$, and an astronomical azimuth of $\phi = 305\,^\circ$. Hall C, which contains both the Borexino and OPERA experiments, is almost perfectly aligned to the beam, providing a subset of CNGS muons crossing both detectors ($\simeq$5% of all CNGS tagged events in Borexino). Therefore utilizing the by far superior track reconstruction resolution of OPERA (order of *mrad*), the accuracy of the Borexino muon trackers can be evaluated via a track-by-track comparison.

Due to the spherical symmetry of the ID, its corresponding muon tracking is independant on the direction of the incident muon. However, the OD features only an axial symmetry, and thus its performance depends on the inclination of the muon (see Figure 4.20). With the focus on the ID muon tracking system, the comparison of the common CNGS muon sample with the high-resolution OPERA muon reconstruction yields the most precise results, and will be presented in the

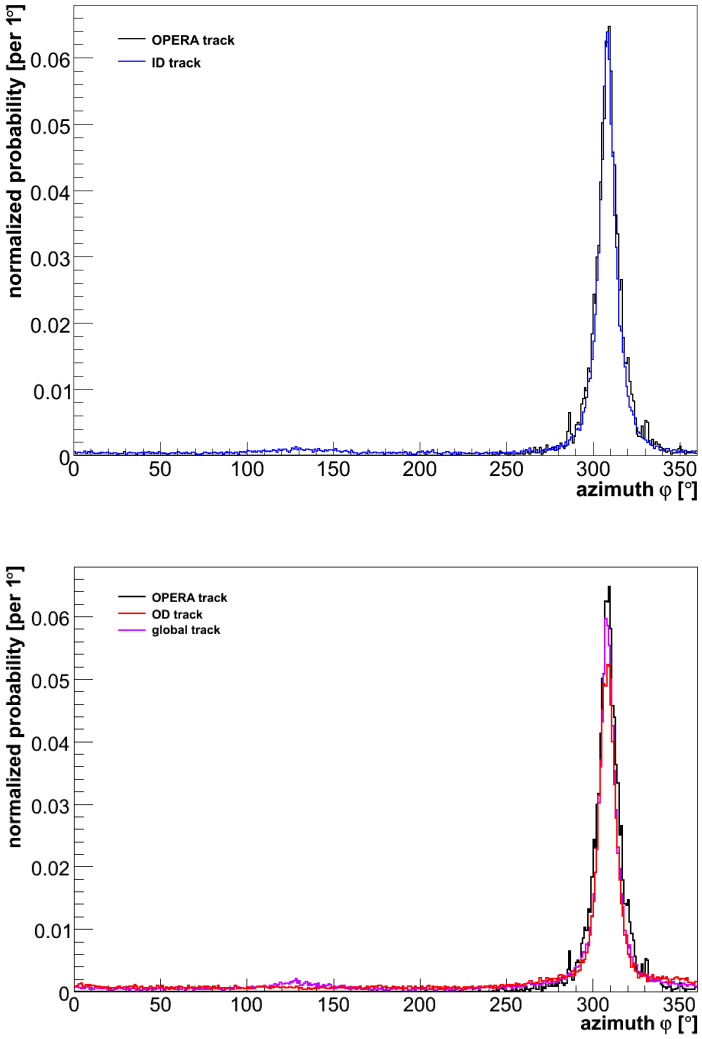

Figure 4.21: Azimuth angle distribution of CNGS-induced muons, reconstructed by the ID (top plot), OD, and global tracking (bottom plot). The distribution reconstructed by OPERA is shown for comparison (black). The CNGS beam is expected under the angle of $\phi = 305\,°$, which is well reconstructed by all three Borexino muon trackers. [64]

following. A detailed description of all cross-checks can be found in [32].

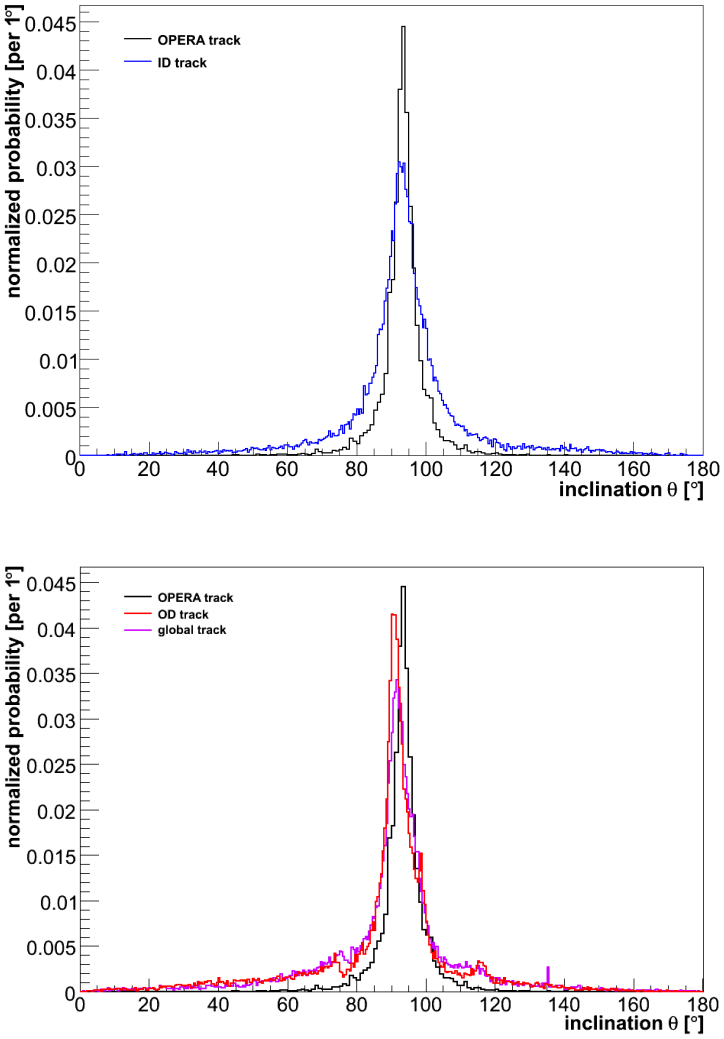

Figure 4.22: Inclination angle distribution of CNGS-induced muons, reconstructed by the ID (top plot), OD, and global tracking (bottom plot). The distribution reconstructed by OPERA is shown for comparison (black). The CNGS beam is expected under the angle of $\theta = 93.2\,°$, which is well reconstructed by the ID tracking. *Bottom:* The horizontal CNGS muon tracks are reconstructed by the OD at an about $2\,°$ lower inclination angle, as a result of the missing PMT instrumentation on the lower quarter of the SSS (see Figure 4.20). Being the combination of ID and OD tracking, the global tracking is also affected by this. [64]

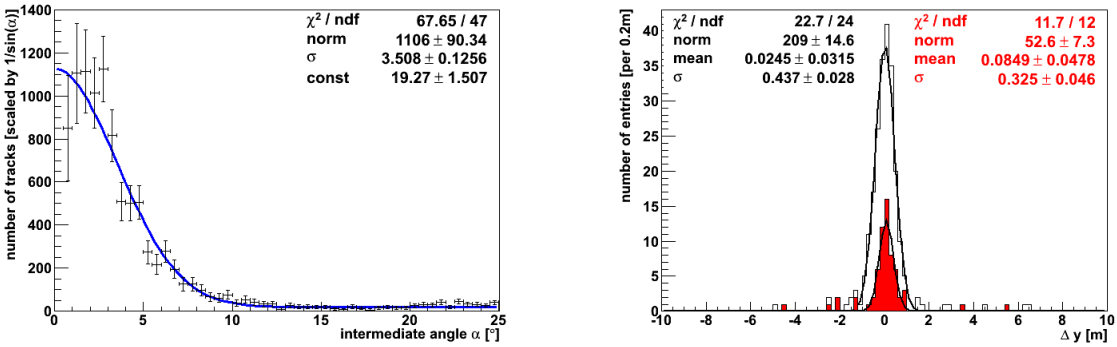

Figure 4.23: Track reconstruction of CNGS muons, detected by both Borexino and OPERA. *Left:* Intermediate angle α between the direction vectors of muon tracks reconstructed in OPERA and the Borexino OD tracking. The width of the Gaussian fit corresponds to the OD angular resolution. *Right:* y-distance distribution between reconstructed tracks in the Borexino yz-plane, comparing OPERA and Borexino global tracking. The lateral resolution σ_y improves if only muons are selected, which cross the IV (shaded red area). [32]

4.6.1 Reconstruction Resolution

The CNGS muon candidates are required to cross the Borexino SSS, signaled by almost synchronous light production in ID and OD. Figures 4.21 and 4.22 illustrate the reconstructed angular distributions of the three Borexino muon trackers (i.e. ID, OD, and global tracking), as well as the OPERA muon tracking. A clear peak structure at the expected CNGS beam orientation is visible. The OD muon tracker suffers from the missing PMT instrumentation on the lower quarter of the SSS (see Figure 4.20). As a result, the horizontal CNGS-induced muons are reconstructed in average at an about 2 ° lower inclination. Being the combination of the ID and OD muon tracking, the global muon tracking is also affected by this.

To derive the angular resolution of the Borexino muon trackers via the OPERA detector, a common CNGS muon data set is selected (about 3000 muons). To avoid deflection of the muons on the path between the two detectors, muon candidates in this data sample have an energy larger than $20\,GeV$ reconstructed by the OPERA detector. The indermediate angle α between the reconstructed track orientation vectors provided by Borexino and OPERA, $\hat{\mu}(\varphi, \theta)$ and $\hat{\nu}(\phi, \vartheta)$ is given by

$$\alpha = \arccos(\hat{\mu}(\varphi, \theta) \cdot \hat{\nu}(\phi, \vartheta)) \tag{4.12}$$

Figure 4.23 presents the distribution of α for the OD muon tracker, weighted with

ID-μ's	σ_α [°]	σ_y [cm]	σ_z [cm]	σ_{lat} [cm]
OD tracking	3.51±0.13	53±4	198±13	-
ID tracking	5.13±0.25	42±3	40±5	42±3
Global tracking	2.83±0.13	44±3	87±12	-
IV-μ's	σ_α [°]	σ_y [cm]	σ_z [cm]	σ_{lat} [cm]
OD tracking	3.01±0.15	28±7	45±7	-
ID tracking	2.44±0.19	36±5	31±6	34±4
Global tracking	2.31±0.13	33±5	35±7	-

Table 4.2: Fit results for angular and lateral resolutions obtained from a common Borexino/OPERA CNGS muon data set. The spherical symmetry of the ID muon tracking allows to statistically combine the lateral resolutions in y- and z-direction to a total lateral resolution σ_{lat}. The σ_z lateral resolution of the OD muon tracking suffers in the reconstruction of the horizontal CNGS muons as a result of the missing PMT instrumentation on the lower quarter of the SSS (see Figure 4.20). The global tracking, being the combination of the ID and OD tracking, provides an intermediate lateral resolution. [32]

$(\sin\alpha)^{-1}$ to achieve a constant angular surface density. The distribution is fitted with a Gaussian and a constant offset allowing for misreconstructed tracks. The latter is mainly caused by muons produced in CC reactions inside the Borexino ID, spoiling the reconstruction of the tracking modules designed for crossing muons. In addition, the comparison with OPERA also allows for determining the lateral resolution of Borexino's muon track reconstructions in the yz-plane perpendicular to the beam orientation. As an example, the distibution of the global tracking in the y-distance, combined with a Gaussian fit, is shown in Figure 4.23.

The full results of the comparison between Borexino and OPERA are presented in Table 4.2. In general, the lateral resolution of the ID muon tracking is the same in y- and z-direction, a consequence of the spherical geometry of the SSS. In consequence, the corresponding reconstruction resolutions σ_y and σ_z can be statistically combined to a total lateral resolution σ_{lat} for the ID tracking.
In case of muons crossing the ID (ID-μ's), the angular resolution of the ID tracking is worse than the OD tracking. This is caused by muons crossing the ID close to the periphery. As the total light output of the muon has approximately a linear dependance on the track path, photon statistics in the ID are low for peripheral muon tracks, reducing the track reconstruction resolution. In contrast, the OD offers every ID-μ at least $2\,m$ of water to generate Čerenkov light. However, due to the lack of PMT instrumentation on the lower quarter of the SSS, the OD tracking deteriorates in case of horizontal ID-μ crossing the lower hemisphere. These

	ID-μ's	IV-μ's
OD tracking	2.0%	1.2%
ID tracking	5.2%	0.8%
Global tracking	3.2%	2.1%

Table 4.3: Percentage of misreconstructed (upward-going) muons crossing the ID, and the IV in particular.

muons tend to be pushed either towards the sphere or the water tank floor. While this effect dissapears by selecting only ID-μ's crossing the upper hemisphere, the total OD tracking lateral resolution in z-direction suffers.
The tracking performance improves for both trackers in case of CNGS muons crossing the IV (IV-μ's), identified by generating more than 7000 ID hits in Borexino. The huge photon statistic significantly improves the angular and lateral resolution of the ID tracking. With an IV radius of $4.25\,m$, the OD tracking benefits from the connected geometrical selection of muons crossing mainly the instrumented area of the SSS. By combining the information of both trackers, the global tracking gains in angular resolution, while its lateral resolution obtains an intermediate value.

With the EMT being sensitive to vertical muons, and the neutron lateral distance study being independent of muon orientation, these analyses provide complementary tests of the tracking. In general, horizontal and semi-contained muon tracks are best recontructed by the ID tracker, while OD and global tracking produce the best results in case of vertical and crossing muons. The performance of the trackers is determined to an angular resolution $\simeq 3^\circ$ in case of OD and global, and $\simeq 5^\circ$ for the ID tracking. The lateral resolutions range from 40-50 cm for vertical muons, being the bulk of the cosmic muon background.

4.6.2 Cosmic Muon Angular Distribution

Figure 4.24 illustrates the angular distributions of cosmic muons, as measured by the three Borexino trackers. The muon flux arriving under a certain solid angle is indirectly proportional to the corresponding rock coverage. With the LNGS being located under Monte Aquilla, shielding is reduced towards the flanks of the mountain. The measured angular distributions are in reasonable agreement with each other. This is especially noteworthy, as the ID and OD tracking provide truly independant muon track reconstructions. Consistent with the previous results, the ID muon tracking features the lowest angular resolution.
Due to CC reactions of upward-going atmospheric ν_μ, a fraction of $\simeq 10^{-5}$ of all muons detected in Borexino is expected to be of upward orientation [63, 65, 66].

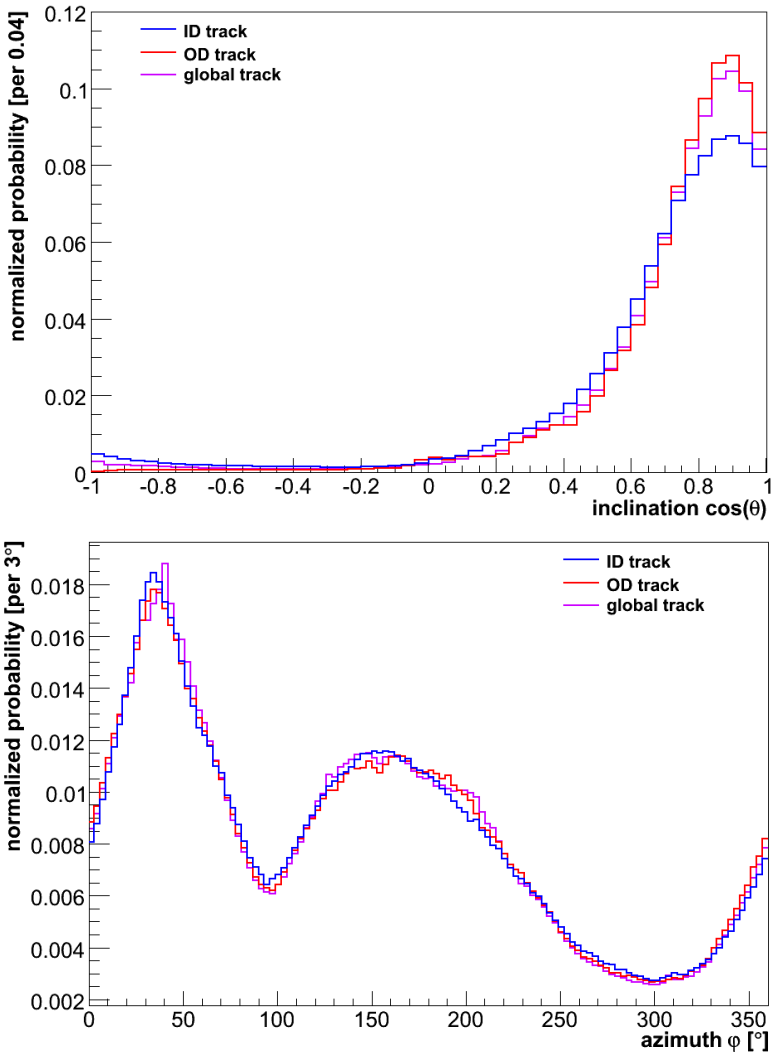

Figure 4.24: Inclination $\cos\theta$ (top plot) and azimuth angle ϕ (bottom plot) distributions of cosmic muons, reconstructed by the ID, OD, and global tracking. The angular distributions measured by the three Borexino trackers are in reasonable agreement with each other. [64]

However, the angular distributions of all three Borexino trackers feature an excess of events at $\cos\theta < 0$, accounting for about 2-5% of all muons crossing the ID. The majority of these events are misreconstructed peripheral muons, with the EP and XP being too close to properly identify the direction of motion of the muon. Restricting the study on muons crossing the IV, this number reduces to 1-2%. Table 4.3 summarizes the results on tracks of reconstructed upward orientation.

Chapter 5

Cosmogenic Neutrons

Cosmic muons crossing the *Inner Detector* (ID) of Borexino can produce neutrons in spallation processes on the Carbon nuclei intrinsic to the organic liquid scintillator. Depending on its initial momentum, such a cosmogenic neutron can travel from centimeters up to meters, thermalizing via scattering on protons within a few nanoseconds after production. The prompt signals of these scatterings cannot be seen in Borexino, as they are covered by the much larger muon light output. Eventually after a mean time of $\simeq 260 \mu s$, the neutron is captured on Hydrogen or ^{12}C, creating an excited Deuteron or ^{13}C nucleus. In the deexciation of the Deuteron a $2.23\,MeV$ γ is emitted, while in the case of ^{13}C a total γ energy of $4.95\,MeV$ is released. Based on the chemical composition of the liquid scintillator in Borexino and the respective thermal neutron capture cross sections, 99% of all thermal neutron captures are expected on Hydrogen.
Muon-induced neutron production is usually accompanied by the formation of radioactive isotopes. In consequence, an efficient identification of these neutrons via their capture γ's provides a crucial input for tagging cosmogenic radionuclides. Especially the tagging and rejection of the long-lived Carbon isotopes ^{10}C ($\tau = 27.8\,s$) and ^{11}C ($\tau = 29.4\,min$) rely heavily on the identification of the corresponding knock-off neutrons (see Chap. 6). Beyond this, cosmogenic neutrons on their own constitute a major background source for rare-event search experiments like dark matter, neutrino-less double-β-decay, and neutrino detectors. By studying the production characteristics of muon-induced neutrons, Borexino can provide important information for these experiments.

With a length of $16\,\mu s$, the standard trigger gate containing the muon itself, features about 6% of all muon-induced neutron captures. However, the majority of the neutrons is captured in the subsequent neutron gate of a duration of $1.6\,ms$. According to the respective background hit environments present in these two trigger gates, two neutron search algorithms have been developed and implemented

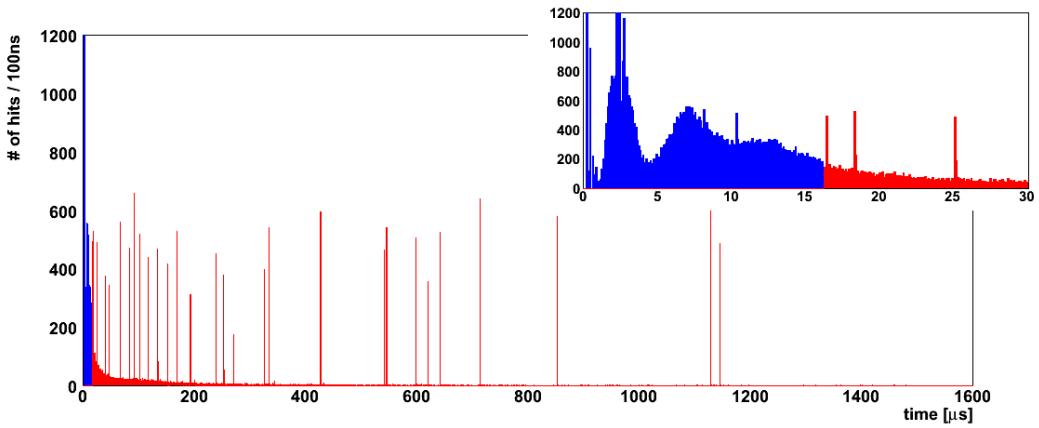

Figure 5.1: Hit time distribution of a sample muon trigger (blue) and the associated neutron trigger (red). A total of 53 neutron captures peaks were identified. The inset graph is a close-up view of the first 30 μs. [32]

in the *Echidna* data reconstruction framework in the course of this thesis. Besides neutron capture γ's, these algorithms are also sensitive to the other physics events populating the two trigger gates; i.e. muons, muon-decays, and accidental coincidences. The first part of this Chapter is dedicated to the description of the two detection algorithms, while the second part presents the studies on the events detected in the two trigger gates. Particular emphasis is placed on muon-induced neutron captures, presenting in detail studies on the corresponding detector response and physics observables. These studies conclude in the measurements of the mean neutron capture time (Sec. 5.5), the neutron production rate and yield (Sec. 5.8), and the neutron multiplicity distribution (Sec. 5.9).

5.1 Neutron Detection

With a length of 16 μs, the standard Borexino trigger gate is not sufficient to record all neutron captures following a muon ($\tau \simeq 260\,\mu s$). On that account, after a muon crosses Borexino, a subsequent neutron capture acquisiton gate of 1.6 ms is issued. Due to the electronics delays in the trigger formation, a tiny gap between these two gates of $(150 \pm 50)\,ns$ is present [32]. However, on the time scale of neutron captures, this introduces a negligible deadtime. The two consecutive triggers will be denoted as *muon trigger* and *neutron trigger* throughout this Chapter. Furthermore, the terms *muon trigger* and *muon gate* will be used as synonyms; the same approach applies to the *neutron trigger*.

In Figure 5.1, an example hit time distribution for both gates is shown. The scintillation light of the neutron capture γ's is visible as peak structures of width below $100\,ns$ on top of the continous noise distribution caused by the huge muon light output. While the $2.2\,MeV$ Deuteron γ is expected to feature about $\simeq$700 photomultiplier (PMT) hits (^{13}C gamma energy : $4.9\,MeV \cong$ 1200 hits), two effects can reduce the visible light output.

- **Geometrical boundary effects**
  Neutron captures close to the *Inner Vessel* (IV) boundaries (on either side) can generate gammas only partialy contained in the active scintillation volume. In consequence, the corresponding light output can be significantly reduced.

- **Electronics saturation**
  Muons can produce a huge amount of secondary particles (e.g. gammas, pions, electrons, neutrons, and protons) in hadronic and electromagnetic showers. If the energy of the muon and its secondaries is deposited in the active IV volume, the tremendous light output and the following PMT afterpulses can saturate the memory of the Borexino *Laben* digital boards, which were designed for low energy physics. As each digital board administers a group of PMTs close to each other, preferrably boards corresponding to PMTs close to the muon are saturated. After a board saturates, it remains unavailable for data acquisition (DAQ) for the remaining muon and subsequent neutron gate. This electronics saturation reduces the effective detection surface of the Borexino detector, and in consequence decreases the visible energy of physics events. In case of the neutron trigger, the number of boards being already unavailable at gate start can be easily identified. The affected boards feature a complete absence of hits in the gate, and are therefore denoted as *empty boards*. The corresponding number is stored in the *Echidna* variable *laben.empty_boards*, ranging from zero to a maximum of 280 *Laben* boards. However, this approach does not return the boards saturating during the read-out of the gate, and thus is not feasible for the muon trigger.

Depending on the the saturation state of the detector and the position of the neutron capture relative to the active volume, the visible signals of the capture γ's range from $\simeq$1200 hits for a capture on ^{12}C down to a few hits. In addition, muon events can produce up to 600 neutrons captured in the IV, further complicating the neutron detection.

Clustering Algorithm

The default ID clustering algorithm runs on the data recorded in the standard 16 μs trigger gate, and is designed for the detection of neutrino-interactions, as well as radioactive decays (α,β, and γ). It identifies peak structures of correlated hits, so-called *Clusters*, by scanning the *decoded hits* time profile in the trigger gate. The algorithm expects only a low background hit environment caused by PMT darknoise, late pulses, and PMT afterpulse hits (see Sec. 3.1). In consequence, it is not suited for the muon and neutron gates, which are highly populated by muon-induced noise hits. To detect extremely degenerated neutron capture signals in this high noise environment, combined with neutron multiplicities ranging up to several hundreds, sophisticated neutron detection algorithms were developed in the course of this thesis.
About 6 % of the neutrons are captured in the 16 μs muon gate, while the majority of the captures is expected in the 1.6 ms neutron gate. As can be seen in Figure 5.1, the fluctuations in the PMT noise distribution put different requirements on the detection algorithm logics for the two gates. As a result, two individual neutron detection algorithms were developed, one for each gate. Though designed and tuned for their respective application, both neutron clustering algorithms feature similiarities in the design concept.

The *bx_laben_findcluster* module's main routine provides the time profile of the *decoded hits* in the gate as a histogram of 16 ns wide bins to the neutron search algorithms. Both algorithms loop over their respective histograms, evaluating at every bin the local noise level and checking for a peak of excess hits above the same. A detected excess tags the start time of a potential neutron capture peak. Both codes search for the falling edge of the peak, and identify the time it takes for the peak structure to decay, i.e. till the peak tail is in statistical agreement with the baseline. These peak shape observables provide quality vetos on the identified peak, based on the decay time of the scintillator (fast decay time: $\simeq$3 ns) and the expected time spread due to light propagation (up to 40 ns). As a single muon can produce up to several hundreds of neutrons, both algorithms check each peak for a double-peak-structure, thus disentangling pile-up neutron captures.
Pushing the detection threshold to a minimum, while at the same time avoiding misclustering of noise, was the key challenge in developing and tuning the neutron detection algorithm logics. The identification of the peak start relative to the afterpulse background takes a central role in this regard.

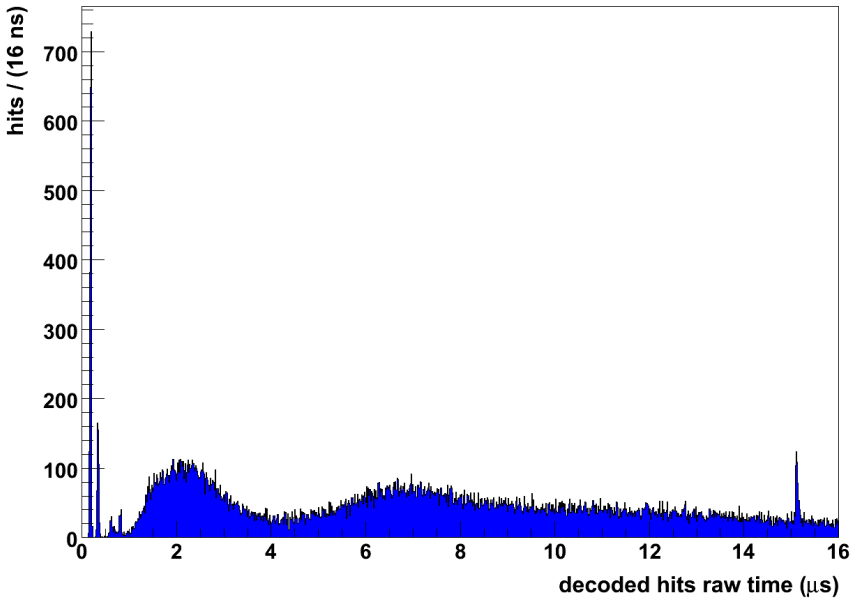

Figure 5.2: Hit time distribution of a sample muon trigger, containing a neutron capture γ candidate at time $t = 15.1\,\mu s$ after gate start. The present structures are described in the text.

Peak start identification in the Muon Gate

The first peak in the muon gate at time $t = 0.2\,\mu s$ after gate start originates from the scintillation and Čerenkov light, produced by the muon crossing the ID (see Figure 5.2). The huge light ouptut illuminates all 2212 PMTs, which in turn require $140\,ns$ to acquire new data (see description of the electronics in Sec. 3.2.2). As a result, the muon peak is sharply defined, followed by a gap. The second smaller peak structure originates from the same mechanism. After this initial muon illumination, a hit distribution with strong fluctations on the timescale of microseconds follows, typical for the ionic component of PMT afterpulses (see Sec. 3.1). To search for a peak structure on top of this noise, the neutron detection algorithm loops over all time bins and estimates at each bin i the local baseline level. Checking the hit distribution of previous bins in the relative time range of [-176,-16] ns, the mean value λ_i and the standard deviation σ_i of the local baseline are evaluated. A potential peak start is identified, if the bin i of population y_i features an excess of hits satisfying the equation:

$$y_i \;>\; a \cdot \lambda_i + b \cdot \sigma_i + c \cdot f_{\mathrm{PMT}} \qquad \text{with } a = 2,\, b = 3,\, c = 10 \tag{5.1}$$

Here, f_{PMT} denotes the fraction of live PMTs normalized to 2000 channels. The empirical function (6.3) is inspired by the confidence level calculation based on a

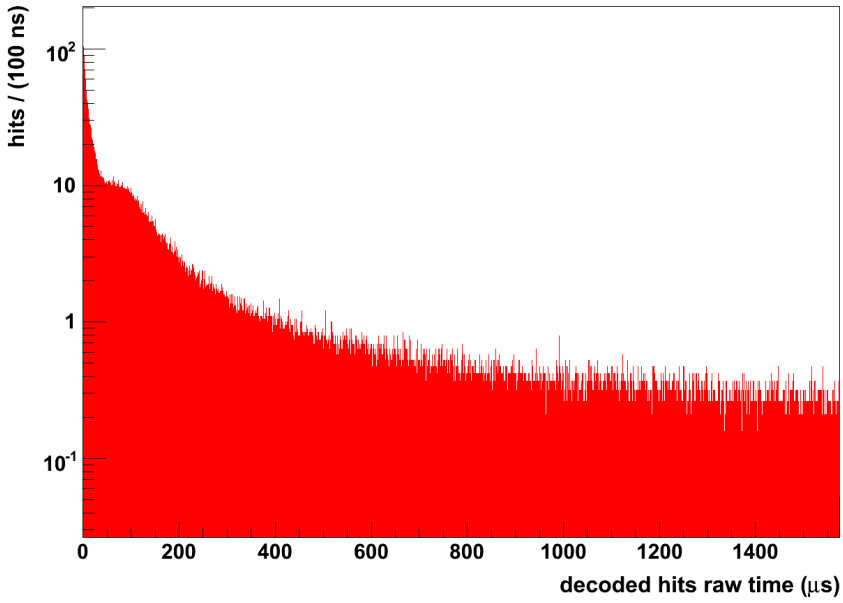

Figure 5.3: Average hit time distribution of neutron triggers containing high noise levels of more than 18k background hits. The distribution has been purged of hit clusters associated with physics events.

normal distribution. The parameter c allows for a constant offset, scaled by the number of working channels f_{PMT}. The values for the parameter set (a, b, c) have been derived from event scanning and tuning operations. Hit clusters detected in this way have to satisfy a threshold of 40 hits, corresponding to a visible energy deposition of $80\,keV$. The resulting clustering algorithm can handle the strong afterpulse fluctuations present in the muon gate. The probability to misidentify a noise peak is estimated to be less than 10^{-10}.

Peak start identification in the Neutron gate

While the clustering in the muon gate requires to deal with strong baseline fluctuations, the situation changes for the neutron gate. Figure 5.3 shows the noise hit time distribution averaged over several neutron gates of high noise levels, i.e. each containing more than 18k background hits. As can be seen, the noise distribution constantly drops over the gate length of $1.6\,ms$, allowing for a much more sensitive peak search method. Especially in the later part of the gate, the noise baseline can drop to only few hits in hundreds of nanoseconds, consequently following a poisson distribution. For every time bin i, the algorithm estimates the baseline using the distribution of previous bins as follows:

- ignore the closest $80\,ns$ to bin i
- ignore bins which are associated with an already detected cluster of correlated hits
- collect noise statistics of 200 bins containing hits

Based on the background information sampled in a time frame of at least $3.2\,\mu s$, the baseline is extrapolated to the time bin i using an analytical straight line fit. The weight of each bin in the fit is set to '1', giving importance to statistical fluctuations in the data. The extrapolated local baseline value λ_i serves as input in the poisson distribution:

$$p(\lambda_i, k) = \frac{\lambda_i^k \cdot e^{-\lambda_i}}{k!} \tag{5.2}$$

The poisson distribution is a discrete probability density function, returning the probability p of a population k for a given mean value λ_i. The neutron clustering algorithm uses a likelihood estimator $\mathcal{L}$ to quantify the agreement of a given (whole-number) bin population y_j with the baseline distribution:

$$\mathcal{L}(\lambda_i, y_j) = \begin{cases} \sum_{k=y_j}^{\infty} p(\lambda_i, k) & \text{for } y_j > \lambda_i \\ 1 & \text{else} \end{cases} \tag{5.3}$$

In case a local bin population y_j is above the mean baseline value of λ_i, the function returns the discrete integral of the poisson distribution. As the algorithm searches for excess structures on top of the baseline, fluctuations resulting in a population deficit (i.e. $y_j \leq \lambda_i$) are not considered. For these cases, the likelihood estimator returns '1', corresponding to an agreement between bin population y_j and the baseline. According to equation (5.3), the invidual ($\mathcal{L}_i$, $\mathcal{L}_{i+1}$, $\mathcal{L}_{i+2}$) and total ($\mathcal{L}_{tot,i} = \prod_{n=0}^{2} \mathcal{L}_{i+n}$) likelihoods of three consecutive time bins (i, $i+1$ and $i+2$) are evaluated. A peak has to satisfy the following conditions:

- $\mathcal{L}_i < 0.1$: the first bin features a significant excess of hits on top of the baseline
- $\mathcal{L}_{i+1} < \mathcal{L}_i$: the excess of hits increases in the second time bin
- $\mathcal{L}_{tot,i} < 10^{-8}$: the combined structure features a low likelihood of being in agreement with baseline fluctuations

As equation (5.3) is non-linear, the arrangment of neutron capture hits over the $16\,ns$ time bins influences the likelihood calculation. While this is insignificant for peaks of high visible energy deposition, it plays a role for very degenerated

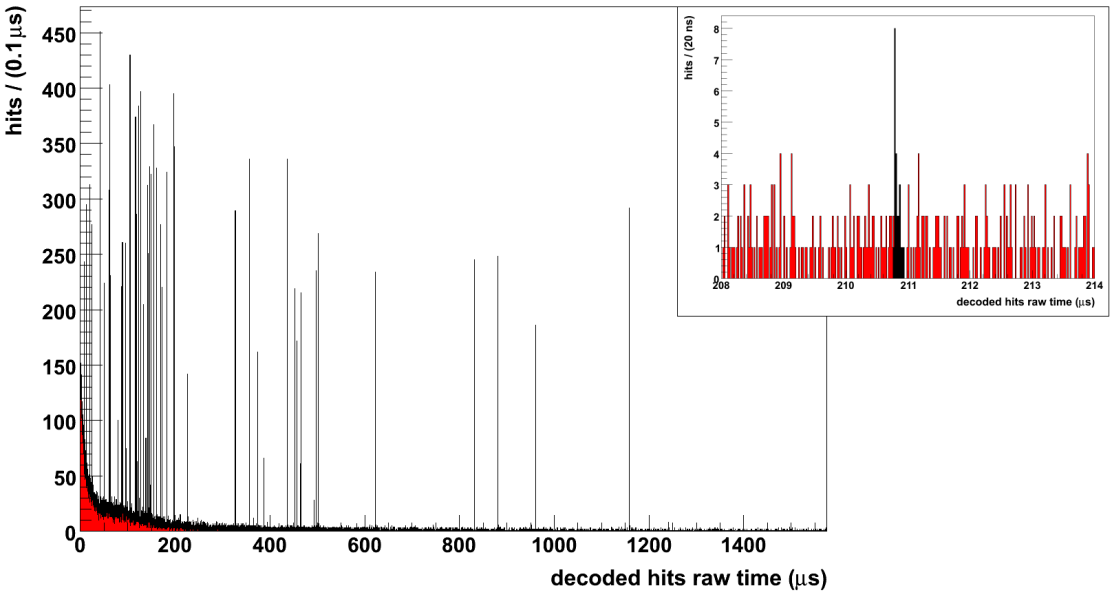

Figure 5.4: Hit time distribution of a sample neutron trigger containing 57 neutron capture γ candidates. The inset graph presents a physiscs event of low visible energy, as detected by the clustering algorithm at 210.8 μs after gate start. The cluster (black) contains 24 hits, of which 9 are associated with background.

peaks. This issue is solved by a time binning check, revealing peak structures lost to unlucky hit binning. However, this increased sensitivity comes at the price of a higher probability to cluster noise peaks. The corresponding probability was investigated with Monte Carlo simulations and the data itself (see Sec. 5.6), and found to be less than $4 \cdot 10^{-6}$.
The described method is extremely sensitive, pushing the detection threshold of neutron capture peaks down to clusters of only 5 hits, corresponding to 10 keV of visible energy deposition; an requirement detrimental in detecting capture γ's degenerated by boundary effects and electronics saturation. Figure 5.4 presents a neutron trigger of high neutron multiplicity (57), recorded with several saturated *Laben* boards (73). While the neutron captures inside the IV produce visible energies of about 400 PMT hits for the given saturation state of the detector, several neutron capture peaks feature smaller visible energies as the corresponding γ's deposit their energies partially in the buffer liquid. The described clustering algorithm is able to identify even extremely degenerated hit clusters, as demonstrated in the inset of the Figure.

Cluster contamination

While physics events are identified by the peak-structure of time-correlated PMT hits, it is impossible to identifiy the nature of individual hits, i.e. whether they originate from scintillation light or noise. As shown in Figure 5.4, all hits recorded during the cluster length are associated with the physics event, including background hits. The amount of background hits in the cluster can be estimated statistically by evaluating the local baseline, and is stored in the *Echidna* variable *nhits_bkg*. However, reconstruction modules relying on the information of individual hits -like position reconstruction- suffer from the noise hits contamination (see Section 5.4.5). As the muon-induced noise level variies in time over the duration of the trigger gate, so does the level of cluster corruption.

5.2 Energy Observable: Number of cluster hits

As has been described in Section 3.3.3, the charge information of detected clusters is compromised in the muon and neutron gates. This is caused by instabilities in the channel integrator outputs of the front-end electronics as a result of the large muon light output. As energy observable, the number of clustered hits normalized to 2000 live PMTs ($N_{\text{hits}}^{\text{norm}}$) is used in this Chapter instead. A description of this observable can be found in Section 3.3.3.

5.3 Muon Event Clusters

Several types of physics events inside the $16\,\mu s$ muon gate are accessible to the implemented clustering algorithm: muons, muon-decays, neutron capture γ's, and accidental coincidences. Figure 5.5 shows the time distribution of the detected clusters in the gate, and serves as the main reference for the description of the different particle types.

5.3.1 Muons and Muon Decays

The large structure at $0.4\,\mu s$ after gate start consists of muons, being the first physics events in every muon gate. In addition, it constitutes the largest event population in the gate as every muon trigger is caused by a muon crossing both *Inner* and *Outer Detector* (OD).

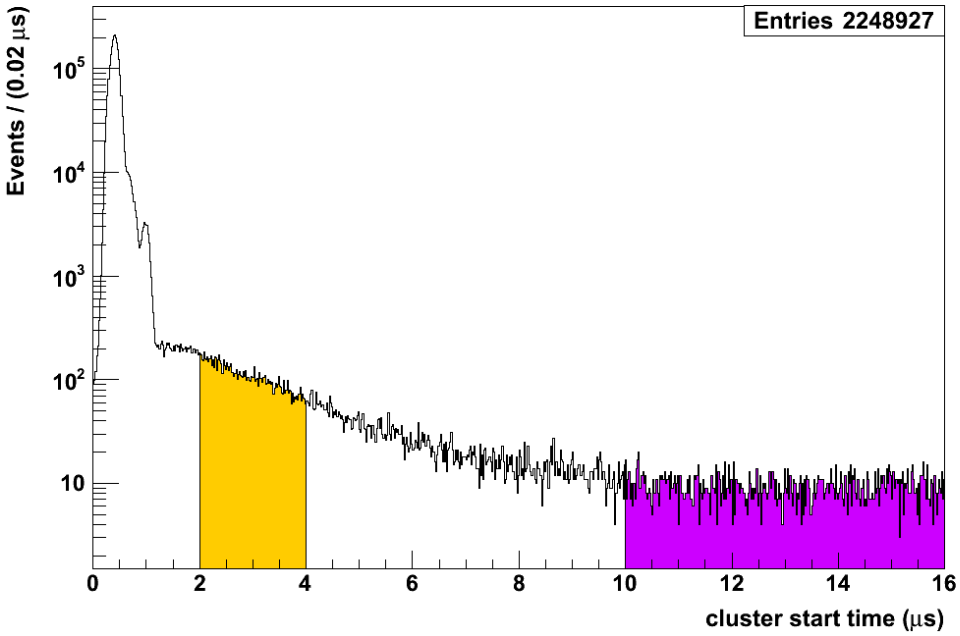

Figure 5.5: Time distribution of hit clusters detected inside of muon triggers. The dominant peak structure at $0.4\,\mu s$ after gate start is populated by muons crossing the ID and triggering the data acquisition. The decay/capture of stopped muons is visible as an exponential decline. Due to the long mean capture time of the muon-induced neutrons ($\tau \simeq 260\,\mu s$), the corresponding capture γ's feature an almost flat distribution over the $16\,\mu s$ gate; only a small fraction of accidental coincidences contributes to the flat component (see text). Data samples rich in muon decays (yellow shaded area; $t \in [2,4]\,\mu s$) and neutron capture γ's (violet shaded area; $t \in [10,16]\,\mu s$) can be extracted via the time profile.

Muon Lifetime Theory

With a mean energy of $280\,GeV$ at the LNGS underground site [61], only a small fraction of the cosmic muons ($\mu^{\pm}$) crossing Borexino is expected to stop inside the ID ($\simeq$1%). Yielding a Q-value of $105.2\,MeV$, the stopped muons decay with a lifetime of $\tau_{\mathrm{d}} = 2.197\,\mu s$ [67] via the process

$$\mu^+ \rightarrow e^+ + \overline{\nu_\mu} + \nu_e \tag{5.4}$$
$$\mu^- \rightarrow e^- + \nu_\mu + \overline{\nu_e} \tag{5.5}$$

Before decaying, stopped muons of negative charge are caught in the Coloumb potential of Hydrogen or Carbon, intrinsic to the scintillator liquid *pseudocumene*

(PC, $C_6H_3(CH_3)_3$). A muon in an atomic orbital of Hydrogen is quickly transferred to Carbon, which provides a higher proton number and therefore a greater binding energy [68]. The muon eventually populates the first atomic level in Carbon, where its wavefunction features a large overlapp with the nucleus, thus allowing for a nuclear capture of the muon. The most important capture reactions are:

$$\mu^- + {}^{12}\mathrm{C} \xrightarrow{\simeq 80\,\%} {}^{12}\mathrm{B} + \nu_\mu \tag{5.6}$$

$$\xrightarrow{\simeq 10\,\%} {}^{12}\mathrm{B}^* + \nu_\mu\,, \quad {}^{12}\mathrm{B}^* \rightarrow {}^{12}\mathrm{B} + \gamma \tag{5.7}$$

$$\xrightarrow{\simeq 10\,\%} {}^{12-\kappa\cdot n}\mathrm{B} + \kappa \cdot n + \nu_\mu \tag{5.8}$$

The variable κ denotes the number of neutrons emitted in the muon capture process. The estimates for the reaction probabilities have been taken from [69, 70, 71]. The additional capture channels reduce the total lifetime τ_t of a stopped μ^- in the scintillator according to:

$$\frac{1}{\tau_\mathrm{t}} = \frac{1}{\tau_\mathrm{d}} + \frac{1}{\tau_\mathrm{c}} \tag{5.9}$$

Here, τ_d and τ_c denote the mean times for muon decay and muon capture, respectively. For Carbon, the following measured values are given in literature [68, 72]:

$$\tau_\mathrm{t}({}^{12}\mathrm{C}) = (2028 \pm 2)\,ns\,, \quad \tau_\mathrm{c}({}^{12}\mathrm{C}) = (26.4 \pm 0.4)\,\mu s \tag{5.10}$$

As Carbon is a light nucleus, the probability for a muon capture is low and thus the total mean lifetime is dominated by the muon decay time $\tau_\mathrm{d} = 2.197\,\mu s$ [67].

As μ^+ and μ^- feature different lifetimes in the scintillator liquid, the expected muon reaction time profile follows:

$$\begin{aligned} M(t) &= \epsilon^+ \cdot \frac{N_{\mu^+}}{\tau^+} e^{-\frac{t}{\tau^+}} + \epsilon^- \cdot \frac{N_{\mu^-}}{\tau^-} e^{-\frac{t}{\tau^-}} \\ \text{with } \tau^+ &= \tau_\mathrm{d}\,, \quad \tau^- = \tau_t \end{aligned} \tag{5.11}$$

Here, $N_{\mu^\pm}$ stand for the number of positive (negative) stopped muons, and $\tau^\pm$ for the respective lifetimes. The parameters $\epsilon^\pm$ give the fraction of visible prompt $\mu^\pm$ reactions. With a Q-value of $105.2\,MeV$, muon decays are easily detected in the active volume of Borexino. Even in the buffer liquid, the majority of muon decays produce a detectable signal, despite the solved DMP light quencher and the limited angular acceptance of the ID PMTs equipped with light concentrators ($\simeq$83% of all ID PMTs). The two effects reduce the visible signals of buffer events by factors of about 20 and 5, respectively. Of the muon capture reactions, only channels (5.7) and (5.8) produce a prompt scintillation signal via γ-emission and/or neutron-proton scattering. With corresponding energy depositions of a few MeV in the

detector liquids, an efficient detection of these reactions is only possible inside the IV.
The muon charge ratio N_{μ^+}/N_{μ^-} has been measured for single- and multi-muon-events by the OPERA collaboration [73] to:

$$\begin{aligned} R_\mu(n_\mu = 1) &= 1.377 \pm 0.014_{(\text{stat})}\, {}^{+0.017}_{-0.015(\text{syst})} \\ R_\mu(n_\mu > 1) &= 1.23 \pm 0.06 \end{aligned} \tag{5.12}$$

As single-muon events account in OPERA for about 97% of all muon events [73], the average muon charge ratio is estimated to $\langle R_\mu \rangle = 1.37 \pm 0.03$ in this thesis. According to this, a fraction of $\omega^- = 1 - \omega^+ \simeq 42\%$ of all muons are expected to be of negative charge. According to this, the number of positive (negative) stopped muons can be expressed as:

$$N_{\mu^\pm} = N_\mu \cdot \omega^\pm \tag{5.13}$$

Here, the total number of stopped muons is given by N_μ. Based on this, Equ. (5.11) can be rewritten to

$$\begin{aligned} M(t) &= N_\mu \cdot \left(\frac{\epsilon^+ \cdot \omega^+}{\tau^+} e^{-\frac{t}{\tau^+}} + \frac{\epsilon^- \cdot \omega^-}{\tau^-} e^{-\frac{t}{\tau^-}} \right) \\ &\overset{\tau^+ \simeq \tau^-}{\simeq} \frac{N_\mu \cdot \eta}{\tau_{\text{eff}}} \cdot e^{-\frac{t}{\tau_{\text{eff}}}} \qquad (5.14) \\ \text{with } \tau_{\text{eff}} &= \frac{\epsilon^+ \cdot \omega^+ \cdot \tau^+ + \epsilon^- \cdot \omega^- \cdot \tau^-}{\eta} \qquad (5.15) \\ &\in [\tau^-, \tau^+] \\ \text{and } \eta &= \epsilon^+ \cdot \omega^+ + \epsilon^- \cdot \omega^- \qquad (5.16) \end{aligned}$$

Because the lifetimes τ^+ and τ^- are of similar value, a first order taylor-series expansion[1] was applied in Equ. (5.14) to derive a single exponential function with

[1] Given a function $f(x)$ of continuous derivative of first order, evaluating the function at the points x_1 and x_2, with $x_1 \simeq x_2$, the following approximation holds in first order taylor-series expansion (TE):

$$\alpha \cdot f(x_1) + \beta \cdot f(x_2) \simeq (\alpha + \beta) \cdot f\left(\frac{\alpha \cdot x_1 + \beta \cdot x_2}{\alpha + \beta} \right)$$

Proof. Applying the TE around point x_1 on both sides of the relation, we obtain:

$$\begin{aligned} \text{left side} &\simeq (\alpha + \beta) \cdot f(x_1) + \beta \cdot (x_2 - x_1) \cdot f'(x_1) \\ \text{right side} &\simeq (\alpha + \beta) \cdot f(x_1) + \beta \cdot (x_2 - x_1) \cdot f'(x_1) \end{aligned}$$

■

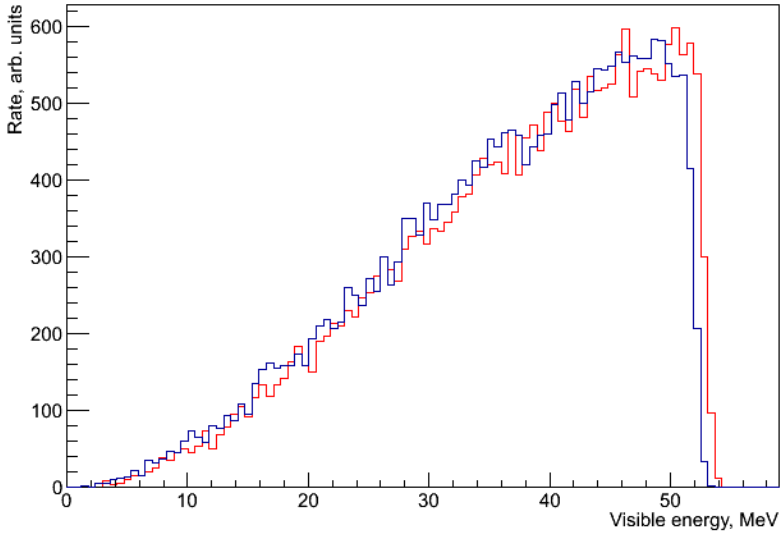

Figure 5.6: Simulated spectra of the energy deposition in μ^+ (red) and μ^- (blue) decays. The spectral shape of the μ^+ decay is shifted by an energy of $1.022\,MeV$ with respect to the μ^- decay as a result of the annihilation of the final state positron with an electron (see reactions (5.4) and (5.5)). [74]

an effective lifetime τ_{eff}. As the effective lifetime is described by a weighted mean of τ^- and τ^+, it is an element of the interval $[\tau^-, \tau^+] = [2.028, 2.197]\,\mu s$. The parameter η states the fraction of all muon reactions producing a prompt and visible signal in the detector.
Equation (5.15) can be easily evaluated with (5.16) for muons stopping inside the buffer liquid. The detection of the capture processes ((5.6) - (5.8)) is suppressed in the buffer liquid due to the light quencher and the limited angular acceptance of the ID PMTs, and thus prompt visible signals are dominated by $\mu^\pm$ decays. The μ^+ decay provides a slightly higher visible energy than μ^- decays, as in case of μ^+ the final state positron annihilates with an electron to two γ's of a total additional energy of $1.022\,MeV$ (see reaction (5.4)). Figure 5.6 presents the Monte Carlo results on the energy deposition in $\mu^\pm$ decays [74]. As can be seen, the effect of the additional energy release in the positron annihilation can be neglected in first order approximation. According to this, the following relation for the fraction of visible prompt muon signals in the buffer can be derived:

$$\epsilon^- \simeq \epsilon^+ \cdot \frac{\tau^-}{\tau_{\text{d}}} \tag{5.17}$$

The equation expresses the fact that $\mu^{\pm}$ decays feature almost the same detection efficiency due to the similar amount of deposited energy. The fraction ϵ^{-} is reduced relative to ϵ^{+} by the factor $\tau^{-}/\tau_{\mathrm{d}}$, constituting the percentage of μ^{-} decays to all μ^{-} reactions. With a visible energy threshold of the clustering algorithm of $80\,keV$, the detection efficiency of muon decays inside the buffer has been determined to $\epsilon^{+} \simeq 85\%$ via Monte Carlo simulations.
Evaluating Equ. (5.15) and (5.16) accordingly with the input of Equ. (5.17), the following effective mean lifetime of buffer muon signals is expected:

$$\tau_{\mathrm{eff}}^{\mathrm{buffer}} = (2.13 \pm 0.01)\,\mu s \tag{5.18}$$

This analytical result has been cross-checked and confirmed via a toy Monte Carlo simulation.

Muon Lifetime Measurement

As can be seen in Figure 5.5, muons entering the ID populate the peak structure at $0.4\,\mu s$ after gate start. The peak width of about $100\,ns$ corresponds to the jitter in the trigger formation. Hence, to derive the muon lifetime, physics events detected inside the muon gate are referenced in time to the prompt signal of the entering muon on an event-by-event basis. Figure 5.7 presents the time profile derived in this way. As can be seen, the first $1\,\mu s$ after the muon features excess populations of electronic origin, which occur in multiples of $140\,ns$ after the muon. These are caused by the huge light output of the entering muon, which illuminates all 2212 PMTs. The PMTs require $140\,ns$ before they are able to record new hits, resulting in a sharp gap in the hit time distribution (see description of the electronics in Sec. 3.2.2). In the wake of the muon signal, this mechanism can lead to multiple artificial peaks separated by $140\,ns$. This effect is visible in the hit time distribution of the sample muon trigger in Figure 5.2 on page 87. The clustering algorithm identifies these peak structures as physics events.

The decays and captures of stopped muons inside the Borexino ID are visible as an exponential decline about $1.5\,\mu s$ after the muon. To investigate the muon lifetime, Figure 5.7 is fitted with the sum of an exponential and a constant contribution in the range $t \in [2, 15.5]\,\mu s$ according to:

$$F(t) = \frac{A}{\tau} \cdot \exp\left(-\frac{t}{\tau}\right) + C \tag{5.19}$$

The variable t gives the cluster time relative to the time the muon has entered the ID. In consequence, the variable A denotes the number of reactions caused by stopped muons. The fit yields a decay time of $(1.66 \pm 0.03)\,\mu s$, which clearly

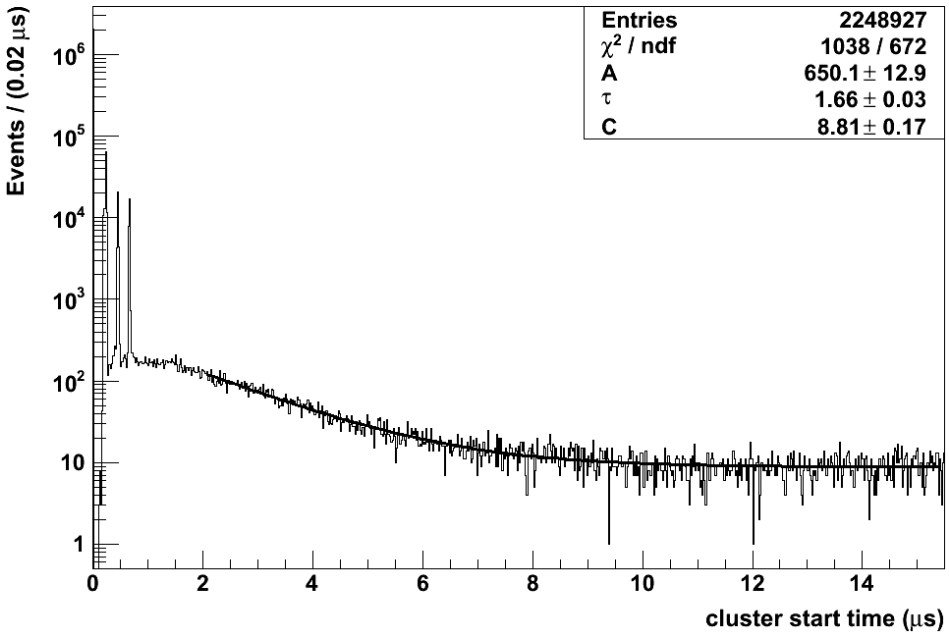

Figure 5.7: Time distribution of hit clusters detected inside of muon triggers. The clusters are referenced in time to the prompt signal of the entering muon on an event-by-event basis. The peak structures in the first $1\,\mu s$ after the muon are of electronic origin (see text). Fitting the time distribution in the range $[2, 15.5]\,\mu s$ with the sum of an exponential and constant function (Equ. (5.19)), an exponential decay time of $\tau = (1.66 \pm 0.03)\,\mu s$ is found.

deviates from the expected value range of $[2.028, 2.197]\,\mu s$ (see Equ. (5.15)). The discrepancy originates from the saturation of digital boards during the data acquisition of the muon gate (see Sec. 5.1). The number of unavailable digital boards increases over the time span of the acquisition gate, leading to a time-dependant detection efficiency of physics events. This results in a depopulation of muon decays in the later part of the gate, and thus to a steeper decline in the time profile. The fit interprets this as a faster decay of muons. This effect is mainly present for muons crossing the IV, as they produce huge amounts of scintillation light and subsequent PMT afterpulses.

However, as has been mentioned, with an energy deposition of up to $105.2\,MeV$, the majority of muon decays inside the buffer liquid still produces enough residual light for detection. By selecting muons traversing only the buffer region, so-called *buffer muons*, the effect of the electronics saturation can be avoided. As the muon

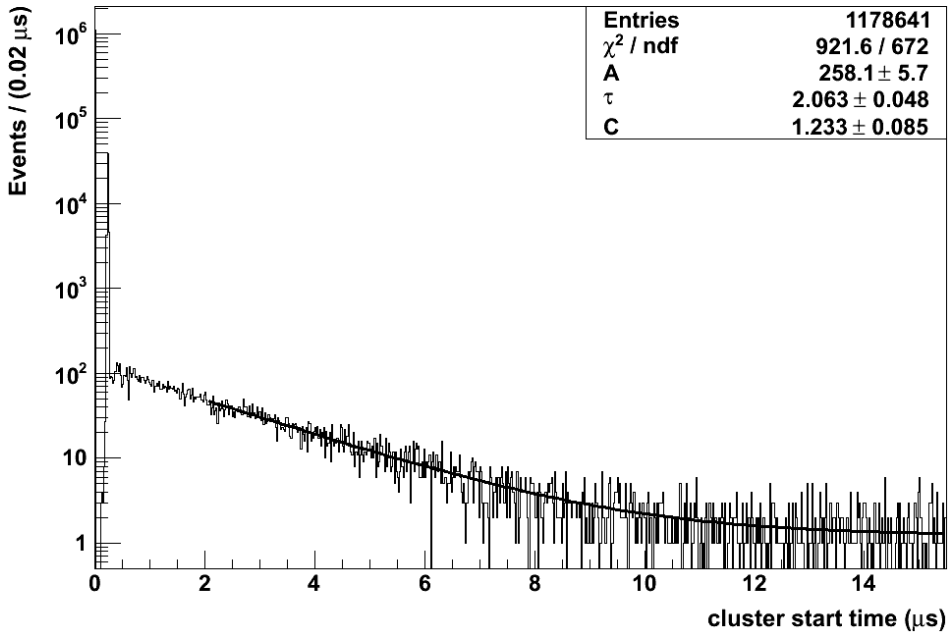

Figure 5.8: Time distribution of hit clusters detected inside of muon triggers. The clusters are referenced in time to the prompt signal of the entering muon on an event-by-event basis. Based on the visible energy deposition, only muons with an impact parameter larger than $\simeq 4.5\,m$ were selected. The peak structure at about $0.2\,\mu s$ after the muon is of electronic origin (see text). The time profile fit (Equ. (5.19)) in the range $[2, 15.5]\,\mu s$ yields a decay time of $\tau = (2.06 \pm 0.05)\,\mu s$, in agreement with the expected effective muon lifetime of $\tau_{\text{eff}}^{\text{buffer}} = (2.13 \pm 0.01)\,\mu s$.

track algorithms described in Chapter 4 are designed for muons fully crossing the *Stainless Steel Sphere* (SSS), they don't produce reliable results for stopping muons. Instead, the number of decoded hits in the gate (*laben.n_decoded_hits*) is used as a rough estimator for the muon impact parameter[2] (see Figure 4.17 on page 71). Considering only triggers containing less than 4000 decoded hits, buffer muons of impact parameters larger than $\simeq 4.5\,m$ are selected. The time distribution of clusters identified in these triggers is fitted in the time range $[2, 15.5]\,\mu s$, as presented in Figure 5.8. The fit returns a muon lifetime of $\tau = (2.06 \pm 0.05)\,\mu s$, in agreement with the expectation of $\tau_{\text{eff}}^{\text{buffer}} = (2.13 \pm 0.01)\,\mu s$.

[2]The muon impact parameter is defined as the distance between the muon track and the center of the Inner Detector.

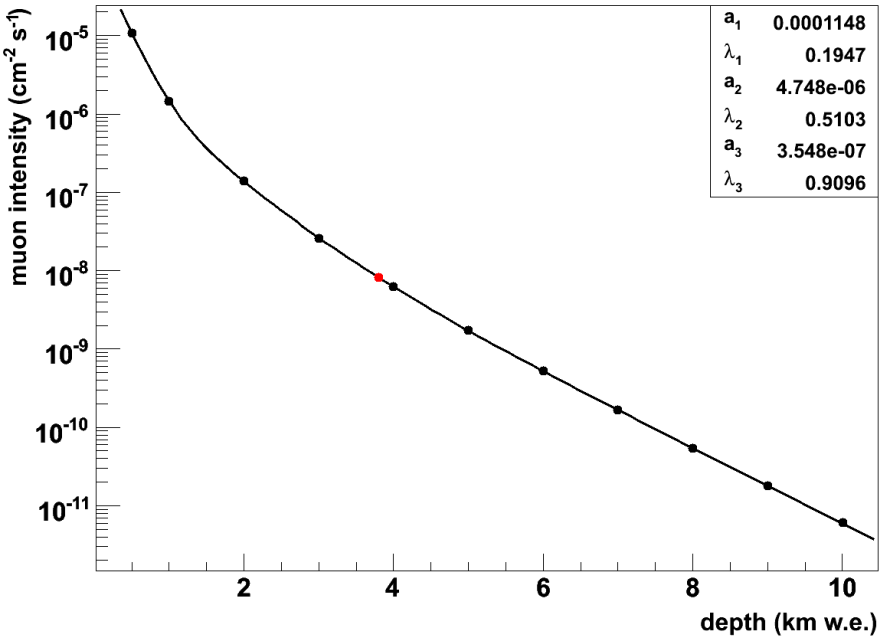

Figure 5.9: Vertical muon intensity as a function of the traversed rock coverage [75]. With an input muon spectrum at sea level derived from LVD data [76], the muons were propagated through *standard rock* (mean proton number $\langle Z \rangle = 11$, mean nucleon number $\langle A \rangle = 22$). The depths are given in kilometer of water equivalent [$km\,w.e.$]. The red dot marks the LNGS underground site at a depth of 3.8 $km\,w.e.$ and an interpolated vertical muon intensity of $\simeq 8 \cdot 10^{-9}\,cm^{-2}s^{-1}$.

Stopping Muon Fraction

The detected fraction of stopping muons can be compared with the expectation. The probability for a muon to stop within a given distance l_μ is given by:

$$\begin{aligned} \mathrm{P}_\mu^{\mathrm{stop}}(l_\mu) &= \frac{\rho_{\mathrm{PC}}}{\lambda} \int_0^{l_\mu} exp\left(-\rho_{\mathrm{PC}} \cdot \frac{x}{\lambda}\right) \mathrm{d}x \\ &\overset{l_\mu \ll \lambda}{\simeq} \rho_{\mathrm{PC}} \cdot \frac{l_\mu}{\lambda} \end{aligned} \tag{5.20}$$

Here, $\rho_{\mathrm{PC}} = (0.8802 \pm 0.0004)\,g/cm^3$ [21] denotes the density of pseudocumene, which is the solvent for both the active liquid scintillator inside the IV and the buffer liquid. The parameter λ constitutes the effective absorption length of cosmic muons after passing the LNGS rock coverage of 3800 $m.w.e.$[3], and is estimated via the publication by Kudryavtsev, Spooner, and McMillan [75]. Starting with the

[3]meter of water equivalent

surface muon spectra in energy and angular orientation, the group propagated muons through rock using the MUSIC simulation code [77]. Figure 5.9 presents the results on the vertical muon flux I_μ^{vert} as a function of the traversed rock coverage. The distribution can be approximated by the sum of three exponential functions:

$$I_\mu^{\text{vert}}(x) = \sum_{i=1}^{3} a_i e^{-\frac{x}{\lambda_i}} \tag{5.21}$$

The variable x states the depth in $km\,w.e.$. Evaluating the parameterization for the LNGS depth of $3.8\,km\,w.e.$, an absorption length of $\lambda \simeq 720\,m.w.e.$ is found. As the apsorption length is large relative to the Borexino ID dimensions ($R_{\text{ID}} = 6.82\,m$), the approximation in Equ. (5.20) is justified. With the linearisation of the equation, the average survival probability can be written as:

$$\langle \mathrm{P}_\mu^{\text{stop}} \rangle \simeq \rho_{\text{PC}} \cdot \frac{\langle l_\mu \rangle}{\lambda} \tag{5.22}$$

The parameter $\langle l_\mu \rangle$ constitutes the average muon path length in the experiment. As the muons are distributed homogenously over the ID (i.e. the muon flux Φ_μ is location-independent), $\langle l_\mu \rangle$ can be easily calculated in spherical coordinates (ϱ, θ, ϕ). With the radial-dependent muon path length $l_\mu(\varrho) = 2\sqrt{R_{\text{ID}}^2 - \varrho^2}$ we obtain:

$$\begin{aligned} \langle l_\mu \rangle(R_0, R_1) &= \frac{\int_{R_0}^{R_1} \Phi_\mu \, l_\mu(\varrho)\, \varrho \, \mathrm{d}\varrho}{\int_{R_0}^{R_1} \Phi_\mu \; \varrho \, \mathrm{d}\varrho} = \frac{\int_{R_0}^{R_1} \sqrt{R_{ID}^2 - \varrho^2}\, \varrho \, \mathrm{d}\varrho}{\int_{R_0}^{R_1} \varrho \, \mathrm{d}\varrho} \\ &= -\frac{4}{3} \frac{(R_{ID}^2 - \varrho^2)^{\frac{3}{2}}\Big|_{R_0}^{R_1}}{\varrho^2|_{R_0}^{R_1}} \end{aligned} \tag{5.23}$$

Evaluating the equation in the same radial regime as used in Figure 5.8 (i.e. $[4.5\,m, R_{\text{ID}}]$ with $R_{\text{ID}} = 6.82\,m$), the average muon path length is derived to $6.8\,m$. According to Equ. (5.22), the expected fraction of stopping buffer muons results in $\simeq$1%. Extracting the number of muon decays from the time profile fit in Figure 5.8, one obtains $(1.29 \pm 0.03) \cdot 10^4$ muon decays. As has been mentioned in this Section, about 85% of all muon decays in the buffer liquid generate a visible energy deposition above the clustering threshold of $80\,keV$. Evaluating Equ. (5.16) and (5.17) according to this, it is expected that the measured number of muon decays accounts for $\simeq$82% of all stopped muons. With a total of $1.26 \cdot 10^6$ buffer muon triggers in the data set, the corresponding fraction of stopping muons of $\simeq$1% is in agreement with the expectation.

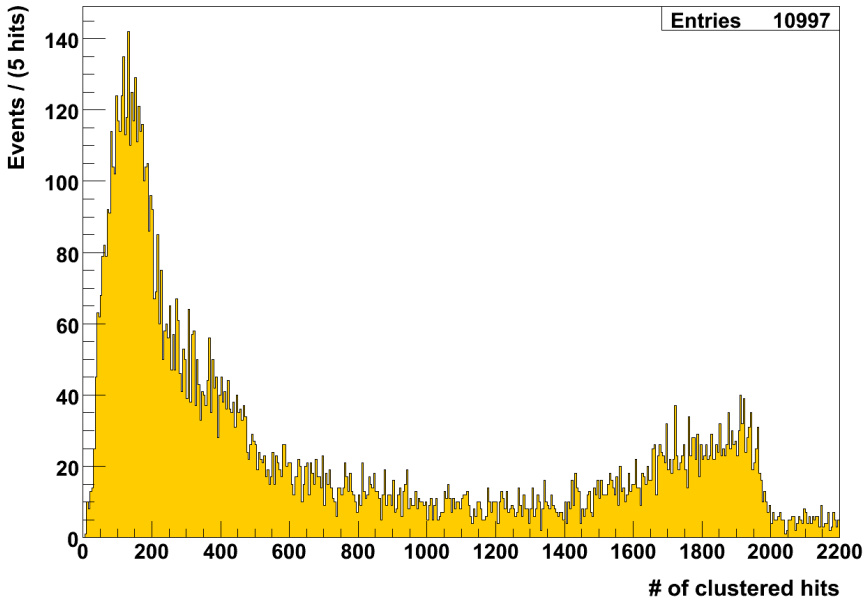

Figure 5.10: Visible energy ($N_{\text{hits}}^{\text{norm}}$) of muon decays selected in the time window $[2,4]\,\mu s$ after gate start (see Figure 5.5).

Stopping Muon Energy Response

A sample rich in μ-decays can be extracted by selecting clusters of start times in the regime [2,4] μs after gate start (yellow shaded area in Figure 5.5). The corresponding energy distribution of the data sample is presented in Figure 5.10. With a Q-value of 105.2 MeV the bulk of muon decays inside the IV are expected to illuminate all live PMTs, resulting in a peak structure around $N_{\text{hits}}^{\text{norm}} \simeq 2000$ hits. However, due to the described electronics saturation, the peak is less pronounced and leaks down to lower visible energies.
In case of muon decays inside the buffer, the visible energy signal is reduced by a factor of $\simeq$20 due to the quencher DMP. In adition, the effective light yield of these buffer events drops further due to the limited angular acceptance of most of the ID PMTS. As a result, muon captures inside the buffer populate the large peak structure at low visible energies ($N_{\text{hits}}^{\text{norm}} < 600$ hits).

5.3.2 Neutron Captures and accidental Coincidences

Neutron captures on Hydrogen and ^{12}C yield a total γ energy of 2.2 MeV and 4.9 MeV, respectively. As these energies are too low for an effective light emis-

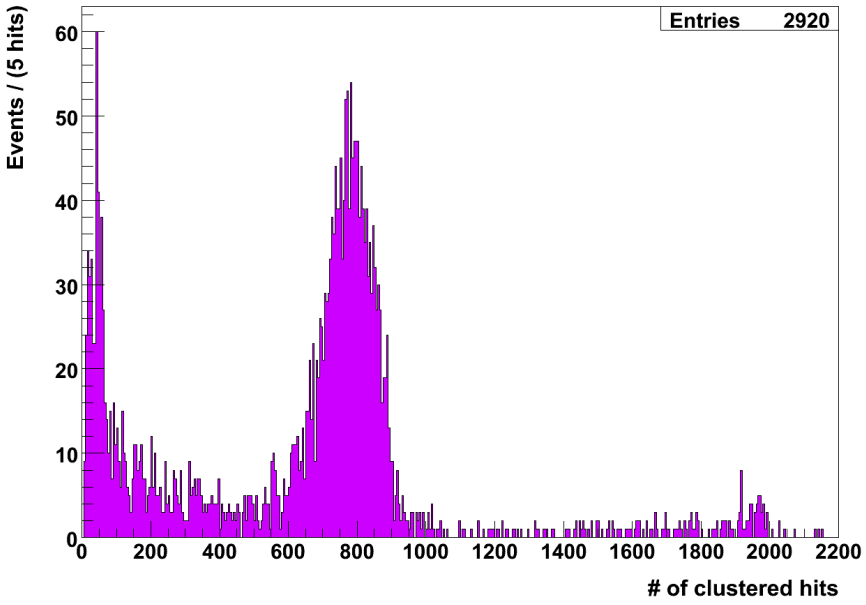

Figure 5.11: Visible energy ($N_{\text{hits}}^{\text{norm}}$) of neutron capture γ's selected in the time window $[8, 16]\,\mu s$ after gate start (see Figure 5.5). The peak structure at 770 hits originates from the $2.2\,MeV$ γ emitted in the neutron capture on Hydrogen. The lower-energetic events are dominated by capture γ's degenerated in signal by IV boundary effects and electronics saturation. About 5% of the sample consists of muon decays/captures and accidental ^{14}C decays ($Q = 156.5\,keV$).

sion in the buffer region, only γ's are detected, which deposit their energy mainly within the IV (nominal mass of $278\,t$). With a decay time of $\simeq 260\,\mu s$, these captures feature an almost flat distribution in the time profile of the $16\,\mu s$ muon gate. While in principle also accidental coincidences add to the flat component, their contribution is negligible. With a rate of $\simeq 7\,Hz$ above the detection threshold of $80\,keV$, the scintillator-intrinsic ^{14}C β-decay is by far the most dominant source of accidental coincidences. However, the probability to pick up a ^{14}C decay inside the $16\,\mu s$ muon gate is only $1.1 \cdot 10^{-4}$. With a total of $2.3 \cdot 10^6$ muon triggers in the data sample, ^{14}C coincidences account only for $\simeq 250$ counts. This compares to a total of $(7.0 \pm 0.1) \cdot 10^3$ counts derived from the flat component in the time profile fit of Figure 5.5. From this, a neutron capture rate of about $(15 \pm 2)\,d^{-1}$ is found in the data sample of 476 days for a nominal IV mass of 278 tons. The given uncertainty is a conservative estimate, including systematic effects (e.g. deviations of the IV mass from the nominal value during the data taking period). Referencing to $100\,t$ of target mass, this result translates to a rate of $(5 \pm 1)\,(d\,100\,t)^{-1}$. A precision

measurement of the neutron production rate and yield in Borexino based on the $1.6\,ms$ neutron gate is presented in Section 5.8. The result of the corresponding analysis yields a total neutron rate of $(90.2 \pm 2.0_{\text{stat}} \pm 2.4_{\text{syst}})\,(d\,100\,t)^{-1}$. As can be seen, only a fraction of $(6 \pm 1)\%$ of all neutron captures are located within the $16\,\mu s$ muon gate. This is well in agreement with the expected fraction of 6%, according to a mean neutron capture time of $\simeq 260\,\mu s$.

A neutron-enhanced data sample can be prepared by selecting clusters in the range of $[10{,}16]\,\mu s$ after gate start, as indicated by the violet shaded area in Figure 5.5. The affiliated energy spectrum is shown in Figure 5.11. A clear peak at 770 hits is visible in the energy distribution, corresponding to the $2.2\,MeV$ γ emitted in the neutron capture on Hydrogen. The lower energetic tail of the distribution consists of neutron capture γ's, degenerated in signal by boundary effects and electronics saturation, as has been described at the beginning of Section 5.1. In addition, a small contribution of ^{14}C ($\simeq$90 counts) and muon decays/captures ($\simeq$50 counts) are present. For reference, the energy spectrum of neutron captures identified in the $1.6\,ms$ neutron gate can be found in Figure 5.12 on page 105.

5.4 Neutron Event Clusters

Subsequent to the $16\,\mu s$ muon gate, the neutron gate of $1.6\,ms$ length is well suited for the detection of muon-induced neutrons, encompassing about 94% of all capture γ's ($\tau \simeq 260\,\mu s$). Contrariwise, the neutron gate is also susceptible to accciden-tal coincidences due to the long gate length. These consist of misclustered noise peaks, ^{14}C decays ($Q = 156.5\,keV$) intrinsic to the organic liquid scintillator, and a low-energetic background component ($E_{\text{vis}} \leq 40\,keV \simeq 20$ PMT hits) presumed to originate from decays in the buffer liquid. The spatial origin of the latter is unknown, as the position reconstruction in Borexino is not able to properly recon-struct the event vertex at these low visible energies. The accidental coincidences of cosmic muons with the neutron gate contribute as a negligible background. A rate determination of the uncorrelated background components can be found in Section 5.6.
The data collected in the neutron trigger gate is the foundation of the neutron physics analyses performed in this thesis. As the detection and reconstruction of the capture γ's is complicated by time-dependent muon-induced noise hits, as well as the saturation of digital boards, a careful and intensive study of the detection efficiency, as well as systematic effects is indispensable. Quantifying these depen-dencies was key in retrieving a manifold of neutron physics observables, culminat-ing in the precision measurement of the neutron production yield as presented in Section 5.8.

5.4.1 Statistical Neutron Fluctuations

As cosmogenic neutrons are produced by muons, the statistical fluctuations of the detected neutron and corresponding muon numbers are strongly correlated. Assuming a number of muons $N_\mu(m)$, each producing a neutron multiplicity of m, the total neutron number of this multiplicity is given by the expression

$$N_n(m) = N_\mu(m) \cdot m \tag{5.24}$$

An uncertainty in the muon number $\Delta N_\mu(m) = \sqrt{N_\mu(m)}$ translates to a neutron number uncertainty of

$$\Delta N_n(m) = \Delta N_\mu(m) \cdot m = \sqrt{N_\mu(m)} \cdot m \tag{5.25}$$

With $m \in \mathbb{N}$, this uncertainty is larger than the one associated with the neutron statistics only, i.e. $\sqrt{N_n(m)} = \sqrt{N_\mu(m) \cdot m}$.
Generalizing this concept to a data set consisting of muons which produce neutrons in various mulitplicities, the total neutron number and the associated statistical uncertainty are given by:

$$N_{n,\mathrm{tot}} = \sum_m N_n(m) = \sum_m N_\mu(m) \cdot m \tag{5.26}$$

$$\Delta N_{n,\mathrm{tot}} = \sqrt{\sum_m \left(\Delta N_n(m)\right)^2} \overset{(5.25)}{=} \sqrt{\sum_m N_\mu(m) \cdot m^2} \tag{5.27}$$

In this thesis, calculations on the statistical uncertainty of detected neutron numbers take these relations into account.

5.4.2 Energy Response

As has been described in Section 5.1, the saturation of the *Laben* digital boards by a muon and its afterpulses reduces the effective detection surface of the Borexino ID, leading to a degeneration in the visible energy of a following physics event. The dependance of the visible energy (given by $N_{\mathrm{hits}}^{\mathrm{norm}}$) on the number of saturated boards N_{eb} is depicted in the top plot of Figure 5.12. The main band crossing the ordinate axis at $\simeq$730 hits is populated by the $2.2\,MeV$ γ rays emitted in the neutron capture on Hydrogen. The clear degeneration of the γ signal due to the saturation of the detector is visible. The lower plot of Figure 5.12 presents the data taken with a fully functional detector (i.e. $N_{\mathrm{eb}} = 0$). The highest energetic (orange) population at $\simeq$2000 hits corresponds to cosmic muons in accidental coincidence with the neutron gate. The green species at $\simeq$1100 hits consists of neutron captures on ^{12}C ($E_\gamma = 4.9\,MeV$). Containing only 2% of all captures, it is small

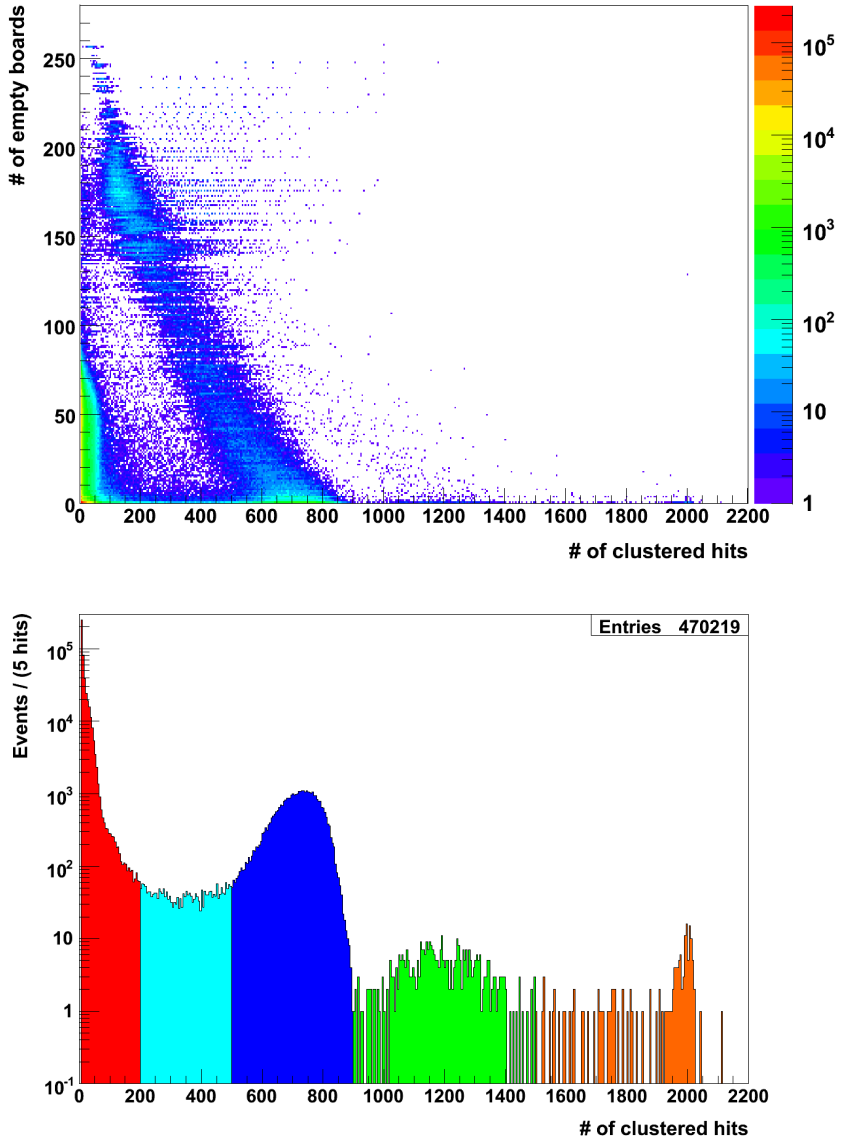

Figure 5.12: Visible energy of hit clusters ($N_{\text{hits}}^{\text{norm}}$) detected inside of neutron triggers. *Top:* Energy as a function of the number of saturated boards (N_{eb}). *Bottom:* Energy spectrum without the effect of electronics saturation ($N_{\text{eb}} = 0$). The color coded species are dominated by accidental muons (orange), neutron captures inside the IV on ^{12}C (green) and Hydrogen (blue), capture γ's partialy contained in the IV (teal), and a combination of neutron captures inside the buffer, accidental decays, and noise events (red).

compared to the main (blue) contribution at ≃730 hits, populated by the 2.2 MeV γ rays emitted in the neutron capture on Hydrogen. The sparse lower-energetic events (teal) are dominated by 2.2 MeV γ's only partialy contained inside the IV. As the amount of visible energy generated by these γ's depends on the fraction of energy deposited inside the IV volume, the corresponding distribution covers the whole low-energy regime. In the (red) energy range, misclustered noise events, as well as accidental coincidences (^{14}C decays and buffer events) with the 1.6 ms neutron gate dominate. Furthermore, this energy range is populated by neutron captures in the buffer region. As a result of the light quencher and the limited field of view of the PMTs, neutron captures on Hydrogen in the buffer liquid are expected to produce about 10 PMT hits. A Monte Carlo simulation of the detector response to neutron captures on Hydrogen and Carbon can be found in Section 5.7.

5.4.3 Neutron Detection Efficiency

The detection efficiency of cosmogenic neutrons decreases noticably if more than ≃170 boards are saturated by the parent muon (see Figure 5.12). Using the auxiliary Princeton analog data acquisition system, this effect was evaluated as described in the following.

Princeton Analog System

The *Princeton Analog System* (PAS) is a parallel single-channel data acquisiton system, based on the culmulative analog output of all 2212 ID PMTs (see Section 3.4). While this auxiliary system shares the central electronic components with the main DAQ (i.e. PMTs and front-end electronics), its data acqusition runs independently. Furthermore, it by-passes the *Laben* digital boards, and therefore is not affected by the memory saturation caused by extreme muon events. In consequence, it is perfectly suited to measure the neutron detection inefficiency of the main DAQ introduced by saturation effects.
Like the main DAQ neutron gate, the PAS trigger window features a length of 1.6 ms. Figure 5.13 presents the first 200 μs of a sample event as seen by the PAS and the main DAQ. The large structure in the PAS data within the first 30 μs after the muon is of electronic origin [78]. The neutron capture γ's are clearly visible as (negative) voltage peaks on top of the analog baseline. Based on the analog sum output, a peak search algorithm identifies the voltage peaks and derives physics observables. The pulse shape of muon events in accidental coincidence with the acquisition gate differs from neutron capture γ's, allowing for an efficient veto. In the used PAS data sample, these accidental muons have been removed. The pulse height of identified peaks is used as energy estimator, the corresponding

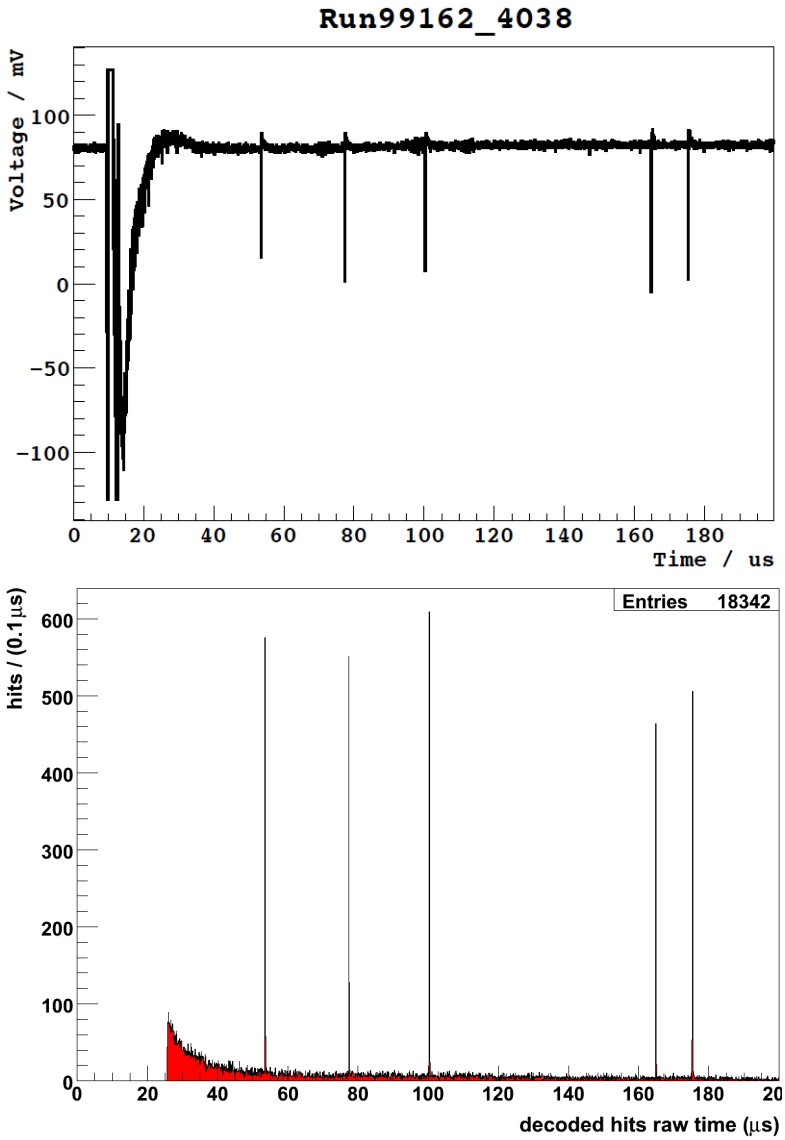

Figure 5.13: Signals recorded by the PAS and main DAQ in the first 200 μs after a sample muon crossing the ID. *Top:* Culmulative analog voltage signal of all ID PMTs as recorded by the PAS [78]. The large structure in the first 30 μs after the muon is of electronic origin. The system identifies five neutron capture peaks in the shown time window. *Bottom:* Hit time distribution of the corresponding neutron trigger of the main DAQ. The distribution has been shifted by 28 μs relative to the gate start to allow for a better comparison. The neutron capture peaks are visible as clusters of time-correlated hits.

distribution being shown in Figure 5.14. The populations at 66 mV and 150 mV

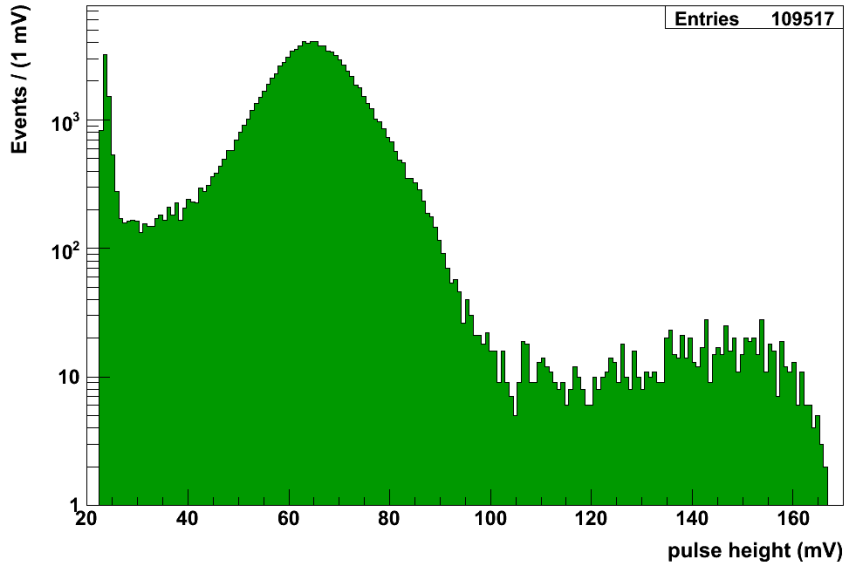

Figure 5.14: Pulse height of voltage peaks identified by the PAS. The peaks centered at 66 mV and 150 mV correspond to the 2.2 MeV and 4.9 MeV γ emissions by the neutron captures on Hydrogen and ^{12}C, respectively. Accidental muon events have been removed via pulse shape discrimation. The increase of events at pulse heights below 30 mV is caused by the misidentification of electronics noise [78].

originate from the 2.2 MeV and 4.9 MeV γ emissions by the neutron captures on Hydrogen and ^{12}C, respectively. The structure at 25 mV results from electronics noise on the analog sum output [78]. Applying a pulse height cut of 38 mV, this noise is efficiently removed, leaving a pure neutron capture sample [78]. Assuming a linear relation between the pulse height and the energy deposition, this cut corresponds to an energy threshold of 1.3 MeV. If not stated otherwise, neutrons detected by the PAS are subjected to this energy cut for further analyses.
To cross-calibrate the two systems, the neutron captures detected by both systems have to be identified and the respective observables compared. The used PAS neutron data was collected in the time period of February 2008 till November 2009.

Neutron Matching Procedure

Though a common set of neutron capture peaks can be identfied via time-matching the two systems, this approach is complicated by the poor time resolution of the PAS. For unidentified reasons, the jitter in the determination of the trigger GPS

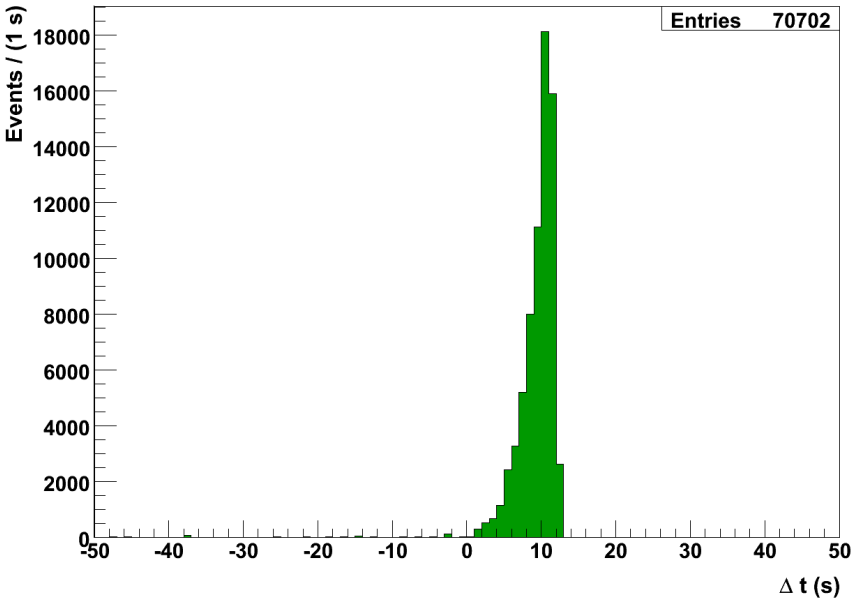

Figure 5.15: Difference in GPS-times Δt of muon-induced triggers recorded by the main and Princeton DAQ. The poor global time resolution of the PAS causes a spread in the Δt distribution of $\sigma_{\Delta t} \simeq 2\,s$. However, the distinctive timing patterns of neutron capture γ's inside the triggers allow for a highly efficient matching of neutrons detected by both systems.

time is about 2 seconds. Figure 5.15 presents the difference in GPS time between the two systems. However, as demonstrated in Figure 5.13, the recorded neutron triggers show distinctive finger prints in the timing signature of neutron captures relative to the parent muon. Based on this principle, a highly efficient matching algorithm was written within this thesis.
In the first step, the algorithm identifies time segments with both systems running; based on the used PAS data, a common data set of 425 live days was found. In these common time periods, the algorithm searches within $\pm 100\,\mathrm{s}$ to every PAS trigger for main DAQ neutron triggers, and matches them according to the neutron capture time signatures. Figure 5.16 presents the matched γ peaks with respect to the main DAQ in visible energy ($N_{\mathrm{hits}}^{\mathrm{norm}}$) versus the number of saturated boards N_{eb}. As the matched events are subject to the $1.3\,MeV$ PAS threshold and a pulse shape cut, low-energetic physics events and accidental muons are cut compared to Figure 5.12.

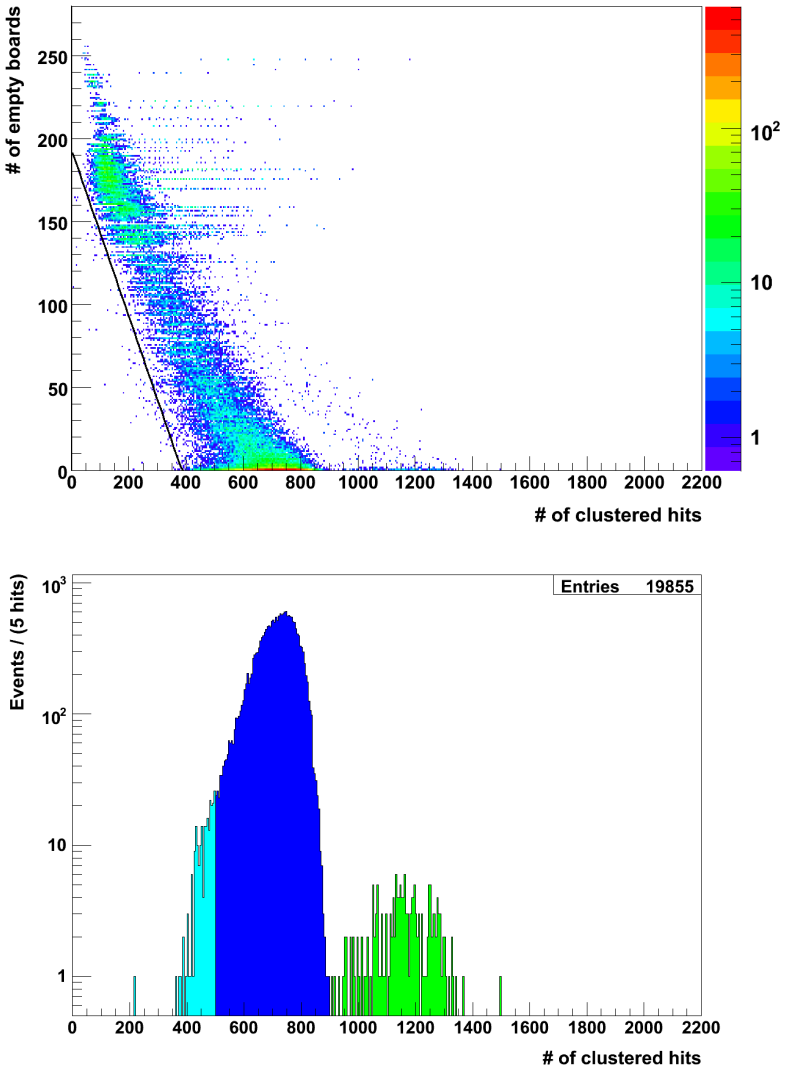

Figure 5.16: Visible energy of neutron capture candidates ($N_{\text{hits}}^{\text{norm}}$) detected by both the main and PAS DAQ. An energy cut of 1.3 MeV is present, removing low-energetic physics events compared to Figure 5.12. *Top:* Energy as a function of the number of saturated boards (N_{eb}). Based on the shown data, a 2-dimensional response function of the 1.3 MeV threshold in main DAQ observables can be derived and is shown as a black line (see Sec. 5.4.4, Equ. (5.29)). *Bottom:* Energy spectrum without the effect of electronics saturation ($N_{\text{eb}} = 0$). The color coded species are dominated by neutron captures inside the IV on ^{12}C (green) and Hydrogen (blue), as well as partialy contained captures on Hydrogen (teal). The PAS energy threshold results in a clear cut-off at $\simeq$400 hits.

Results

To determine the neutron detection efficiency of the main DAQ, a neutron sample of high quality is required. This is achieved by the following selection cuts on the PAS neutron sample:

- Energy cut: As has been described above, the application of a pulse height cut ($> 38\,mV$) introduces a threshold of $1.3\,MeV$ on the visible energy, effectively cutting misidentified noise pulses.
- Time cut: As the analog sum baseline requires about $30\,\mu s$ after a muon to stablize, the analysis is restricted to the time interval [$30\,\mu s$, $1.6\,ms$].

In the common data taking period of both systems, the PAS identified a total of 71003 neutron captures satisfying these cuts. As the efficiency evaluation is based on the number of detected neutrons, the statistical considerations of Section 5.4.1 apply.

While the majority of neutrons in Borexino are produced by cosmic muons ($\langle E_\mu \rangle = 280\,GeV$), the detector was also target for muons created by the CNGS ν_μ beam of $17\,GeV$ mean energy. Due to the different energy scales, neutron production yields and the response of the detector electronics are expected to differ for the two event classes. For the main DAQ, CNGS-induced events are tagged by a time-of-flight coincidence check with the CERN ν_μ beam spills. However, this is not possible for the PAS, which suffers from the bad timing resolution. To retrieve the detection efficiency for cosmogenic neutrons, a subset of 273 days without CNGS ν_μ activity is selected from the common data set. After application of the cuts described above, a total of 43620 neutron captures were identified by the PAS in this subset. Of these neutrons, the main DAQ identified 40115. Taking into acount the statistical fluctuations in the neutron number according to Equ. (5.27) (Sec. 5.4.1), the neutron detection efficiency for cosmic muons is evaluated to

$$\epsilon_{\mathrm{det}}^{\mathrm{cosm}} = (92.0 \pm 1.7)\% \tag{5.28}$$

The complimentary data set containing time periods of an active CNGS beam encompasses cosmogenic and CNGS-induced neutrons. In this data set of 152 live days, 27383 neutron captures identified by the PAS survive the selection cuts. Of these, the main DAQ identifies 25253, translating to a total neutron detection efficiency of $(92.2 \pm 2.2)\%$. Due to the lack of a precise time tagging of the PAS data, the detection efficiency of the CNGS-induced neutrons $\epsilon_{\mathrm{det}}^{\mathrm{CNGS}}$ can be evaluated by statistical calculus only. The efficiency is found to be $\epsilon_{\mathrm{det}}^{\mathrm{CNGS}} = 94.2^{+5.8}_{-21.8}\%$. Due to the lower mean energy, muons originating from the CNGS beam are expected to deposit less energy in hadronic and electromagnetic showers inside the detector

than cosmic muons. In consequence, the detection efficiency for CNGS-induced neutrons is assumed to be higher than the one for cosmogenic neutrons. However, the large error margin of the former value does not allow for a conclusive confirmation of this hypothesis.
The found detection efficiencies are valid within the limits of the data selection desribed above; i.e. for neutron captures above a visible energy of $1.3\,MeV$ and later than $30\,\mu s$ after the parent muon. The relatively high inefficiency in neutron detection is connected to the production mechanism of the neutrons. Muons generating extended hadronic and electromagnetic showers produce high numbers of neutrons, ranging in the hundreds. However, at the same time these extreme events are also likely to saturate a high fraction of electronic boards. As will be desribed in detail in Section 5.9, about 50% of all neutrons are produced by muons events of neutron multiplicities larger than 12. At the same time, these events make up only $(5.0 \pm 0.1)\%$ of all neutron producing muons.
The results of the cross-calibration and detection efficiency determination via the PAS are valid for data taken before the 2^{nd} of February 2010. To increase the detection efficiency of cosmogenic neutrons, the memory reservation of the digital boards was altered at that date in cooperation with G. Korga. In addition, the Borexino collaboration performed a modification of the channel gain of the ID PMTs in the same operation. Both effects result in a slight change of the detector reponse in terms of visible energy and electronics saturation. As no data of the PAS is currently available for the time period after this modification, the change in the neutron detection efficiency can not be determined on an event-by-event basis. However, an increase in the number of detected neutrons is observed, indicating an increase in the detection efficiency by a factor of 1.05 ± 0.03. This corresponds to a neutron detection efficiency for cosmic muons of about $(96 \pm 3)\%$ after the modification.

5.4.4 Energy Treshold Definition

As the found detection efficiencies are derived from a $1.3\,MeV$ threshold, the determination of the corresponding energy parametrization in terms of main DAQ observables is mandatory. While this energy threshold is defined in the PAS by a 1-dimensional pulse height cut ($> 38\,mV$), the situation is more complicated for the main DAQ due to the electronics saturation. The top plot in Figure 5.16 presents the response of the main DAQ in energy ($N_{\text{hits}}^{\text{norm}}$) and number of saturated boards (N_{eb}) for neutron capture γ's, identified by the PAS to be of a visible energy above $1.3\,MeV$. The population distribution in this 2-dimensional plot allows for an energy threshold parametrization in terms of main DAQ observables. Requiring a fully functional detector ($N_{\text{eb}} = 0$), the corresponding energy distribution is presented in the lower plot of Figure 5.16, featuring a clear cut at $\simeq$400 hits due

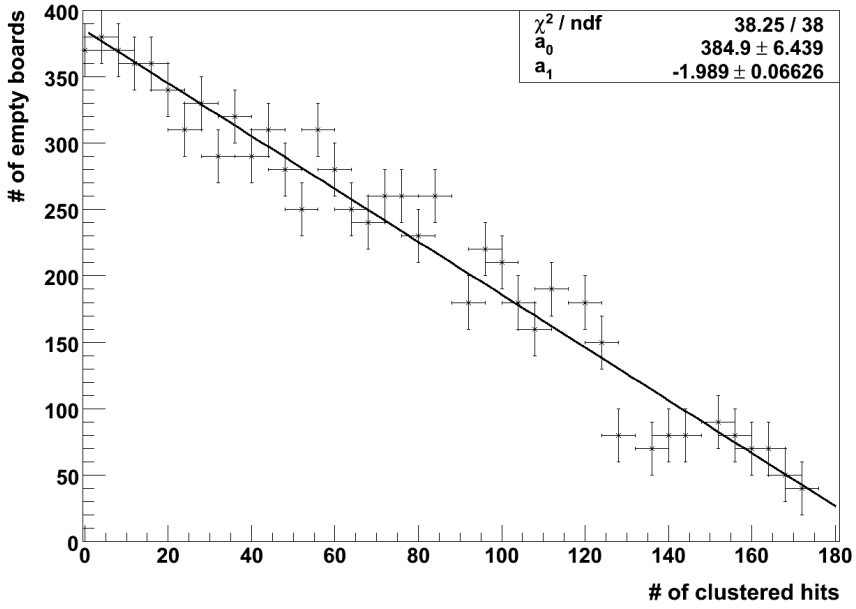

Figure 5.17: Main DAQ response to the $1.3\,MeV$ threshold applied to neutron capture candidates detected by both main and PAS DAQ. The cut-off in the $N_{\text{hits}}^{\text{norm}}$ distribution is presented as a function of the number of saturated boards N_{eb}. The data is fitted with a straight line, resulting in Equ. (5.29).

to the $1.3\,MeV$ PAS cut-off. An algorithm was written to identify this cut-off in the $N_{\text{hits}}^{\text{norm}}$ distribution, repeating the procedure for every discrete number of empty boards. The result is a response function of the main DAQ neutron gate to the $1.3\,MeV$ threshold, shown in Figure 5.17. The data points are well fitted with a straight line, yielding the parameterization:

$$N_{\text{hits}}^{\text{norm}} = a_1 \cdot N_{\text{eb}} + a_0 \quad \text{with } a_1 = 384.9 \pm 6.4, a_0 = -1.989 \pm 0.066 \qquad (5.29)$$

The definition of a common reference energy threshold in both systems is a key requirement for the application of the found neutron detection efficiencies. Likewise, the energy threshold definition is only valid for data taken before the 2$^{\text{nd}}$ of February 2010, as the a hardware modification in channel gain and digital memory reservation of the ID has been performed at that date.

5.4.5 Position Reconstruction

After a physics event has been identified by the clustering module, the associated PMT hits in the first $500\,ns$ of the cluster are used for reconstructing the event position. The algorithm scans the ID volume, comparing the respective

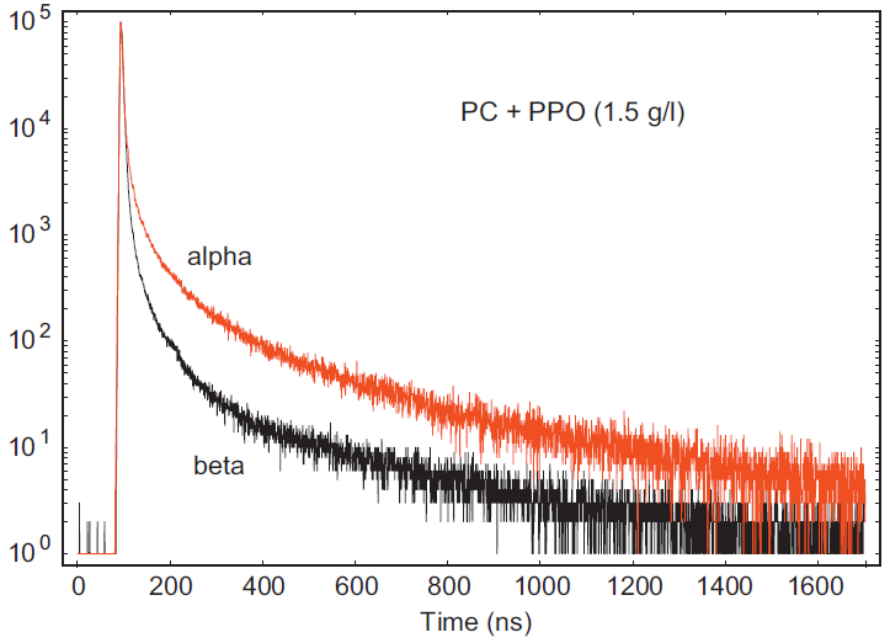

Figure 5.18: Time profile of the scintillation light emission by the Borexino scintillator mixture (PC and 1.5 g/l PPO) for α and β particles [31]. The position reconstruction is most sensitive to the prompt scintillation light. The different scintillation pulse shapes at late times for α and β particles are utilized for α/β discrimination.

PMT activation profile with a probability density function (PDF) $\mathcal{L}(x, y, z, t)$; the coordinates refer to the position and time the physics event occured. The PDF includes the scintillation emission profile for the Borexino scintillator mixture (see Figure 5.18) and the photon time-of-flight to each individual PMT. By maximizing $\mathcal{L}(x, y, z, t)$, the position vertex and event time are reconstructed.

The Borexino position reconstruction algorithms have been developed assuming negligible levels of background hits in the detected clusters. While this is true for non-cosmogenic events, the clusters identified in the wake of muons can be highly contaminated with noise hits. Furthermore, the loss of digital boards by memory saturation decreases the detector uniformity, aggravating the effect of noise hits on the position reconstruction.

- **Noise Hits**:
  Especially PMTs close to the muon track are subject to higher illumination and thus will record higher rates of noise. Therefore, these noise hits will shift the reconstructed position outwards.

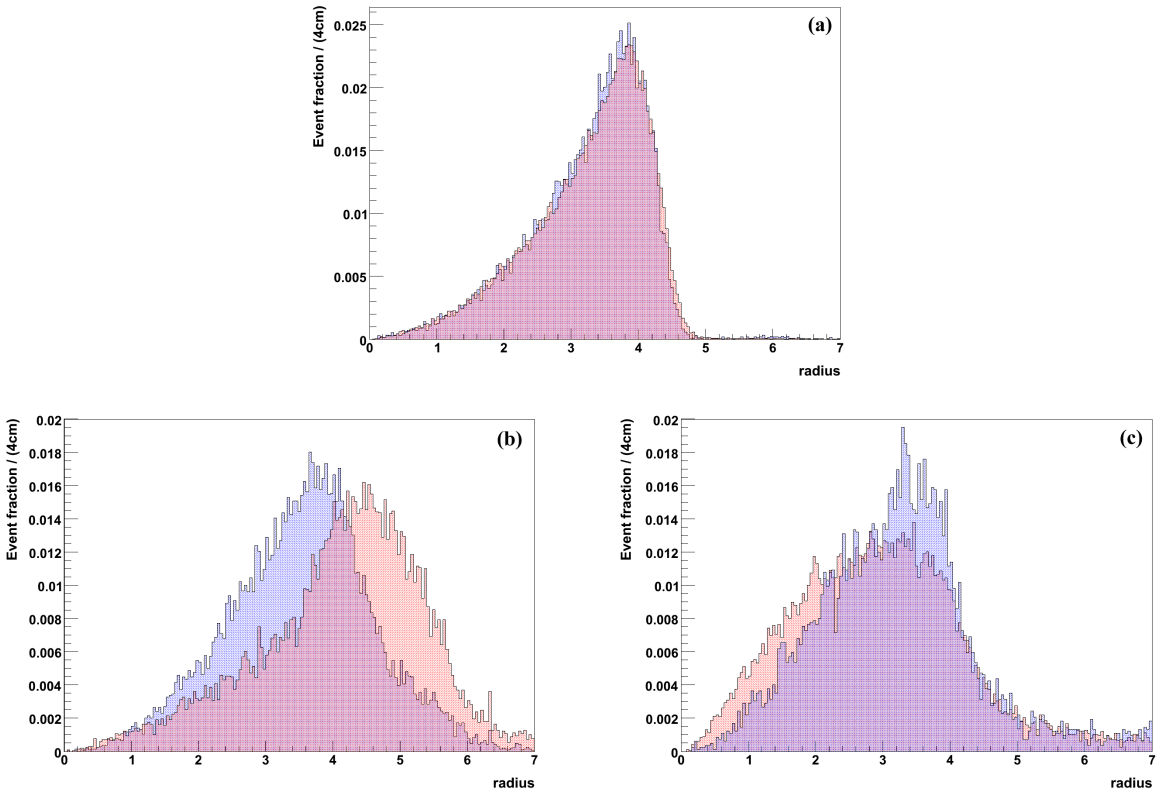

Figure 5.19: Reconstructed radii of neutron captures γ's. The color code refers to events identified within the first $400\,\mu s$ after gate start (red) and later (blue), respectively. The IV nominal radius is $4.25\,m$. *Plot a:* Capture γ's of more than 200 detected PMT hits. The position reconstruction is unaffected by the high noise levels at gate start. *Plot b:* Semi-contained captures γ's at the IV boundary and ^{14}C decays. Events with hits in the range $[30, 200]$ and without electronics saturation ($N_{\mathrm{eb}} = 0$) were selected. The lower limit rejects the unidentified background population $E_{\mathrm{vis}} \leq 40\,keV \simeq 20$ PMT hits), which is poorly reconstructed in space due to its low visible energy. A strong effect of the noise at gate start is visible, pushing the reconstructed vertex outwards. *Plot c:* Captures γ's degenerated by saturation effects ($N_{\mathrm{eb}} \geq 100$). As has been described in the text, the reconstructed position is shifted away from the detector surface blinded by the muon track. This manifests in an average inward shift of the radial distribition.

- **Saturated Boards**:
  The reconstruction is further complicated by the saturation of digital boards. Especially those boards saturate which correspond to PMT groups close to the muon track, blinding the respective surface of the ID. The resulting asymmetric distribution of noise hits shifts the reconstructed position away

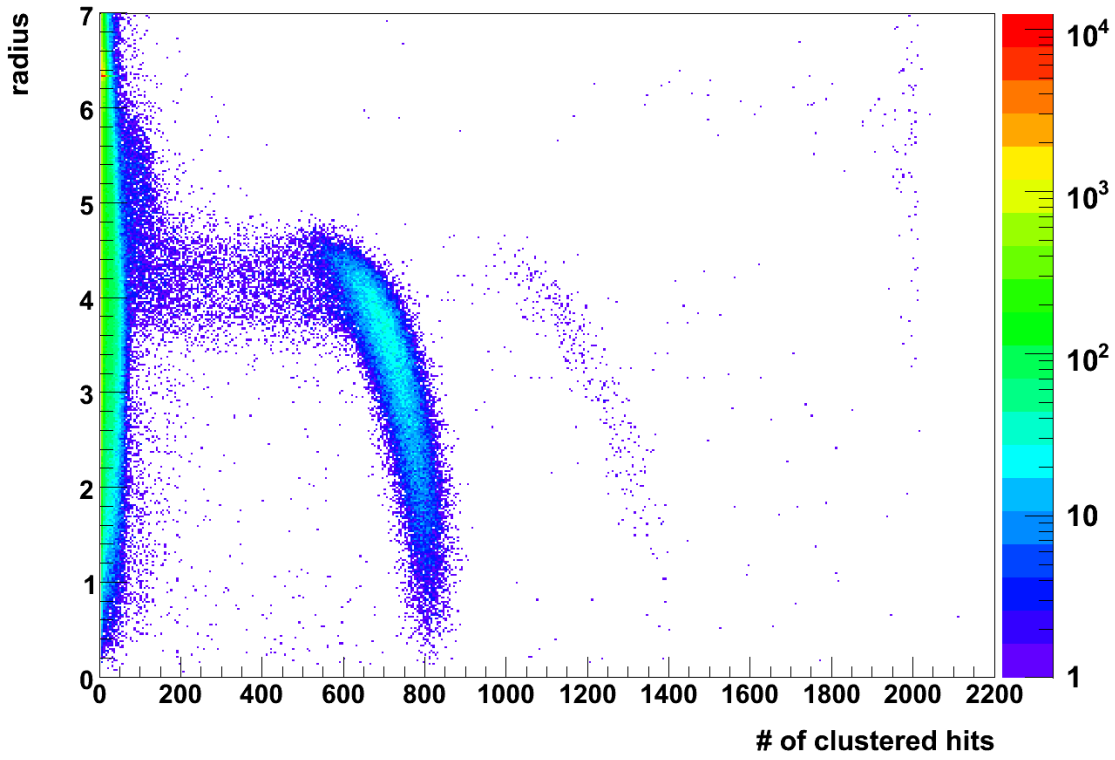

Figure 5.20: Visible energy ($N_{\text{hits}}^{\text{norm}}$) of neutron capture γ's versus the reconstructed radius. The data set is restricted to events without electronics saturation ($N_{\text{eb}} = 0$). Neutron captures on ^{12}C and Hydrogen are visible as bands at about 1200 and 700 hits, respectively. The visible energy of the captures γ's drops significantly at the IV boundary of $4.25\,m$. The low-energetic events below 70 hits are poorly reconstructed, spreading spatially over the whole ID volume. The corresponding events originate from ^{14}C decays ($Q = 156.5\,keV$), neutron captures in the buffer liquid, and an unidentified background component ($E_{\text{vis}} \leq 40\,keV \simeq 20$ PMT hits). For a comparison with Monte Carlo simulations of the detector response to neutron capture γ's, see Figures 5.28 and 5.29.

from the blinded surface.

As the noise level variies inside the neutron gate, so does the fraction of noise hits inside the detected clusters (see Figure 5.3 on page 88). The position reconstruction for neutron captures of sufficient light output (i.e. larger than 200 PMT hits) is barely affected by this noise contamination. However, neutron captures located close to the IV boundary and/or recorded with many empty boards are low in

visible hits and thus suffer severe shifts in the reconstructed position. A proper reconstruction of these event types is only possible in the later parts of the gate (i.e. later than about $400\,\mu s$ after gate start), for which the noise level has decreased to negligible levels (Figure 5.3, page 88). The effect of noise contamination on the reconstructed position for the different neutron capture types is shown in Figure 5.19. Figure 5.20 presents the visible energy of clusters $N_{\text{hits}}^{\text{norm}}$ identified in neutron triggers without saturated digital boards ($N_{\text{eb}} = 0$) versus the reconstructed position. The bands of neutron captures on Hydrogen and ^{12}C are visible at about 700 and 1200 hits, respectively. The curvature to larger radii of these bands is the result of the higher chance of multiple PMT hits at off-center positions, which are not resolved properly by the $N_{\text{hits}}^{\text{norm}}$ variable (see Sec. 3.3.3 for more details). The poor position reconstruction for events below 50 hits results in a spread-out of the reconstructed position over the whole ID volume; a phenomenom well reproduced by the Borexino MC (see Figures 5.28 and 5.29 on pages 127 and 128, respectively).

5.5 Neutron Capture Time

Based on the chemical composition of the Borexino liquid scintillator (organic solvent pseudocumene, $C_6H_3(CH_3)_3$), the ratio of Hydrogen to Carbon nuclei is 4:3. Combined with the corresponding thermal neutron capture cross-sections $\sigma(\text{H}) = (332.6\pm0.7)\,mb$ and $\sigma(^{12}\text{C}) = (3.89\pm0.06)\,mb$ [81], a fraction of about 99% of all thermal neutron captures are expected on Hydrogen. Figure 5.21 presents the FLUKA simulations of the time profiles on the respective nuclei. While the captures on Hydrogen follow a purely exponential function, captures on Carbon feature an excess at early times in the non-thermalized regime due to a $10\,MeV$ resonance in the neutron-^{12}C-interaction cross-section (Figure 5.22). These captures account for about 1% of all neutron captures according to FLUKA simulations [79]. When the neutron trigger is issued about $16\,\mu s$ after the muon, all free neutrons have been thermalized and the total capture time profile is expected to be purely exponential.
The upper plot in Figure 5.23 shows the time profile of physics events detected inside the neutron gate. A high population of accidental coincidences and noise events contribute as a flat component, while the neutron captures are visible as an exponential decay. The profile is distorted in the first $300\,\mu s$ as a result of the particularly high noise levels present at the beginning of the gate (see Figure 5.3 on page 88). Neutron capture peaks degenerated by IV boundary effects and/or electronics saturation are less likely to be identified in this more noisy part of the gate, leading to a time-dependent detection efficiency.
By applying a visible energy threshold of $1.3\,MeV$ according to Equ. (5.29), uncor-

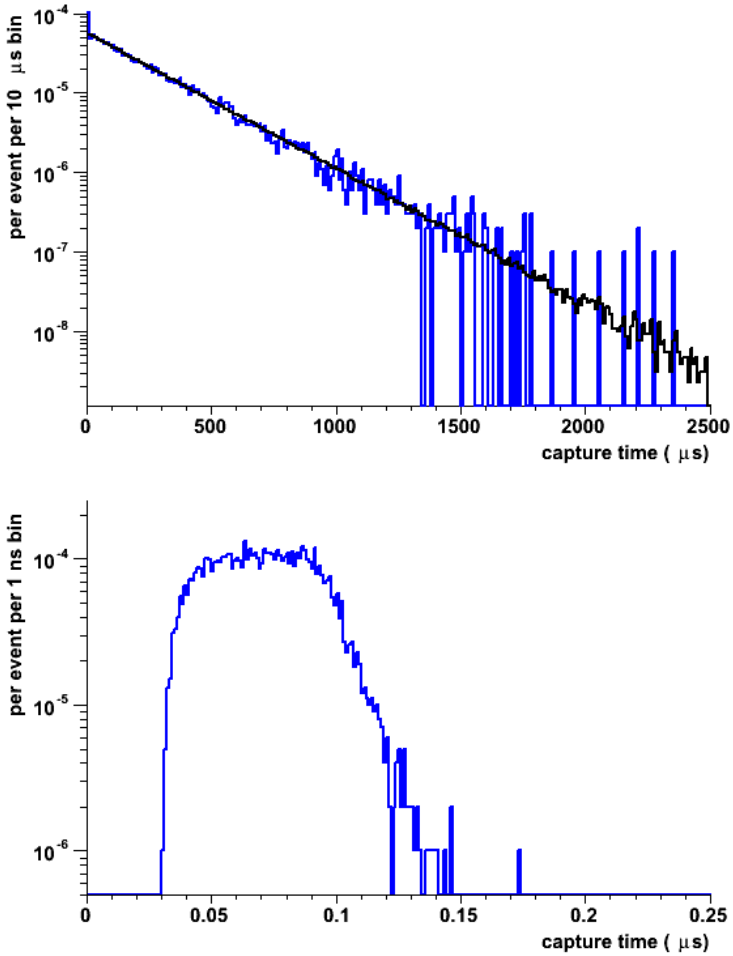

Figure 5.21: Time profiles of neutron captures on ^{1}H (black) and ^{12}C (blue) in Borexino, as simulated with the FLUKA Monte Carlo code [79]. *Top:* The neutrons thermalize within the first microsecond, and are captured eventually with a mean time of $(253.4 \pm 0.6)\,\mu s$ on Hydrogen or Carbon. While the time profile of captures on Hydrogen features a pure exponential behaviour, the captures on Carbon show a small excess population in the first time bin. This is the result of a nuclear resonance in the neutron-^{12}C-interaction at about $10\,MeV$ (see Figure 5.22). About 1% of all neutrons are captured due to this resonance before being thermalized. *Bottom:* Time profile of non-thermal neutron captures on ^{12}C due to the $10\,MeV$ nuclear resonance. The absorption process occurs within the first $0.2\,\mu s$ after production.

related background events are removed from the data sample. The corresponding time profile is shown in the lower plot of Figure 5.23, featuring a recovered expo-

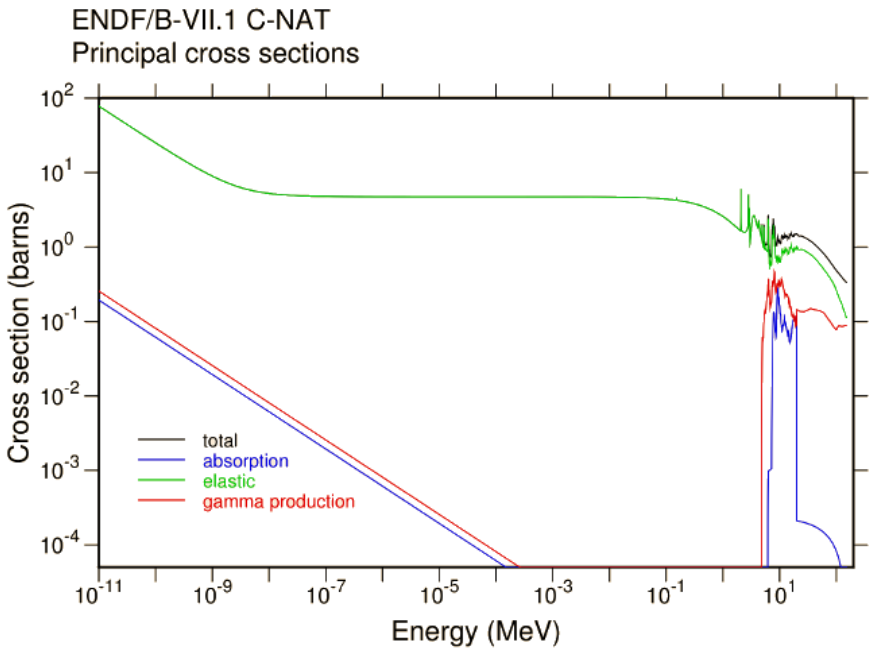

Figure 5.22: Cross-sections of neutron interactions with the ^{12}C nucleus as a function of the neutron energy [80]. The absorption resonance at an energy of about $10\,MeV$ results in fast captures ($\Delta t < 0.2\,\mu s$) of non-thermal neutrons on ^{12}C.

nential distribution. The applied energy cut results in a data set containing also neutrons low in detected hits due to boards saturation. As these are less likely to be identified at the noise gate start, a small distortion of the time profile is still visible in the first $30\,\mu s$. To extract the mean neutron capture time τ_n of thermal neutrons, the time profile is fitted with the function

$$f(t) = \frac{A}{\tau_n} e^{-\frac{t}{\tau_n}} + C \qquad t \in [t_0, t_1] \tag{5.30}$$

The fit is performed in the range $[200, 1600]\,\mu s$ after gate start, where the muon-induced noise levels have decreased to a few hits per $100\,ns$ (see Figure 5.3 on page 88) and thus the neutron detection efficiency is uniform. The mean neutron capture time is found to be $\tau_n = (259.7 \pm 1.3_{\text{stat}})\,\mu s$. Scanning the parameter space in energy, electronics-saturation, and fit interval selection, the systematic uncertainty is determined to $2.0\,\mu s$. The measurement of the mean (thermal) neutron capture time in pseudocumene is reported as:

$$\tau_n = (259.7 \pm 1.3_{\text{stat}} \pm 2.0_{\text{syst}})\,\mu s \tag{5.31}$$

The result can be compared with measurements from an AmBe neutron emitter

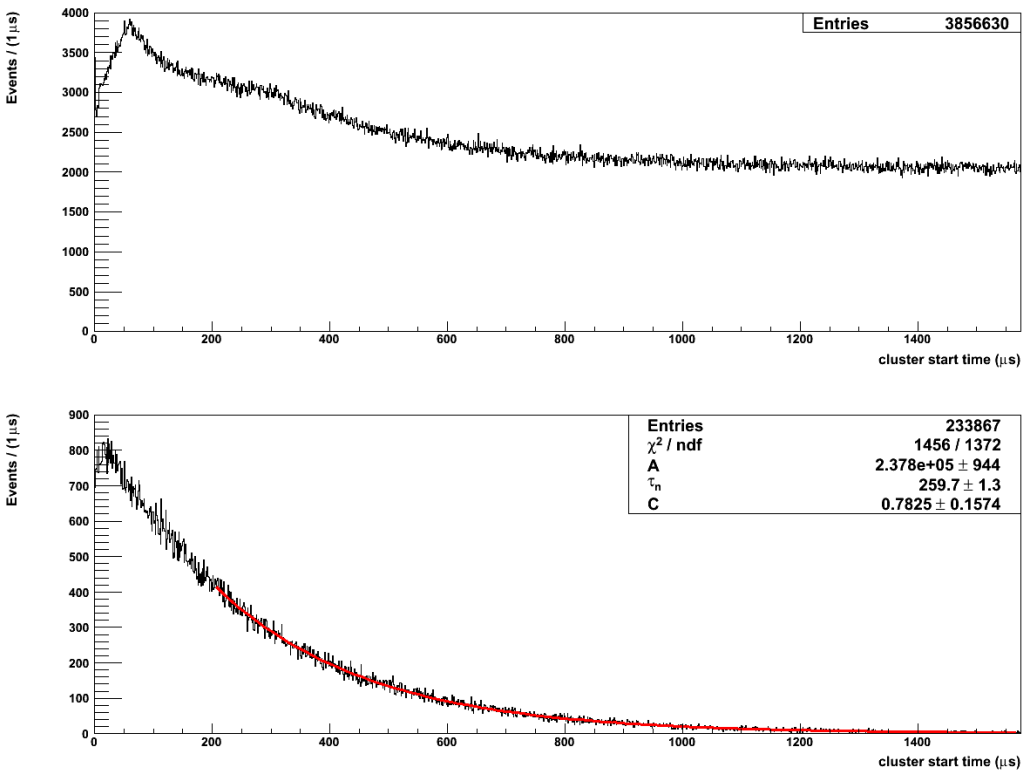

Figure 5.23: Time profile of of hit clusters detected inside of neutron triggers before (top plot) and after (bottom plot) the application of a 1.3 MeV visible energy threshold (see Equ. (5.29)). *Top:* The expected sum of an exponential (neutron captures) and constant (accidental coincidences) function is distorted in the first 300 μs due to high muon-induced noise levels after gate start. *Bottom:* The energy cut efficiently removes noise events, accidental coincidences, and neutrons which are not fully contained inside the IV, recovering the exponential neutron capture time profile.

source, which was deployed during the extensive Borexino calibration campaing in June 2009 in 20 positions throughout the IV. The fast coincidences between the prompt gamma and the delayed neutron signals were identified by a separation in space and time of less than 2 m and 1.6 ms, respectively. Figure 5.24 presents the time difference between the two signals for the AmBe source located at the center of the detector; the fit returns a mean neutron capture time of $(254.3 \pm 0.8_{\text{stat}})\,\mu s$. Taking the fit results from all source positions into account, the mean neutron capture time is determined to $\tau_n = (254.3 \pm 1.8)\,\mu s$.
A slight discrepancy between the results obtained from cosmogenic neutrons and

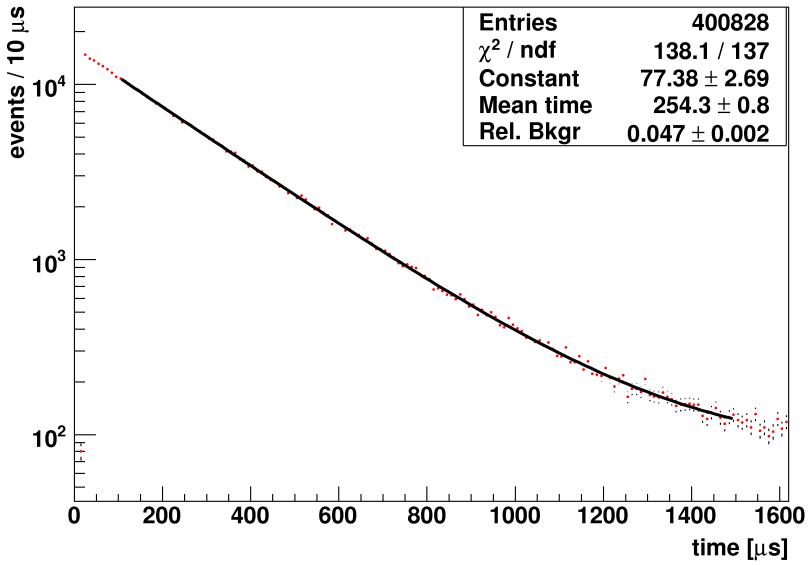

Figure 5.24: Distribution of the time difference between the prompt γ's and the corresponding delayed neutron captures of an AmBe calibration source at the center of Borexino [32]. Fitting the distribution with the sum of an exponential and a constant function, a mean neutron capture time of $(254.3 \pm 0.8_{\mathrm{stat}})\,\mu s$ is found.

the calibration source is present. A similar deviation has been reported by the Kamland collaboration. For the liquid scintillator mixture of 80% dodecane and 20% pseudocumene in Kamland, mean neutron capture times of (207.5 ± 0.3) and $(205.2 \pm 0.5)\,\mu s$ were found for neutrons produced by cosmic muons, respectively by an AmBe calibration source [82]. It is speculated, that this discrepancy arises from neutrons being captured on the stainless steel encapsulation of the source.

The evaluation of the neutron production rate and yield presented in the following Section is based on thermal neutrons being captured later than $30\,\mu s$ after the parent muon. For later reference, the corresponding selection efficiency $\varepsilon_{\mathrm{t}}^{\mathrm{therm}} = (89.1 \pm 1.0)\%$ is evaluated, based on an exponential extrapolation using the observed cosmogenic neutron capture time (Equ. (5.31)).

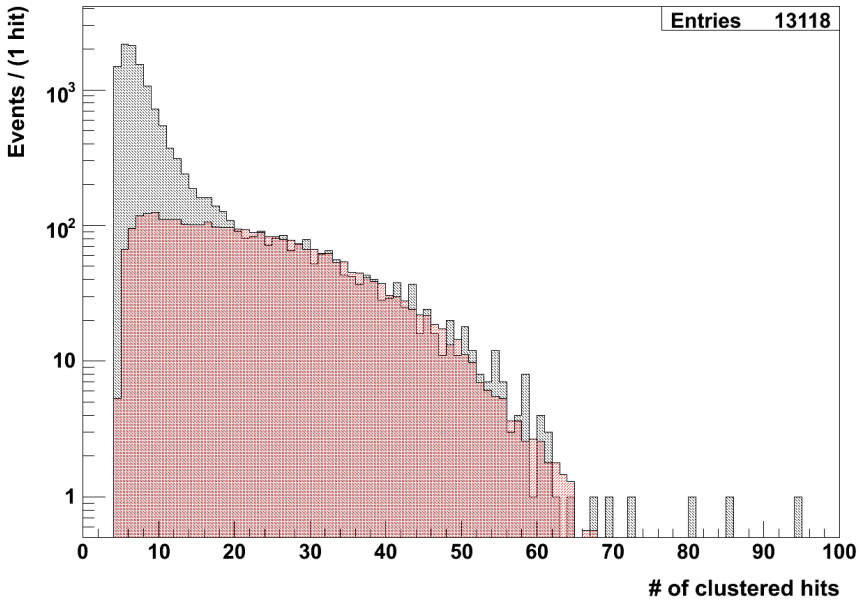

Figure 5.25: Visible energy of hit clusters ($N_{\text{hits}}^{\text{norm}}$) detected in the last $50\,\mu s$ of the neutron gate, corresponding to about $1570\,\mu s$ after the muon. The events are required to be taken with fully functional electronics ($N_{\text{eb}} = 0$). The (black shaded) data is superimposed by the (red shaded) spectral shape of ^{14}C decays, as simulated by the Borexino Monte Carlo. The excess of events at low energies ($N_{\text{hits}}^{\text{norm}} < 20$) is associated with the residual light from decays in the buffer liquid, and misidentified noise events. The outliers present at energies above 70 hits are in agreement with the expected fraction of neutron captures in the selected time window.

5.6 Uncorrelated Background and Noise Events

As has been mentioned, with a length of $1.6\,ms$, the neutron gate records a significant amount of uncorrelated background events. These consist of misidentified noise events, ^{14}C decays, and a low-energetic background presumed to orginate from decays in the buffer liquid. Based on the time profile of detected events in the neutron gate (see top plot in Figure 5.23), a background-enriched datasample can be prepared. In addition, the events are required to be recorded with fully functional electronics ($N_{\text{eb}} = 0$) to obtain an undistorted energy spectrum. Figure 5.25 presents the spectral distribution of events selected in the last $50\,\mu s$ of the gate, corresponding to about $1570\,\mu s$ after the muon. The visible cut-off at 5 hits is connected to the minimum hit threshold required by the neutron clustering

routine described in Sec. 5.1. While the data is presented by the black shaded distribution, the output of a Borexino Monte Carlo simulation of ^{14}C decays is superimposed in red. The latter distribution has been scaled to match the measured number of events at energies above 25 hits (i.e. $N_{25} = 1173$ entries) and is in good agreement with the observation.

^{14}C decays

The specific ^{14}C decay rate is found to be

$$\begin{aligned} R(^{14}\mathrm{C}) &= \frac{N_{25}}{V_{\mathrm{IV}} \cdot \rho_{\mathrm{PC}} \cdot N_{\mathrm{trigger}} \cdot \Delta t} \cdot \frac{1}{\varepsilon_{\mathrm{MTB}} \cdot f_{\mathrm{eb}} \cdot f_{25}} \\ &= (38.7 \pm 1.2)\, Hz/(100\, t) \end{aligned} \tag{5.32}$$

Here, $V_{\mathrm{IV}} = (306.9 \pm 2.9)\,\mathrm{m}^3$ and $\rho_{\mathrm{PC}} = (0.8802 \pm 0.0004)\,\mathrm{g/cm}^3$ denote the average IV volume of the studied data set (Sec. 5.7) and the scintillator density [21], respectively. The parameter $\varepsilon_{\mathrm{MTB}} = 0.9925(2)$ gives the trigger efficiency of the neutron gate, which is issued by the OD *Muon Trigger Board* (MTB) (Sec. 4.1). The parameter $f_{\mathrm{eb}} = 32.1\%$ states the fraction of events fullfiling the requirement of fully functional electronics. A fraction of $f_{25} = 29.1\%$ of all ^{14}C decays satisfy the energy cut of 25 hits. During the data set livetime of 559 live days, the neutron trigger was issued $N_{\mathrm{trigger}} = 2.41 \cdot 10^6$ times. The parameter $\Delta t = 50\,\mu s$ refers to the time selection of the last $50\,\mu s$ of the time gate. The observed rate is in good agreement with measurements of the specific ^{14}C rate of $(38.98 \pm 0.02)\, Hz/(100\, t)$, using the random trigger gate [83].

Noise events and decays inside the buffer

With a fraction of $f_5 = 78.9\%$ above the clustering threshold of 5 hits, ^{14}C decays can only explain about 3150 ± 56 events of a total of 13118 events in the selected data set. The remaining events, manifesting as an excess at energies below 20 hits ($\simeq 40\, keV$), are attributed to noise events and the residual light from decays in the buffer liquid. The spatial origin of the latter is compromised by the insufficient position reconstruction resolution of Borexino at these low energies (see Sec. 5.4.5). Above the clustering threshold of 5 hits, the combined rate of these excess events is measured to be

$$R_{\mathrm{bkg}} = 256\, Hz \tag{5.33}$$

By assuming, that all excess events are caused by misclustered noise, an upper limit of $4 \cdot 10^{-6}$ on the misidentification probability of the clustering algorithm can be derived.

Cosmic Muons

Though comparatively rare, also cosmic muons contribute to the accidental background in the neutron gate. With a muon rate of $R_\mu = (4310 \pm 2_{\text{stat}} \pm 10_{\text{syst}})\, d^{-1}$ [63], the probability of an accidental muon inside the $1.6\, ms$ neutron gate can be estimated as

$$P_\mu = R_\mu \int_0^{1.6\, ms} e^{-R_\mu \cdot t}\, \mathrm{d}t \simeq 10^{-4} \tag{5.34}$$

Taking as reference the data set used for the lower plot in Figure 5.12 on page 105 (i.e. $7.7 \cdot 10^5$ issued neutron triggers with fully functional electronics), about 80 accidental muon events are expected. This is in good agreement with the observation of 75 muon candidates (orange distribution in the Figure).

5.7 Effective Detection Volume

As preparation for the measurement of the neutron production rate and yield in Sec. 5.8, a neutron detection volume has to be defined. However, as has been demonstrated in Section 5.4.5, only a subset of the neutron captures detected in Borexino feature a correct position reconstruction. As a result, the detection volume cannot be defined by a software selection cut on the reconstructed position of the captures. Based on the visible energy threshold for neutrons of $1.3\, MeV$, the determination of the effective detection volume is outlined in the following.

At first order, the detection volume is given by the physical boundaries of the *Inner Vessel* (IV). However, neutron captures in the buffer liquid close to the IV can create γ's crossing the vessel and producing a visible signal in the scintillator. Contrariwise, γ's generated inside the IV can leak into the buffer and fall below the visible energy threshold. This spill-in/spill-out effect was studied with the Borexino Monte Carlo code. For more information on the Borexio Monte Carlo framework, see Section 3.5.

Inner Vessel Volume

Based on software evaluation of the vessel surface contamination, the shape and contained volume of the IV is monitored in Borexino. Figure 5.26 presents the change of the IV volume over the course of the studied data sample. The impact of a small leak appearing in the IV in autumn 2008 is clearly visible as a steady decrease of the active scintillation liquid and a corresponding deflation of the vessel. A large refilling operation in May 2009 (day 517) marks a sudden increase

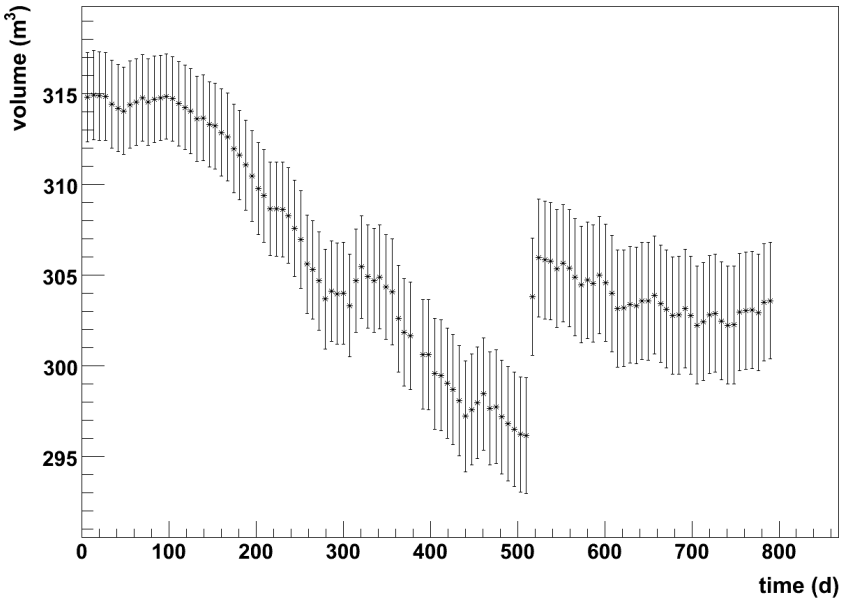

Figure 5.26: Reconsctructed IV volume as a function of time. The time is given in days since the 1st of January 2008. A steady decrease of the volume is visible beginning in autumn 2008 as a result of a small leak in the vessel. The loss of scintillator was counteracted by refilling about $10\,m^3$ of scintillator in May 2009 (day 517). Adjusting the density levels of the scintillator and buffer liquid by reducing the DMP concentration in the buffer, the leak flow has been reduced to negligible levels. Since beginning of 2010 ($\simeq$ day 720), the IV volume remains almost stable.

in volume. By reducing the DMP concentration in the buffer liquid, the byoance forces on the IV have been reduced and the scintillator loss reduced to minimal levels, as is indicated by the stable IV volume since the beginning of 2010 ($\simeq$ day 720). Weighting the shown volume profile with the detector live time distribution, an average IV volume of $(306.9 \pm 2.9)\,\mathrm{m}^3$ is found.

Monte Carlo Evaluation

The effect of the $1.3\,MeV$ energy threshold, as well as spill-in/spill-out effects of partially contained γ's were investigated with the Borexino Monte Carlo code within the frame of this thesis. As Hall C of the LNGS underground laboratory is expected to be radiated homogenously by cosmic muons, the muon-induced neutron captures are expected to be homogeneous within the ID as well. This is re-

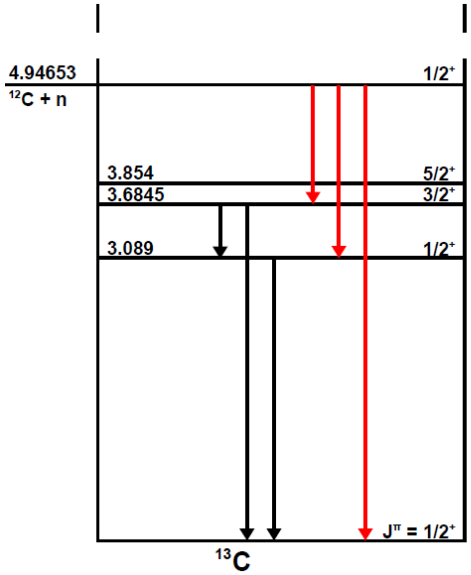

E_γ^{H} $[keV]$	E_{i} $[keV]$	E_{f} $[keV]$	P_{trans} [%]
3089.057 ± 0.009	3089.451	0	0.429 ± 0.022
595.015 ± 0.009	3684.480	3089.451	0.247 ± 0.011
3683.920 ± 0.009	3684.480	0	31.7 ± 0.9
1261.765 ± 0.009	Capture State	3684.480	32.2 ± 0.9
1856.717 ± 0.009	Capture State	3089.451	0.161 ± 0.011
4945.301 ± 0.003	Capture State	0	67.8 ± 1.7

Figure 5.27: Level transitions of ^{13}C generated by the thermal neutron capture on ^{12}C. The corresponding transition probabilities and gamma energies are stated in the table. [81]

flected in the simulation by a homogenous distribution of isotropic γ-emitters over the ID volume. For neutron captures on Hydrogen, γ's of an energy of 2.23 MeV are generated. In case of captures on Carbon, the decay scheme of the excited ^{13}C nucleus is taken into account (see Figure 5.27). Ignoring level transitions of sub-percent probability, 67.8% of all ^{13}C de-excitations yield a single 4.95 MeV γ, while in the remaining 32.2% two γ's of energies 3.68 MeV and 1.26 MeV are generated. The IV volume is set to the average value found in the data, i.e. $(306.9 \pm 2.9)\,\mathrm{m}^3$ corresponding to $(22.8 \pm 0.2)\%$ of the ID volume.
Figures 5.28 and 5.29 present the energy and position reconstruction response of the detector for neutron captures on Hydrogen and ^{12}C, respectively. As can be seen, the visible energy drops drastically for capture γ's in the buffer liquid. Projecting on the energy axis, the green shaded areas in the lower plots of Figures 5.28 and 5.29 illustrate the fraction of γ's above the 1.3 MeV energy threshold (Equ.

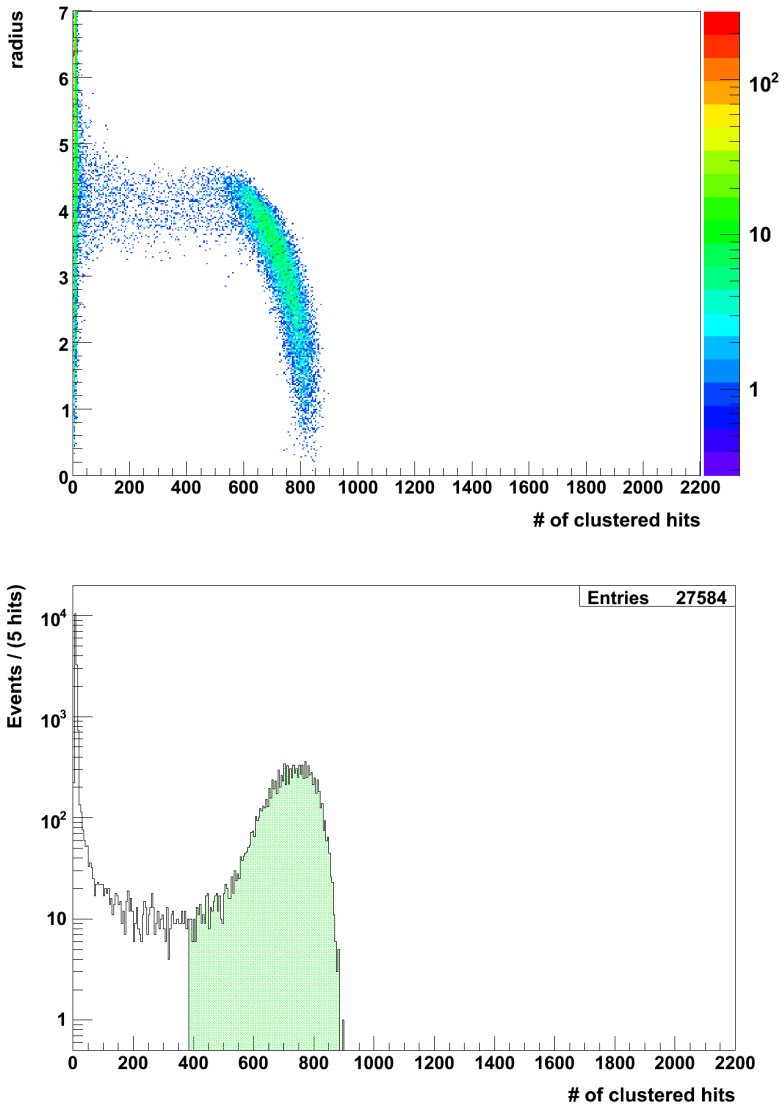

Figure 5.28: Simulated visible energy response ($N_{\text{hits}}^{\text{norm}}$) of 2.2 MeV γ's, homogenously distributed over the ID volume. *Top:* The visible energy is shown as a function of the reconstructed radius. The position reconstruction of γ's located in the buffer liquid suffers from the low visible energy. Buffer events featuring less than 50 PMT hits are reconstructed in space all over the ID volume. *Bottom:* Energy distribution of the 2.2 MeV γ's. The green shaded area contains the γ's above the energy threshold of 1.3 MeV, corresponding to a fraction of $\varepsilon_{\text{vol}}^{\text{H}} = (23.0 \pm 0.3)\%$.

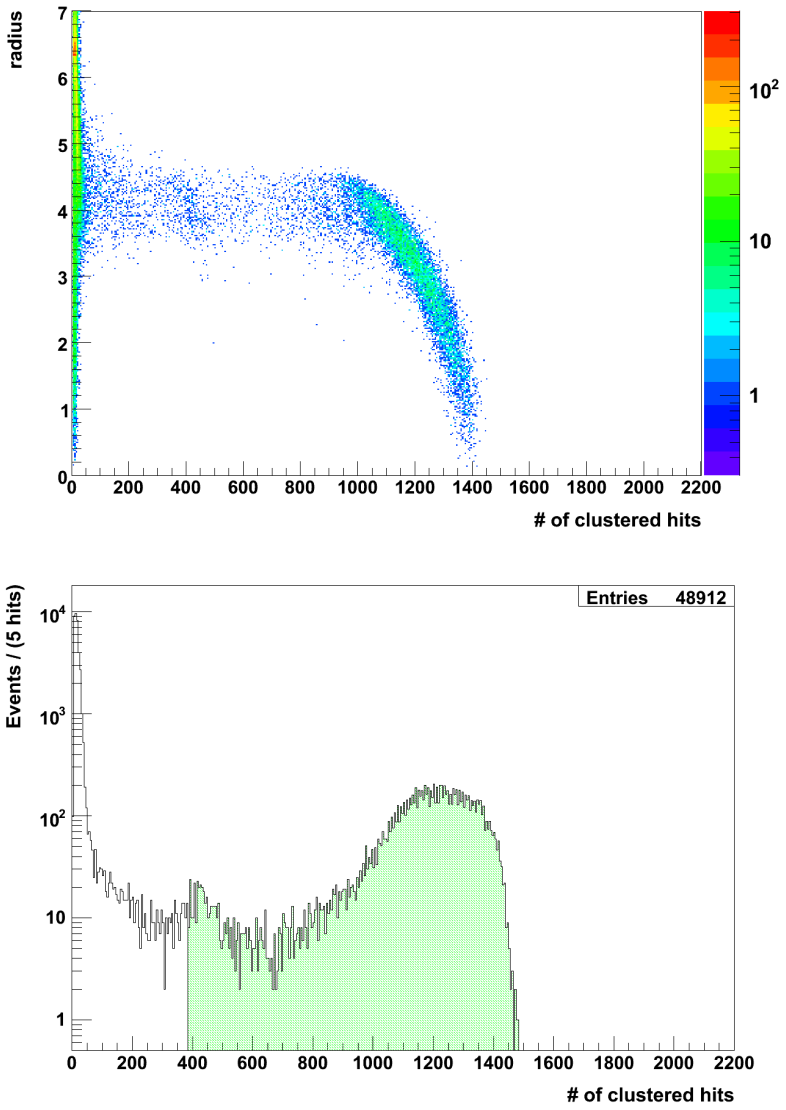

Figure 5.29: Simulated visible energy response ($N_{\text{hits}}^{\text{norm}}$) of captures γ's according to the energies and transition probabilities of thermal neutron capture on ^{12}C (Figure 5.27). The γ's were distributed homogeneously over the ID volume. *Top:* The visible energy is shown as a function of the reconstructed radius. *Bottom:* Energy distribution of the γ's. The green shaded area contains the γ's above the energy threshold of $1.3\,MeV$, corresponding to a fraction of $\varepsilon_{\text{vol}}^{\text{C}} = (24.2 \pm 0.3)\%$.

(5.29)). The effect of electronics saturation is not modeled in the Monte Carlo, and thus the number of empty boards is by definition zero. The corresponding detection inefficiency has been independently evaluated using the *Princeton Analog*

Variable	Value	Reference
ρ_{PC}	$(0.8802 \pm 0.0004)\, g/cm^3$	[21]
t_{L}	$559\, d$	
$\langle l_\mu \rangle$	$9.10\, m$	Sec. 5.3, Equ.(5.23) with $\langle l_\mu \rangle(0, R_{\mathrm{ID}})$ and $R_{\mathrm{ID}} = (6.821 \pm 0.005)\, m$ [84]
$\varepsilon_{\mathrm{MTB}}$	0.9925(2)	Sec. 4.1
$\varepsilon_{\mathrm{det}}^{\mathrm{cosm}}$	$(92.0 \pm 1.7)\%$	Sec. 5.4.3
$\varepsilon_{\mathrm{t}}^{\mathrm{therm}}$	$(89.1 \pm 1.0)\%$	Sec. 5.5
$\varepsilon_{\mathrm{vol}}$	$(23.0 \pm 0.3)\%$	Sec. 5.7

Table 5.1: List of input variables for the calculation of the thermal neutron capture rate and yield according to Equ. (6.7).

System, as described in Section 5.4.3.
The fraction of neutron captures in the ID above the energy threshold is found to be $\varepsilon_{\mathrm{vol}}^{\mathrm{H}} = (23.0 \pm 0.3)\%$ for captures on Hydrogen, and $\varepsilon_{\mathrm{vol}}^{\mathrm{C}} = (24.2 \pm 0.3)\%$ on ^{12}C, respectively. In case of neutron captures on Hydrogen, the observed volume fraction is well in agreement with the IV volume set in the simulation, i.e. $306.9\,\mathrm{m}^3$ corresponding to 22.8% of the ID volume. The application of the $1.3\, MeV$ compensates the spill-in/spill-out effects of partially contained $2.2\, MeV$ γ's. Due to the higher energy of the capture γ's on ^{12}C, the volume fraction of captures on Carbon is slightly higher than for captures on Hydrogen. This is connected to the larger range of the ^{12}C γ's, which results in a more pronounced spill-in effect.
Weighting these fractions with the chemical abundances (H : C = 4 : 3) and thermal neutron capture cross-sections ($\sigma(\mathrm{H}) = (332.6 \pm 0.7)\, mb$ and $\sigma(^{12}\mathrm{C}) = (3.89 \pm 0.06)\, mb$ [81]), a volume fraction of

$$\varepsilon_{\mathrm{vol}} = (23.0 \pm 0.3)\% \tag{5.35}$$

is expected for captures above the energy threshold. As captures on Hydrogen dominate, the effective IV volume is identical to $\varepsilon_{\mathrm{vol}}^{\mathrm{H}} = (23.0 \pm 0.3)\%$, and in agreement with the the IV volume.

5.8 Neutron Production Rate and Yield

The analyis is based on a data set of 559 days of live time, covering the time period from 6$^{\mathrm{th}}$ of January 2008 till 2$^{\mathrm{nd}}$ of February 2010. The beginning of the data set is defined by the addition of the neutron acquisition trigger to the DAQ, while the end is marked by modifications in channel gain and memory reservation of the digital boards, altering the detector response function. Removing CNGS on-time

events from the data sample and statistically subtracting random coincidences, the number of neutron captures N_n detected in the ID later than $30\,\mu s$ after the parent muon and with a visible energy above $1.3\,MeV$ is retrieved. The saturation state of the detector is taken into account in the energy threshold definition according to relation (5.29) on page 113. As has been demonstrated in Section 5.5, thermal neutron captures follow an exponential time profile and allow to extrapolate the number of neutron captures based on the mean capture time. As a result, the rate R_n^{therm} and yield Y_n^{therm} are given for thermal neutrons, based on the following equation:

$$\begin{aligned} R_n^{\text{therm}} &= \frac{N_n}{V_{\text{ID}} \cdot \rho_{\text{PC}} \cdot t_{\text{L}}} \cdot \frac{1}{\varepsilon_{\text{det}}^{\text{cosm}} \cdot \varepsilon_t^{\text{therm}} \cdot \varepsilon_{\text{vol}} \cdot \varepsilon_{\text{MTB}}} \\ Y_n^{\text{therm}} &= \frac{N_n}{N_\mu \cdot \langle l_\mu \rangle \cdot \rho_{\text{PC}}} \cdot \frac{1}{\varepsilon_{\text{det}}^{\text{cosm}} \cdot \varepsilon_t^{\text{therm}} \cdot \varepsilon_{\text{vol}}} \end{aligned} \tag{5.36}$$

Here, V_{ID} constitutes the ID volume and ρ_{PC} the liquid scintillator density. The variable t_{L} states the lifetime of the data set. The number of muons in the data sample, as well as the mean muon path length through the ID are given by N_μ and $\langle l_\mu \rangle$. The detection efficiencies connected to the electronics saturation and the time cut are denoted with $\varepsilon_{\text{det}}^{\text{cosm}}$ and $\varepsilon_t^{\text{therm}}$, respectively. The OD *Muon Trigger Board* (MTB) flags muons and triggers the $1.6\,ms$ neutron gate. The corresponding efficiency is denoted by ε_{MTB}. The effective detection volume of neutron captures with a visible energy above $1.3\,MeV$ corresponds to a fraction of ε_{vol} of the whole ID volume.
Table 5.1 presents the compilation of input variables for Equ. (6.7) along with the corresponding values. Evaluating the equation, the rate and yield of thermal neutron captures in Borexino are found to be

$$\begin{aligned} R_n^{\text{therm}} &= (90.2 \pm 2.0_{\text{stat}} \pm 2.4_{\text{syst}})\,(d\,100\,t)^{-1} \\ Y_n^{\text{therm}} &= (3.10 \pm 0.07_{\text{stat}} \pm 0.08_{\text{syst}}) \cdot 10^{-4}\, n/(\mu \cdot (g/cm^2)) \end{aligned} \tag{5.37}$$

Statistical fluctuations in the neutron number have been taken into account according to Equ. (5.27)) on page 104). The correct treatment of the statistical uncertainties in the neutron production results in a final statistical error, which is by a factor of $\simeq$7 larger than the uncertainty expected on the basis of $\Delta N_n = \sqrt{N_n}$.

As has been measured by the Macro collaboration, the average muon energy at the LNGS underground site is $(283 \pm 19)\,GeV$ [61]. With a similar average muon energy of $(260 \pm 8)\,GeV$ at the depth of the Kamioka Observatory (about $2700\,m.w.e.$), the Borexino result can be compared with the neutron production yield in Kamland, published in 2010 [82]. Based on the density of Carbon nuclides in the respective liquid-scintillator mixtures, and the average muon energies at both sites, the

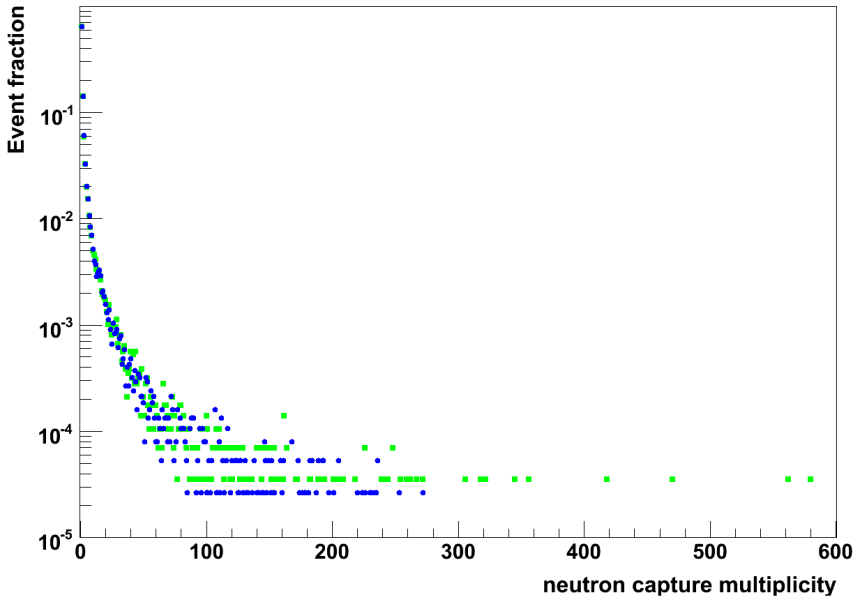

Figure 5.30: Normalized cosmogenic neutron multiplicities of neutron-producing muons, as detected by the main DAQ (blue spheres) and the PAS (green rectangulars), respectively. While the PAS detects up to 600 neutrons after a single muon event, the main DAQ distribution is limited to a neutron multiplicity of about 300 by inefficiencies due to electronics saturation effects.

Kamland result is scaled to Borexino for better comparison:

$$Y_n^{\mathrm{therm}}(\mathrm{Kl}) \quad = \quad (3.11 \pm 0.39) \cdot 10^{-4}\, n/(\mu \cdot (g/cm^2)) \tag{5.38}$$

The result is in good agreement with the neutron yield derived with Borexino data. The applied scaling method is presented in detail in Sec. 6.5 on page 169 together with a comprehensive comparison of all cosmogenic production yields in Borexino and Kamland.

5.9 Rate of neutron-producing Muons and Neutron Multiplicity

Besides the total neutron production rate, also the multiplicity of neutrons produced by cosmic muons is of interest. Though strongly detector dependant, the observed neutron multiplicity distribution is valuable for the validation of simulation codes like Geant4 and FLUKA. The analysis presented in this Section is

based on cosmogenic neutrons with a visible energy above of $1.3\,MeV$ (see Sec. 5.4.4, Equ. (5.29)) and a capture time later than $30\,\mu s$ after the parent muon. Figure 5.30 shows the normalized distributions of detected neutron multiplicities for the main DAQ and the *Princeton Analog System* (PAS), respectively. While the PAS data extends up to 600 neutrons detected after a single muon event, the main DAQ distribution shows a deficit of events at these high multiplicities. Such high multiplicities are expected to be generated in extended muon-induced electromagnetic and hadronic showers. As these events produce a huge amount of scintillation light in the experiment, a large fraction of the digital boards is expected to saturate (see Sec. 5.1). The corresponding detection inefficiency limits the neutron multiplicities detected by the main DAQ to about 300 neutrons. As the PAS does not suffer from these effects, and shows no mulitplicity-dependant detection efficiencies [85], observables are retrieved from the PAS data in this Section if not stated otherwise.
While the majority (i.e. $(65.9 \pm 0.5)\%$) of neutron-producing muons features only one neutron, about 50% of all neutrons are produced in muon events of neutron multiplicities larger than 12. However, muon events of these multiplicities account only for a fraction of $(5.0 \pm 0.1)\%$ of all neutron-producing muons. Though rare, these high-mulitplicity events have a significant impact on production rate and detection efficiency of neutrons. The decreased detector performance in high-multiplicity events dominates the total detection efficiency of the main DAQ for cosmogenic neutrons $\epsilon_{\mathrm{det}}^{\mathrm{cosm}} = (92.0 \pm 1.7)\%$ (see Sec. 5.4.3).

Observable Multiplicities

As has been mentioned, the neutrons selected for the multiplicity distribution shown in Figure 5.30 have to satisfy a visible energy threshold of $1.3\,MeV$ and have to be captured later than $30\,\mu s$ after the parent muon. The application of the energy threshold compensates the spill-in/spill-out effects of the neutron capture γ's and effectively restricts the neutron captures to the IV volume (see Sec. 5.7). Though, the time cut has a more pronounced effect on the multiplicity distribution. With a neutron capture time of $\tau_n = (259.7 \pm 1.3_{\mathrm{stat}} \pm 2.0_{\mathrm{syst}})\,\mu s$ (Sec. 5.5, Equ. 5.31), the probability/efficiency to detect a thermal neutron $30\,\mu s$ after the parent muon is

$$p = \varepsilon_t^{\mathrm{therm}} = (89.1 \pm 1.0)\% \tag{5.39}$$

In the following, the effect of the time cut on the multiplicity distribution will be presented. Assuming a muon producing n neutrons, the probability $M(k)$ to

detect k neutrons will follow the bionomial distribution

$$M(k) = \binom{n}{k} \cdot p^k \cdot (1-p)^{n-k} \qquad \text{with } n \geq k \tag{5.40}$$

$$\langle k \rangle = p \cdot n \tag{5.41}$$

The effect of the efficiency p shifts the real neutron multiplicity n to an average detected multiplicity of $p \cdot n$.

Assuming that the number of the initial neutron multiplicity n is not fixed, but follows a probability distribution $N(n)$, Equ. (5.40) extends to

$$M(k) = \sum_{n=k}^{\infty} N(n) \cdot \binom{n}{k} \cdot p^k \cdot (1-p)^{n-k} \tag{5.42}$$

$$= \sum_{n=0}^{\infty} N(n) \cdot a_{kn} \tag{5.43}$$

$$\text{with } a_{kn} = \begin{cases} \binom{n}{k} \cdot p^k \cdot (1-p)^{n-k} & \text{for } n \geq k \\ 0 & \text{else} \end{cases} \tag{5.44}$$

The equation system can be expressed by a matrix A of elements a_{kn}, and vectors $\vec{M}$ and $\vec{N}$ of infinite size. Theoretically, by inverting matrix A, the real muliplicity distribution $\vec{N}$ can be derived from the observed distribution $\vec{M}$ ($\vec{N} = A^{-1}\vec{M}$). However, computational inaccuracies complicate the numerical matrix inversion.

It is possible though to analytically derive the fraction of neutron-producing muons, which lost all their neutrons due to the time cut (i.e. $M(0)$). We can manipulate Equ. (5.42) according to [86]:

$$\frac{M(k)(1-p)^k}{p^k} = \sum_{n=k}^{\infty} N(n) \binom{n}{k} (1-p)^n \tag{5.45}$$

Applying the alternating sum over k, we receive

$$\sum_{k=0}^{\infty} (-1)^k M(k) \left(\frac{1-p}{p}\right)^k = \sum_{k=0}^{\infty} \sum_{n=k}^{\infty} (-1)^k N(n) \binom{n}{k} (1-p)^n \tag{5.46}$$

With the binomial coefficient $\binom{n}{k} = 0$ for $k > n$, we can extend the sum over n to the interval $[0, \infty]$ and limit the sum over k to the interval $[0, n]$:

$$\overset{(5.46)}{=} \sum_{n=0}^{\infty} N(n)(1-p)^n \sum_{k=0}^{n} (-1)^k \binom{n}{k}$$

$$\overset{(5.48)}{=} N(0) \tag{5.47}$$

For the last step, the following identity

$$\sum_{k=0}^{n}(-1)^k\binom{n}{k} = \delta_{n0} \tag{5.48}$$

was used. As only neutron-producing muons are considered in the analysis, it follows that $N(0) \stackrel{!}{=} 0$ by definition. Combining this results with Equ. (5.46), we obtain the final formula:

$$M(0) = \sum_{k=1}^{\infty}(-1)^{k+1}M(k)\left(\frac{1-p}{p}\right)^k \tag{5.49}$$

The corresponding fraction of neutron-producing muons, which feature at least one detected neutron after the time cut of $30\,\mu s$ is

$$\begin{aligned} M(k \geq 1) &= 1 - M(0) \\ &= 92.5\% \end{aligned} \tag{5.50}$$

These equations allow to calculate and correct for the inefficiency in detecting at leat one neutron, which is induced by the time cut of $30\,\mu s$. Using the PAS data, a fraction of $M(k \geq 1) = (92.5 \pm 0.3\%)$ is found. The observed value is in agreement with results obtained from neutron production multiplicities, which were simulated with the Geant4 Monte Carlo code [74].

Results

With the threshold on the visible neutron energy of $1.3\,MeV$ and the time cut of $30\,\mu s$ after the muon, a raw rate of $(62.0 \pm 0.3_{\text{stat}} \pm 0.1_{\text{syst}})\,d^{-1}$ of neutron-producing muons is found in the data set. Correcting for the inefficiencies $M(k \geq 1) = (92.5 \pm 0.3)\%$ (Equ. 5.50) and $\varepsilon_{\text{MTB}} = 0.9925(2)$ (Sec. 4.1) imposed by the time cut and the muon detection efficiency respectively, the corrected rate of neutron-producing muons is found to be

$$R_n^{\mu} = (67.5 \pm 0.4_{\text{stat}} \pm 0.2_{\text{syst}})\,d^{-1} \tag{5.51}$$

This refers to about 1.5% of all muons crossing the ID. As has been mentioned, the energy cut restricts the neutron captures to the IV, which encompasses in the selected time period a volume of $(306.9 \pm 2.9)\,\text{m}^3$, corresponding to a mass of $(270.2 \pm 2.6)\,t$. Combining this result with the neutron production rate measured by the main data acquisition of $R_{\text{n}}^{\text{therm}} = (90.2 \pm 2.0_{\text{stat}} \pm 2.4_{\text{syst}})\,(d\,100\,t)^{-1}$ (Equ.

(5.37)), the mean (thermal) neutron multiplicity of neutron captures inside the IV is derived to

$$\langle n \rangle = 3.61 \pm 0.08_{\text{stat}} \pm 0.09_{\text{syst}} \tag{5.52}$$

for neutron-producing cosmic muons.

Chapter 6

Cosmogenic Radioisotopes

After crossing the LNGS rock coverage of 3800 m.w.e.[1], the residual muons feature a mean energy of $(283 \pm 19)\,GeV$ and a flux of $1.2\,m^{-2}h^{-1}$ [61, 63]. Besides neutrons, these muons produce a significant amount of radioactive isotopes in spallation processes on Carbon nuclei in the Borexino liquid scintillator. Tagging and measuring this so-called cosmogenic background is key for a multitude of Borexino's physics analyses, covering the detection of ^{8}B-, pep/CNO- and geo-neutrinos [4, 5, 34]. Furthermore, measurements on cosmogenic production yields and lateral profiles serve as input for other liquid-scintillator experiments performing rare-event searches (e.g. θ_{13} reactor experiments), as well as for the validation of simulation codes like Geant4 and FLUKA [60, 87].
Based on the correlation with the parent muon and possible accompanying neutrons, the production of cosmogenic isotopes can be identified by the characteristic exponential decay time profile. However, as some of the radionuclides feature similar lifetimes, additional information from the expected decay energy spectra is necessary to disentangle the contributions. By applying simultaneous fits on the time profiles and energy spectra, the production rates and yields of all major cosmogenic radioisotopes in Borexino have been evaluated in this thesis.
The beginning of this Chapter presents the applied simultaneous fitting technique of the candidate events in time and energy. This is followed by the description of the decay energy spectra prepared via Monte Carlo simulations. As Geant4 (version 4.9.2.p02) does not include the correct hadronic deexcitations of excited states in light nuclides, modifications of several simulated cosmogenic isotope decay chains were performed in the course of this thesis. These modifications for the cosmogenic isotopes ^{12}N, ^{12}B, ^{8}B, ^{8}Li, ^{9}C, ^{8}He, ^{9}Li, and ^{11}Be are described in detail. Based on these simulated spectral shapes, the second part of the Chapter is dedicated to the measurements of the cosmogenic production yields in Borexino. The

[1] meter of water equivalent

Cosmogenic Isotope	**Decay Type**	**Lifetime**	**Q-value** $[MeV]$
^{12}N	β^+	$15.9\,ms$	17.3
^{12}B	β^-	$29.1\,ms$	13.4
^{8}He	β^-/n	$171.7\,ms$	10.7
^{9}C	β^+	$182.5\,ms$	16.5
^{9}Li	β^-/n	$257.2\,ms$	13.6
^{8}B	β^+	$1.11\,s$	18.0
^{6}He	β^-	$1.16\,s$	3.51
^{8}Li	β^-	$1.21\,s$	16.0
^{11}Be	β^-	$19.9\,s$	11.5
^{10}C	β^+	$27.8\,s$	3.65
^{11}C	β^+	$29.4\,min$	1.98

Table 6.1: List of cosmogenic isotopes expected to be produced by muons in organic scintillators in measurable rates.

analysis is concluded with the comparison to results from the liquid-scintillator experiment Kamland. The figures, descriptions, and results of the analyses on cosmogenic isotopes are part of a Borexino publication on cosmic background [88].

6.1 Theory of Simultaneous Fits

Based on the lifetimes and energy spectra of the respective isotope decays, candidate events are selected via their visible energy E and the time difference Δt to their parent muon. Table 6.1 gives an overview on the decay types, lifetimes, and Q-values of the expected cosmogenic radionuclides. Analyzing a group of radioisotopes, the time gate t_g for the candidate selection is chosen to be sereval times the largest lifetime of the studied radionuclides. As in average every 20 seconds (t_μ) a cosmic muon crosses the *Inner Detector* (ID) of Borexino, the probabilty for cosmogenic isotopes to have more than one preceding muon within the time gate t_g is given by $P = 1 - \exp(-t_\mathrm{g}/t_\mu)$. A time gate of $10\,s$ already features a 40% probability to contain more than one muon. Thus, matching to the parent muon is in general ambiguous, resulting in multiple values of Δt for a given candidate, only one of which will be physically correlated. The distribution in Δt is fit with the function:

$$F(\Delta t) = \sum_i \frac{N_i^t}{\tau_i} e^{-\frac{\Delta t}{\tau_i}} + \frac{N_\mathrm{b}^t}{t_\mathrm{g}} + \frac{N_\mathrm{um}^t}{t_\mathrm{g}} \tag{6.1}$$

For each considered isotope, N_i^t denotes the number of decays in the time profile and τ_i its lifetime. The flat contributions N_{b}^t and N_{um}^t account respectively for uncorrelated background events and for the physically uncorrelated matches mentioned above. The latter is a property of the selected data set and can be calculated.
The given fit function is valid for time scales, which are much shorter than the average run duration of the data set ($\simeq 6\,h$ in Borexino). As can be seen from Table 6.1, this is true for all cosmogenic isotopes but ^{11}C. As will be presented in Section 6.4.7, a distortion of the time profile by run boundary effects can be avoided by a time cut of candidate events relative to the run start.

To disentangle isotopes of similar lifetimes, the Δt profile of the candidate events is fitted simultaneously with the visible energy (E) distribution in an unbinned maximum likelihood fit. The spectral shapes of the respective isotopes are generated with the Geant4 based Borexino Monte Carlo code (see Section 6.3). The spectral fit function $G(E)$ is given by:

$$G(E) = \sum_i N_i^E g_i(E) + N_{\mathrm{b}}^E g_{\mathrm{b}}(E) \tag{6.2}$$

The spectral shapes of the considered isotopes are denoted as $g_i(E)$ and N_i^E is the respective number of decays. The uncorrelated background is addressed with the spectral shape $g_{\mathrm{b}}(E)$ and N_{b}^E is the number of entries. The spectral shape $g_{\mathrm{b}}(E)$ is derived directly from the data, using muon-uncorrelated events.
The unbinned maximum likelihood fit is applied to the visible energy distribution of candidate events occurring within a time interval t_E relative to preceding muons. To enhance the signal-to-noise ratio, t_E is chosen to be in the order of the mean lifetimes of the respective cosmogenic radionuclides. The number of isotope decays in the time and energy fit (N_i^t and N_i^E), as well as the background events (N_{b}^t and N_{b}^E), are related via the known selection cut efficiencies in time and energy.

6.2 Energy Observable: Cluster charge

As the simulation reproduces the full detector response, spectral fits can be performed directly on the observed energy distribution of the candidate events. In Borexino, these physics events are identified as clusters of correlated photon hits on the ID photomultiplier tubes (PMT). As has been presented in Section 3.3.3, the observable charge information of a cluster, scaled to 2000 live PMTs, is well suited as energy estimator in this analysis ($N_{\mathrm{charge}}^{\mathrm{norm}}$). This observable provides a high linearity with the deposited energy, scaling with 500 photo-electrons (p.e.) per MeV of deposited energy in β decays, and features an almost position-independent re-

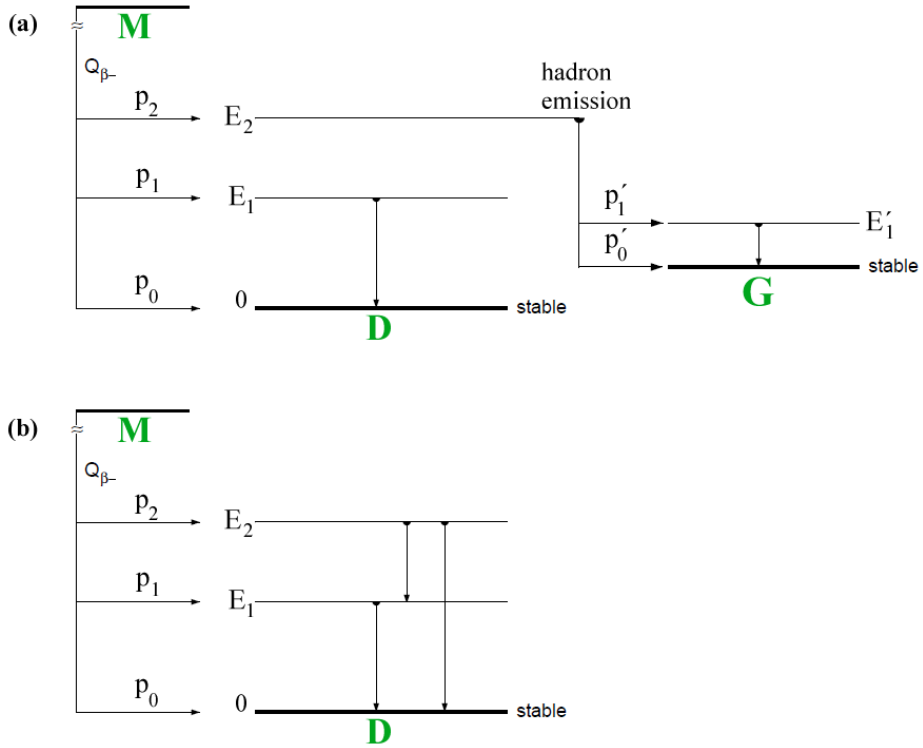

Figure 6.1: Schematics of a sample radioactive decay chain, consisting of mother nucleus M with daughter nuclei D and G (a), as well as the corresponding output of Geant4 to this scenario (b). The paramters p_i and p'_j state the population probability of the nuclear states in the respective deexcitation processes. Nuclear level E_2 is unstable to hadronic deexcitation (i.e. emission of an α, p, and/or n), resulting in the secondary daughter nucleus G. This process is not correctly modeled by Geant4, which instead deexcites the respecitve nuclear level by gamma emission(s).

sponse. For easier reference, this conversion factor is used to state energy selection cuts in the unit $[MeV]$ in the following analyses on cosmogenic isotopes.

6.3 Generation of Spectral Shapes

Fitting the energy distribution of the candidate events according to equation (6.2) requires the spectral shapes of all considered cosmogenic radionuclides $g_i(E)$ and of the uncorrelated background $g_{\mathrm{b}}(E)$. While the latter can be prepared from the data itself by studying muon-uncorrelated events, the cosmogenic decay spectra are derived from Monte Carlo simulations. For this task, the Geant4 based Borexino simulation framework was employed, which is described in Section 3.5 and [89]. For each cosmogenic radionuclide, ten thousands of nuclear decays were simulated homogeneously distributed within the *Fiducial Volume* (FV, $R_{\mathrm{FV}} = 3\,m$). The simulation chain (*G4Bx*, *BxElec*, *Echidna*) models the detector response in terms of physics, electronic processing, and software reconstruction. The final output is a root-file identical in structure to the real data file.

Designed for high energy physics the Geant4 simulation code (version 4.9.2.p02) exhibits an incomplete treatment of the deexcitation mechanisms in light nuclei. Albeit excited nuclear levels can deexcite via γ emission, Geant4 does not include hadronic deexcitations in the radioactive decays, i.e. hadronic particle emission (p, n, α) or nucleus disintegration. Instead, it deexcites these states by an incorrect γ emission.
The cosmogenic isotopes of interest are subject to β-decay from the nuclear ground state, and therefore are not directly affected by this issue. However, the decays can populate excited levels in the daughter nucleus, which in turn might be unstable to hadronic deexcitation. A typical situation is shown in Figure 6.1. Subfigure (a) pictures the true decay scheme in the example, a β-decay of the mother isotope M populating the ground state and two excited states of the daughter nucleus D with the probabilities p_0, p_1, and p_2, respectively. The second excited level of energy E_2 relative to the ground state of D is unstable to hadron deexcitation, generating a third generation nucleus G which in turn can be populated in different nuclear levels and can even produce further deexcitation radiation. Subfigure (b) presents the output of Geant4 to this scenario, neglecting hadronic emission and deexciting the second excited level of nucleus D via γ emission.

Scanning the list of expected cosmogenic isotopes (Table 6.1), the following isotopes are found to feature daughter nuclei with excited states unstable to hadronic deexcitation: ^{12}N, ^{12}B, ^{8}B, ^{8}Li, ^{9}C, ^{8}He, ^{9}Li, and ^{11}Be. The corresponding hadronic deexcitations occur on a time scale of $\simeq 10^{-23}\,s$, much faster than the nanosecond

Particle / Radionuclide	**Atomic Mass** $[u]$	**Atomic Mass** $[GeV/c^2]$
$e^{\pm}$	$0.548580 \cdot 10^{-3}$	$0.510998 \cdot 10^{-3}$
p	1.007276	0.938272
n	1.008665	0.939565
α	4.001506	3.727379
^{5}Li	5.012538	4.669149
^{7}Li	7.016005	6.535367
^{8}Be	8.005305	7.456894
^{11}B	11.009305	10.255103
^{11}Be	11.021662	10.266612
^{12}C	12.000000	11.177929

Table 6.2: Atomic masses of particles and istopes required for the calculations of decay kinematics performed in this thesis. [81]

time resolution of the Borexino experiment. As a result, the visible energy spectra of these cosmogenic isotope decays are superimposed by the subsequent deexcitation radiation of the daughter nuclei as well. A proper simulation of these secondary decay processes is therefore essential in reproducing the correct spectral decay shape as observed by the detector.

Modification of the Simulation Output

Based on the decay schemes of cosmogenic isotopes and their daughter nuclei, erroneous gamma deexcitations are removed and replaced by the proper deexcitation modes. The kinetic energies for the respective particles are retrieved from the Q-value of the decay process. In case of nuclei in the ground state, data is retrieved from literature [81, 90, 91]. For particle emission from excited states, the Q-values are evaluated analytically by equation:

$$D^* \rightarrow \sum_i \Omega_i \qquad Q = m_D + E_D^{\text{exc}} - \sum_i m_{\Omega_i} \tag{6.3}$$

Here, m_D and E_D^{exc} denote the rest mass and excitation energy of nucleus D, and Ω_i the final state particles of masses m_{Ω_i}. In this thesis, calculations performed for the respective cosmogenic radionuclides ignore the binding energies of orbital electrons. Table 6.2 presents the atomic masses of the cosmogenic radionuclides and daughter nuclei of interest, as well as of the respective emission particles

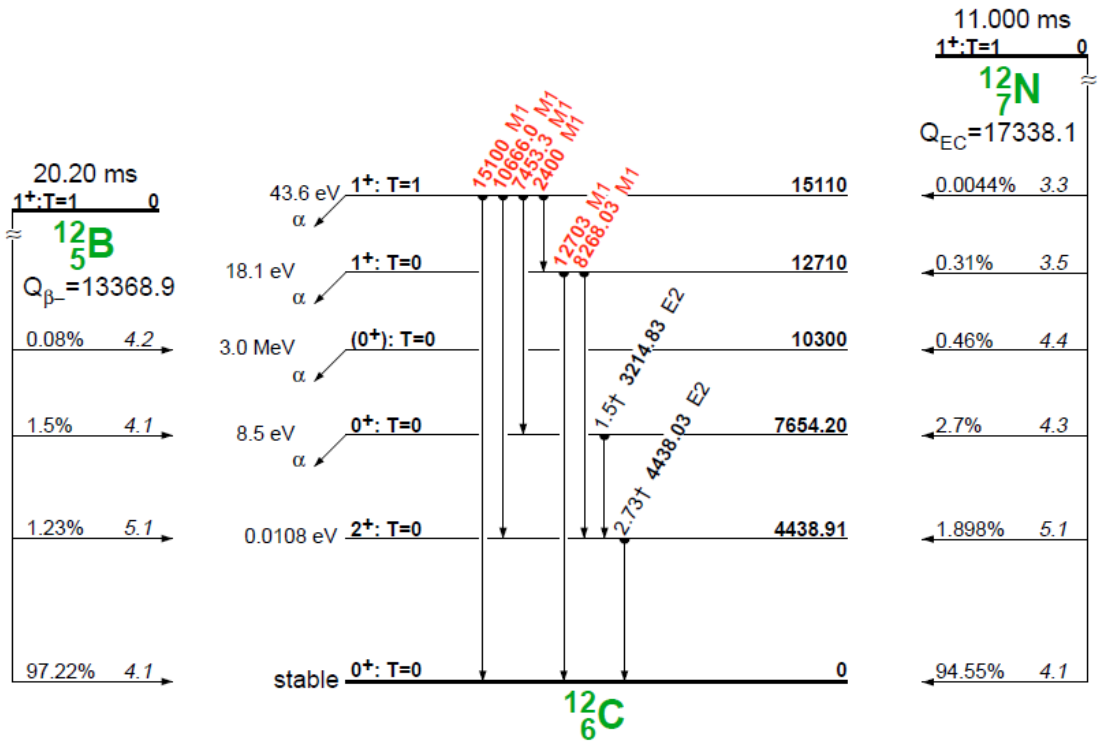

Figure 6.2: Decay scheme of ^{12}B and ^{12}N according to [90]. The γ transition of the excited ^{12}C level 7654.20 keV to 4438.91 keV is suppressed with respect to the α-emission channel [91].

(electron, proton, neutron, and alpha). In the following, the modifications of the decay chains of the isotopes ^{12}N, ^{12}B, ^{8}B, ^{8}Li, ^{9}C, ^{8}He, ^{9}Li, and ^{11}Be are presented.

^{12}N and ^{12}B

Both the β^+-decay of ^{12}N and the β^--decay of ^{12}B populate nuclear levels of the ^{12}C daughter nuclide, as shown in Figure 6.2. Only γ emission ($E_\gamma = 4438.03\,keV$) in the transition of the first excited ^{12}C level to the ground state is expected according to [91]. Higher ^{12}C levels deexcite mainly via α emission to ^{8}Be, of which the second excited ^{12}C level (7654.20 keV) is the one most populated by the decays of ^{12}N and ^{12}B [90]. The corresponding probabilities are 2.7% and 1.5% in ^{12}N decays and ^{12}B decays, respectively. After the α emission, the ^{8}Be daughter nucleus almost instantly ($\Delta E = 6.8\,eV \simeq 10^{-15}\,s$) disintegrates in two α's. The effective 3α-disintegration of ^{12}C can be written as:

$$^{12}\mathrm{C}^* \rightarrow {}^{8}\mathrm{Be} + \alpha \rightarrow 3\alpha \tag{6.4}$$

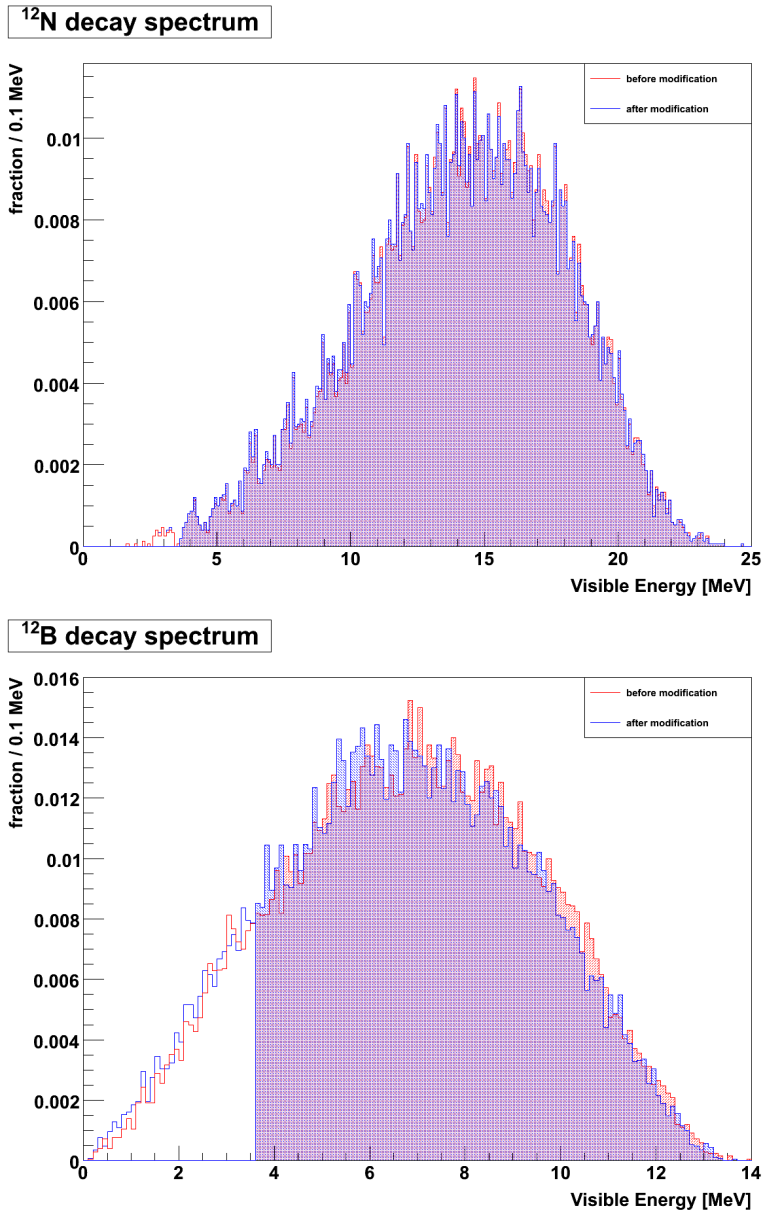

Figure 6.3: Simulated (normalized) visible energy response of the decay chains of the cosmogenic isotopes ^{12}N (top plot) and ^{12}B (bottom plot). The color coded spectra present the Borexino Monte Carlo output before (red) and after (blue) the modifications of the decay chains. The start of the shaded areas indicates the energy threshold ($3.6\,MeV$) of the respective analysis in Sec. 6.4.1.

The α emission of the excited ^{12}C levels, as well as the ^{8}Be 2α-disintegration are not present in Geant4. As has been described, Geant4 deexcites the higher ^{12}C

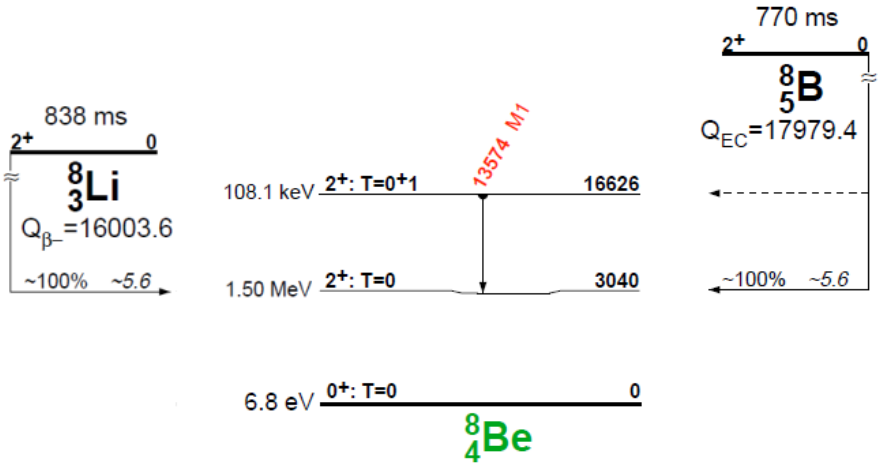

Figure 6.4: Decay scheme of ^{8}B and ^{8}Li according to [90].

levels by γ emission instead.
In this thesis, the erroneous γ emissions are removed and replaced by alpha particle emission. Neglecting the sub-percent populated excitation levels, only the alpha disintegration of level 7654.20 keV (E_D^{exc}) has to be considered. The corresponding Q-value is calculated to 0.38 MeV based on equation (6.3). As has been described in Section 3.3.3, alpha particles produce significantly less light than electrons of the same energy due to quenching effects. Using Equations (3.4) and (3.7) of Section 3.3.3, a maximum visible light of 20 keV equivalence is expected for the three α's. With an energy threshold of 3.6 MeV in the ^{12}N and ^{12}B analysis, the additional energy deposition of the ^{12}C 3α-disintegration is negligible. Figure 6.3 presents the simulated energy distributions for ^{12}N and ^{12}B before and after the decay chain modifications.

^{8}B and ^{8}Li

With a probability of almost 100% the 3040 keV excited state of ^{8}Be is populated in the β^{+}-decay of ^{8}B and β^{-}-decay of ^{8}Li [90], which in turn disintegrates in two α's (see Figure 6.4). The Monte Carlo simulation of the corresponding decay spectra suffers from 2 effects:

- Overpopulation of ^{8}Be nuclear level 16626 keV:
  While expected to be populated by a sub-percent fraction of all ^{8}B decays [90, 91], this level contains 12% of all simulated decays. Furthermore, Geant4 deexcites this level via γ radiation.

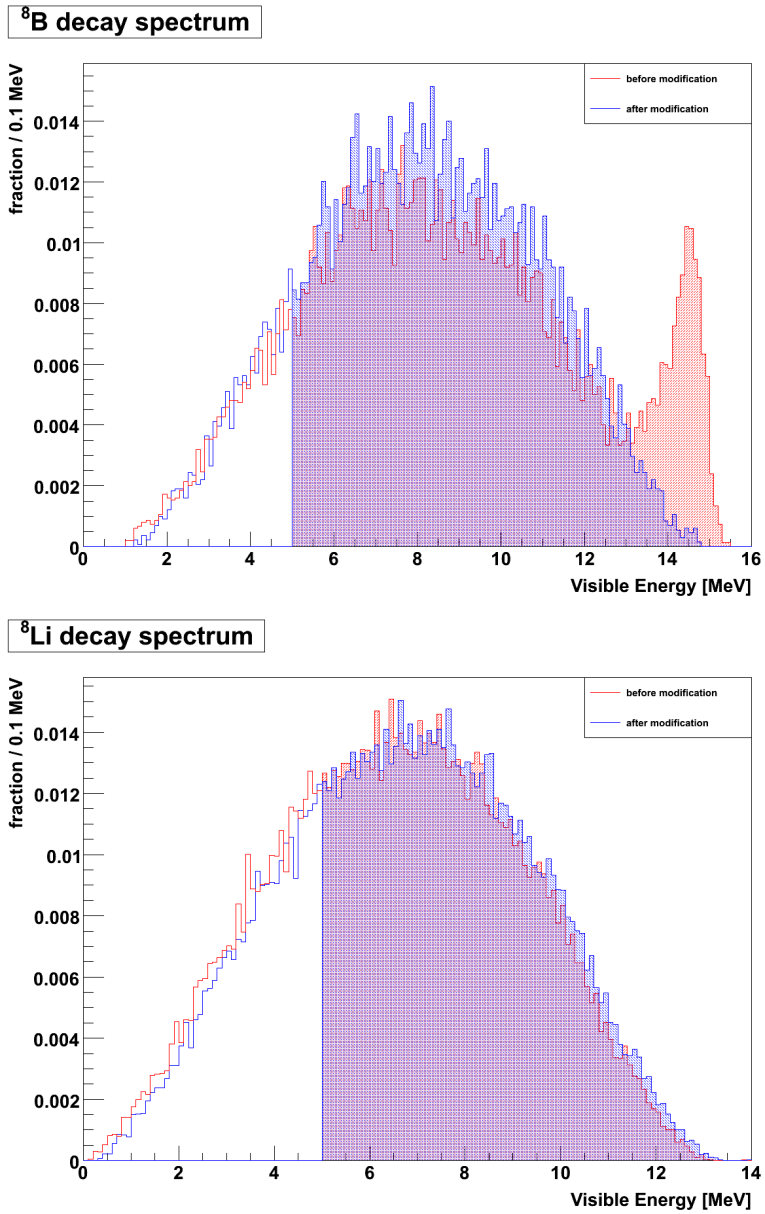

Figure 6.5: Simulated (normalized) visible energy response of the decay chains of the cosmogenic isotopes ^{8}B (top plot) and ^{8}Li (bottom plot). The color coded spectra present the Borexino Monte Carlo output before (red) and after (blue) the modifications of the decay chains. The start of the shaded areas indicates the energy threshold ($5\,MeV$) of the respective analysis in Sec. 6.4.3.

- Missing ^{8}Be 2α-disintegration:
  The decays of ^{8}B and ^{8}Li lead to the $3040\,keV$ excited ^{8}Be state, which

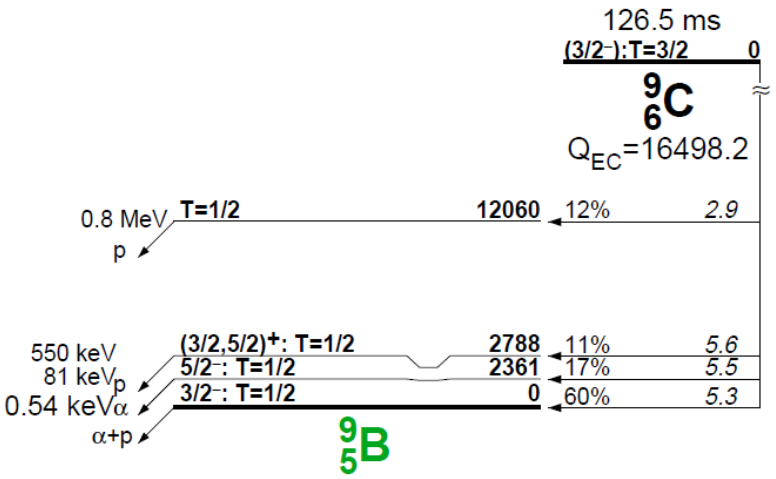

Figure 6.6: Decay scheme of ^{9}C according to [90].

disintegrates in two α's. The isotope ^{8}Be is not a bound nuclear state and features a positive binding energy of 91.8 keV [91], which results in a total α energy of 3.13 MeV. In this two-body process, the α's receive the same amount of kinetic energy, i.e. 1.565 MeV. Taking the α-quenching into account (Equ. (3.4) and (3.7), Sec. 3.3.3), a visible energy deposition of $\simeq$170 keV is expected, shifting the total energy spectrum of the decay chain. As has been pointed out before, Geant4 does not treat the 2α-disintegration of ^{8}Be.

The impact of removing the overpopulated level, and including the 2α-disintegration of ^{8}Be on the energy distributions of ^{8}B and ^{8}Li is shown in Figure 6.5. The additional energy of the two alphas (each E_α = 1.565 MeV) is quenched to an electron-equivalent energy deposition of $\simeq$170 keV, resulting in an energy shift of the distributions.

^{9}C

The cosmogenic radionuclide ^{9}C decays via β^+ emission to the isotope ^{9}B. As can be seen in the decay scheme presented in Figure 6.6, all nuclear levels of ^{9}B are subject to nuclear disintegration via the decay modes:

$$^{9}\mathrm{B} \rightarrow {}^{5}\mathrm{Li} + \alpha \rightarrow 2\alpha + p \tag{6.5}$$

$$^{9}\mathrm{B} \rightarrow {}^{8}\mathrm{Be} + p \rightarrow 2\alpha + p \tag{6.6}$$

Depending on the deexcitation mode, the total energy of the nucleus disintegration is shared differently between the two α particles and the proton. Geant4

^{9}B nuclear level energy [keV]	population probability [%]	hadronic decay mode	Q-value [keV]	final state particles	mean kinetic energies [keV]
0	60	$^9\mathrm{B} \rightarrow {}^8\mathrm{Be} + p$	185.1	p	164.4
		$^8\mathrm{Be} \rightarrow 2\alpha$	91.8	α	56.2
				α	56.2
2361	17	$^9\mathrm{B}^* \rightarrow {}^5\mathrm{Li} + \alpha$	672	α	374
		$^5\mathrm{Li} \rightarrow \alpha + p$	1690	α	578
				p	1410
2788	11	$^9\mathrm{B}^* \rightarrow {}^8\mathrm{Be} + p$	2935.1	p	2601.1
		$^8\mathrm{Be} \rightarrow 2\alpha$	91.8	α	209.9
				α	209.9
12060	12	$^9\mathrm{B}^* \rightarrow {}^8\mathrm{Be} + p$	12375	p	10992
		$^8\mathrm{Be} \rightarrow 2\alpha$	91.8	α	737
				α	737

Table 6.3: Decay modes and kinetic energies of the final state particles in the ^{9}C decay chain (see Figure 6.6). The nuclear level energies are given relative to the ^{9}C ground state. Data on nuclear levels, population probabilities, and Q-values have been taken from [90, 91]. The recoil energy of the nucleus was taken into account in the calculation of the kinetic energies (given in laboratory frame).

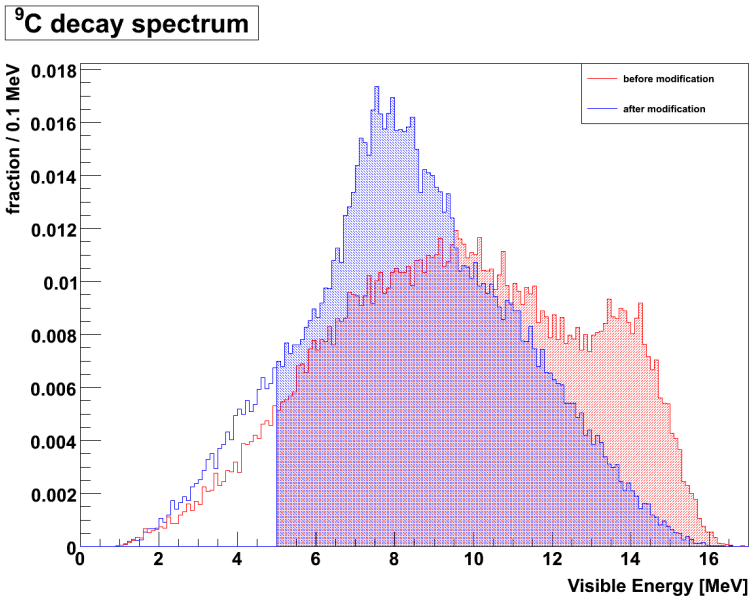

Figure 6.7: Simulated (normalized) visible energy response of the ^{9}C decay chain. The color coded spectra present the Borexino Monte Carlo output before (red) and after (blue) the modifications of the decay chains. The start of the shaded areas indicates the energy threshold ($5\,MeV$) of the respective analysis in Sec. 6.4.4.

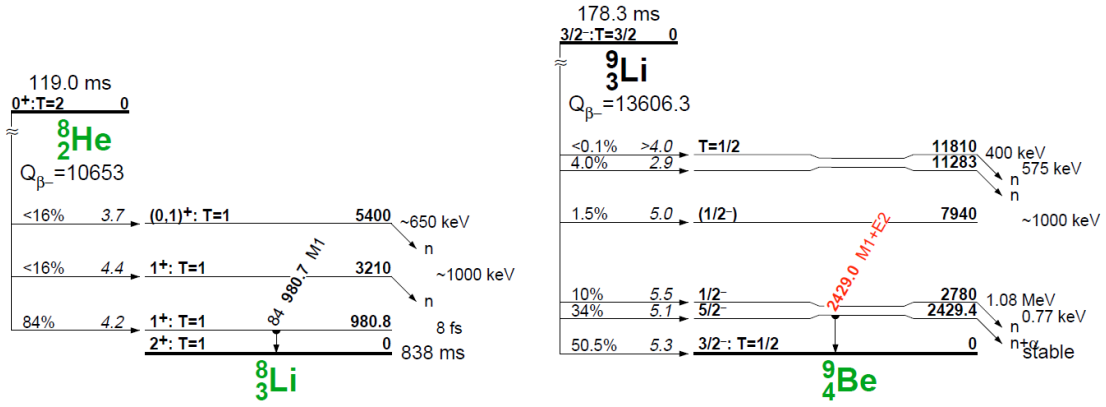

Figure 6.8: Decay schemes of ^{8}He and ^{9}Li according to [90].

however deexcites these levels via γ emission.
Based on nuclear data from [90, 91] and the masses of the participating particles [81] (Table 6.2), the Q-values of the respective hadronic deexcitations were calculated. The kinetic energies of final state particles were evaluated applying the laws of classical Newtonian mechanics. Table 6.3 gives an overview on the Q-values of the hadronic deexcitations, as well as the mean kinetic energies of the corresponding final state particles. Figure 6.7 presents the results of the Monte Carlo simulation before and after replacing erroneous γ emissions by hadronic emissions.

^{8}He and ^{9}Li

The isotopes ^{8}He and ^{9}Li feature daughter nuclides (i.e. ^{8}Li and ^{9}Be) with nuclear levels unstable to neutron (and nα) emission. These levels are populated in 16% and 49.5% by the β^- decays of ^{8}He and ^{9}Li, respectively (see Figure 6.8) [90]. The consequent hadronic deexcitation of these excited levels is not covered by Geant4. However, as main background for the analysis of geo- and reactor-antineutrinos (published in [34]), these isotopes have been fixed by the Borexino collaboration in the past. In this thesis, the already existing Borexino Monte Carlo module for ^{8}He and ^{9}Li decays is used for simulating the corresponding decay spectra. Figures 6.9 and 6.10 present the visible energy spectra for the βn branches and the full decay chains for both isotopes. For comparison, also the standard Geant4 output (i.e. without running the dedicated Borexino module) is shown in red color.

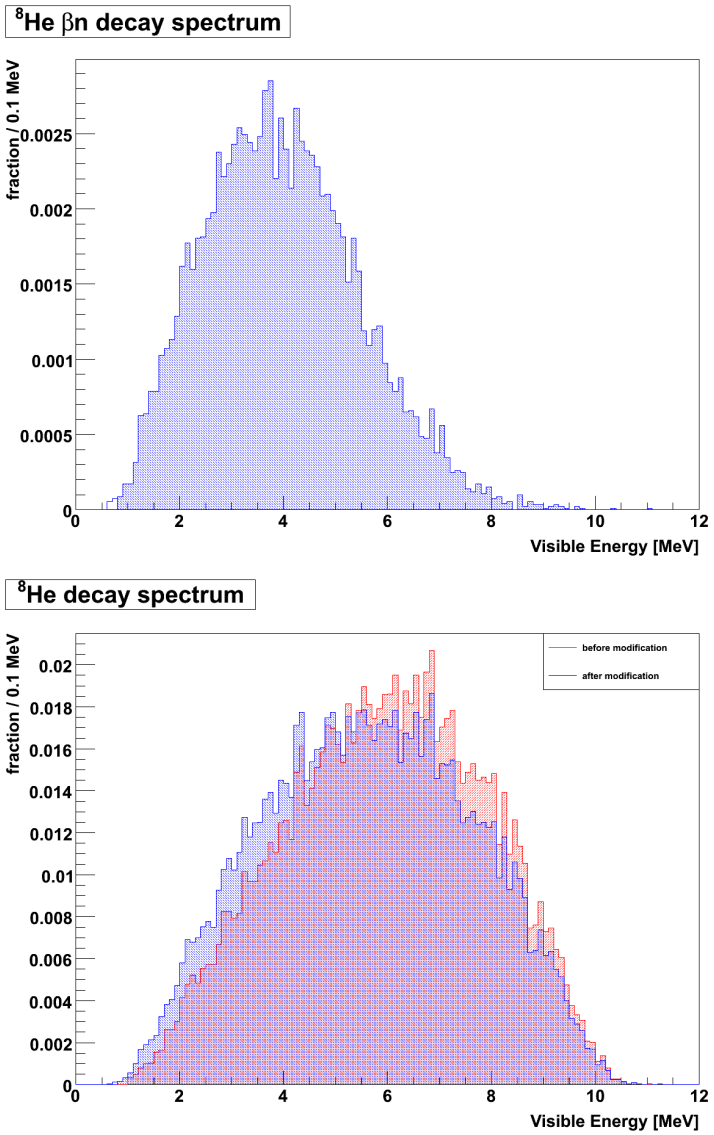

Figure 6.9: Simulated (normalized) visible energy response of the decay chain of the cosmogenic isotope ^{8}He. The top plot presents the visible energy spectrum of ^{8}He β^--decays featuring an additional neutron emission by the daughter nucleus ^{8}Li (16% of all β^--decays [90]), while the lower plot gives the spectrum of the full ^{8}He decay chain. The color coded spectra present the simulation output with (blue) and without (red) using the Borexino Monte Carlo module for ^{8}He decays. The start of the shaded areas indicates the energy threshold ($0.8\,MeV$) of the respective analysis in Sec. 6.4.2.

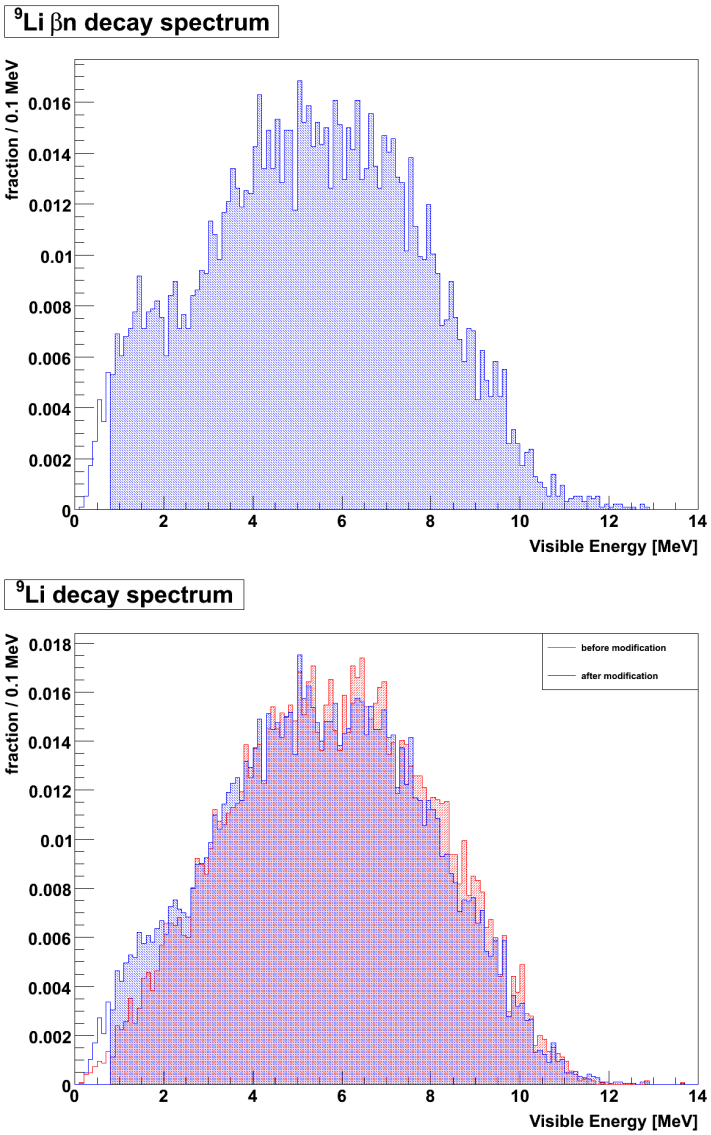

Figure 6.10: Simulated (normalized) visible energy response of the decay chain of the cosmogenic isotope ^{9}Li. The top plot presents the visible energy spectrum of ^{9}Li β^--decays featuring an additional neutron emission by the daughter nucleus ^{9}Be (49.5% of all β^--decays [90]), while the lower plot gives the spectrum of the full ^{9}Li decay chain. The color coded spectra present the simulation output with (blue) and without (red) using the Borexino Monte Carlo module for ^{9}Li decays. The start of the shaded areas indicates the energy threshold ($0.8\,MeV$) of the respective analysis in Sec. 6.4.2.

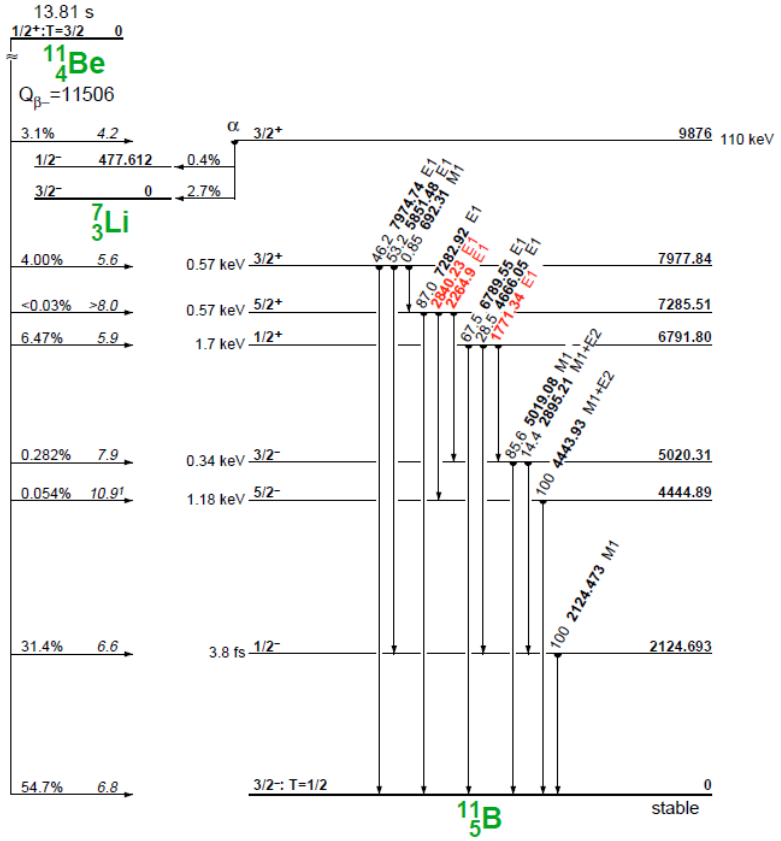

Figure 6.11: Decay scheme of ^{11}Be according to [90].

hadronic decay mode	probability [%]	Q-value [keV]	final state particles	kinetic energies [keV]
$^{11}\mathrm{B}^* \rightarrow {}^{7}\mathrm{Li} + \alpha$	87.1	1209	α ^{7}Li	790 419
$^{11}\mathrm{B}^* \rightarrow {}^{7}\mathrm{Li}^* + \alpha$ $^{7}\mathrm{Li}^* \rightarrow {}^{7}\mathrm{Li} + \gamma$	12.9	732 477	α γ ^{7}Li	478 477 254

Table 6.4: Decay modes and kinetic energies of the final state particles of the 9873 excited ^{11}B nuclear level (see Figure 6.11). Data on nuclear levels, population probabilities, and Q-values have been taken from [90, 91]. The recoil energy of the nucleus was taken into account in the calculation of the kinetic energies (given in laboratory frame).

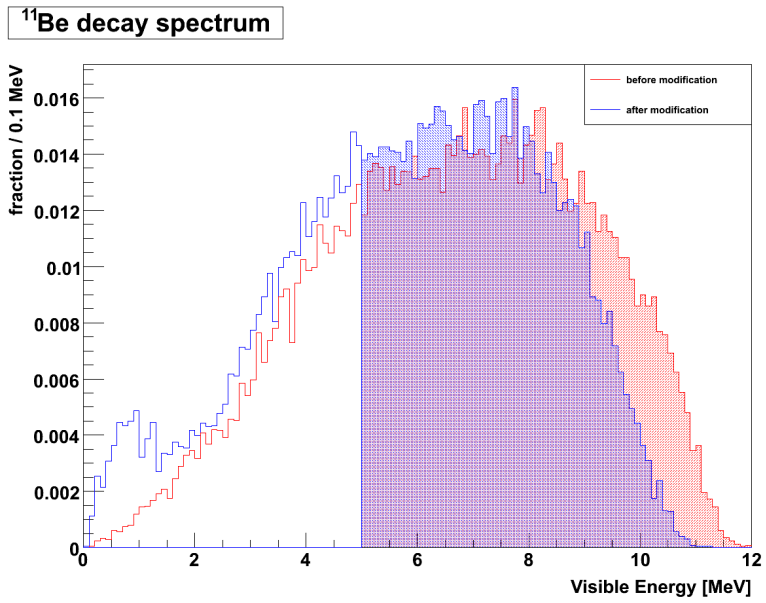

Figure 6.12: Simulated (normalized) visible energy response of the ^{11}Be decay chain. The color coded spectra present the Borexino Monte Carlo output before (red) and after (blue) the modifications of the decay chains. The start of the shaded areas indicates the energy threshold ($5\,MeV$) of the respective analysis in Sec. 6.4.5.

^{11}Be

In 3.1% of the β^--decays of ^{11}Be, the α-emitting 9876 keV nuclear level of ^{11}B is populated [90]. With a fraction of 13%, the α emission leads to the 477.6 keV excited level of ^{7}Li which in turn deexcites via γ emission. In the remaining 87%, the ground state of ^{7}Li is directly reached in the α emission. In the Monte Carlo however, the α emission is not treated, resulting in a multitude of γ emissions in the deexcitation of the highly excited ^{11}B level.
Table 6.4 gives an overview on the branching ratios, Q-values and calculated mean kinetic energies of the final state particles (α, γ, and ^{7}Li) [90, 91]. For the calculations, the kinematic laws of Special Relativity were employed. Figure 6.12 shows the results of taking the missing hadronic decay branches into account.

6.4 Cosmogenic Production Rates and Yields

Based on the fit approach outlined in Section 6.1, the distributions in visible energy (E) and time relative to preceding muons (Δt) are used in a simultaneous fit to disentangle and measure the number of radioactive isotopes produced by cosmic muons in Borexino. The energy spectra of the respective decay chains were prepared with the Borexino Monte Carlo code, which was modified for several cosmogenic isotopes to cover hadronic deexcitations, as described in Section 6.3. As most of the cosmogenic radionuclides are expected to be of very low rate, standard cuts are applied to reduce accidental coincidences: muons are rejected by means of the *Outer Detector* (OD) *Muon Trigger Board* (MTB) and the *Inner Detector* (ID) pulse shape flag (so-called *Inner Detector Flag* (IDF)), as described in Section 4.1. The effect of the pulse shape selection criteria on the spectral shape of the respective radioactive decays is taken into account in the Monte Carlo energy spectra generated for this analysis. The cosmogenic production rates and yields are calculated according to:

$$\begin{aligned} R_i &= \frac{N_i}{V \cdot \rho_{\mathrm{PC}} \cdot t_{\mathrm{L}}} \cdot \frac{1}{\varepsilon_E \cdot \varepsilon_{\Delta t} \cdot \varepsilon_{\mathrm{MTB}}} \\ Y_i &= \frac{N_i}{N_\mu \cdot \langle l_\mu \rangle \cdot \rho_{\mathrm{PC}}} \cdot \frac{1}{\varepsilon_E \cdot \varepsilon_{\Delta t}} \end{aligned} \tag{6.7}$$

Here, N_i states the number of decays of the isotope i, as retrieved from the simultaneous fit. The variables ε_E and $\varepsilon_{\Delta t}$ denote the know selection cut efficiencies in visible energy and time relative to preceding muons, respectively. As cosmogenic isotopes are identified via the coincidence with their parent muons, tagged by the OD, the muon detection efficiency of $\varepsilon_{\mathrm{MTB}} = 0.9925(2)$ (Sec. 4.1) is taken into account. The number of muons in the data sample, as well as the mean muon path

length through the volume V are given by N_μ and $\langle l_\mu \rangle$. Based on the volume used for the respective analysis, the mean muon path length is calculated according to Equ. (5.23) on page 100. If not stated otherwise, candidate events of cosmogenic isotopes are required to be reconstructed in space within the *Fiducial Volume* (FV, $R_{\mathrm{FV}} = 3\,m$). With a density of $\rho_{\mathrm{PC}} = (0.8802 \pm 0.0004)\,g/cm^3$ [21], this volume corresponds to a mass of $99.6\,t$. The systematic uncertainty in the reconstructed volume at the decay energies of interest is estimated to $\pm 3.8\,t$ [4]. By default, the analyses are based on the same data set used for the neutron yield analysis in Section 5.8; i.e. 559 live days (t_{L}) taken between January 6$^{\mathrm{th}}$ 2008 and February 2$^{\mathrm{nd}}$ 2010.
In the following, the analyses of the muon-induced radioisotopes ^{12}N, ^{12}B, ^{8}He, ^{9}C, ^{9}Li, ^{8}B, ^{6}He, ^{8}Li, ^{11}Be, ^{10}C, and ^{11}C are presented. A list of the respective decay characteristics (decay type, lifetime, and Q-value) are given in Table 6.1 on page 138.

6.4.1 ^{12}N and ^{12}B

Candidate events for the decays of ^{12}N (β^+-emitter, $\tau = 15.9\,ms$, $Q = 17.3\,MeV$) and ^{12}B (β^--emitter, $\tau = 29.1\,ms$, $Q = 13.4\,MeV$) are selected within an energy range $E \in [3.6, 18]\,MeV$ and a time gate $\Delta t \in t_{\mathrm{g}} = [2\,ms, 10\,s]$ to a preceding muon event. The energy distribution is built from events with $\Delta t \in t_E = [2, 60]\,ms$, hereby increasing the signal-to-noise ratio. After each muon, a $2\,ms$ veto is applied to avoid muon-induced secondaries (mainly neutrons), inducing a negligible amount of dead time. Furthermore, decays of the cosmogenic isotopes ^{8}He, ^{9}C, ^{9}Li, ^{8}B, and ^{8}Li are considered as contaminations and fitted alongside ^{12}N and ^{12}B. The upper limit of the time gate t_{g} (i.e. $10\,s$) is driven by the lifetimes of the isotopes ^{8}B ($\tau = 1.11\,s$) and ^{8}Li ($\tau = 1.21\,s$). In addition, a fraction of $(86.2 \pm 0.2)\%$ of all ^{11}Be decays is expected within the selected energy range. However, due to its low production rate and long live time ($\tau = 19.9\,s$), this contribution is estimated to be less than 1% in the time profile and negligible in the energy distribution (see section 6.4.5). The background spectral shape is built from events of $\Delta t > 10\,s$ to avoid accidental coincidences of cosmogenic isotopes. Figure 6.13 presents the simultaneous fit in energy and time. The efficiency of the energy cut is evaluated via the simulated spectral shapes to $\varepsilon(^{12}\mathrm{N}) = (79.3 \pm 0.4)\%$ and $\varepsilon(^{12}\mathrm{B}) = (84.0 \pm 0.3)\%$, with the errors stemming from the uncertainty in the detector energy response. The simultaneous fit yields a rate of $R(^{12}\mathrm{N}) < 0.03\,(d\,100\,t)^{-1}$ at $3\,\sigma$ level, and $R(^{12}\mathrm{B}) = (1.62 \pm 0.07_{\mathrm{stat}} \pm 0.06_{\mathrm{syst}})\,(d\,100\,t)^{-1}$. These translate to production yields of $Y(^{12}\mathrm{N}) < 1.1 \cdot 10^{-7}\,/(\mu \cdot (g/cm^2))$ and $Y(^{12}\mathrm{B}) = (55.6 \pm 2.5_{\mathrm{stat}} \pm 2.1_{\mathrm{syst}}) \cdot 10^{-7}\,/(\mu \cdot (g/cm^2))$.
^{12}B is clearly the dominating cosmogenic isotope for the selected time window ($\Delta t \in [2, 60]\,ms$), constituting $(94.6 \pm 0.3)\%$ of all events. Figure 6.14 shows the

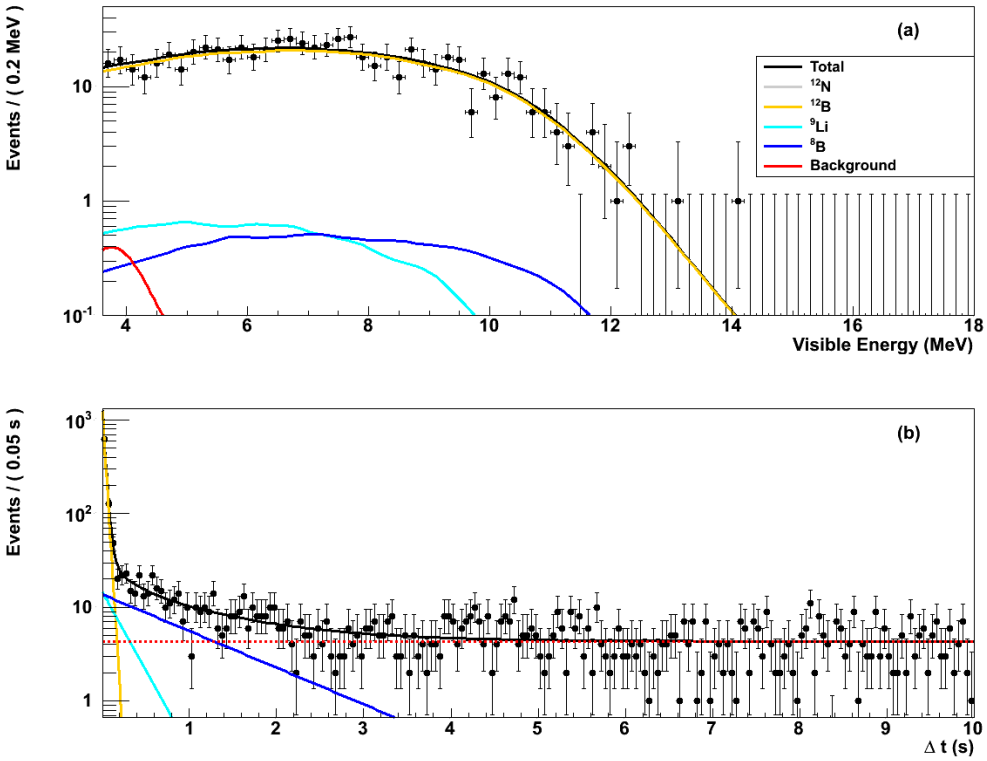

Figure 6.13: Simultaneous fit of the cosmogenic isotopes ^{12}N (grey) and ^{12}B (yellow) in visible energy deposition (a) and decay time relative to preceding muons (b), including the isotopes ^{8}He, ^{9}C, ^{9}Li (cyan), ^{8}B (blue), and ^{8}Li as contaminants. The fit returns only upper limits for the isotopes ^{12}N, ^{8}He, ^{9}C, and ^{8}Li. The goodness of the simultaneous fit is $\chi^2/\mathrm{ndf} = 348/236$.

lateral production profile of this isotope with respect to the reconstructed track of the parent muon.

6.4.2 ^{8}He and ^{9}Li

Both β^--emitters ^{8}He ($\tau = 171.7\,ms$, $Q = 10.7\,MeV$) and ^{9}Li ($\tau = 257.2\,ms$, $Q = 13.6\,MeV$) exhibit daughter nuclei with neutron-unstable excited states. With a 16% branching ratio, the β-decay of ^{8}He populates such a state in ^{8}Li. For ^{9}Li, the branching ratio to a neutron-unstable state in ^{9}Be is 51%. The subsequently emitted neutron is captured mainly on Hydrogen with a mean capture time of $(259.7 \pm 3.3)\,\mu s$ (Section 5.5), emitting a distinctive $2.2\,MeV$ gamma. The triple-coincidence of a muon, a beta-emission and a delayed neutron capture provides a

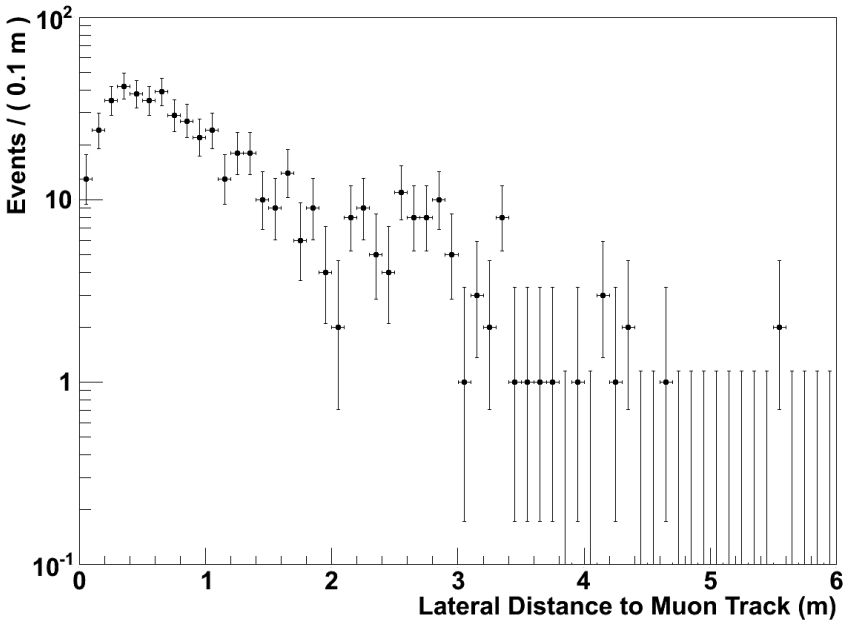

Figure 6.14: Measured lateral production profile of cosmogenic ^{12}B candidates inside the FV with respect to the parent muon track. For improved spatial resolution only muon tracks are considered, which cross the IV at an impact parameter of $R_{\mathrm{I}} < 4\,m$.

very clean signature, thus allowing to utilize the whole mass of the *Inner Vessel* (IV). An enlarged data set of 1366 live days taken between January 6$^{\mathrm{th}}$ 2008 and August 31$^{\mathrm{st}}$ 2012 is used for the analysis, featuring a mean IV volume of $(304.8 \pm 3.2)\,m^3$, corresponding to a mass of $(268.2 \pm 2.8)\,t$. The analysis on the IV volume has been performed analagously to Section 5.7. The requirements for candidate events for the β-emissions are $\Delta t \in [2\,ms, 2\,s]$ and $E \in [0.8, 14]\,MeV$. The energy distribution is taken from events with $\Delta t \in [2\,ms, 1\,s]$. The subsequent neutron capture candidates are selected by $E \in [1.7, 2.6]\,MeV$ and required to be within a radius of $1\,m$ and a time of $1.3\,ms$ to the β-like event. The uncorrelated background spectrum is derived from events with $\Delta t > 1\,s$. Figure 6.15 shows the simultaneous fit in energy and time of ^{8}He and ^{9}Li. The βn selection cut efficiency has been evaluated to $\varepsilon(\beta n) = (79.3 \pm 0.4)\%$ via the Borexino Monte Carlo, using the dedicated module for ^{8}He and ^{9}Li decays. The energy cut efficiencies are estimated to $\varepsilon(^8\mathrm{He}) = (99.49 \pm 0.05)\%$ and $\varepsilon(^9\mathrm{Li}) = (96.99 \pm 0.11)\%$. Via the simultaneous fit, the production rates are measured to $R(^8\mathrm{He}) < 0.042\,(d\,100\,t)^{-1}$ at $3\,\sigma$ level, and $R(^9\mathrm{Li}) = (0.083 \pm 0.009_{\mathrm{stat}} \pm 0.001_{\mathrm{syst}})\,(d\,100\,t)^{-1}$. The corresponding yields

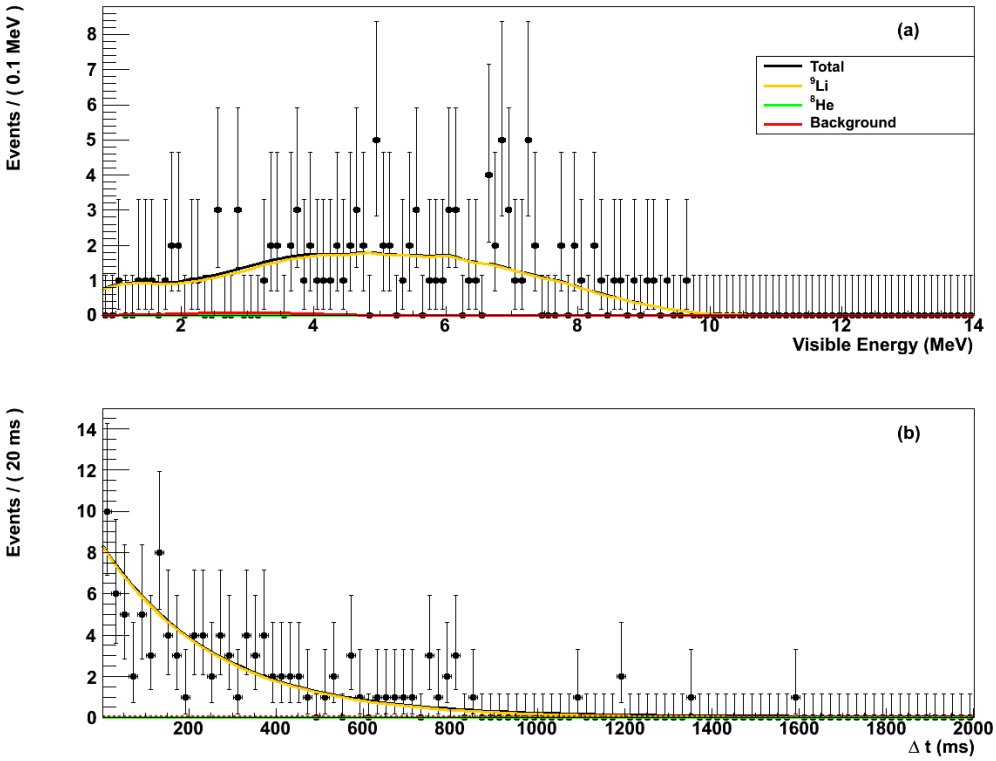

Figure 6.15: Simultaneous fit of the cosmogenic isotopes ^{8}He (green) and ^{9}Li (yellow) in visible energy deposition (a) and decay time relative to preceding muons (b). The fit returns only an upper limit for the isotope ^{8}He. The goodness of the simultaneous fit is $\chi^2/\mathrm{ndf} = 71/98$.

are $Y(^{8}\mathrm{He}) < 1.5 \cdot 10^{-7}\,/(\mu \cdot (g/cm^2))$ and $Y(^{9}\mathrm{Li}) = (2.9 \pm 0.3) \cdot 10^{-7}\,/(\mu \cdot (g/cm^2))$.

6.4.3 ^{8}B, ^{6}He and ^{8}Li

The cosmogenic isotopes ^{8}B (β^{+}-emitter, $\tau = 1.11\,s$, $Q = 18.0\,MeV$), ^{6}He (β^{-}-emitter, $\tau = 1.16\,s$, $Q = 3.51\,MeV$), and ^{8}Li (β^{-}-emitter, $\tau = 1.21\,s$, $Q = 16.0\,MeV$) feature similar lifetimes, yet the significantly lower Q-value of ^{6}He enables a partial disentanglement of these radionuclides via cuts in visible energy and time. To this end, the energy range is separated in two regimes, denoted as ER1 ($E \in [2, 3.2]\,MeV$), respectively ER2 ($E \in [5, 16]\ MeV$). Regime ER1 comprises decays of all three isotopes, whereas in ER2 only ^{8}B and ^{8}Li are present. The two energy intervals are fitted simultaneously with their respective time profiles in a single unbinned maximum likelihood fit. The spectral shape

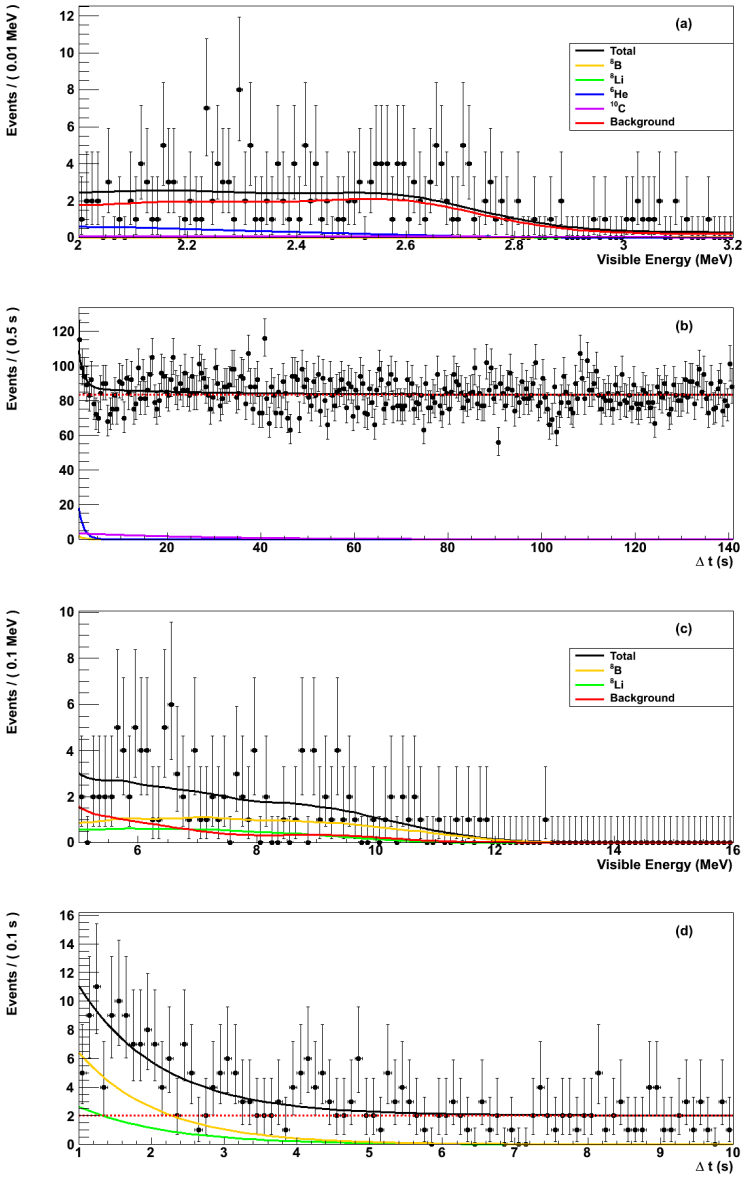

Figure 6.16: Simultaneous fit of the cosmogenic isotopes ^{8}B (yellow), ^{6}He (blue), and ^{8}Li (green) in visible energy deposition (a and c) and decay time relative to preceding muons (b and d) for the energy regimes ER1 ($E \in [2, 3.2]\,MeV$) and ER2 ($E \in [5, 16]\,MeV$). The isotope ^{10}C (violet) is included as contaminant. The goodness of the simultaneous fit is $\chi^2/\mathrm{ndf} = 457/499$.

of uncorrelated background is derived from events with $\Delta t > 140\,s$. Table 6.5 summarizes the energy selection efficiencies and the chosen time gates for the

Energy regime	**Time Gate** $t_g\,[s]$	**Time Gate** $t_E\,[s]$	**Cosmogenic Isotope**	**Lifetime** $[s]$	**Energy Cut Efficiency** [%]
ER1 $E \in [2, 3.2]\,MeV$	$[1, 140]$	$[1, 2]$	^{8}B	1.11	4.0 ± 0.3
			^{6}He	1.16	16.8 ± 0.3
			^{8}Li	1.21	8.1 ± 0.2
			^{10}C	27.8	77.1 ± 0.2
ER2 $E \in [5, 16]\,MeV$	$[1, 10]$	$[1, 3]$	^{8}B	1.11	81.6 ± 0.4
			^{8}Li	1.21	67.5 ± 0.4

Table 6.5: Selection cuts of the candidate events in energy (E) and time (t_g, t_E) for the two regimes ER1 and ER2. In addition, the expected cosmogenic isotopes are given with their lifetimes and energy cut efficiencies. The latter have been evaluated with the simulated spectral shapes described in Section 6.3. For each energy regime, the time profile is built from events within the time interval t_g relative to preceding muons. The upper limit is chosen to fully contain the exponential decays of all contributing cosmogenic isotopes. To enhance the signal-to-noise ratio, the energy distribution is based on events in the time interval t_E. The interval is chosen to be in the order of the mean lifetimes of the respective isotopes. The corresponding distributions and the result of a simultaneous fit in time and energy to both regimes is shown in Figure 6.16.

time and energy distributions in the two energy regimes. Due to the lower energy threshold of ER1, an additional contribution of the cosmogenic isotope ^{10}C (β^+-emitter, $\tau = 27.8\,s$, $Q = 3.65\,MeV$) is included as a free parameter in the fit. To avoid contaminations of short-living cosmogenic isotopes, a $1\,s$ veto after each muon is applied for both regimes, inducing a dead time of 3.6 %. The result of the simultaneous fit is shown in Figure 6.16 for the energy regimes ER1 and ER2, respectively. The isotope production rates are found to be $R(^8\mathrm{B}) = (0.41 \pm 0.16_{\mathrm{stat}} \pm 0.03_{\mathrm{syst}})\,(d\,100\,t)^{-1}$, $R(^6\mathrm{He}) = (1.11 \pm 0.45_{\mathrm{stat}} \pm 0.04_{\mathrm{syst}})\,(d\,100\,t)^{-1}$ and $R(^8\mathrm{Li}) = (0.21 \pm 0.19_{\mathrm{stat}} \pm 0.02_{\mathrm{syst}})\,(d\,100\,t)^{-1}$, the corresponding yields are $Y(^8\mathrm{B}) = (1.4 \pm 0.6_{\mathrm{stat}} \pm 0.1_{\mathrm{syst}}) \cdot 10^{-6}\,/(\mu \cdot (g/cm^2))$, $Y(^6\mathrm{He}) = (3.80 \pm 1.53_{\mathrm{stat}} \pm 0.14_{\mathrm{syst}}) \cdot 10^{-6}\,/(\mu \cdot (g/cm^2))$ and $Y(^8\mathrm{Li}) = (7.1 \pm 6.6_{\mathrm{stat}} \pm 0.7_{\mathrm{syst}}) \cdot 10^{-7}\,/(\mu \cdot (g/cm^2))$.

6.4.4 ^{9}C

Candidate events for the decay of ^{9}C (β^+-emitter, $\tau = 182.5\,ms$, $Q = 16.5\,MeV$) are selected by $E \in [5, 18]\,MeV$ and $\Delta t \in [250\,ms, 10.25\,s]$. The lower energy threshold avoids decays of ^{6}He in the data set. Events occurring for $\Delta t \in [250, 600]\,ms$ are employed in the generation of the energy distribution. After each muon, a $250\,ms$ veto is applied, rejecting contributions from shorter-lived cosmogenic radionuclides and reducing the live time of the data set by 0.9%. The

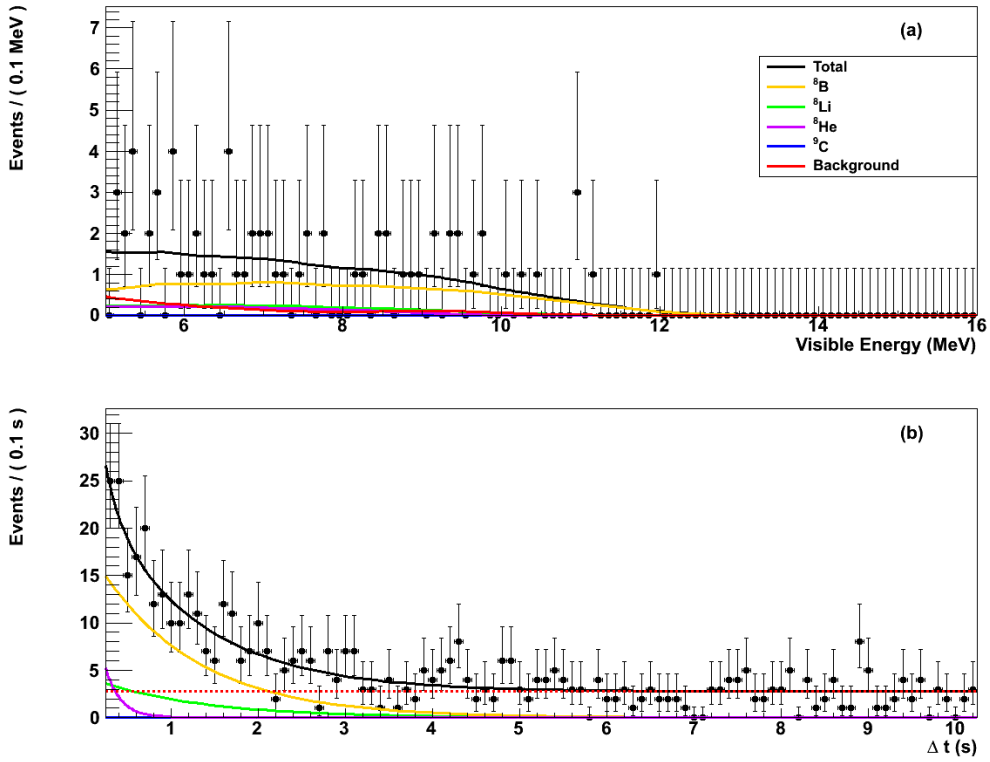

Figure 6.17: Simultaneous fit of the cosmogenic isotope ^{9}C (blue) in visible energy deposition (a) and decay time relative to preceding muons (b), including the isotopes ^{8}He (violet), ^{9}Li, ^{8}B (yellow), and ^{8}Li (green) as contaminants. The fit returns only upper limits for the isotopes ^{9}C and ^{9}Li. The goodness of the simultaneous fit is $\chi^2/\mathrm{ndf} = 218/268$.

isotopes ^{8}He, ^{9}Li, ^{8}B, and ^{8}Li are taken into account as contaminants. Events for $\Delta t > 10.25\,s$ are used to build the spectral shape of uncorrelated background. To confine the rates of ^{8}B and ^{8}Li in the simultaneous fit, the energy distribution of regime ER2 ($E \in [5, 16]\,MeV$, $t_E \in [1, 3]\,s$) prepared in the ^{8}B, ^{6}He, and ^{8}Li analysis is used as additional complementary information (see section 6.4.3).
The best fit result of the time profile and both energy distributions is shown in Figure 6.17. Within the energy range of ^{9}C candidates, a fraction of $\varepsilon(^{9}\mathrm{C}) = (73.4 \pm 0.4)\%$ of all ^{9}C candidates is expected. Correcting for the efficiencies, rate and yield of ^{9}C are determined to an upper limit of $R(^{9}\mathrm{C}) < 0.47\,(d\,100\,t)^{-1}$, and $Y(^{9}\mathrm{C}) < 1.6 \cdot 10^{-6}\,/(\mu \cdot (g/cm^2))$ at $3\,\sigma$ level.

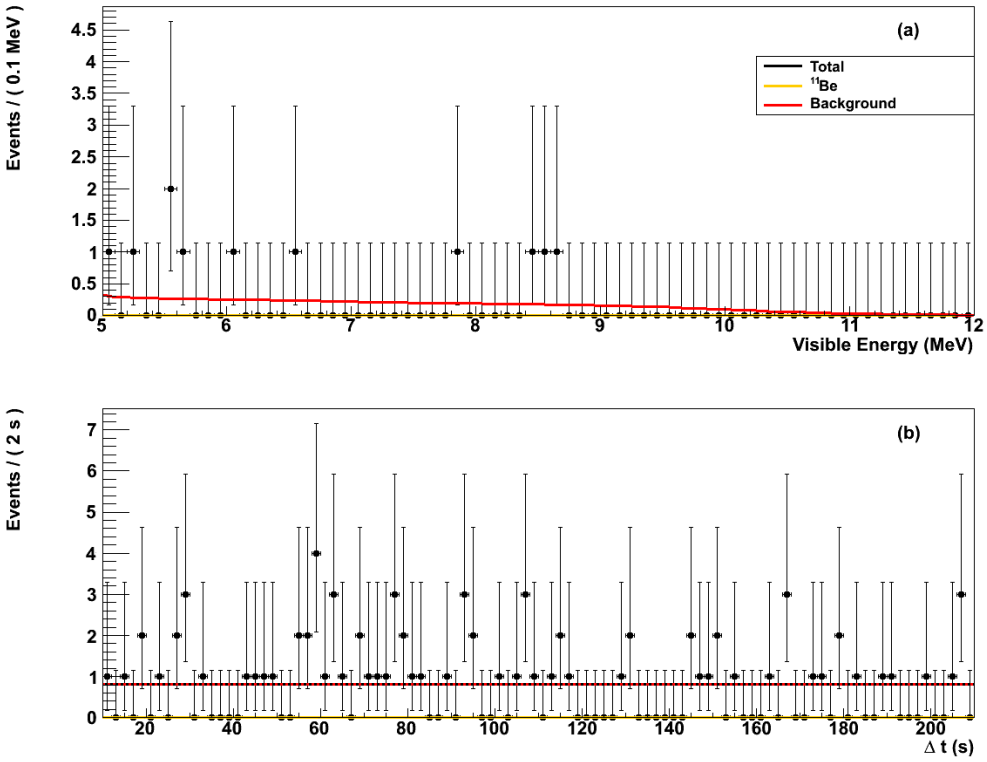

Figure 6.18: Simultaneous fit of the cosmogenic isotope ^{11}Be (yellow) in visible energy deposition (a) and decay time relative to preceding muons (b). The fit returns only an upper limit for the isotope ^{11}Be. The simultaneous fit yields a χ^2/ndf of 30/61. It has to be noted, that the low value of the reduced χ^2 is connected to the low statistics of the data set fitted in the maximum likelihood fit.

6.4.5 ^{11}Be

For the determination of the ^{11}Be (β^--emitter, $\tau = 19.9\,s$, $Q = 11.5\,MeV$) rate, events with $E \in [5, 12]\,MeV$ are chosen, avoiding contaminations from the cosmocenic isotopes ^{10}C and ^{11}C, as well as the external γ-background from ^{208}Tl. To increase the signal-to-noise ratio, the time profile is built for $\Delta t \in [10, 210]\,s$ to a preceding muon whose track is reconstructed within $1.5\,m$ to the ^{11}Be candidate event position. The energy distribution is comprised of events with $\Delta t \in [10, 40]\,s$, applying the same muon track cut. A $10\,s$ veto after each muon rejects the shorter-lived cosmogenic radionuclides, decreasing the lifetime of the data set by 28.4% and leaving ^{11}Be as the only cosmogenic isotope. The background spectral shape is de-

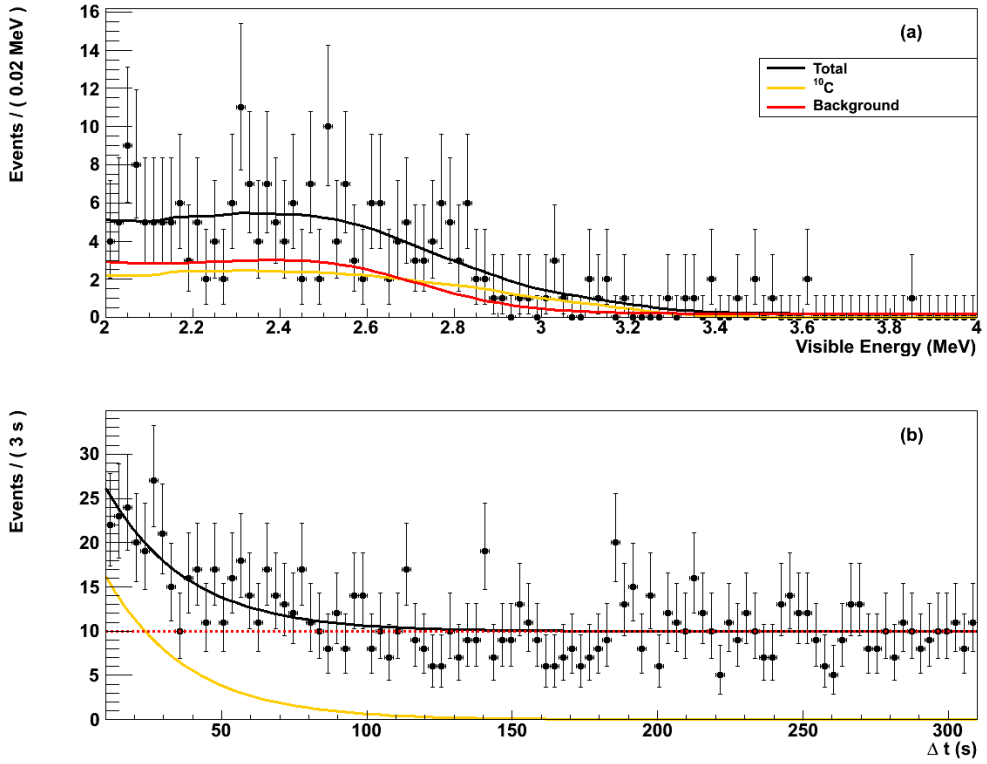

Figure 6.19: Simultaneous fit of the cosmogenic isotope ^{10}C (yellow) in visible energy deposition (a) and decay time relative to preceding muons (b). The goodness of the simultaneous fit is $\chi^2/\text{ndf} = 153/162$.

rived from events satisfying the muon track cut and occurring later than 210 s after the muon. The best fit results are shown in Figure 6.18. The selection efficiency of the muon track cut is estimated to $(63.3 \pm 2.5)\%$ via the time and lateral distribution of cosmogenic ^{12}B to preceding muon tracks. The fraction of decays in the selected visible energy range is calculated to $\varepsilon(^{11}\text{Be}) = (69.3 \pm 0.6)\%$. The isotopic production rate and yield of ^{11}Be are measured to be $R(^{11}\text{Be}) < 0.20\,(d\,100\,t)^{-1}$ and $Y(^{11}\text{Be}) < 7.0 \cdot 10^{-7}\,/(\mu \cdot (g/cm^2))$ at $3\,\sigma$ level.

6.4.6 ^{10}C

The production of ^{10}C (β^+-emitter, $\tau = 27.8\,s$, $Q_{\text{EC}} = 3.65\,MeV$) in muon-initiated spallation processes on ^{12}C is usually accompanied by the emission of at least one free neutron. The neutrons are eventually captured on Hydrogen or Carbon with a mean capture time of $(259.7 \pm 3.3)\,\mu s$ (Sec. 5.5). Applying a three-

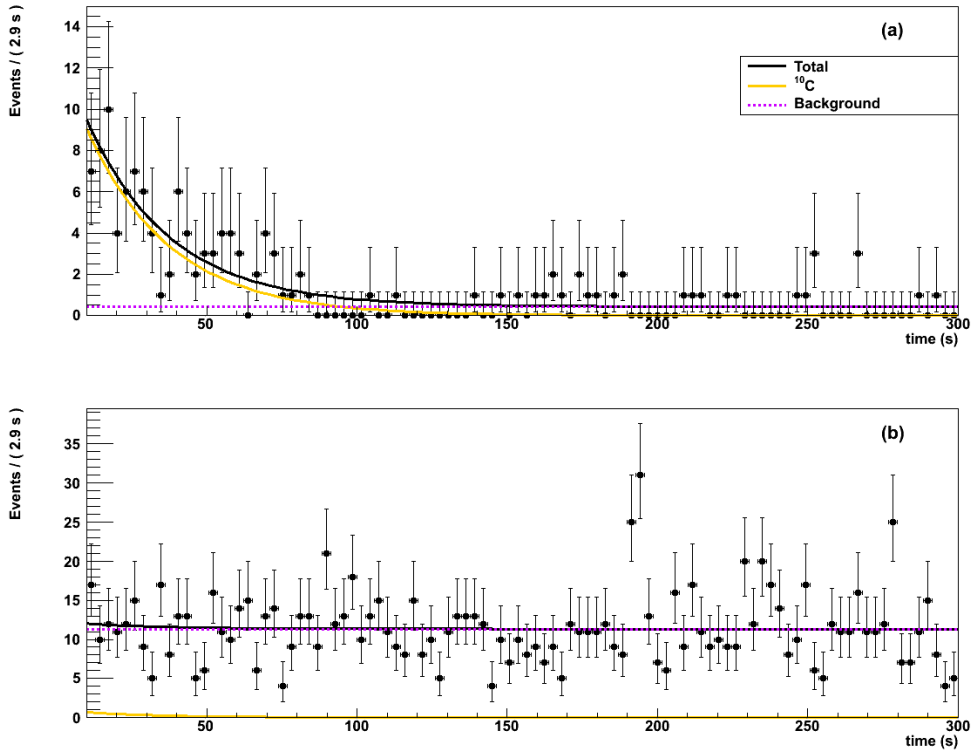

Figure 6.20: Time profiles of ^{10}C candidates relative to preceding muons. The candidate events have to fullfill the selection cuts in time ($[10, 310]\,s$) and lateral distance ($[0, 1]\,m$) to previous muon tracks. The global muon tracking is employed for reconstructing the tracks. Plot (a) presents the time profile for muons featuring at least one accompanying neutron of a visible energy higher than $1.3\,MeV$ (so-called μn-coincidence), while plot (b) shows the profile for the complementary subset. Fitting both time profiles, a fraction of $\varepsilon_n(^{10}\mathrm{C}) = (92.5^{+7.5}_{-20.0})\%$ of all ^{10}C decays is found in correlation with μn-coincidences. The reduced chisquare of the fits is given by $\chi^2/\mathrm{ndf} = 36/48$ and $\chi^2/\mathrm{ndf} = 205/98$ for plot (a) and (b), respectively.

fold coincidence of a muon, at least one subsequent neutron capture, and a ^{10}C decay candidate, accidental background is significantly reduced. Neutron captures of a minimum energy of $1.3\,MeV$ are selected inside the full neutron trigger gate of $[16, 1600]\,\mu s$ after the muon event, while the ^{10}C candidates have to satisfy a cut in visible energy of $[2, 4]\,MeV$ and occur within $[10, 310]\,s$ to a preceding μn-coincidence. The lower energy threshold of $2\,MeV$ avoids a contribution of ^{11}C decays in the data set. The energy distribution of the ^{10}C candidates is built from

events with $\Delta t \in [10, 50]\,s$. Only ^{11}Be contributes as cosmogenic contaminant in this parameter selection. Based on the selection cuts and the additional requirement of a μn-coincidence, the contribution of ^{11}Be is estimated to be less than $6 \cdot 10^{-3}\,\mathrm{cp}(d\,100\,t)$ and taken into account as systematic uncertainty. The spectral shape of uncorrelated background is derived from events at $\Delta t > 310\,s$. The simultaneous fit is depicted in Figure 6.19. The fraction of ^{10}C decays accompanied by a muon in coincidence with at least one detected neutron capture is estimated via a test sample of ^{10}C candidates. Lifting the neutron requirement, ^{10}C candidates are selected by $\Delta t \in [10, 310]\,s$ and a lateral distance of $1\,m$ to a parent muon. The numbers of ^{10}C decays in the subset satisfying the neutron requirements, as well as in the complementary subset, are derived by time profile fits and compared. Figure 6.20 presents the time profile fits of the two subsets, using the Borexino global muon tracking (see Section 4.5) for the muon track reconstruction. The ^{10}C tagging efficiency due to the neutron requirement is evaluated to $\varepsilon_n(^{10}\mathrm{C}) = (92.5^{+7.5}_{-20.0})\%$. Varying the selection cut on the lateral distance to the muon, consistent results are observed. The large uncertainty of the ^{10}C tagging efficiency is caused by the high number of physically uncorrelated matches of ^{10}C candidates with preceding muons, causing a low signal-to-noise ratio in case of matches with muons, which are not accompanied by neutrons (see plot (b) in Figure 6.20). Based on the Monte Carlo, we expect $\varepsilon(^{10}\mathrm{C}) = (79.0 \pm 0.5)\%$ of all ^{10}C decays within the selected energy range. Taking into account these corrections, the ^{10}C rate and yield are determined by the simultaneous fit to $R(^{10}\mathrm{C}) = (0.52 \pm 0.07_{\mathrm{stat}}{}^{+0.11}_{-0.06\mathrm{syst}})\,(\mathrm{d}\,100\,\mathrm{t})^{-1}$ and $Y(^{10}\mathrm{C}) = (1.79 \pm 0.25_{\mathrm{stat}}{}^{+0.38}_{-0.20\mathrm{syst}}) \cdot 10^{-6}\,/(\mu \cdot (g/cm^2))$.

6.4.7 ^{11}C

Like ^{10}C, neutron emission is expected in the muon-induced production of cosmogenic ^{11}C (β^+-emitter, $\tau = 29.4\,\mathrm{min}$, $Q = 1.98\,MeV$). Therefore, an analogous three-fold coincidence of muon, subsequent neutron capture(s), and ^{11}C candidates is applied in the rate determination. Candidates of ^{11}C decays are selected within the energy range of $[1, 2]\,MeV$ and the time gate of $[0.1, 3.6]\,h$ to a preceding muon-neutron coincidence. The events for the energy distribution are selected in the same time interval. As a result of the long mean lifetime of ^{11}C and an average run duration of $\simeq 6\,h$ in Borexino, effects of run boundaries on the time profile are not negligible. To avoid a distortion of the time profile, ^{11}C decays within the first $3.6\,h$ after run start are not considered in the analysis. The restriction reduces the data set to a lifetime of 188 days. For the formation of the background spectral shape, events within $2\,h$ and $4\,m$ to any neutron capture vertex of a μn-coincidence are vetoed. The remaining events are used to derive a spectrum containing only μn-uncorrelated background sources, i.e. non-cosmogenic background, and ^{11}C produced without the detection of a accompanying neutron capture. The latter

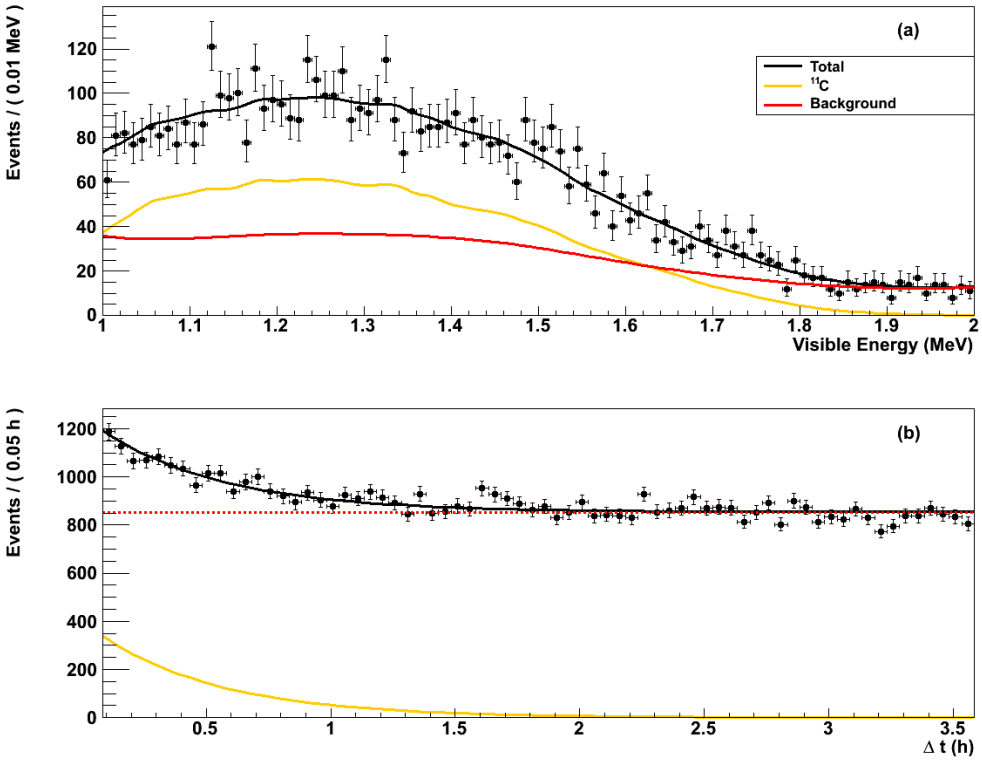

Figure 6.21: Simultaneous fit of the cosmogenic isotope ^{11}C (yellow) in visible energy deposition (a) and decay time relative to preceding muons (b). The goodness of the simultaneous fit is $\chi^2/\mathrm{ndf} = 189/168$.

contribution is the result of the limited neutron detection efficiency in case the detector electronics are saturated by the parent muon event, as well as so-called *invisible* channels. Invisible channels denote all muon-induced production processes, yielding ^{11}C with no free knock-off neutron in the final state [92, 82].
The result of a simultaneous fit in energy and time is shown in Figure 6.21. The fraction of ^{11}C decays correlated with a muon and at least one detected neutron is estimated in the same manner as in the ^{10}C analysis described in section 6.4.6. The selection of the subset of ^{11}C candidates is chosen within $\Delta t \in [0.1, 3.6]\,h$ and a lateral distance of $1\,m$ to a preceding μn-coincidence (employing the global muon tracking). The time profile fits of both subsets is shown in Figure 6.22, and the efficiency for the neutron requirement determined to $\varepsilon_n(^{11}\mathrm{C}) = (86.8 \pm 6.9)\%$. The measured efficiency is consistent with results obtained for other lateral distance selections to preceding μn-coincidences. Like in the ^{10}C analysis, the uncertainty in the efficiency determination is caused by the high number of physically uncorre-

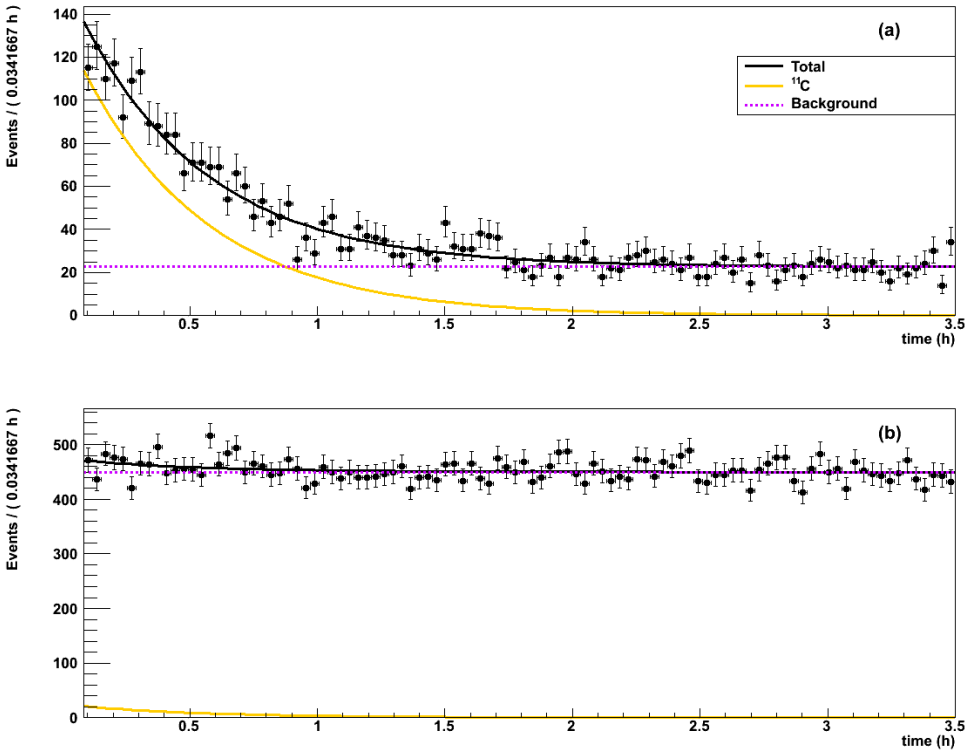

Figure 6.22: Time profiles of ^{11}C candidates relative to preceding muons. The candidate events have to fullfill the selection cuts in time ($[0.1, 3.6]\,h$) and lateral distance ($[0, 1]\,m$) to previous muon tracks. The global muon tracking is employed for reconstructing the tracks. Plot (a) presents the time profile for muons featuring at least one accompanying neutron of a visible energy higher than $1.3\,MeV$ (so-called μn-coincidence), while plot (b) shows the profile for the complementary subset. Fitting both time profiles, a fraction of $\varepsilon_n(^{11}\mathrm{C}) = (86.8 \pm 6.9)\%$ of all ^{11}C decays is found in correlation with μn-coincidences. The reduced chisquare of the fits is given by $\chi^2/\mathrm{ndf} = 106/98$ and $\chi^2/\mathrm{ndf} = 80/98$ for plot (a) and (b), respectively.

lated matches of ^{11}C candidate events with preceding muons (see plot (b) in Figure 6.22). Considering that a fraction of $\varepsilon(^{11}\mathrm{C}) = (92.2 \pm 0.4)\%$ of all decays deposits a visible energy in the selected parameter space, the cosmogenic production rate is found to be $R(^{11}\mathrm{C}) = (25.8 \pm 1.3_{\mathrm{stat}} \pm 3.2_{\mathrm{syst}})\,(\mathrm{d}\,100\,\mathrm{t})^{-1}$) with a corresponding yield of $Y(^{11}\mathrm{C}) = (8.86 \pm 0.45_{\mathrm{stat}} \pm 1.10_{\mathrm{syst}}) \cdot 10^{-5}\,/(\mu \cdot (g/cm^2))$. The rate of ^{11}C decays detected in coincidence with cosmic muons and associated neutrons provides a consistency check with results obtained from spectral fits without the coincidence re-

Cosmogenic Isotope yield $[10^{-7}/(\mu \cdot (g/cm^2))]$	**Kamland**	**Kamland scaled**	**Borexino**
^{12}**N**	1.8 ± 0.4	2.0 ± 0.5	< 1.1
^{12}**B**	42.9 ± 3.3	47.9 ± 4.6	55.6 ± 3.3
^{8}**He**	0.7 ± 0.4	0.8 ± 0.5	< 1.5
^{9}**C**	3.0 ± 1.2	3.4 ± 1.4	< 16
^{9}**Li**	2.2 ± 0.2	2.5 ± 0.3	2.9 ± 0.3
^{8}**B**	8.4 ± 2.4	9.4 ± 2.7	14 ± 6
^{6}**He**	not reported	-	38.0 ± 15.4
^{8}**Li**	12.2 ± 2.6	13.6 ± 3.0	7.1 ± 6.6
^{11}**Be**	1.1 ± 0.2	1.2 ± 0.2	< 7.0
^{10}**C**	16.5 ± 1.9	18.4 ± 2.4	17.9 ± 4.6
^{11}**C**	866 ± 153	966 ± 180	886 ± 115
Cosmogenic Neutrons yield $[10^{-4}/(\mu \cdot (g/cm^2))]$	2.79 ± 0.31	3.11 ± 0.39	3.10 ± 0.11

Table 6.6: Cosmogenic production yields in Borexino and Kamland. The Borexino results have been obtained in this thesis in Sections 5.8 and 6.4, while the Kamland results are taken from [82]. In addition, the Kamland results scaled to the Carbon density and average muon energy of Borexino are shown (see Equ. (6.8)). The uncertainties of the Borexino measurements have been obtained by quadratically summing the respective statistical and systematical errors. Upper boundaries are given in 3σ limits.

quirement. Modeling all signal components in the energy range of $[270, 1600]\,keV$, the ^{11}C rate was found to be $R(^{11}\mathrm{C}) = (28.5 \pm 0.2_{\mathrm{stat}} \pm 0.7_{\mathrm{syst}})\,(\mathrm{d}\,100\,\mathrm{t})^{-1}$ in the precision measurement of the ^{7}Be solar neutrino interaction rate in Borexino [33]. The results of the two analysis approaches are in good agreement.

6.5 Compilation of Results and Comparison to Kamland

The organic-liquid scintillator experiment Kamland published in 2010 a comprehensive list of cosmogenic production yields. Located at the underground site of the Kamioka Observatory at $2700\,m.w.e.$ depth, the Kamioka experiment is subject to a residual muon flux of $(5.37 \pm 0.41)\,m^{-2}h^{-1}$ [82]. This flux is by a factor of $\simeq$4 higher than the residual muon flux of $(1.228 \pm 0.004)\,m^{-2}h^{-1}$ at the Borexino site [63], which is located in the underground laboratory *Laboratory Nazionali del Gran Sasso* at about $3800\,m.w.e.$ depth. However, both sites feature

similar average muon energies, with $\langle E_\mu \rangle_{\mathrm{KL}} = (260 \pm 8)\, GeV$ for Kamland and $\langle E_\mu \rangle_{\mathrm{BX}} = (283 \pm 19)\, GeV$ for Borexino [61, 82]. Due to the similarities of both experiments in design, material composition [93], and muon energy, comparable cosmogenic production yields are expected. Based on data obtained from accelerator experiments at CERN [94], the ratio of the cosmogenic production yields Y between Kamland and Borexino is expected to be

$$\frac{Y_{\mathrm{KL}}}{Y_{\mathrm{BX}}} = \frac{N^{\mathrm{C}}_{\mathrm{KL}}}{N^{\mathrm{C}}_{\mathrm{BX}}} \left(\frac{\langle E_\mu \rangle_{\mathrm{KL}}}{\langle E_\mu \rangle_{\mathrm{BX}}} \right)^{\alpha} = 0.90 \pm 0.05 \tag{6.8}$$

Here, $N^{\mathrm{C}}_{\mathrm{KL}}$ and $N^{\mathrm{C}}_{\mathrm{BX}}$ denote the densities of Carbon nuclides in the respective experiments. Based on the liquid-scintillator compositions in Borexino (pseudocumene: $C_6H_3(CH_3)_3$) and Kamland (20% pseudocumene, 80% dodecane: $C_{12}H_{26}$), the expected Carbon nuclides per $100\, t$ target mass are $N^{\mathrm{C}}_{\mathrm{BX}} = 4.52 \cdot 10^{30}$ and $N^{\mathrm{C}}_{\mathrm{KL}} = 4.30 \cdot 10^{30}$ [82], respectively. The muon energy exponent $\alpha = 0.73 \pm 0.10$ is taken from [94]. Table 6.6 gives the summary of the results for both experiments, as well as the Kamland measurements scaled to the Borexino Carbon density and average muon energy. The fluctuations between the Borexino and the scaled Kamland results are well in agreement with the associated uncertainties. Only noticable outlier is the measurement of cosmogenic ^{12}N. Assuming in first order approximation, that the respective measurement uncertainties are described by gaussian probability distributions, the observed deviation of the production yields corresponds to a $3.4\, \sigma$ effect. The origin of this discrepancy is yet unknown.
The production of cosmogenic neutrons and radioisotopes in Borexino was simulated by the Borexino collaboration, using the FLUKA and Geant4 Monte Carlo codes. An extensive comparison between the simulation results and the measurements performed in this thesis can be found in the Borexino publication on cosmogenic brackgrounds [88].

Chapter 7

Conclusion

Several open questions in the field of astroparticle and particle physics are currently addressed by low-count rate experiments. The direct search for dark matter, the existence of a neutrino-less double-beta decay ($0\nu\beta\beta$), and the measurements of low-energetic neutrinos of various sources are only few to name. To shield these experiments against the huge cosmic flux at the Earth surface ($\simeq 7 \cdot 10^5\, m^{-2}h^{-1}$), they are usually located in underground laboratories providing rock coverages from few hundreds up to two-thousand meters. However, despite the significant reduction in muon flux, residual muons, and the neutrons and radioisotopes they produce in nuclear spallation processes, still constitute a severe background for many underground experiments. The work presented in this thesis focusses on these cosmogenic background signals in the neutrino experiment Borexino, which is located at the *Laboratori Nazionali del Gran Sasso* (LNGS) underground site at a depth of 3800 meters of water equivalent. The identification and spatial reconstruction of cosmogenic signals is crucial for most of Borexino's physics studies. Cosmogenic ^{12}B ($\tau = 15.9\, ms$), ^{11}Be ($\tau = 19.9\, s$), and ^{10}C ($\tau = 27.8\, s$) pose significant backgrounds in the solar ^{8}B-neutrino analysis, while the cosmogenic β/n-emitters ^{8}He ($\tau = 171.7\, ms$) and ^{9}Li ($\tau = 257.2\, ms$) are the main contaminations in the study of anti-neutrinos from the Earth's interior. In particular, cosmogenic ^{11}C ($\tau = 29.4\, min$) is the dominant background in the measurement of solar pep- and CNO-neutrinos. Surpassing the neutrino signal by one order of magnitude, an efficient tagging of this background is detrimental. The muon-induced production of ^{11}C yields a free neutron with a probability of 95% [92]. By identifying and reconstructing the parent muon and the accompanying neutron, correlations between the three particles in time and space can be used to suppress the ^{11}C background in the data.

The studies on muons, neutrons, and cosmogenic radioisotopes performed in this thesis cover signal identification, spatial reconstruction, and the comprehensive determination of production rates and yields.

Cosmic Muons

Cosmic muons crossing the Borexino detector are reconstructed in space via the characterstic light emission in both the water-filled Outer Detector (OD) and the scintillator-filled Inner Detector (ID). While in the OD, light emission is caused only by the Čerenkov effect, tracks crossing the ID also generate light via scintillation. To improve the resolution of the OD muon track reconstruction, a calibration routine was programmed and implemented as a module in the Borexino data reconstruction software *Echidna*. Using the external LED-system, the routine calibrates each of the 208 OD photomultiplier tubes (PMT) in charge and timing response, which are essential inputs for the OD muon tracking. The calibration significantly improves the time resolution from $3.5\,ns$ to $2.1\,ns$, while the charge single-photo-electron spectrum is reproduced in more detail. Furthermore, the calibration allows to identify electronics channels, which deviate in their signal response from the norm. The identification criteria and visualization routines for these problematic channels have been developed and incorporated into the Borexino maintenance framework.
In addition to the calibration code for the OD muon tracking, a muon track reconstruction algorithm was developed for the ID and implemented in *Echidna*. The algorithm is designed for muons crossing the ID, reconstructing the track by identifying the entry and exit point of the muon on the ID surface via a time-of-flight analysis. The reconstruction approach capitalizes on the symmetry in the illumination of the spherical ID surface by the axial light emission along the muon track. By comparing the track reconstruction of Borexino and the adjacent OPERA experiment via a common set of muons induced by the *CERN Neutrinos to Gran Sasso* (CNGS) beam, the angular and lateral resolution of the ID muon tracking is found to be $\sigma_{\text{ang}} = (5.13 \pm 0.25)^\circ$ and $\sigma_{\text{lat}} = (42 \pm 3)\,cm$ for muons crossing the ID. The resolution significantly improves when selecting muons crossing the Inner Vessel (IV, radius of $4.25\,m$) to $\sigma_{\text{ang}} = (2.44 \pm 0.19)^\circ$ and $\sigma_{\text{lat}} = (34 \pm 4)\,cm$. A fraction of 5.2% of all ID crossing cosmic muons are misreconstructed (upward-going), while this reduces to 0.8% for muons crossing the IV.
Based on detection algorithms described in the next section, physics observables of cosmic muons stopping inside Borexino have been investigated. About 1% of all detected muons stop inside the buffer liquid, contained in the ID. The combined capture/decay time of the μ^+ and μ^- is measured to $\tau = (2.06 \pm 0.05)\,\mu s$. The effect of μ^--captures on ^{12}C nuclei is clearly observed in this lifetime measurement. The measured fraction and lifetime of stopped muons are in agreement with the expectations.

Cosmogenic Neutrons

Muons crossing the ID of Borexino can produce neutrons in spallation processes on the Carbon nuclei intrinsic to the organic liquid scintillator. The neutrons thermalize within the first microsecond after production, and are eventually captured with a fraction of 99% on Hydrogen, resulting in the emission of a $2.2\,MeV$ gamma. The capture on Carbon accounts for the remaining 1% of the neutrons, and yields a gamma energy of $4.9\,MeV$. To detect these neutron captures, two neutron search algorithms were developed for the two consecutive data acquisition gates of lengths $16\,\mu s$ and $1.6\,ms$. The neutron capture time in the scintillator pseudocumene is measured to $\tau_n = (259.7 \pm 1.3_{\text{stat}} \pm 2.0_{\text{syst}})\,\mu s$. A slight discrepancy is observed with measurements from an AmBe calibration source in Borexino, yielding a neutron capture time of $(254.3 \pm 1.8)\,\mu s$. This phenomenom is also observed by the Kamland experiment [82], and speculated to be caused by additional neutron captures inside the calibration encapsulation. Evaluating the neutron detection efficiency of Borexino via Monte Carlo simulations and cross-calibration with data acquisition reference systems, a cosmogenic neutron production yield of $(3.10 \pm 0.07_{\text{stat}} \pm 0.08_{\text{syst}}) \cdot 10^{-4}\, n/(\mu \cdot (g/cm^2))$ is found. Taking into account the different scintillator Carbon densities and average muon energies, the corresponding measurement from the Kamland experiment results in a production yield of $(3.11 \pm 0.39)\, n/(\mu \cdot (g/cm^2))$, in good agreement with the Borexino value.
It is observed, that cosmogenic neutrons are mainly produced in high multiplicity events. While in Borexino the majority of neutron-producing muons feature only one neutron, about 50% of all neutrons are produced in muon events of neutron multiplicities larger than 12. However, muon events of these multiplicities account only for a fraction of (5.0 ± 0.1)% of all neutron-producing muons. The rate of neutron-producing muons is measured to $(67.5 \pm 0.4_{\text{stat}} \pm 0.2_{\text{syst}})\, d^{-1}$, each yielding in average $3.61 \pm 0.08_{\text{stat}} \pm 0.09_{\text{syst}}$ associated neutrons.

Cosmogenic Radioisotopes

Besides neutrons, a multitude of radioisotopes can be produced by muon-induced nuclear spallation processes on ^{12}C. The lifetimes of these isotopes range from a few miliseconds ($\tau(^{12}\text{N}) = 15.9\,ms$) up to half an hour ($\tau(^{11}\text{C}) = 29.4\,min$). Based on the correlation with the parent muon and possible accompanying neutrons, the production of all major cosmogenic isotopes has been studied. As several isotopes feature similar lifetimes and overlapping decay spectra, the production rates/yields are derived via simultaneous fits in the energy and time distributions of the candidate events. Based on 559 live days taken between January 6$^{\text{th}}$ 2008 and February

2nd 2010 (part of the Borexino phase I period) the following production yields have been found (in units of $[10^{-7}/(\mu \cdot (g/cm^2))]$):

$Y(^{12}\mathrm{N}) < 1.1$	$Y(^{12}\mathrm{B}) = 55.6 \pm 3.3$	$Y(^{8}\mathrm{He}) < 1.5$
$Y(^{9}\mathrm{C}) < 16$	$Y(^{9}\mathrm{Li}) = 2.9 \pm 0.3$	$Y(^{8}\mathrm{B}) = 14 \pm 6$
$Y(^{6}\mathrm{He}) = 38.0 \pm 15.4$	$Y(^{8}\mathrm{Li}) = 7.1 \pm 6.6$	$Y(^{11}\mathrm{Be}) < 7.0$
$Y(^{10}\mathrm{C}) = 17.9 \pm 4.6$	$Y(^{11}\mathrm{C}) = 886 \pm 115$	

Exploiting the distinctive signature of the βn-decays of the cosmogenic isotopes ^{8}He and ^{9}Li, the corresponding yields were derived with an enlarged data set of 1366 live days taken between January 6th 2008 and August 31st 2012. Except for ^{12}N, the measurements are in agreement with Kamland results scaled to the Borexino Carbon density and mean muon energy. Assuming in first order approximation gaussian uncertainty distributions, the discrepancy in the ^{12}N production yield is observed at a $3.4\,\sigma$ level.

Outlook

After the completion of phase I spanning May 2007 till May 2010, and an extensive calibration and purification campaign in 2010/2011, Borexino is currently in phase II since October 2011. The phase is foreseen to last till December 2015, with its major goal being the improved measurement of the solar pep and CNO-neutrinos. Especially the contribution of the CNO-cycle in the solar fusion is of elementary importance in astrophysics, as it constitutes the main energy production mechanism in heavy stars of at least a few solar masses. While the pep-ν have been measured in phase I with a 20% relative uncertainty, only an upper limit on the CNO-ν flux could be derived. Main limitations on the direct measurement of both fluxes are the cosmogenic background from ^{11}C and the intrinsic contamination of the scintillator by ^{210}Pb and its daughter ^{210}Bi. Utilizing the correlation of ^{11}C in time and space with the parent muon and the knock-off neutron, this background is reduced by $(90 \pm 1)\%$ in the pep/CNO-analysis of phase I data. The efficiency to detect the accompanying neutron is an elementary part of this suppression method. As result of the modified memory reservation in the digital boards, the analysis of phase II data will benefit of an increase in the neutron detection efficiency in the order of 5%. In case of the ^{210}Bi background, a statistical evaluation via the radioactive equilibrium with its daughter nuclide ^{210}Po is foreseen, based on the additional lifetime of 1200 days in phase II. Furthermore, the increased lifetime is essential for a precise measurement of the solar pep and CNO neutrino branches. In addition, all physics analyses in Borexino will benefit from this increased lifetime. In case of the solar ^{8}B-ν analysis, the published analysis was performed on a data set of 488 days. The increased statistics will help to analyze the survival probability of solar neutrinos in the transition region between vacuum- and matter-

dominated neutrino oscillations. Furthermore, it will allow to directly measure the cosmogenic ^{11}Be production rate in Borexino, which has been determined with an upper limit in this thesis. This isotope denotes a relevant background in the ^{8}B-ν analysis, and is currently scaled from Kamland results to Borexino for statistical subtraction.
Though highest in rate, the solar pp-flux is experimentally challenging as the corresponding signal is similar to pile-up events generated by the intrinsic ^{14}C contamination in the scintillator. The research on these pile-up events and potential calibration approaches are in progress. This phase will also improve the statistics of the geo-neutrino analysis from 537.2 live days to 2500. The increase in statistical significance will allow for a measurement of the geo-neutrino rate at a relative precision of about 13%. Besides the solar neutrino programm, the collaboration plans for the investigation of the sterile neutrino oscillation scenario with an artificial external $200 - 400\,PBq$ ^{51}Cr neutrino source.

By the direct measurement of the solar ^{7}Be-, ^{8}B-, and pep-ν in phase I, Borexino has fortified our understanding of the solar fusion processes and the mechanism of the MSW neutrino oscillation effect. Phase II aims for the remaining solar neutrino fluxes (except hep-ν), and an investigation of elementary neutrino properties.
More results can be expected from this unique experiment.

Chapter 8

Appendix

Tables 8.1 - 8.3 contain the physics observables reconstructed by the *Echidna* data processing software for the Borexino *Inner Detector* (ID) and *Outer Dector* (OD). The list is reduced to the variables, which have been used for the software development and data analyses performed in the course of this thesis. In case the *Echidna* reconstruction is applied on Monte Carlo generated data, the true Monte Carlo information of a simulated event is stored in the *mctruth* class. The corresponding variables are listed in Table 8.3. The developed modules for the Outer Detector photomultiplier calibration (*bx_calib_muon_time_alignment* and *bx_calib_muon_charge_peak*) can be tuned by via a configuration file (*echidna.cfg*) in *Echidna*. The description of the tuning parameters and their default values are given in Table 8.4.

Class/Variable	**Description**
event	construct containing all recorded and reconstructed data of the respective DAQ trigger
run, evnum	run and *event* number
is_tracked_global	'*true*' : a global track has been reconstructed
tags[]	array containing physics tags '16' : event on-time with CNGS spill '17' : events following a CNGS spill within $2\,ms$
trigger	class containing trigger information
.btb_inputs	Borexino Trigger Board input '0' : only ID triggered '4' : OD triggered
.trgtype	type of the issued trigger '1' : ID triggered '2' : only OD triggered '8' : ID laser and OD LED calibration '32' : ID/OD pulser calibration '64' : artifical random trigger '128' : neutron trigger (issued after an IDμ[1])
.gpstimes[]	array containing the gpstime of the *event* in $[ns]$
laben	class containing ID data
.empty_boards	number of saturated *Laben* boards $\in [0, 280]$
.trigger_time	trigger time in $[ns]$ relative to internal gray counter
.n_live_pmts, n_invalid_pmts	# of PMTs with (in-)valid timing response
.n_live_charge, n_invalid_charge	# of PMTs with (in-)valid charge response
.n_decoded_hits	# of decoded hits
.n_clusters	# of detected clusters
.n_clusters_muons	# of detected '*muon*' clusters
.is_tracked_tof	'*true*' : an ID track has been reconstructed
.decoded_hits[]	class containing data on each decoded hit
.lg	DAQ channel identification number
.raw_time	raw time in $[ns]$ relative to internal gray counter
.charge	recorded PMT charge

Table 8.1: List 1 of the *Echidna* classes and variables used for the software development and data analyses performed in this thesis.

[1] A muon crossing ID and OD, tagged by *trgtype* '1' and *btb_inputs* '4'.

Class/Variable	Description
laben.clusters[]	class containing data on each cluster
.nhits	# of PMT hits inside the cluster
.nhits_bkg	extrapolated # of background hits inside the cluster
.charge	sum of PMT hit charge inside the cluster
.start_time	start time relative to internal gray counter
.mean_time	mean time relative to the cluster start time
.npeaks	# number of peaks identified in the cluster timing structure (usually 1)
.peak_times[]	array containing the peak times relative to the cluster start time
.position_lngs	class containing data on the position reconstructed by the LNGS algorithm
.x, y, z	coordinates in *x*, *y*, *z*
.dx, dy, dz	corresponding uncertainties
.clusters_muons[]	class containing data on each '*muon*' cluster, identical in structure to *laben.clusters[]*
.track_tof	class containing data on the ID reconstructed muon track
.x1, y1, z1, dx1, dy1, dz1	reconstr. entry point with uncertainties
.x2, y2, z2, dx2, dy2, dz2	reconstr. exit point with uncertainties
.theta, phi, dtheta, dphi	track angles with uncertainties
.impact, dimpact	impact parameter with uncertainty

Table 8.2: List 2 of the *Echidna* classes and variables used for the software development and data analyses performed in this thesis.

Class/Variable	**Description**
muon	class containing OD data
.n_clusters	# of detected clusters
.is_tracked	'*true*' : a OD track has been reconstructed
.track	class containing data on the OD reconstructed muon track, identical in structure as *laben.track_tof*
track_global	class containing data on the global reconstructed muon track
.alpha, beta, gamma, delta	track parametrization variables
.alpha_error, ...	corresponding uncertainties
.chi2	χ^2 of the 3-dimensional straight line fit
.theta, phi, dtheta, dphi	track angles with uncertainties
.impact, dimpact	impact parameter with uncertainty
mctruth	class containing Monte Carlo data
.n_frames	# of interaction frames
.n_daughters	# of particle daughters
.frames[]	class continaining data on each interaction frame
.pdg	particle type according to PDG[2] particle numbering scheme
.n_daughters	# of associated particle daughters
.daughters[]	class containing data on each particle daughter
.num_frame	# of the associated interaction frame
.pdg	particle type (see *mctruth.frames[].pdg*)
.energy	particle energy

Table 8.3: List 3 of the *Echidna* classes and variables used for the software development and data analyses performed in this thesis. Futhermore, in case of Monte Carlo generated data, the variables on the true Monte Carlo information are listed.

[2] *Particle Data Group*

Control Parameter	Default Setting	Description
Common parameters		
minimum_efficiency	0.001	allowed minimum photon statistics relative to the total number of calibration events
large_drift	*true*	'*true*' : calibration data in time and/or charge is discarded in case of large variations
update_threshold	0.6	required minimum fraction of calibrated channels to update database
Time calibration module : *bx_calib_muon_time_alignment*		
time_allowance	10.	half fit range centered around the LED peak, in $[ns]$
max_time_offset	20.	allowed maximum displacement from the average calibration result, in $[ns]$
min_time_rms	0.	allowed minimum root-mean-square of the calibration result, in $[ns]$
max_time_rms	10.	allowed maximum root-mean-square of the calibration result, in $[ns]$
time_drift	10.	allowed drift from the previous calibration result, in $[ns]$
Charge calibration module : *bx_calib_muon_charge_peak*		
time_offset	717	expected offset of the LED peak from gate start, in $[ns]$
time_allowance	40.	half selection-range of hits centered around the LED peak at *time_offset*, in $[ns]$
min_charge_rms	0.	allowed minimum root-mean-square of the calibration result, in $[p.e.]$
max_charge_rms	13.	allowed maximum root-mean-square of the calibration result, in $[p.e.]$
max_charge_offset	30.	allowed maximum displacement from the average calibration result, in $[p.e.]$
charge_drift	5.	allowed drift from the previous calibration result, in $[p.e.]$
chi2_min	0.1	allowed minimum χ^2 of the charge fit, divided by the degrees of freedom
chi2_max	4	allowed minimum χ^2 of the charge fit, divided by the degrees of freedom

Table 8.4: Parameters and default settings of the OD photomultiplier calibration modules, as set in the *Echidna* configuration file. If not stated otherwise, the parameters refer to the individual calibration of a channel. The unit for charge parameters is given in $[p.e.]$, i.e. the number of photo-electrons.

List of Figures

1.1 Solar electron neutrino survival probability 6
1.2 Solar fusion processes 8
1.3 Solar neutrino spectra 10
1.4 Geo-neutrino spectra 11
1.5 Supernova-neutrino luminosity/mean-energy 12

2.1 Schematics of the Borexino experiment 17
2.2 Solar ^{7}Be-neutrino measurement 20
2.3 Solar ^{8}B-neutrino measurement 22
2.4 Solar pep-neutrino measurement 24
2.5 Solar electron neutrino survival probability 24
2.6 Borexino energy spectrum 25
2.7 Geo-neutrino measurement 26
2.8 CNGS-ν speed measurement 28

3.1 Schematics of a photomultiplier tube 32
3.2 Average ETL9351 charge spectrum 33
3.3 ETL9351 time spectra 34

4.1 Muon ID pulse shape discrimination 47
4.2 OD PMT activation profile 49
4.3 OD calibration system 51
4.4 OD timing calibration 53
4.5 OD charge calibration 54
4.6 Impact of the LED calibration 56
4.7 Typical calibration results 57
4.8 Maintenance plots for a problematic OD channel 58

4.9 OD long term stability 60
4.10 Muon light emission and ID illumination 61
4.11 ID entry point reconstruction 63
4.12 ID entry point reconstruction (fit) 64
4.13 Muon tracking symmetry plane 66
4.14 Symmetry plane reconstruction 67
4.15 ID exit point reconstruction 68
4.16 ID exit point reconstruction (fit) 69
4.17 OD muon impact parameter versus number of hits 71
4.18 ID reconstructed muon track 72
4.19 Global muon track 74
4.20 Schematics of the Borexino Outer Detector 76
4.21 Azimuth angle distribution of CNGS-induced muons 77
4.22 Inclination angle distribution of CNGS-induced muons 78
4.23 Angular and lateral resolution of CNGS-induced muons 79
4.24 Inclination and azimuth angle distributions of cosmic muons 82

5.1 Sample muon/neutron trigger hit time distribution 84
5.2 Sample muon trigger hit time distribution 87
5.3 Neutron trigger noise hit time distribution 88
5.4 Sample neutron trigger hit time distribution 90
5.5 Time distribution of physics events inside of muon triggers - 1 . . . 92
5.6 Simulated muon decay energy spectra 95
5.7 Time distribution of physics events inside of muon triggers - 2 . . . 97
5.8 Time distribution of physics events inside of muon triggers - 3 . . . 98
5.9 Vertical muon intensity as a function of the traversed rock coverage 99
5.10 Visible energy distribution of muon decays 101
5.11 Visible energy distribution of neutron capture gammas 102
5.12 Visible energy distribution of physics events inside of neutron triggers 105
5.13 Signals recorded by the PAS and main DAQ after a sample muon . 107
5.14 Pulse height distribution measured by the PAS 108
5.15 Difference in GPS-times between the main DAQ and the PAS . . . 109
5.16 Visible energy distribution of neutron capture candidates detected by both the main DAQ and the PAS 110
5.17 Main DAQ response to the 1.3 MeV threshold 113

5.18 Time profile of the Borexino scintillation light emission 114
5.19 Position reconstruction of neutron capture gammas 115
5.20 Visible energy of neutron capture gammas versus the reconstructed radius 116
5.21 Simulated time profiles of neutron captures on ^{1}H and ^{12}C 118
5.22 Cross-sections of neutron interactions with ^{12}C 119
5.23 Time profiles of physics events inside of neutron triggers 120
5.24 Time profile of the AmBe calibration source events 121
5.25 Visible energy distribution of muon-uncorrelated events inside of neutron triggers 122
5.26 Reconstructed IV volume as a function of time 125
5.27 Level transitions of ^{13}C generated by the thermal neutron capture on ^{12}C 126
5.28 Simulated visible energy response of gammas emitted in the neutron capture on ^{1}H 127
5.29 Simulated visible energy response of gammas emitted in the neutron capture on ^{12}C 128
5.30 Neutron multiplicity distribution of neutron-producing muons . . . 131

6.1 Schematics of a sample radioactive decay chain 140
6.2 Decay scheme of ^{12}B and ^{12}N 143
6.3 Simulated visible energy response of the decay chains of ^{12}N and ^{12}B 144
6.4 Decay scheme of ^{8}B and ^{8}Li 145
6.5 Simulated visible energy response of the decay chains of ^{8}B and ^{8}Li 146
6.6 Decay scheme of ^{9}C 147
6.7 Simulated visible energy response of the ^{9}C decay chain 149
6.8 Decay schemes of ^{8}He and ^{9}Li 150
6.9 Simulated visible energy response of the ^{8}He decay chain 151
6.10 Simulated visible energy response of the ^{9}Li decay chain 152
6.11 Decay scheme of ^{11}Be 153
6.12 Simulated visible energy response of the ^{11}Be decay chain 154
6.13 Simultaneous fit of the isotopes ^{12}N and ^{12}B 157
6.14 Lateral production profile of cosmogenic ^{12}B 158
6.15 Simultaneous fit of the isotopes ^{8}He and ^{9}Li 159
6.16 Simultaneous fit of the isotopes ^{8}B, ^{6}He, and ^{8}Li 160
6.17 Simultaneous fit of the isotope ^{9}C 162

6.18 Simultaneous fit of the isotope ^{11}Be 163
6.19 Simultaneous fit of the isotope ^{10}C 164
6.20 Determination of the ^{10}C μn-coincidence efficiency 165
6.21 Simultaneous fit of the isotope ^{11}C 167
6.22 Determination of the ^{11}C μn-coincidence efficiency 168

List of Tables

1.1 Neutrino oscillation parameters 4
1.2 Solar neutrino fluxes 9

4.1 Muon tag efficiencies 48
4.2 List of angular and lateral muon tracking resolutions 80
4.3 Percentage of misreconstructed (upward-going) muons 81

5.1 List of input variables for the calculation of the neutron capture rate and yield 129

6.1 List of cosmogenic isotopes 138
6.2 Atomic masses of particles and istopes 142
6.3 Decay modes and kinetic energies of the final state particles in the ^{9}C decay chain 148
6.4 Decay modes and kinetic energies of the final state particles of the 9873 excited ^{11}B nuclear level 153
6.5 ^{8}B, ^{6}He, and ^{8}Li analysis: selection cuts of the candidate events in energy and time 161
6.6 Comparison of cosmogenic production yields in Borexino and Kamland 169

8.1 List of *Echidna* variables - 1 178
8.2 List of *Echidna* variables - 2 179
8.3 List of *Echidna* variables - 3 180
8.4 Parameters of the calibration modules 181

Bibliography

[1] C. l. Cowan et al., *Detection of the Free Neutrino: a Confirmation*, Science **124** (July, 1956).

[2] B. T. Cleveland et al., *Measurement of the Solar Electron Neutrino Flux with the Homestake Chlorine Detector*, Astrophysical Journal **496** (1998), no. 1 505.

[3] C. Arpesella et al., *First real time detection of ^{7}Be solar neutrinos by Borexino*, Physics Letters B **658** (2008), no. 4 101 – 108.

[4] G. Bellini et al., *Measurement of the solar ^{8}B neutrino rate with a liquid scintillator target and 3 MeV energy threshold in the Borexino detector*, Phys. Rev. D **82** (2010) 033006. Copyright (2010) by the American Physical Society.

[5] G. Bellini et al., *First Evidence of pep Solar Neutrinos by Direct Detection in Borexino*, Phys. Rev. Lett. **108** (Feb, 2012) 051302. Copyright (2012) by the American Physical Society.

[6] J. N. Bahcall et al., *Are Standard Solar Models Reliable?*, Phys. Rev. Lett. **78** (Jan, 1997) 171–174.

[7] J. N. Bahcall and H. A. Bethe, *Solution of the solar-neutrino problem*, Phys. Rev. Lett. **65** (Oct, 1990) 2233–2235.

[8] Q. R Ahmad et al., *Direct Evidence for Neutrino Flavor Transformation from Neutral-Current Interactions in the Sudbury Neutrino Observatory*, Phys. Rev. Lett. **89** (Jun, 2002) 011301.

[9] K. Nakamura and Particle Data Group, *Review of Particle Physics*, Journal of Physics G: Nuclear and Particle Physics **37** (2010), no. 7A 075021.

[10] Y. Fukuda et al., *Evidence for Oscillation of Atmospheric Neutrinos*, Phys. Rev. Lett. **81** (Aug, 1998) 1562–1567.

[11] K. Eguchi et al., *First Results from KamLAND: Evidence for Reactor Antineutrino Disappearance*, Phys. Rev. Lett. **90** (Jan, 2003) 021802.

[12] J. K. Ahn et al., *Observation of Reactor Electron Antineutrinos Disappearance in the RENO Experiment*, Phys. Rev. Lett. **108** (May, 2012) 191802.

[13] B. Kayser, *Neutrino Mass, Mixing, and Flavor Change*, `arXiv:0804.1497`.

[14] J. Beringer et al. (Particle Data Group) Phys. Rev. D86, 010001 (2012).

[15] L. Wolfenstein, *Neutrino oscillations in matter*, Phys. Rev. **D17** (1978) 2369.

[16] S. P. Mikheyev and A. Y. Smirnov, *Resonant neutrino oscillations in matter*, Prog. Part. Nucl. Phys. **23** (1989) 41–136.

[17] L. Baudis et al., *Limits on the Majorana neutrino mass in the 0.1-eV range*, Phys.Rev.Lett. **83** (1999) 41–44.

[18] C. Weinheimer et al., *High precision measurement of the tritium spectrum near its endpoint and upper limit on the neutrino mass*, Physics Letters B **460** (1999), no. 12 219 – 226.

[19] V. M. Lobashev et al., *Direct search for mass of neutrino and anomaly in the tritium beta-spectrum*, Physics Letters B **460** (1999), no. 12 227 – 235.

[20] S. Hannestad et al., *Cosmological constraints on neutrino plus axion hot dark matter*, Journal of Cosmology and Astroparticle Physics **2007** (2007), no. 08 015.

[21] R. Saldanha, *Precision Measurement of the ^{7}Be Solar Neutrino Interaction Rate in Borexino*, Ph.D.Thesis, Princeton University (2012).

[22] E. G. Adelberger et al., *Solar fusion cross sections. II. The pp chain and CNO cycles*, Rev. Mod. Phys. **83** (Apr, 2011) 195–245. Copyright (2011) by the American Physical Society.

[23] A. M. Serenelli, W. C. Haxton, and C. Peña-Garay, *Solar Models with Accretion. I. Application to the Solar Abundance Problem*, arXiv **743** (2011) 24, [`arXiv:1104.1639`].

[24] N. Grevesse and A. J. Sauval , *Standard solar composition*, Space Science Review **85** (1998) 161.

[25] M. Asplund, N. Grevesse, A. J. Sauval, and P. Scott, *The chemical composition of the Sun*, Annual Review of Astronomy and Astrophysics **47** (2009) 481–522.

[26] T. Araki et al., *Experimental investigation of geologically produced antineutrinos with KamLAND*, Nature **436, 499** (2005).

[27] J. H. Davies and D. R. Davies, *Earth's surface heat flux*, Solid Earth **1** (2010), no. 1 5–24.

[28] M. Wurm et al., *The next-generation liquid-scintillator neutrino observatory LENA*, Astropart.Phys. **35** (2012) 685–732, [arXiv:1104.5620].

[29] T. Fischer et al., *Protoneutron star evolution and the neutrino-driven wind in general relativistic neutrino radiation hydrodynamics simulations*, Astronomy and Astrophysics **517** (2010) A80.

[30] S. Horiuchi, J. F. Beacom, and E. Dwek, *Diffuse supernova neutrino background is detectable in Super-Kamiokande*, Phys. Rev. D **79** (Apr, 2009) 083013.

[31] G. Alimont et al., *The Borexino detector at the Laboratori Nazionali del Gran Sasso*, Nucl. Instrum. Meth. A **600** (2009) 568. Reprinted by permission of Elsevier.

[32] G. Bellini et al., *Muon and cosmogenic neutron detection in Borexino*, Journal of Instrumentation **6** (2011), no. 05 P05005. Reprinted by permission of the American Astronomical Society.

[33] G. Bellini et al., *Precision Measurement of the ^7Be Solar Neutrino Interaction Rate in Borexino*, Phys. Rev. Lett. **107** (Sep, 2011) 141302. Copyright (2011) by the American Physical Society.

[34] G. Bellini et al., *Observation of Geo-Neutrinos*, Phys. Lett. B **687** (2010) 299. Reprinted by permission of Elsevier.

[35] G. Bellini et al., *Absence of a day/night asymmetry in the ^7Be solar neutrino rate in Borexino*, Physics Letters B **707** (2012), no. 1 22 – 26. Reprinted by permission of Elsevier.

[36] B. Aharmim et al., *Low-energy-threshold analysis of the Phase I and Phase II data sets of the Sudbury Neutrino Observatory*, Phys. Rev. C **81** (May, 2010) 055504.

[37] J. P. Cravens et al., *Solar neutrino measurements in Super-Kamiokande-II*, Phys. Rev. D **78** (Aug, 2008) 032002.

[38] O. Smirnov, *private communication*, 2010.

[39] J. B. Birks, *The Theory and Practice of Scintillation Counting*, Pergamon Press, London (1964).

[40] A. Gando et al., *Partial radiogenic heat model for Earth revealed by geoneutrino measurements*, Nature Geoscience **647-651** (2011).

[41] M. Ikeda et al., *Search for Supernova Neutrino Bursts at Super-Kamiokande*, Astrophysical Journal. **669** (2007) 519–524.

[42] N. Y. Agafonova et al., *On-line recognition of supernova neutrino bursts in the LVD*, Astroparticle Physics **28** (2008), no. 6 516 – 522.

[43] R. Abbasi et al., *IceCube Sensitivity for Low-Energy Neutrinos from Nearby Supernovae*, Astron.Astrophys. **535** (2011) A109, [arXiv:1108.0171].

[44] C. Rubbia et al., *Underground operation of the ICARUS T600 LAr-TPC: first results*, Journal of Instrumentation **6** (2011), no. 07 P07011.

[45] R. Acquafredda et al., *First events from the CNGS neutrino beam detected in the OPERA experiment*, New J.Phys. **8** (2006) 303.

[46] P. Alvarez Sanchez et al., *Measurement of CNGS muon neutrino speed with Borexino*, Phys.Lett. **B716** (2012) 401–405. Reprinted by permission of Elsevier.

[47] T. Adam et al., *Measurement of the neutrino velocity with the OPERA detector in the CNGS beam*, JHEP **1210** (2012) 093.

[48] M. Antonello et al., *Measurement of the neutrino velocity with the ICARUS detector at the CNGS beam*, Phys.Lett. **B713** (2012) 17–22.

[49] P. Adamson et al., *Measurement of neutrino velocity with the MINOS detectors and NuMI neutrino beam*, Phys. Rev. D **76** (Oct, 2007) 072005.

[50] M. Tippmann, *private communication*, 2012.

[51] A. Ianni et al., *The measurements of 2200 ETL9351 type photomultipliers for the Borexino experiment with the photomultiplier testing facility at LNGS*, Nuclear Instruments and Methods in Physics Research A **537** (Feb., 2005) 683–697. Reprinted by permission of Elsevier.

[52] W. R. Leo, *Techniques for Nuclear and Particle Physics Experiments*, Springer Verlag, (1994).

[53] ET Enterprises, *Understanding Photomultipliers*, www.et-enterprises.com (2011).

[54] Burle, *Photomultiplier Handbook*, psec.uchicago.edu (1980).

[55] A. Brigatti et al., *The photomultiplier tube testing facility for the Borexino experiment at LNGS*, Nuclear Instruments and Methods in Physics Research A **537** (Feb., 2005) 521–536.

[56] O. Smirnov, P. Lombardi, and G. Ranucci, *Precision Measurements of Time Characteristics of ETL9351 Photomultipliers*, Instruments and Experimental Techniques **47** (2004), no. 1 69–80. Reprinted by permission of Springer.

[57] D. D'Angelo, *Towards the detection of subMeV solar neutrinos in Borexino: data readout, data reconstruction and background identification*, Ph.D.Thesis, Università di Genova (2004).

[58] D. Manuzio, *Towards the detection of submev solar neutrinos in Borexino: data reconstruction and analysis tools*, Ph.D.Thesis, Technische Universität München (2006).

[59] The ROOT System, *http://root.cern.ch* .

[60] Geant4, *geant4.cern.ch* .

[61] M. Ambrosio et al., *Measurement of the residual energy of muons in the Gran Sasso underground Laboratories*, Astropart. Phys. **19** (2003) 313–328.

[62] M. Wurm, *Cosmic Background Discrimination for Rare Neutrino Event Search in Borexino and LENA*, Ph.D.Thesis, Technische Universität München (2009).

[63] G. Bellini et al., *Cosmic-muon flux and annual modulation in Borexino at 3800 m water-equivalent depth*, Journal of Cosmology and Astroparticle Physics **2012** (2012), no. 05 015.

[64] M. Wurm, *private communication*, 2013.

[65] Y. Fukuda et al., *Measurement of the Flux and Zenith-Angle Distribution of Upward Through-going Muons by Super-Kamiokande*, Phys. Rev. Lett. **82** (Mar, 1999) 2644–2648.

[66] A. Habig, *Neutrino induced upward going muons in Super-Kamiokande*, `hep-ex/9903047`.

[67] K. Hagiwara et al., *Review of Particle Physics*, Physical Review D **66** (2002) 010001+.

[68] D. Measday, *The nuclear physics of muon capture*, Physics Reports **354** (2001) 243 – 409.

[69] H. V. Argo, F. B. Harrison, H. W. Kruse, and A. D. McGuire, *Absorption of μ^- Mesons in C^{12}*, Phys. Rev. **114** (Apr, 1959) 626–633.

[70] E. J. Maier, R. M. Edelstein, and R.T. Siegel, *Measurement of the Reaction $\mu^- + C^{12} \to B^{12} + \nu$*, Phys. Rev. **133** (Feb, 1964) B663–B675.

[71] G. T. Reynoldset al., *Muon Capture on Carbon*, Phys. Rev. **129** (Feb, 1963) 1790–1794.

[72] T. Suzuki, D. F. Measday, and J. P. Roalsvig, *Total nuclear capture rates for negative muons*, Phys. Rev. C **35** (Jun, 1987) 2212–2224.

[73] N. Agafonova et al., *Measurement of the atmospheric muon charge ratio with the OPERA detector*, The European Physical Journal C **67** (2010) 25–37.

[74] R. Möllenberg, *private communication*, 2012.

[75] V. Kudryavtsev, N. Spooner, and J. McMillan, *Simulations of muon induced neutron flux at large depths underground*, Nucl.Instrum.Meth. **A505** (2003) 688–698.

[76] M. Aglietta et al., *Muon "depth-intensity" relation measured by the LVD underground experiment and cosmic-ray muon spectrum at sea level*, Phys. Rev. D **58** (Oct, 1998) 092005.

[77] P. Antonioli et al., *A three-dimensional code for muon propagation through the rock: MUSIC*, Astroparticle Physics **7** (1997), no. 4 357 – 368.

[78] A. Chavarria, *Neutron Detection in Borexino*, internal Borexino report (2008).

[79] A. Empl, *private communication*, 2012.

[80] Los Alamos National Laboratory, US Evaluated Nuclear Data File, *http://t2.lanl.gov/nis/data.shtml*, 2013.

[81] International Atomic Energy Agency, *http://www.iaea.org*, 2012.

[82] S. Abe et al., *Production of Radioactive Isotopes through Cosmic Muon Spallation in KamLAND*, Phys.Rev. **C81** (2010) 025807. Reprinted by permission of Nature Publishing Group.

[83] O. Smirnov, *pp-neutrino analysis*, internal Borexino presentation (2011).

[84] D. D'Angelo, *private communication*, 2012.

[85] P. Mosteiro, *private communication*, 2009.

[86] R. Saldanha, *Reduction of ^{11}C background in Borexino*, internal Borexino report (2009).

[87] FLUKA, *http://www.fluka.org* .

[88] G. Bellini et al., *Cosmogenic Backgrounds in Borexino at 3800 m water-equivalent depth*, to be submitted.

[89] G.Bellini et al., *The Borexino detector response and its full simulation*, to be submitted.

[90] R. B. Firestone, V. S. Shirley, C. M. Baglin, S.Y. Frank Chu, and J. Zipkin, *Table of Isotopes CD- ROM Edition, Version 1.0, March 1996*, *http://ie.lbl.gov/* . Reprinted by permission of R. B. Firestone and the John Wiley & Sons, Inc..

[91] Triangle Universities Nuclear Laboratory, *http://www.tunl.duke.edu*, 2012.

[92] C. Galbiati et al., *Cosmogenic ^{11}C production and sensitivity of organic scintillator detectors to pep and CNO neutrinos*, Phys. Rev. C **71** (May, 2005) 055805.

[93] K. Eguchi et al., *First Results from KamLAND: Evidence for Reactor Antineutrino Disappearance*, Phys. Rev. Lett. **90** (Jan, 2003) 021802.

[94] T. Hagner et al., *Muon-induced production of radioactive isotopes in scintillation detectors*, Astroparticle Physics **14** (2000), no. 1 33 – 47.

Acknowledgements

An erster Stelle möchte ich meinen Professoren Stefan Schönert, Lothar Oberauer und Franz von Feilitzsch danken, die es mir ermöglicht haben, diese Doktorarbeit zu verfassen. Den Freiraum bei der Umsetzung meiner Projekte, sowie die damit verbundene Eigenverantwortung, habe ich sehr geschätzt. Als Mitglied des Borexino-Experiments konnte ich darüber hinaus fachliche, aber vor allem persönliche Erfahrungen sammeln, die unbezahlbar sind. Des Weiteren danke ich dem Excellence Cluster Universe, welches diese Doktorarbeit finanziert hat.

Mein besonderer Dank gilt Randolph Möllenberg, der sich durch meine gesamte Dissertation gekämpft hat. Die Arbeit profitierte sehr von seiner sorgfältigen Korrektur, der nicht einmal zahlreiche Auszüge offizieller Borexino-Publikationen gerecht wurden. Aber auch während meiner Promotion stand er immer für fachliche, wie auch lustige Diskussionen zur Verfügung.

Des Weiteren möchte ich mich bei meinen Bürokollegen Timo Lewke, Marc Tippmann und Jürgen Winter bedanken. Dank ihnen hatte ich wirklich eine tolle Zeit während meiner Promotion. Die gute Stimmung im Büro hat mir immer wieder die nötige Energie gegeben, wenn ich mal wieder an technischen Problemen verzweifelte. Auch ein Dankeschön an den Exil-Münchner Michi Wurm, mit dem ich während meiner Promotion sehr eng zusammengearbeitet habe.

Vielen Dank auch dem gesamten E15 Lehrstuhl; leider kann ich hier nicht jedem Einzelnen danken, da wir einfach zu viele Leute sind. Ich möchte aber betonen, dass ich während meiner Promotion das kollegiale und freundschaftliche Miteinander an unserem Lehrstuhl sehr geschätzt habe. Die Diskussionen über technische Probleme und anderen Unsinn haben meine Doktorarbeit und/oder meine Stimmung immer positiv beeinflusst. Ich möchte mich auch bei unserer Sekretärin Maria Bremberger bedanken, die für uns Doktoranden immer wieder bürokratische Klippen umschifft hat, und uns so den den Rücken für die Doktorarbeit freigehalten hat.

I also thank my colleagues from the Borexino collaboration. I'm in particular grateful to all the people, with whom I worked together on the seemingly endless effort to measure all the cosmogenic stuff in Borexino: Margherita Buizza Avanzini, Davide D'Angelo, Stefano Davini, Anton Empl, Evgeny Litvinovich, Werner Maneschg, Pablo Mosteiro, Yury Suvorov, and Michael Wurm. Unfortunately, the list of people who also supported me with good advice and input for my thesis is too long to be written down here. So, I simply say a big 'Thank you' to the whole Borexino collaboration.

Mein größter Dank gilt meiner Familie, die mich während der gesamten Doktorarbeit immer unterstützt hat. Vor allem meine Frau Sanja hat trotz Schwangerschaft alles getan, um mich zu entlasten und mir die Zeit zu geben, diese Dissertation zu verfassen. Ohne deine Unterstützung und Geduld wäre diese Doktorarbeit nicht möglich gewesen. Auch ein Dankeschön an meine Tochter, die mit ihrer Geburt gewartet hat, bis ich die Doktorarbeit eingereicht habe.